International School for Advanced Studies

PhD course in Statistical Physiscs

Academic Year 2014/2015

Aspects of Entanglement Negativity in One Dimensional Critical Systems

Thesis submitted for the degree of

Doctor Philosophiae

Supervisor

Dr. Erik Tonni

Candidate

Andrea Coser

October 12th 2015

"Half of these spells are all working on entanglement principles."
"Entanglement *is a spell."*
— Princess Bubblegum and Finn the Human, *Adventure Time*

Abstract

In this thesis we study entanglement in one-dimensional critical quantum many-body systems and in particular we will focus on disconnected regions. Given a system in a pure state, to quantify the amount of entanglement between a multicomponent subsystem and the rest of the full system we can use as an entanglement measure the renowned *entanglement entropy*. However, if we are interested in the entanglement shared among the disconnected regions, the entanglement entropy fails to be a good quantifier. The reason is that the state of the subsystem is in general mixed once the rest is traced out, and the entanglement entropy is a good measure of entanglement only for pure states. A good measure of entanglement in mixed states is the *logarithmic negativity*, which is the quantitative version of Peres' criterion of separability. The main advantage of the negativity with respect to other entanglement measures is the simplicity of its definition in terms of the density matrix describing the quantum state. Since the definition does not require any variational calculus, it is much more easily computable than any other entanglement measure, and therefore we can obtain some results also in complicated settings such as many-body systems.

We will be mostly interested in the configuration where the full system is divided into two parts, A and B. If we do not have access to the degrees of freedom in B, we can describe subsystem A through its reduced density matrix, where the degrees of freedom in B have been traced out. The residual subsystem in A will in general be left in a mixed state. Subsystem A is then divided again into two parts, A_1 and A_2, and we will be interested in the entanglement shared by these two components. Knowing the full density matrix, the logarithmic negativity can be easily computed from the eigenvalues of its partial transpose with respect to the degrees of freedom living in one of the two subsystems A_1 or A_2. However, the full density matrix of a many-body state is in general unaccessible, even numerically, since the size of the matrix grows exponentially with the size of the system. If we concentrate on critical systems whose low-energy physics can be described by a quantum field theory, we can resort to its powerful tools to compute the entanglement properties. In particular the main tool is the replica trick. The entanglement entropy is obtained from the moments of the reduced density matrix, while the negativity can be computed from the moments of the partial transpose. However, even the computation of the integer-order moments is not an easy task, and exact analytical results are known only for the simplest quantum field theories. Hence, throughout the thesis we will usually consider conformal field theories, which have an enhanced set of symmetries and therefore allow for some exact computations.

In the Introduction, we will try to frame this work by briefly reviewing some of the main topics in the literature of quantum many-body systems and quantum field theories where entanglement plays a crucial role. We will also describe what are the main features that are requested to a 'good' measure of entanglement, and we will review some of the main measures that have been considered so far in the context of quantum information. We will define the entanglement negativity and stress its main advantages, as well as its drawbacks. After reviewing some basic facts of conformal field theories, we will give some technical details on the computation of entanglement entropy and logarithmic negativity in general quantum field theories, which will be needed in the rest of the thesis.

In Chap. 2 we will start the study of the entanglement of several disjoint disconnected regions by considering the entanglement that the union of these regions share with the rest of the system. We will compute the integer-order Rényi entropies of the subsystem from which the entanglement entropy can be obtained through the replica limit. Unfor-

tunately, the exact analytic continuation to real order is still out of reach and therefore the entanglement entropy cannot be computed exactly. However numerical extrapolations allow to obtain some accurate estimates.

In the remaining chapters we will focus on the entanglement shared between two non complementary disjoint regions, through the computations of the entanglement negativity in different settings. In Chap. 3, we will consider a global quantum quench starting from a conformal boundary state and evolving through a conformal evolution. A general formula for the mutual information and the logarithmic negativity for two adjacent and disjoint intervals is given in the spacetime limit.

In Chap. 4 we focus on the XY chain and we recover a formula for the partial transpose as a sum of four fermionic auxiliary Gaussian density matrices, by generalizing some previous results for the reduced density matrix of spin systems and for the partial transpose of pure fermionc Gaussian states. Even if the computation of the negativity is still out of reach, we can obtain formulas for the integer-order moments of the partial transpose in terms of the correlation matrices relative to the two components and to the region in between them.

In Chap. 5 we will study the entanglement negativity for a free Dirac fermion field. Starting from the lattice results, we will obtain a path integral representation of the partial transpose which can be easily generalized to the continuum. With this representation of the partial transpose, we can construct all its integer-order moments and compute them for the simple conformal field theory of the free fermion. Again, the computation of the negativity could not be accomplished due to technical difficulties in the analytic continuation to real order. The same computation has been extended also to the modular invariant Dirac fermion and the Ising model, and the obtained formulas coincide with the ones already present in the literature. This analysis draws an interesting connection between some terms appearing in the formulas for the moments of the partial transpose (as well as of the Rényi entropies) found for the lattice models and the ones found for the corresponding theories describing their scaling limit.

Whenever possible, all the analytical results will be checked against numerical calculations performed on simple free chain models. In Chaps. 2 and 3 we will consider bosonic Gaussian states, specifically the harmonic chain in its ground state and out of equilibrium, while in Chaps. 4 and 5 we will consider fermionic systems, specifically the XX and Ising spin chains, and the tight-binding model.

Finally, we will draw some conclusions and discuss some open problems.

Contents

Chapter 1

Introduction

Since the foundation of quantum mechanics, entanglement has been acknowledged as the striking difference between the classical and the quantum world. Already in the early works by Einstein, Podolski and Rosen [1] in 1935, it was understood that entanglement may allow for tasks that are completely impossible in the classical realm [2]. The local action on a subsystem of a quantum system may affect drastically the state of all its other parts, even if spatially very far apart. The peculiar fact is that this change may happen instantaneously, which is intrinsically very different from the effect of usual classical correlations, when a local perturbation of the system may propagate and affect all the rest of it. This propagation is in fact still the result of local interactions in the system and it is strictly limited by some maximum velocity [3]. During those years, the instantaneous change of the quantum state of the system after a measurement was quite disturbing and was considered a great objection to giving to quantum mechanics the stature of a complete, sensible physical theory. Hidden variable theories where formulated to resolve the apparent paradox put forward by Einstein, Podolski and Rosen. In these theories some parameters are added to quantum mechanics and an experimenter who could know their value could also exactly predict the results of single experiments. The probabilistic nature of usual quantum mechanics is then relegated to a mere ignorance of these variables, and its predictions must be interpreted in a statistical sense. In 1964, Bell showed [4] that a hidden variable description is incompatible with the results of quantum mechanics: indeed, to reproduce exactly all of its predictions, one should indeed allow for classical information to propagate instantaneously. Ultimately, entanglement forbids a simple hidden variable interpretation without nonlocalities.

Even if entanglement was at the center of the debate on quantum mechanics since its foundation, it was only in the 1990s that it started to be considered as a resource within the context of quantum information. Entanglement can be exploited to perform tasks that are impossible or extremely inefficient in a pure classical setting, such as quantum teleportation [5] or quantum error correction [6]. Thus, the need of tools to understand how entanglement can be characterized, manipulated and quantified, was evident. In principle, we would like to be able to prepare the system in a state with a certain amount of entanglement, then perform some operations on it and exploit its nonlocal properties to perform some specific tasks. The rate of success is strictly related to the amount of entanglement we can store in our system. In the last decades, the technological advance

made it possible to prepare, manipulate and measure individual quantum systems, without loss of coherence. This means we can finally have access to the quantum world in its full potentiality. It is of the utmost importance to have a way to quantify the entanglement present in a given system, namely to define a measure of entanglement. The problem of understanding if two subsystems are entangled is fairly well defined, however the quantification of entanglement through a unique measure is actually highly nontrivial. Since entanglement is seen as a resource, the guiding principle is mainly operational: an entanglement measure should tell us how much of this resource is present in the state, and the resource is defined as the property that is initially present in the state, and cannot be increased performing a set of allowed operations. These are usually taken to be the local quantum manipulations performed by some experimenters which can act only on specific subsystems, and classical communications between the parties (for the exact definition, see Sec. 1.1.1). In Sec. 1.1.2 we will briefly discuss some of the main important problems and difficulties that one encounters while trying to find a consistent definition of an entanglement measure. Let us here mention that the problem can be essentially solved for bipartite pure states, and in this case the unique measure of entanglement is the Von Neumann entropy of the reduced density matrix of indifferently one of the two subsystems, the renowned *entanglement entropy* [7].

The entanglement entropy has the really nice property that it is defined independently of any observable of the system, and therefore it can be rightfully expected to capture the quantum correlations in a very universal way. Its simple definition, al least with respect to other proposed, more operational entanglement measures (a few examples can be found in Sec. 1.1), makes it amenable to be computed also in complicated situations, such as extended quantum systems. In the last fifteen years indeed, a large effort was produced to study entanglement properties of many-body systems through the computation of the entanglement entropy in different settings. For obvious reasons, it is not possible here to mention them all, we will just give an incomplete and arbitrary list in the following. However, many interesting and useful reviews can be found, discussing some important general aspects as well as specific models. Let us mention here the one by Amico, Fazio, Osterloch and Vedral [8], which is mainly focused on spin chains and condensed matter models of interacting fermions and bosons; the one by Eisert, Cramer and Plenio [9], which deals with the important topic of area laws emerging as a fundamental entanglement property of many-body systems; and finally the series of reviews edited by Calabrese, Cardy and Doyon [10] (and references therein), which cover many different topics where entanglement entropy has been widely studied. This great amount of work was well justified by the success of entanglement entropy in probing the universal features of many-body systems around their critical points. For example, as we shall see in Sec. 1.4, the entanglement entropy of a block of continuous spin in a quantum spin chain at criticality has a very 'clean' dependence on the central charge of the underlying conformal field theory (for the definitions, see Sec. 1.3). This observation provides in many situations the best way to numerically evaluate the central charge of a specific system, thus establishing its universality class.

One of the most important results in the study of entanglement in many body-systems is the appearance of the so called *area law* [11–15]. Consider a general d-dimensional spin system in its ground state, and a block A of contiguous spins. For theories with local interactions, the quantum correlations are expected to be concentrated among spins close to the boundary separating A and its complement. Thus, the amount of entanglement, measured for example by the entanglement entropy, should naturally scale with the area of such boundary, $S_A \sim \mathrm{Area}\left(\partial A\right)/a^{d-1}$, where a is an ultraviolet scale, such as the

lattice spacing. These ideas were actually first put forward and explored in the context of black hole physics [16, 17], where it was suggested that this entanglement property could be at the origin of the black hole entropy, given by the Bekenstein-Hawking formula [18, 19], which is in fact proportional to the area of the boundary surface of the black hole. An important violation of the area law appears for example in critical one-dimensional quantum systems, where it was found [20] that the entanglement entropy scales as the logarithm of the block size. Another important case is the one of certain fermionic systems in higher dimensions with a Fermi surface [21], where again logarithmic corrections are present. Quite surprisingly, with a little effort one can also design specific spin chains with local interactions, whose critical ground state entanglement follows a volume law [22], since the system naturally organizes with an accumulation of singlet bonds across the half chain. This means that, even if area laws are usually intended to follow from the locality of the interaction, this statement must be taken with some care.

In two dimensions, a very interesting class of systems are the ones displaying topological phases. The area law in two dimensions reads $S_A \sim \alpha L/a - \gamma + \ldots$, where L is a typical length of subregion A, the coefficient α is non-universal, the ellipses stand for terms that vanish for large L, and finally γ is called the *topological entropy* [23, 24]. This terminology comes from the fact that γ is shown to be a topological invariant, and it is directly related to the total quantum dimension. In this picture, a topological ordered state is supposed to have nonlocal entanglement, hence by computing the entanglement entropy and isolating the constant term in the size of the subsystem, we have a tool to detect topological order. Prototypical examples of this situation are the Kitaev model [25] and the two-dimensional electron gases in large magnetic fields in the fractional quantum Hall regime [26].

A phenomenon with deep relations with the topological entropy arises also in one-dimensional quantum models in the presence of boundaries, of some defects, or in general of inhomogeneities. Close to the critical point, the entanglement entropy scales logarithmically, but a non-universal additive constant is present [27], and it is related to the boundary entropy g [28], a universal quantity depending only on the boundary conditions. The boundary entropy has been studied for example in spin chains in the presence of a boundary [29], and in the Kondo model [30, 31]. The connections between the impurity entropy in one-dimensional systems and the topological entropy in two-dimensional systems is understood in terms of the connection between a two-dimensional topological insulator and a one-dimensional edge model [32, 33].

Entanglement has also proven to be of fundamental interest in the development of numerical algorithms for simulating quantum systems, as for example the Matrix Product States (MPS) [34, 35]. In turns out that the amount of entanglement of a quantum state determine its possibility to be simulated classically. The number of parameters that should be stored in a classical computer to exactly describe a quantum many-body system grows exponentially with the size, and soon exceeds our technological possibilities. However, the states appearing in many-body quantum systems, and in particular their ground states, are very peculiar and they are not typical states of the full Hilbert space. We can think of these states living in a small corner of the Hilbert space, and by characterizing such corner we can provide a much more efficient description of the interesting states. Ultimately, the number of relevant parameters to have an approximate but faithful description of a quantum state grows with the amount of entanglement present [36]. Usually, these parameters are stored in tensors, whose dimensions should increase exponentially with the entanglement present. Gapped one-dimensional systems in their ground states have a finite amount of entanglement and can therefore be faithfully simulated, and their

properties are indeed computed at a very high precision. On the contrary, ground states of critical one-dimensional systems have much more entanglement. One can still extract some sensible information from the simulations, but more care is in order [37]. Unfortunately, in more than one dimension, the area law forces the tensors to grow exponentially with the size of the system, thus making impossible to reach large system sizes. This explains the failure of Density Matrix Renormalization Group techniques [38, 39] (which are based on MPS [34, 35]) in two dimensions. Other techniques have been studied however to circumvent these difficulties: Tree Tensor Networks (TTN) [40] and the Multiscale Entanglement Renormalization Ansatz (MERA) [41, 42] are designed to deal with critical one-dimensional systems, while Projected Entangled Pair States [43] are a generalization of MPS to two and more dimensions.

The great success of entanglement entropy in the study of many-body physics and its simple definition, make it amenable to compute it also in quantum field theory (QFT). QFT can effectively describe many-body systems at criticality, and its powerful tools can provide a deeper understanding of this regime. In this setting, the entanglement entropy is usually computed through the replica trick [20, 27, 44], which relates the entanglement entropy to the partition functions of the model on n-sheeted Riemann surfaces corresponding to n replicated copies of the system glued together in a particular way [45] (we will largely discuss the replica trick in Sec. 1.4). In QFT a large amount of work has been done to study the entanglement properties of free fields in one dimension [46–48], also for disconnected regions [49], and in two dimensions [50]. Also the case of general dimensionality in conformal field theory (CFT) have been recently considered and many interesting theoretical results have been found [51–54], which match with previous numerical works [55].

It is also worth mentioning the important developments that have followed some early works on entanglement entropy related to c-theorems [56, 57]. Using Lorentz invariance and the strong subadditivity property of the entanglement entropy, it was possible to find a quantity that fulfills the requirements of a good c-function [58] in $1+1$ dimensions (which however is not simply related to Zamolodchikov's c-function), thus showing a deep connection between entanglement and the irreversibility of the Renormalization Group flow between critical points. Historically, the extension of c-theorems to higher dimensions was found to be a very difficult task, and few results were available. For example, only recently in Ref. [59, 60] it was found the long sought proof of the analogous of the c-theorem in four spacetime dimensions, the so called a-theorem. Entanglement opens a new perspective on these problems, and in particular it allows to consider equally even and odd dimensions, that historically presented quite different challenges [61]. Some conjectures were put forward for the case in generic dimension [62, 63], but much of the work was dedicated to $2+1$ dimensions, where entanglement entropy helped again in proving the F-theorem [64–67]. One of the important issues that must be addressed in order to obtain a full generalization of c-theorems to any dimensionality, is the role of the regularization scheme used to deal with the ultraviolet divergences of the QFT. A good candidate for a c-function must in fact be independent of any regulator. Important steps in this direction were made in Refs. [68, 69], where a class of covariant geometric regulators were introduced, which make all the terms in the entanglement entropy assume a geometrical character, and in Ref. [70], were it is suggested that mutual information could be the correct quantity to look at, thanks to its ultraviolet finiteness.

Entanglement properties of QFT can be also studied by means of the holographic principle [71, 72], in the context of the AdS/CFT correspondence [73]. Interestingly enough, the holographic principle originated from the Bekenstein-Hawking entropy of

black holes [18, 19], which exhibits an area law, and thus suggests that the relevant degrees of freedom of a d-dimensional system reside on a $(d-1)$-dimensional surface at its boundary. Since the seminal papers by Ryu and Takayanagi [74–76], an incredible effort has been produced to characterize the entanglement in the holographic context. Ryu and Takayanagi conjectured that the entanglement entropy of a spatial subsystem in a QFT with a holographic dual can be computed in the classical regime from the area of certain minimal surfaces, anchored to the entangling surface in the boundary and extending inside the bulk. Their very simple formula allowed for an extensive study of entanglement in many situations, among which there are the interesting cases of disconnected regions [77–80], out of equilibrium evolution [81–96], and in the context of the c-theorems discussed above [62, 63]. The Ryu-Takayanagi formula, despite being very natural and simple, remained a conjecture for many years and was proven only recently [97–99]. Corrections beyond the leading order of classical gravity in the bulk have been studied [100, 101], but are quite more involved than the zeroth-order formula. Finally, let us mention that in this context it is still not clear how to compute the Rényi enrtopies, a generalization of the entanglement entropy, even if several important steps have been made in that direction [66, 102].

Giving in few pages a complete review of all the research areas where entanglement has had an important role in the last ten years, is evidently an unfeasible task. Many important topics have been reluctantly omitted, even if their importance and the interest that they brought in the community should not be overlooked. Among the others, let us mention the essential role of the so called *entanglement spectrum* [103] in the study of universal features characteristics of many-body systems in their different phases, and the deep insight that the evolution of entanglement [104–106] has brought in the field of out-of-equilibrium physics (this topic will be further discussed in Chap. 3). We hope we could at least give a flavor of the many interconnections that the study of entanglement has brought between seemingly distant fields, such as quantum information, many-body quantum physics and high energy physics. Entanglement plays a crucial role in all these fields in describing and characterizing the systems under investigations, and this eclectic aspect is probably ultimately due to the universal and fundamental role of entanglement in the quantum description. Probably, some of the most surprising aspects of this interplay come from the recently developed connection between quantum information and quantum gravity [107, 108]. A very evocative and intriguing point of contact between these two fields concerns the possibility of the bulk space time in the holographic description of quantum states to be deeply related to the tensor network structure of MERA [109–116].

Its should be clear by now that entanglement is a key quantity to look at in many areas of physics. Its quantification and characterization is very fundamental in quantum information, where entanglement is seen as a resource. In many-body systems, quantum field theory, holography, the entanglement structure of the system gives very important information on the underlying physics, and entanglement measures are the basic tools to quantify the amount of the entanglement present. This role has been egregiously played for pure states by the entanglement entropy. However, for mixed states, the situation is much more complicated since the entanglement entropy fails in correctly quantifying the quantum nonlocal correlations. Many other entanglement measures can be defined, which perfectly work also for mixed states, however they are usually very difficult to compute, even for small systems, and they are practically useless for extended many-body systems. An important exception is provided by the *logarithmic negativity* [117–119], a full entanglement measure based on the observation that the entanglement in a bipartite mixed state is related to the presence of negative eigenvalues in the partial transpose of

the density matrix [120]. Its simple definition makes its computation much more accessible, and therefore it is a good candidate to be a practical and useful tool to quantify entanglement in complicated settings such as many-body systems [121–133]. Moreover, a systematic path integral approach to construct the moments of the partial transpose of the reduced density matrix has been developed and from this the negativity in 1+1 dimensional relativistic quantum field theories is obtained via a replica trick very similar to the one for the entangelemnent entropy [134, 135]. This recent approach has been successfully applied to the study of one-dimensional conformal field theories (CFT) in the ground state [134–136], in thermal state [137, 138], and in non-equilibrium protocols [138–140], as well as to topological systems [141–143].With the same techniques it is also possible to consider massive QFT [144], where the negativity displays a very high level of universality. The CFT predictions have been tested for several models [135–137, 145, 146], especially against exact results [126, 135, 137] for free bosonic systems (such as the harmonic chain). Indeed for free bosonic models, the partial transposition corresponds to a time-reversal operation leading to a partially transposed reduced density matrix which is Gaussian [147] and that can be straightforwardly diagonalised by correlation matrix techniques [148–151]. Focusing on one-dimensional CFT in the ground state, the negativity is explicitly known only for the simple (but non trivial) geometry of two adjacent intervals embedded in a larger system. For the very important case of the entanglement between two disjoint intervals only the limit of close intervals is explicitly known. For arbitrary distances between the intervals, the main difficulty is to find the analytic continuation of the even-integer moments of the partial transpose, although these moments are analytically known in a few cases [135, 136]. However, the numerical interpolation techniques introduced in Ref. [152] and which we are going to discuss in Sec. 2.6, can been exploited to have an approximate prediction for the negativity. A deeper analysis of the negativity is of course of great interest, and this thesis is devoted to the study of different aspects of this entanglement measure in various settings, both in lattice systems and in QFT. We will concentrate on critical one-dimensional systems which can be described by CFT.

In the remainder of this Introduction, in Sec. 1.1 we will give a brief review of the requirements needed by a function of the state to be a good entanglement measure and what are the problems that one encounters when trying to define such measures. Sec. 1.2 slightly deviates from the main topic of this thesis and discuss how it is possible to actually measure the amount of entanglement in an extended system in real experiments. This task, that for many years was suspected to be impossible, is now approachable with the modern technologies developed in cold-atom systems. In Sec. 1.3 we will review some basic aspects of CFT, especially focusing on the results that we will be using in the rest of the thesis. Finally, in Sec. 1.4 we will discuss how the negativity can be computed in QFT, and especially in CFT, define some of the quantities that will be recurrently used throughout the thesis, and describe their main properties. Finally, in Sec. 1.5 we will give the outline of the thesis, together with the references to the original works.

1.1 Local quantum operations, entanglement measures and logarithmic negativity: a quantum information perspective

Since entanglement has proven to be a fundamental tool in many areas of physics to better understand the properties of quantum systems, it is of course of the utmost importance to develop a coherent description aimed at the quantification of the entanglement present in a quantum state. This is a highly non trivial problem, since even the characterization

of entanglement is not so immediate. This goal was historically first sought in the field of quantum information, where entanglement is seen as a resource to perform tasks that are impossible (or very inefficient) by using only classical tools. One of the most famous examples in that respect is quantum teleportation [5]. From this point of view, with entanglement considered as a resource, its characterization is strongly operational and it is related to the possible operations that can be performed on the system. The typical setting is the one where to parties, usually denoted by Alice and Bob, share a quantum system, but they are separated in space and can only act on the system locally (local in a sense to be specified later). If we restrict the operations that can be performed on the system to, for example, the local operations performed by Alice and Bob, any state that cannot be created with these operations becomes a resource, since it allows to overcome the constraint imposed by the choice of admissible operations.

Taking this operational perspective, many measures of entanglement can be defined depending on what specific task is considered, however there are some requirements that all 'good' measures of entanglement must satisfy [153, 154]. There are then other properties that may be desirable, but are not considered strictly necessary. In the literature there are many proposed entanglement measures, and they all have pros and cons and may be more or less useful depending on the specific task which is at hand. A complete, precise picture is still lacking, a part for some specific cases, for example the pure-state entanglement of a bipartite system, in some asymptotic sense [7].

In the following we will try to give a brief review of the possible characterization of the local operations that can be performed by Alice and Bob, as well as a (forcibly) incomplete discussion on some of the most important entanglement measures that have been proposed. We will finally focus our attention on the logarithmic negativity, whose computation in different settings in strongly correlated extended systems is the main topic of this thesis. We will try to give a characterization of this quantity from the quantum information perspective, in order to establish its usefulness as a quantifier of the amount of entanglement of a given system, as well as some of its limitations.

1.1.1 LOCC and PPT transformations

As already mentioned, the typical setting we consider is the one where two parties, Alice and Bob, share a quantum system but they can act locally only on a specific subsystem, that will be denoted respectively as A and B. They are also allowed to communicate classically, namely they can send classical information one to the other. For example, Alice may report to Bob the outcome of a measurement she performed on her subsystem, and Bob may then choose to act on his share of the system depending on such classical outcome. The set of transformations combining *local quantum operations* (LO) and *classical communication* (CC) is usually denoted LOCC, and it is very difficult to precisely characterize mathematically. Let us stress again that the definition of a set of operations allows to define entanglement as the resource that cannot be created by these transformations only. LOCC operations are not completely local, since classical communication is allowed, however it is evident that they do not exhaust all possible operations, as for example they do not allow for the exchange of quantum information between the parties. In order to perform general nonlocal quantum operations within the LOCC constraint the resource of inherent quantum correlations is necessary. In this context, *classical correlations* can be defined as the ones that can be created by LOCC, while *quantum correlations* are the ones that are already present in the system, and cannot be generated by acting locally on subsytems A and B.

A mathematical simple characterization of LOCC is very hard and it is indeed still lacking. It is easier to first consider the most general quantum operation on a system, which can be divided into three basic steps: one or more ancillae particles are added to the system, then some unitary operation and some measurements are performed to the joint system, and finally some particles are discarded, possibly according to the results of the previous measurements. Mathematically, this situation can be described in the formalism of completely positive superoperators [155]. The result of any operation on the density matrix ρ of the system can be described by means of Kraus operators as follows,

$$\rho \to \rho_k = \frac{1}{p_k} \sum_j V_{k,j}\, \rho\, V_{k,j}^\dagger, \qquad p_k = \mathrm{Tr}\Big[\sum_j V_{k,j}\, \rho\, V_{k,j}^\dagger \Big]. \tag{1.1}$$

Here the index j refers to the possibility that some of the outcomes of the measurements that took place in the process might not be accessible, and the resulting state might be a mixed state, even if the original one was pure (a process called decoherence). The index k corresponds instead to the outcomes of the measurements when all the information is retained. The process is stochastic, and the result ρ_k is obtained with probability p_k. When there is only one $p_k = 1$, the process is a deterministic state-to-state operation, and $\rho \to \sum_j V_j\, \rho\, V_j^\dagger$. The normalization of probabilities implies that Kraus operators $V_{k,j}$ must satisfy $\sum_{k,j} V_{k,j}^\dagger V_{k,j} = 1$.

It would be natural to think that the local quantum operations in the LOCC setting correspond to the so called *separable* operations, whose Kraus operators are in a product decomposition according to subsystems A and B, $V_{k,j} = A_{k,j} \otimes B_{k,j}$. Actually, every LOCC operation (not only LO) can be cast in this form, but it can be proven [156] that there exist some operations of this kind that cannot be completed with LOCC only, and require for example to transmit a finite amount of quantum information. Hence we have LOCC $\subset$ separable. There exists an even more general class of operations, which is very important for the study of the logarithmic negativity, that is the positive partial transpose preserving operations (PPT) [157, 158]. On a given local orthonormal basis $|e_i^A,\, e_j^B\rangle$, the density matrix can be written as $\rho = \sum_{ijkl} \rho_{ij,kl}\, |e_i^A,\, e_j^B\rangle\, \langle e_k^A,\, e_l^B|$, and its partial transposition with respect to subsystem B is given by

$$\rho^{T_B} = \sum_{i\,j\,k\,l} \rho_{ij,kl}\, |e_i^A,\, e_l^B\rangle\, \langle e_k^A,\, e_j^B|\,. \tag{1.2}$$

The density matrix ρ is a positive definite operator, however this is not assured for the partial transposed operator. It has been proven that a necessary condition for a state to be separable (and therefore contain no entanglement) is the positivity of its partial transpose [120, 159, 160]. The converse is not true in general, meaning that there exist states with positive partial transpose that are not separable. The PPT operations are the completely positive maps Φ such that $\Gamma_B \circ \Phi \circ \Gamma_B$ is also completely positive, Γ_B being the partial transposition with respect to B. It makes sense to study the classes of separable and PPT operations since they are much easier to deal with mathematically than the LOCC operations. Moreover, since it is possible to prove the strict inclusions LOCC $\subset$ separable $\subset$ PPT, by optimizing a given task in these classes one may find bounds on what may be achieved by LOCC.

1.1.2 Entanglement measures

Once the set of allowed operations is specified, and the concept of entanglement as a resource is well defined, the next step is to provide some measures of entanglement which

can quantify the amount of the resource in a given system. Let us first make some important observations. *Separable states* [161] are the ones whose density matrix can be written as

$$\rho = \sum_i p_i \, \rho_A^i \otimes \rho_B^i. \tag{1.3}$$

Any separable state can be converted to any other separable state by LOCC only [162], therefore they are all locally equivalent, their correlations are only classical and they do not contain any entanglement. On the contrary, all non-separable states, namely those that cannot be written as in (1.3), cannot be generated by LOCC only, and they may allow for more general operations. We already mentioned that there were found states that are not separable but have positive partial transpose. From these states it is not possible to distill entanglement in the form of maximally entangled states, which is the golden standard for quantum communication purposes. This type of undistillable entanglement is called 'bound' entanglement [160].

Another important observations is the following. For the same reason that LOCC can only generate separable, non-entangled states, entanglement cannot increase under LOCC manipulations [6]. Consider a state which can be reached starting from another state by performing LOCC only. Then the resources in the final state cannot be more than the ones in the initial state [7, 163, 164]. Moreover, since local unitaries are reversible, any two states that are connected by a local unitary must have the same entanglement. Finally, let us also notice that there exist *maximally entangled states*, namely states from which any other state can be obtained through LOCC operations. In the case of two subsystems of same finite dimension d, the maximally entangled states are the ones unitarily equivalent to

$$|\psi_d^+\rangle = \frac{|0,0\rangle + |1,1\rangle + \cdots + |d-1,d-1\rangle}{\sqrt{d}}. \tag{1.4}$$

Maximally entangled states are the ones used to efficiently perform many quantum communication task and therefore they are considered the 'coin' which can be spent for such purposes.

These observations lead to the hope for the set of density matrices to be totally ordered under the LOCC operations. If this was the case, we could say that the state ρ_1 is more entangled than the state ρ_2 if there exists a transformation which implements $\rho_1 \to \rho_2$. Unfortunately, this turns out to be false, since it can be proven that in general there are incomparable states [165], and therefore LOCC manipulations can only induce a partial order in the set of the quantum states. The last observation makes it very difficult to build a classification of entanglement based on LOCC. In the literature, such operational approach was replaced by an alternative, axiomatic point of view [163]: we can define quantities which satisfy a set of minimal postulates, and use them to try to quantify the entanglement of the states. However, the requirements needed may vary among different authors and many choices of entanglement measures may be more suitable and useful in different situations, depending on the particular need. The minimal property that any map $E(\rho)$ from density matrices to real numbers must satisfy in order to be an *entanglement measure* is monotonicity under any deterministic LOCC transformation [153, 154],

$$E\Big(\sum_j V_j \, \rho \, V_j^\dagger\Big) \leqslant E(\rho), \tag{1.5}$$

where V_j is the Kraus operator introduced in Eq. (1.1). The known entanglement measures usually satisfy the stronger requirement that $E(\rho)$ does not increase on average under

stochastic LOCC operations [162, 166],

$$\sum_k p_k E(\rho_k) \leqslant E(\rho), \tag{1.6}$$

where the ρ_k's and the p_k's are the ones of Eq. (1.1). Notice that monotonicity is requested on average, in the sense that a particular measurement outcome may correspond to an increase of the entanglement. However this process cannot be used to systematically increase the amount of resources of the system. This condition is often easier to prove, but it is less fundamental than (1.5), in the sense that it describes the entanglement of an ensemble $\{p_k, \rho_k\}$, which is a less operational notion than the notion of a state [153, 154]. The monotonicity under LOCC operations implies that for any separable states, $E(\rho)$ takes a constant value, which is its minimal one [162]. Without loss of generality we can set this value to zero. A function satisfying Eq. (1.6) and such that vanishes on separable states is usually called an *entanglement monotone* [153, 162].

There are other postulates that one may ask to be satisfied by an entanglement measure, depending on the particular needs. Such properties are however considered optional, and can be added because they are often mathematically convenient. A common additional requirements is convexity, which is sometimes justified with the notion that entanglement cannot increase under the loss of information due to mixing, $E\big(\sum_i p_i\rho_i\big) \leqslant \sum_i p_i E(\rho_i)$ [162]. This requirement must not be confused with the physical process of discarding information (for example tracing out a marker particle), which is much more fundamental and it is included in (1.6) [153, 167]. Another useful property that can be requested is *additivity*, namely $E(\rho^{\otimes n}) = nE(\rho)$. Notice that for any measure that is not additive, a regularized (or asymptotic) version can be defined, $E^\infty(\rho) = \lim_{n\to\infty}\big[E(\rho^{\otimes n})/n\big]$.

An entanglement measure is often defined to also coincide with the entanglement entropy when computed on pure states [153]. The *entanglement entropy* [7] is defined as the Von Neumann entropy of the reduced density matrix over subsystem A

$$S_A(\rho) = -\operatorname{Tr}_A(\rho_A \log \rho_A), \qquad \rho_A = \operatorname{Tr}_B \rho. \tag{1.7}$$

Notice that S_A is additive. Moreover, it satisfies two important inequalities [168, 169]

$$S_{AB} \leqslant S_A + S_B, \qquad \text{(subadditivity)} \tag{1.8a}$$

$$S_{ABC} + S_B \leqslant S_{AB} + S_{BC}, \qquad \text{(strong subadditivity)} \tag{1.8b}$$

where for example S_{AB} is the entanglement entropy relative to the union of the two subsystems A and B. The reason for this additional requirement is that it is believed to contain all relevant information of entanglement of pure states. However, it is important to stress that this statement is true only under certain hypothesis and in the asymptotic regime, when (infinitely) many copies of the system are taken into consideration. In this limit we can define two fundamental entanglement measures which have a very practical operational meaning, and really capture our intuition of entanglement seen as a resource for quantum information purposes (indeed they were defined and used before the axiomatic approach was considered). If we take n identical copies of the system $\rho^{\otimes n}$, the rate $r = m/n$ of transformation to approximately m copies of the 2-qubit maximally entangled state $|\psi_2^+\rangle\langle\psi_2^+|$, is given by the *entanglement distillation*, that can be defined concisely as follows [153]

$$E_D(\rho) = \sup\left\{r \,:\, \lim_{n\to\infty}\left[\inf_\Phi \operatorname{Tr}\left|\Phi\left(\rho^{\otimes n}\right) - \left(|\psi_2^+\rangle\langle\psi_2^+|\right)^{\otimes rn}\right|\right] = 0\right\}, \tag{1.9}$$

where Φ is a general LOCC operation. Conversely, the asymptotic rate of obtaining approximately n copies of the system starting from m copies of the maximally entangled state $|\psi_2^+\rangle\langle\psi_2^+|$ is called *entanglement cost*

$$E_C(\rho) = \inf\left\{r \,:\, \lim_{n\to\infty}\left[\inf_{\Phi} \mathrm{Tr}\left|\rho^{\otimes n} - \Phi\left(\left(|\psi_2^+\rangle\langle\psi_2^+|\right)^{\otimes rn}\right)\right|\right] = 0\right\}. \tag{1.10}$$

It has been proven that the entanglement cost and the entanglement distillation are extremal measure in the asymptotic limit [170], since they bound any other regularized measure, $E_D \leqslant E^\infty \leqslant E_C$. Moreover, it turns out that entanglement transformations of pure states become reversible in the asymptotic limit, and the rate of transformation is given by the entanglement entropy, $E_D(|\psi\rangle\langle\psi|) = E_C(|\psi\rangle\langle\psi|) = S_A(|\psi\rangle\langle\psi|)$. In practice, reversibility means that given a large number of copies of a pure state $|\psi_1\rangle\langle\psi_1|$, it is possible to distill $\approx nS_A(|\psi_1\rangle\langle\psi_1|)$ maximally entangled states, and then acting on these singlets it is possible to create $m \approx nS_A(|\psi_1\rangle\langle\psi_1|)/S_A(|\psi_2\rangle\langle\psi_2|)$ copies of another pure state $|\psi_2\rangle\langle\psi_2|$ [7]. For these reasons, it turns out that any additive and 'sufficiently continuous' entanglement monotone, must be equal to $S_A(\rho)$ on pure states [162, 170–172]. This strongly suggests that the entanglement entropy is the appropriate measure for pure states. The equivalence of all sufficiently regular measures on pure states is important also from a practical point of view. Indeed, it is very difficult to compute $E_D(\rho)$ and $E_C(\rho)$, since they contain variational expressions. The entanglement entropy is on the contrary much easier to compute.

The entanglement entropy can be seen as the Shannon entropy of the eigenvalues of the reduced density matrix. Analogously, we can define their *Rényi entropies* [173]

$$S_A^{(\alpha)} = \frac{1}{1-\alpha}\,\mathrm{Tr}_A\,\rho_A^\alpha, \tag{1.11}$$

with α a non-negative real number. The Rényi entropies are additive and the entanglement entropy S_A can be seen as a particular case when $\alpha \to 1$. For $0 \leqslant \alpha \leqslant 1$ the Rényi entropies are shown to be entanglement monotones [162] on pure states. Unfortunately, they do not reduce to the entanglement entropy on pure states, since they do not satisfy some asymptotic continuity condition [162]. As we will extensively discuss in Sec. 1.4, in QFT the integer-order Rényi entropies are very important, since there are techniques that allow some analytical and numerical computations.

Many other measures of entanglement can be defined satisfying the postulate of monotonicity under LOCC transformations, some of them also satisfy all or some of the other properties discussed. It is not possible here to make a survey of not even the most important ones, but a satisfactory list can be found in Refs. [153, 154]. Let us stress that with this axiomatic approach we can define quantities that can impose different orderings on the states. This is usually accepted as an evidence that no unique total ordering can be imposed. Different states may contain different form of entanglement, and different measures quantify the amount of entanglement which is useful for different specific operational tasks.

1.1.3 Logarithmic negativity

While the entanglement entropy is understood as the correct quantity to consider in order to quantify entanglement in pure states, there is still no analogous quantity for mixed states. The entanglement cost and the entanglement distillation are known to be different in general [174] and the process of generating a mixed state from a certain number of maximally entangled state is not reversible. If we distill the maximal

possible amount of entanglement from the generated mixed state, we will obtain a number of maximally entangled states smaller than the one we started with. Much effort has been devoted to the study of mixed-state entanglement and many measures have been proposed. One of the most important is the *entanglement of formation* [6], which is the minimal average entanglement over all possible pure state decompositions of ρ, $E_F(\rho) = \inf \left\{ \sum_i p_i S_A(|\psi_i\rangle \langle\psi_i|) \,:\, \rho = \sum_i p_i |\psi_i\rangle \langle\psi_i| \right\}$. It has been proven [175] that the regularized version E_F^∞ is equal to the entanglement cost E_C, but unfortunately it is not known if E_F is additive. Despite E_F being much easier to compute than the entanglement cost and distillation, the computation is still unfeasible in complicated settings such as many-body systems.

The (logarithmic) negativity [117–119] was introduced mainly to have a computable measure of entanglement for mixed states. It turns out that it has many interesting properties and an operational interpretation. The negativity can be seen as the quantitative version of Peres' criterion for separability [120, 159, 160], that we already mentioned in the last section. For any separable state, the partial transpose ρ^{T_B} according to subsystem B, defined in Eq. (1.2), is a positive definite operator. The positivity of the partial transpose however is not a sufficient condition for separability, except for some specific cases. For finite dimensional systems, it is a necessary and sufficient condition only for the smallest non trivial ones, with dimensions $2 \otimes 2$ and $2 \otimes 3$ [176]. Peres' criterion was also studied for oscillators (which are continuous variables, leaving in an infinite dimensional space) in a Gaussian state, where it was found that it also provides a sufficient condition when A contains only one oscillator and B an arbitrary number [177]. In all other cases, Peres' criterion is only a necessary condition. However, let us stress that the main advantage of Peres' criterion resides in its extreme simplicity from the point of view of explicit computations.

The *negativity* quantifies the violation of positivity of the partial transpose,

$$\mathcal{N}(\rho) = \frac{\|\rho^{T_B}\|_1 - 1}{2}. \tag{1.12}$$

Here $||X||_1 = \mathrm{Tr}\sqrt{X^\dagger X}$ is the trace norm, and for Hermitian matrices can be computed as the sum of the modulus of the eigenvalues. It is easy to see that $\mathcal{N}(\rho)$ corresponds to the absolute value of the sum of the negative eigenvalues of ρ^{T_B}. It can be shown [119, 167, 178, 179] that $\mathcal{N}(\rho)$ is an entanglement monotone under LOCC operations (both deterministic and stochastic), it is convex, but it is not additive. The negativity provides an upper bound to teleportation capacity [119], but unfortunately its does not have a striking operational interpretation. In the rest of this thesis we will always consider the logarithmic negativity and, a part from this section, we will often refer to it as the entanglement negativity, or simply negativity. *Logarithmic negativity* [119] is defined as follows[1],

$$\mathcal{E}(\rho) = \log \|\rho^{T_B}\|_1. \tag{1.13}$$

It is additive by construction, and the monotonicity under deterministic LOCC operations is guaranteed by the monotonicity of $\mathcal{N}(\rho)$. It can be also proven the stronger monotonicity condition under stochastic LOCC. Actually, it was proven the monotonicity under the more general class of PPT operations, of both the negativity and the logarithmic negativity [167]. An important drawback of the logarithmic negativity is that it fails to reduce to the entanglement entropy on all pure states [119], since it lacks the required continuity in the asymptotic regime.

[1] In the quantum information community the logarithm is often taken on base 2, while we will usually consider the natural logarithm.

Logarithmic negativity gives an interesting upper bound to distillable entanglement [119], and it also has a direct operational interpretation as it is directly related to the exact entanglement cost under PPT operations [180]. The *exact entanglement cost* has a slightly different definition from $E_C(\rho)$ defined in Eq. (1.10). It is indeed the rate r of preparing exactly n copies of the system from $m = rn$ copies of the maximally entangled state. On the contrary, the entanglement cost requires that such rate is reached only asymptotically. Mathematically, this corresponds to taking the asymptotic limit after the infimum,

$$E_C^{\text{exact}}(\rho) = \lim_{n\to\infty} \inf \left\{ r_n \,:\, \inf_{\Phi} \operatorname{Tr} \left| \rho^{\otimes n} - \Phi\left(\left(|\psi_2^+\rangle \langle \psi_2^+| \right)^{\otimes r_n n} \right) \right| = 0 \right\}. \tag{1.14}$$

It turns out that the logarithmic negativity coincide with $E_C^{\text{exact}}(\rho)$ for states with positive binegativity, $|\rho^{T_B}|^{T_B} \geqslant 0$. It is believed that the vast majority of the states is of this kind. In particular, all Gaussian bipartite states in systems with a finite number of canonical degrees of freedom are in this class [180]. An explicit example would be the ground state of a finite harmonic chain.

Finally, we also mention some recent results about a disentangling theorem involving the entanglement negativity [181]. Computing the negativity allows to understand if a tripartite pure state $|\Psi_{ABC}\rangle$, divided in three subsystem A, B and C, can be factorized in the product of two states $|\Psi_{AB_1}\rangle \otimes |\Psi_{B_2C}\rangle$, for some disjoint bipartition $B = B_1 \cup B_2$. Based on that theorem, the authors of Ref. [181] also conjecture a monogamy inequality for the negativity, which tells us that if a subsystem A is very entangled with B, it cannot be simultaneously very entangled also with C.

1.2 Experimental measures of entanglement

Despite the characterization of entanglement has proven to be an important tool in many areas of physics, from quantum computation to condensed matter physics and high energy physics, it seems difficult to devise a method to measure entanglement in real experiments in extended systems. Some of the main reasons of this difficulty lie exactly in the same features that make entanglement such an interesting property to look at: for example, it has a highly non-local nature, and it is defined without any reference to the observables of the systems. It is however clear that controlled ways to create entangled states and tools to detect and measure such entanglement are of the utmost importance.

In the past years, many proposals have been made for possible ways to quantify the amount of entanglement of a given many-body state, especially by estimating quantities such as the Rényi entropies (and in particular the second Rényi entropy), but a real life experiment which implemented them was still lacking. However, with modern techniques of single atom and single site resolution of strongly interacting systems in extended optical lattices [182, 183], this goal is in reach and experiments are being performed in these days [184–186] which should soon provide a major step towards entanglement detection.

In this section, we will briefly review some of the main proposed techniques to detect and measure entanglement, and we will discuss how some of them are being implemented nowadays in real experiments. Of course this discussion is far from being comprehensive, but the goal is to give further motivations on the importance of the theoretical study of entanglement properties of quantum many body systems.

1.2.1 Entanglement detection through Rényi entropies

Many of the most popular proposal of entanglement detection actually suggest the idea that it is far more easy to devise experiments where it is possible to estimate the integer-

order Rényi entropies of the reduced density matrix relative to a subregion A, Eq. (1.11), rather than the more celebrated entanglement entropy. In particular, the most easily accessible is the second Rényi entropy, which is minus the logarithm of the purity. In QFT, the n-th order Rényi entropy can be computed by means of the replica trick, where n copies of the system are glued together along the entangling region. This corresponds to the insertion of some twist operators, whose role is to implement the correct boundary conditions among the different copies. Experimentally, it is possible to have access to Rényi entropies by preparing n identical copies of the system and letting them interact in a specific way so that it is then possible to extract the expectation value of the shift operator $V^{(n)}$, whose action is to cyclically permute the n copies $V^{(n)} |\psi_1\rangle \dots |\psi_n\rangle = |\psi_n\rangle |\psi_1\rangle \dots |\psi_{n-1}\rangle$. The shift operator can be defined on any subregion of the entire system, for example the operator $V_A^{(n)}$ will permute the copies only in subregion A. This operator is extremely important for estimating the traces of powers of any density matrix ρ, since they can be computed as the expectation values of the shift operator on the replicated system, $\operatorname{Tr} \rho^n = \operatorname{Tr} \left(V^{(n)} \rho^{\otimes n} \right)$ [187]. In the following we will discuss two possible ways to go down this path experimentally: the first one, proposed by Cardy in Ref. [188] and also later exploited by Abanin and Demler in Ref. [189], consists in implementing the shift operation by performing a quantum quench on the n copies of the system. The second, proposed by Alves and Jaksch in Ref. [190] for $n = 2$ and extended to general n by Daley *et al.* in Ref. [191], requires the use of an optical lattice where the copies interfere by switching on the tunneling among them in a controlled way. By observing the system after this controlled interference, it is possible to have access to the value of the shift operator for any desired subsystem. In order to perform such an experiment, it is required single atom and single site resolution. This technology is available nowadays [182, 183, 192, 193] and experiments to estimate the purity of a one dimensional chain of few neutral atoms in an optical lattice are being designed at the time of writing [184–186]. The hope is that this setup could be scaled and larger system sizes will be reached in the future.

Rényi entropies from a quantum quench

The experimental protocol suggested by Cardy in Ref. [188] requires n identical copies of the desired system. In an optical lattice, these identical copies can be obtained preparing n systems in a low-entropy initial state, such as a Mott insulator [194, 195], and then performing the same manipulations of the optical lattices they live in. In this phase, interactions between the different copies are turned off by a large potential depth among them.

The quantum quench is performed as follows. At time $t = 0$, the n copies are disconnected along the entangling surface, separating the desired subregion A_i and its complement B_i. The action of the shift operator is now implemented by reattaching subsystem A_{i+1} to subsystem B_i in a cyclic manner. This operation acts on the Hamiltonian of the problem as the unitary operation $H' = \left[V_A^{(n)}\right]^{-1} H V_A^{(n)}$, and the new ground state can be simply obtained from the ground state $|\Psi\rangle$ of H, as $|\Psi'\rangle = \left[V_A^{(n)}\right]^{-1} |\Psi\rangle$. If we think of $H \to H'$ as a quantum quench, the fidelity is given by the probability of finding the initial state $|\Psi\rangle$ in the ground state of the evolving Hamiltonian H', namely $P_0 = |\langle \Psi' | \Psi \rangle|^2$. Using the Schmidt decomposition of $|\Psi\rangle$, the fidelity is easily seen to be identical to the trace of the integer powers of ρ_A

$$P_0 = \langle \Psi' | \Psi \rangle = \langle \Psi | V_A^{(n)} | \Psi \rangle = \operatorname{Tr} \rho_A^n. \tag{1.15}$$

The optimum would be now to measure the fidelity P_0 and directly obtain the Rényi

entropies. Unfortunately P_0 is not directly experimentally observable, however Cardy suggests to measure the probability $P(E)$ of finding the system in a low-lying excited state of energy E.

An important observation is that when A and B are spatially disjoint regions and H is short-range, the difference between H and H' is restricted to local terms at the boundary between A and B. In QFT, such local changes in the Hamiltonian are implemented by the insertion of operators along the entangling region. In one dimension, these operators are local and they are nothing else but twist fields (which are discussed in Sec. 1.4), hence schematically $V_A^{(n)} = \prod_k \mathcal{T}_n(u_k)$, with the correct combination of twists and anti-twists placed at the points u_k separating A and B. In systems close to a quantum critical point, with a linear dispersion relation, the powerful methods of CFT can be used to compute the twist field multi-point function $P_0 = \langle\Psi|\prod_k \mathcal{T}_n(u_k)|\Psi\rangle$.

The Laplace transform of $P(E)$ can also be written in terms of twist fields, and therefore is universal (remember that $P(E)$ describes the population of the states with energy much less than the energy cutoff)

$$\int \mathrm{d}E\, P(E)\, e^{-E\tau} = \langle\Psi|e^{-(H'-H)\tau}|\Psi\rangle = \langle\Psi|\Big(\prod_k \mathcal{T}_n(u_k,\tau)\Big)\Big(\prod_k \mathcal{T}_n^\dagger(u_k,\tau)\Big)|\Psi\rangle\ . \tag{1.16}$$

With this observation, Cardy shows that for systems close to a quantum critical point described by a CFT, $P(E)$ turns out to be P_0 times a factor which can be computed, at least approximately, for a single twist in ungapped systems, for integrable gapped system with the results of Ref. [45], and for multiple twists with the method described in Ref. [196].

Cardy's proposal shows how in principle Rényi entropies are measurable, but it is not likely to be put in practice. The quantity $P(E)$ can be measured in principle if the system is weakly coupled to other modes that can be analyzed, but its relation with the fidelity P_0 is not straightforward and can be computed only for specific systems (ungapped systems described by CFT, integrable gapped systems) and for simple geometries.

Another way to determine P_0 has been proposed by Abanin and Demler in Ref. [189]. In their setup, the n copies are placed in a way that the points separating A and B are close together and are all coupled with a quantum switch. The switch can be in two states, $|\uparrow\rangle$ and $|\downarrow\rangle$, which controls the connections between the subsystems. If the switch is in state $|\uparrow\rangle$, then subsystem A_j is connected to B_j, while if the switch is in state $|\downarrow\rangle$, A_{j+1} is connected with B_j cyclically.

The authors propose also a way to design such a switch in the context of cold atoms. If A consists of a half chain, then $2n$ half chains are placed in a star geometry, with all half chains close to each others by an endpoint. Each branch of the star is a subsystem A or B alternately. At the center of the star, there are n dipolar molecules which are subject to a potential with $2n$ wells situated on the lines connecting the last sites of the neighboring $2n$ branches. The dipolar molecules interact repulsively between each others, so that their ground state will be doubly degenerate, with the wells alternately occupied and unoccupied. Moreover, they are required to interact repulsively also with the atoms in the chain, thus preventing tunneling among two half chains when the well in between them is occupied.

If the two states of the switch are decoupled, then the full spectrum of the system is divided into two independent sectors, with ground states $|\mathrm{GS}\rangle = |\uparrow\rangle \otimes |\Psi\rangle$ and $|\mathrm{GS}'\rangle = |\downarrow\rangle \otimes |\Psi'\rangle$. It is possible to add dynamics with a term in the Hamiltonian that couples the two states of the switch, $H_t = T\,(|\uparrow\rangle\langle\downarrow| + |\downarrow\rangle\langle\uparrow|)$. We want however to keep the

tunneling parameter T much smaller than the gap Δ between the two ground states and the first excited states in each sector (in a critical system, Δ is given by the finite size of the chain). In such a setup, we can consider only the two states $|\mathrm{GS}\rangle$ and $|\mathrm{GS}'\rangle$ and the effective low-energy Hamiltonian is given by $H_{\text{eff}} = \tilde{T}\left(|\mathrm{GS}\rangle\langle\mathrm{GS}'| + |\mathrm{GS}'\rangle\langle\mathrm{GS}|\right)$, with $\tilde{T} = T\langle\Psi|\Psi'\rangle$. Finally, the coefficient $\tilde{T}$ can be measured experimentally by studying the Rabi oscillations of the system: the switch is prepared in state $|\uparrow\rangle$ and at a certain time the tunneling T is switched on. The population of the two states will oscillate, and the difference of the probability of finding the state in $|\mathrm{GS}\rangle$ and $|\mathrm{GS}'\rangle$ at time t, is $P_{\mathrm{GS}} - P_{\mathrm{GS}'} = \cos(\tilde{T}t/\hbar)$. The renormalized tunneling enters in this expression as the Rabi frequency, which can be extracted by a measurement of the occupation probabilities.

These ideas can be in principle exported to two dimensional systems too, but the realization in real experiment becomes extremely more cumbersome. Moreover, the same setup of the quantum switch proposed in Ref. [189] has been recently extended in Ref. [197] to allow the measure of the evolution of entanglement in time. In this setup, all the copies of the system are prepared in the same product state over all sites, while the quantum switch in the initial state $(1/\sqrt{2})\big(|\uparrow\rangle + |\downarrow\rangle\big)$. The system is then left to evolve up to time t. It is found that a measure of the operator $\sigma^x(t)$ of the quantum switch,gives the n-th Reényi entropy at time t.

Rényi entropies from HOM-interference of many body states

Another approach for measuring the Rényi entropies for neutral bosons in optical lattices is discussed in Refs. [190, 191]. The goal is again to design an experimental apparatus able to determine the value of the shift operator, namely to measure $\mathrm{Tr}\left(V_A^{(n)}\rho_A^{\otimes n}\right)$, from which the Rényi entropies can be directly extracted. While the method described previously works only when the initial state is the ground state of the initial Hamiltonian, this second proposal is valid in principle for any state, even mixed. The idea is to prepare n identical copies of the system, initially switching off the interactions among different copies. This is achieved with a large lattice depth between any two copies. In a second step, the lattice is made deep within each site of a single copy, thus freezing the evolution, and tunneling among the different copies is switched on in a controlled way. With a modulation of the lattice it is in principle possible to implement a discrete Fourier transform among the copies of each site. In the case $n = 2$, if the barrier between the copies is lowered such that J_{12} is the tunneling rate, then the system is evolved up to a time $t = \pi/(4J_{12})$, and this amounts to the following operation on the bosonic annihilation operators of the two wells relative to site j

$$a_{j,1} \to (a_{j,1} + a_{j,2})/\sqrt{2}, \qquad a_{j,2} \to (a_{j,2} - a_{j,1})/\sqrt{2}. \tag{1.17}$$

This transformation is the quantum many body equivalent of the Hong-Ou-Mandel (HOM) interference of two photons [198], and it is often refferred to as a *beam splitter*.

Since the interaction between sites is turned off, we can concentrate on a single site. The shift operator on subsystem A can be built as a product over shift operators on single sites $V_A^{(n)} = \prod_{j\in A} V_{\{j\}}^{(n)}$. For $n = 2$, if we focus on a single site, we can as well think of a double well potential. Let us for a moment consider the case with two atoms living in such potential, and let us start for example from the state with one atom per well, $a_{i,1}^\dagger a_{i,2}^\dagger |0\rangle$. After the particular transformation (1.17), the probability of finding one atom per site vanishes, and the two atoms can only be found in one of the two wells, $(a_{i,1}^\dagger)^2|0\rangle$ or $(a_{i,2}^\dagger)^2|0\rangle$. What is important in this oversimplified example, is that the parity of the

number of bosons is fixed after the beam splitter operation. It turns out that analogous conclusions are also valid for a generic many body state, with arbitrary number of bosons. For $n = 2$, the eigenspaces of $V^{(2)}_{\{j\}}$ at site j, are the two spaces that are symmetric and antisymmetric under exchange of the two sites, with eigenvalues ± 1. It is easy to check that Eq. (1.17) maps the symmetric eigenspace on the subspace with an even number of bosons in copy 2, while it maps the antisymmetric subspace on the subspace with an odd number of bosons in copy 2. So the measurement for a single realization consists in counting modulo 2 the number of bosons in the second copy, and this will give the value of $V^{(2)}_A = (-1)^{\sum_{j\in A} n_{j,2}}$. By repeating the measurement we can estimate the expectation value of $V^{(2)}_A$, which is the purity. Notice that, even if for simplicity we discussed mainly the $n = 2$ case, the generalization to arbitrary n is quite straightforward, at least from a theoretical point of view.

1.2.2 Experimental realizations

In the present days, experiments are being performed by Greiner group at Harvard University [184–186] to measure the purity of a neutral bosons in an optical lattice, according to the scheme presented in Refs. [190, 191] and summarized in the previous section. One of the most popular bosonic atom used in these kinds of experiments is ^{87}Rb. Since it is neutral and do not have long-range interactions, phonon modes are not excited in the lattice. For detecting the parity of the number of bosons on single sites of the lattice, it is necessary to have a resolution up to the atom level. Such precision can be achieved with a high resolution quantum gas microscope [182, 183, 192, 193]. The optical lattice is created with interfering laser beams, by projecting a hologram on the bosons with the same microscope used to perform the imaging of the lattice. The hologram is essentially made of a piece of glass, and the lattice geometry is etched by manipulating the thickness of the glass. With this technique it is possible to engineer much more complicated lattices than by simply making two laser beams interfere. Once the main lattice has been created, since the microscope has a resolution up to a single site, using again the microscope in reverse it is possible to address the shape of the lattice at the same resolution. The projection of an arbitrary additional optical potential on top of the lattice is achieved with spatial light modulators. The imaging is performed by shining the atoms with a laser, and collecting the light they emit. If two atoms are on the same site, when they are hit by the light they combine and form a molecule, which has a high kinetic energy and therefore escapes the lattice. On the resulting image, the corresponding lattice site will result unoccupied. For this reason, only the parity of the number of bosons can be detected by this apparatus. However, this is sufficient to estimate the purity, as we discussed earlier.

The bosons in this setup essentially obey a Bose-Hubbard Hamiltonian

$$H = -J \sum_{\langle i,j \rangle} \left(a_i^\dagger a_j + \text{h.c.} \right) + \frac{U}{2} \sum_i n_i \left(n_i - 1 \right). \tag{1.18}$$

In the experiments, the interaction parameters are tuned by tuning the lattice depth and it is possible to switch from the superfluid phase $U \ll J$ to the Mott insulator phase $J \ll U$.

To perform the experiment for the purity, it is necessary to create two identical copies of the same one-dimensional system. With the experimental apparatus it is possible to create a two-dimensional system deep in the Mott phase. In this state, each lattice site is occupied by a single atom (with very high fidelity) and the entropy is very low. For

this reason the Mott insulator phase is optimal to generate identical copies of the same system. Starting from the two-dimensional Mott insulator, and with the possibility of manipulating the optical potential at the single atom level, it is possible to obtain one-dimensional arrays of atom. The potential barriers between any one-dimensional array and the rest of the lattice are raised, and then the underling optical lattice is removed. At this point all the atoms out of the only barrier left will escape the apparatus. When the lattice is reinserted and the additional potential switched off, the only remaining atoms will be disposed in the desired one-dimensional geometry. The same techniques described to extrapolate the purity can be used to check if the one-dimensional systems generated in this way are actually identical copies. Suppose we have two systems and we must understand if they are in the same state, and we let them interfere through the beam splitter. If the two states are identical, the value of the shift operator of the full system $V^{(2)}$ must be one, and therefore the number of bosons in each copy after the beam splitter is forced to be even. If instead the two states are different, the outcome can be either even or odd. This is the generalization to many sites of the simple example of the double well discussed above. The expectation value of $V^{(2)}$ gives exactly the overlap of the two states, $\langle V^{(2)} \rangle = \mathrm{Tr}(\rho_1 \rho_2)$, which is equal to one only when $\rho_1 = \rho_2$. After the two identical copies in the Mott state are prepared, by lowering the lattice depth the hopping is adiabatically switched on, so that the system ends up in the ground state of the Hamiltonian of Eq. (1.18) and entanglement is generated in the system. Then the experimental procedure is exactly the one described previously. First, the dynamics within each copy is frozen by raising a barrier between the sites. Notice that this procedure slows down the time-scale of the system coherently, and no projection is performed at this stage. Then, the beam splitter is turned on between the sites in different copies and an image of the system is taken. While the total number of boson in a single copy must be even (the initial state is pure and the two copies are identical), if we look at the parity of the number of bosons in any subsystems, we can have direct access to their purity.

The preliminary results for two and four sites presented in [184–186] show already clear signal of entanglement in the second Rényi entropy, when U/J is low and the system is in the superfluid phase. The signal is well above the experimental noise, which can be estimated by the second Rényi of the full system, which should be zero in an ideal setting. On the other side, when the system is in the Mott insulator phase, for large U/J, the second Rényi entropy of a subsystem is of the same order of the one of the full system. Since the experimental noise is essentially classical, the second Rényi of the full system is roughly the sum of the ones of the two subsystems A and B. Once the classical noise is taken into account as a global offset, the experimental measure is in good agreement with the theoretical prediction for the corresponding ground state. As already discussed, this method can be applied not only for ground state entanglement, but for any state. For example, in [184–186] some results are shown for the evolution of entanglement after a global quench. After the copies are prepared in the deep Mott phase, with one atom per site, the Hamiltonian is quenched abruptly to another value of $U/J < \infty$ and the system is left to evolve for a certain time. The measurement is then performed at different times, through freezing and application of the beam splitter.

Clearly, the perspectives opened by this experiment are very promising. By reducing all the sources of noise, the system can be scaled up. The fundamental point is that, a part for the noise and the complications in generating and evolving coherently two identical copies of larger systems, the procedure will always require the same order of measurements. This is an immense advantage with respect to a complete tomography of the system (a measurement of all the density matrix elements), which clearly scales

exponentially with the system size. In principle, it should also be possible to measure experimentally higher order Rényi entropies [191]. With the tools at disposal and the possibility of shaping the optical lattice at the level of a single site, entanglement can be studied also in many dynamical situations, even with added disorder, such as a Many Body Localized phase.

1.3 Conformal Field Theory: basics

In this section we are going to review some very basics facts of Conformal Field Theories (CFT) [199], in order to frame the context of the systems we are going to analyze throughout the thesis – mainly critical, $1+1$-dimensional extended systems, and provide some of the fundamental tools that we are going to need to tackle them.

CFT are a vastly studied subject, both from a purely mathematical point of view and for important applications in physics, as in string theories (where CFT naturally arise to describe the ground states of strings) and in statistical physics, in the study of critical phenomena, where the conformal symmetry may arise as an extended symmetry of scale invariance and Lorentz symmetry. In this thesis we will take the latter point of view and we will have in mind a quantum one-dimensional extended system, generally made by discrete variables, at a critical point. Its description at equilibrium can be related, through the transfer matrix formalism, to the one of a classical two-dimensional system. Conformal symmetry is a property of continuous theories, hence we shall think of our system in the limit of many degrees of freedom and of a correlation length much larger than the lattice spacing $\xi \gg a$, where it can be described by a Quantum Field Theory (QFT). In this limit the microscopic details are washed away and *universality* arises: this means that many different lattice systems, with different features and properties, may display the same behavior in some critical regime, and therefore may be described by the same QFT. Despite this fundamental role played by QFT and their consequent importance in the study of critical phenomena, it is important to remember that from the continuum description of our many-body system we can only hope to recover its universal properties, as for example the critical exponents, while we will never be able ti extract information about quantities that depend on the microscopic details.

Classifying all the QFT is a crucial step towards the classification of all the universality classes. In the literature, it was often followed this approach, of first studying some well-defined QFT, and then look for models that can be described in some limit by these theories. Of course classifying all the possible QFT is a formidable task to accomplish, well beyond our actual possibilities. As we will shortly see, the Hilbert space and the operator content of a conformally invariant theories in two dimensions are strongly conditioned by the symmetry. The classification of all CFT, even if still an extraordinary task, seems much more easy to confront with. Many (actually infinite) CFT are known in two dimensions, among which there are the minimal models, the $c = 1$ compactified boson, Liouville theories, and many others. In the following we will try to give some fundamental notions on CFT, without any presumption of completeness. A deep analysis of the various aspects of CFT can be found for example in Refs. [200–202], which contain also all the relevant references to the original literature.

1.3.1 Conformal invariance, primary fields and the stress-energy tensor

Consider a general d-dimensional sapcetime endowed with a flat metric $g_{\mu\nu}(x) = \eta_{\mu\nu}$ with signature $(d-1, 1)$ (we choose to take one temporal dimension). The metric tensor $g_{\mu\nu}$

transforms covariantly under a change of coordinates $x \to x'$. A conformal transformation is by definition a coordinate transformation whose net effect is to locally rescale the metric tensor $g'_{\mu\nu}(x') = \Lambda(x) g_{\mu\nu}(x)$. An infinitesimal coordinate transformations $x^\mu \to x^\mu + \epsilon^\mu$, turns out to be conformal if it satisfies the following relation,

$$\partial_\mu \epsilon_\nu + \partial_\nu \epsilon_\mu = \frac{2}{d}(\partial \cdot \epsilon)\eta_{\mu\nu}. \tag{1.19}$$

In $d > 2$ (the $d = 1$ case is trivial since all transformations are conformal and the $d = 2$ case will be largely discussed later), this constraint forces $\epsilon^\mu(x)$ to be at most quadratic in x. A part from the usual translations $\epsilon^\mu = a^\mu$, rotations $\epsilon^\mu = \omega^\mu{}_\nu x^\nu$ and dilatations $\epsilon^\mu = \lambda x^\mu$, the constraint (1.19) allows also for the special conformal transformations $\epsilon^\mu = b^\mu x^2 - 2x^\mu b \cdot x$. For each of these infinitesimal transformations it is possible to write the corresponding finite version by exponentiation, the generators of the algebra and their commutation relations. It is also easy to see that for a generic conformal transformation, the number of free parameters is $(d+1)(d+2)/2$.

From now on, we will concentrate on two dimensional conformal field theories in Euclidean signature $g_{\mu\nu} = \delta_{\mu\nu}$ (which can be recovered form the Lorentzian signature $(1,1)$ with the usual Wick rotation to imaginary time), since all the rest of the thesis will be devoted to $1+1$-dimensional systems. In two dimensions, the constraint (1.19) reduces to the Cauchy-Riemann equation

$$\partial_1 \epsilon_1 = \partial_2 \epsilon_2, \qquad \partial_1 \epsilon_2 = -\partial_2 \epsilon_1. \tag{1.20}$$

This means that any conformal transformation is an analytic transformation $z \to f(z)$, $\bar{z} \to \bar{f}(\bar{z})$, of the coordinates[2] $z = x^1 + \mathrm{i}x^2$, $\bar{z} = x^1 - \mathrm{i}x^2$. If we consider all the analytic functions on the plane satisfying (1.20) without further specification, since they can all be expanded in Laurent series, we can take the following generators,

$$\ell_n = -z^{n+1}\partial_z, \qquad \bar{\ell}_n = -\bar{z}^{n+1}\partial_{\bar{z}}, \qquad n \text{ in } \mathbb{Z}, \tag{1.21}$$

which satisfy the following commutation relations

$$\big[\ell_m, \ell_n\big] = (m-n)\ell_{m+n}, \qquad \big[\bar{\ell}_m, \bar{\ell}_n\big] = (m-n)\bar{\ell}_{m+n}. \tag{1.22}$$

The ℓ_n's and the $\bar{\ell}_n$'s commute among each others, therefore the algebra is the direct sum of a holomorphic and an antiholomorphic subalgebras. The coordinates z and $\bar{z}$ are often considered independent variables in $\mathbb{C}$, and only at the end the physical condition $\bar{z} = z^*$ is imposed. Notice that even if all the transformations satisfying Eq. (1.19) are locally analytic, they may not be so globally, due to singularities either at $z \to 0$ or at $z \to \infty$. The only true conformal transformations correspond to well defined, invertible, globally analytic functions, whose generators are $\{\ell_0, \ell_{\pm 1}\}$, and $\{\bar{\ell}_0, \bar{\ell}_{\pm 1}\}$. This means that the infinitesimal globally analytic transformations are the ones at most quadratic in z, as discussed for the $d > 2$ case. Notice that ℓ_{-1} and $\bar{\ell}_{-1}$ generate the translations, $\mathrm{i}(\ell_0 - \bar{\ell}_0)$ generates the rotations, $\ell_0 + \bar{\ell}_0$ the dilatations, and finally ℓ_1 and $\bar{\ell}_1$ the special conformal transformations. The finite versions of these transformations are the only bijective biholomorphic automorphisms of the Riemann sphere, the so called Möbius transformations

$$z \to \frac{az+b}{cz+d}, \qquad \bar{z} \to \frac{\bar{a}\bar{z}+\bar{b}}{\bar{c}\bar{z}+\bar{d}}, \tag{1.23}$$

[2] The complex coordinate z and $\bar{z}$ in Euclidean signature would correspond to the light-cone coordinates $x \pm t$ in Minkowski space.

for a, b, c, $d \in \mathbb{C}$ and $ad - bc = 1$.

All locally analytic transformations satisfying Eq. (1.20) but which are not Möbius (1.23), are still of great importance, since we can define some fields which behave covariantly under these transformations. The existence of these fields is taken as a postulate, and will strongly constraint the resulting theory. A *primary field* $\Phi(z, \bar{z})$ is defined such that the element $\Phi(z, \bar{z}) \mathrm{d}z^h \mathrm{d}\bar{z}^{\bar{h}}$ is invariant, for some *conformal weight* $(h, \bar{h})$. Under any conformal transformation the primary fields transform as follows,

$$\Phi(z, \bar{z}) \to \left(\partial_z f\right)^h \left(\partial_{\bar{z}} \bar{f}\right)^{\bar{h}} \Phi\left(f(z), \bar{f}(\bar{z})\right). \tag{1.24}$$

One usually defines also quasi-primary operators, which transform as in (1.24) only for global conformal transformations. The quasi-primaries can be defined in an analogous way also in higher dimensional CFT.

The transformation properties (1.24) of the primaries put severe constraints on their two- and three-point functions. Let us focus for the moment on the two-point function of two primaries, $G^{(2)}(z_i, \bar{z}_i) = \langle \Phi_1(z_1, \bar{z}_1) \Phi_2(z_2, \bar{z}_2) \rangle$. First, translational invariance implies that $G^{(2)}$ is a function of $z_{12} = z_1 - z_2$ and $\bar{z}_{12} = \bar{z}_1 - \bar{z}_2$, while rotational and scale invariance implies that $G^{(2)} \sim 1/\left(z_{12}^{h_1+h_2} \bar{z}_{12}^{\bar{h}_1+\bar{h}_2}\right)$. Finally, invariance under special conformal transformations fixes $h_1 = h_2 \equiv h$ and $\bar{h}_1 = \bar{h}_2 \equiv \bar{h}$. Putting all together, global conformal invariance forces the form of the two-point function of primaries to be

$$G^{(2)}(z_i, \bar{z}_i) = \frac{1}{z_{12}^{2h}\, \bar{z}_{12}^{2\bar{h}}}. \tag{1.25}$$

Notice that conformal invariance does not fix the proportionality constant in front of the last expression. This is instead fixed by the field normalization, which is uninteresting and we can choose it such that $G^{(2)}$ takes the form (1.25). Similar arguments lead to the following expression for the three-point function $G^{(3)} = \langle \Phi_1 \Phi_2 \Phi_3 \rangle$,

$$G^{(3)}(z_i, \bar{z}_i) = C_{123} \frac{1}{z_{12}^{h_1+h_2-h_3} z_{23}^{h_2+h_3-h_1} z_{13}^{h_1+h_3-h_2}} \frac{1}{\bar{z}_{12}^{\bar{h}_1+\bar{h}_2-\bar{h}_3} \bar{z}_{23}^{\bar{h}_2+\bar{h}_3-\bar{h}_1} \bar{z}_{13}^{\bar{h}_1+\bar{h}_3-\bar{h}_2}}. \tag{1.26}$$

In the case of the three-point function we cannot fix the proportionality constant, since the fields are already normalized such that (1.25) is valid. On the other hand, the four-point function of primaries cannot be fixed by conformal invariance only. Indeed, with four points we can construct invariant ratios under global conformal transformations, for example $x = z_{12} z_{23} / (z_{13} z_{24})$, and the corresponding $\bar{x}$. Therefore the dependence of the four-point function on such invariant ratios cannot be fixed by general argument, and we can write for example

$$G^{(4)}(z_i, \bar{z}_i) = \left[\left(\frac{z_{13} z_{24}}{z_{12} z_{14} z_{23} z_{34}} \right)^{2h} \times \text{antihol} \right] f(x, \bar{x}). \tag{1.27}$$

Conformally invariant theories are usually quantized by compactifying the 'spatial' Euclidean coordinate σ on a cylinder parametrized by the complex coordinate $\zeta = \tau + \mathrm{i}\sigma$ and $\bar{\zeta} = \tau - \mathrm{i}\sigma$. With the conformal map $\zeta \to z = \exp(\tau + \mathrm{i}\sigma)$ the cylinder is mapped onto the complex plane parametrized by $(z, \bar{z})$. Equal 'time' surfaces on the cylinder are mapped in the plane to circles centered in the origin, the origin $z = 0$ is therefore the infinite past, and the point at infinity $z = \infty$ is the infinite future. Hence, time and space translations on the cylinder correspond respectively to dilatations and rotations

on the plane. This means that the dilatation operator on the plane can be seen as the Hamiltonian of the system, while the linear momentum will be given by the rotation operator.

A fundamental role in CFT is played by the *stress-energy tensor* $T_{\mu\nu}$. In general QFT, under an arbitrary change of coordinates $x^\mu \to x^\mu + \epsilon^\mu$, the action changes as follows,

$$\delta S = \frac{1}{2}\int \mathrm{d}^d x\, T^{\mu\nu}\left(\partial_\mu \epsilon_\nu + \partial_\nu \epsilon_\mu\right), \tag{1.28}$$

where we assumed that $T_{\mu\nu}$ is symmetric, which is always true for Lorentz invariant theories. Using Eq. (1.19), we see that for a conformal transformation

$$\delta S = \frac{1}{d}\int \mathrm{d}^d x\, T^{\mu}{}_{\mu}\partial_\rho \epsilon^\rho. \tag{1.29}$$

It can be shown [203] in two dimensions that, under certain broad conditions, translational, rotational and scale invariance force the trace of the stress-energy tensor to vanish, which in turn implies from (1.29) conformal invariance (see Ref. [204] for an explicit counterexample). The component of the stress-energy tensor on the complex plane parametrized by $z = x_1 + \mathrm{i}x_2$ are given by $T_{zz} = \frac{1}{4}\big(T_{22} - 2\mathrm{i}T_{12} - T_{11}\big)$, $T_{\bar{z}\bar{z}} = \frac{1}{4}\big(T_{22} + 2\mathrm{i}T_{12} - T_{11}\big)$ and $T_{z\bar{z}} = T_{\bar{z}z} = \frac{1}{4}\big(T_{11} + T_{22}\big)$. Using the traceless condition, $T_{z\bar{z}} = 0$, and imposing the conservation law $\partial_\mu T^{\mu\nu} = 0$, we can also show that $\partial_{\bar{z}} T_{zz} = \partial_z T_{\bar{z}\bar{z}} = 0$. Therefore one usually defines the holomorphic and antiholomorphic components of the stress-energy tensor, respectively $T(z) \equiv T_{zz}(z)$ and $\overline{T}(\bar{z}) = T_{\bar{z}\bar{z}}(\bar{z})$. It is also possible to write down the set of Ward identities related to translational, rotational and scale invariance in a holomprphic form. For any product of n primary fields, the conformal Ward identities are given by

$$\begin{aligned}&\langle T(z)\Phi_1(w_1,\bar{w}_1)\Phi_2(w_2,\bar{w}_2)\ldots\Phi_n(w_n,\bar{w}_n)\rangle = \\ &\quad\sum_{i=1}^{n}\left(\frac{h_i}{(z-w_i)^2} + \frac{1}{z-w_i}\partial_{w_i}\right)\langle\Phi_1(w_1,\bar{w}_1)\Phi_2(w_2,\bar{w}_2)\ldots\Phi_n(w_n,\bar{w}_n)\rangle\,.\end{aligned} \tag{1.30}$$

Another very important ingredient is the operator product expansion (OPE), namely the representation of the product of two local operators as a (possibly infinite) sum over the local operators of the theory,

$$A(x)B(y) \sim \sum_i c_i(x-y)O_i(y), \tag{1.31}$$

where the O_i's are a complete set of regular local operators, and the $c_i(x-y)$ are c-valued functions. When two local fields at position x and y respectively, approach one another $x \to y$, singularities may in general appear, and they must be encoded in the coefficients $c_i(x-y)$. For two-dimensional CFT, we can choose a basis of fields with fixed conformal weight, and from dimensional analysis we can fix the form of the c_i's

$$\Phi_i(z,\bar{z})\Phi_j(w,\bar{w}) \sim \sum_k \frac{C_{ijk}}{(z-w)^{h_i+h_j-h_k}(\bar{z}-\bar{w})^{\bar{h}_i+\bar{h}_j-\bar{h}_k}}\Phi_k(w,\bar{w}). \tag{1.32}$$

When the Φ_i's are normalized such that the two-point function is given by Eq. (1.25), by using (1.32) in (1.26) for any two of the z_i's getting close one to the other, it is easy to see that the C_{ijk} appearing in the OPE and the ones appearing in the three-point

functions are the same. They are called the *structure constants* of the theory. Notice that the OPE expression must be understood to be valid only within correlation functions. That is why we did not write them as an exact equality. The conformal Ward identities of Eq. (1.30) tell us the singular behavior of primary fields approaching the stress-energy tensor, therefore we can read off the divergent part of their OPE,

$$T(z)\Phi(w,\bar{w}) \sim \frac{h}{(z-w)^2}\Phi(w,\bar{w}) + \frac{1}{z-w}\partial_w\Phi(w,\bar{w}) + \text{regular terms}, \tag{1.33}$$

and analogously for $\overline{T}(\bar{z})\Phi(w,\bar{w})$.

1.3.2 Central charge, Virasoro algebra and the structure of the Hilbert space

By performing two conformal transformations in succession, we see that the OPE of the holomorphic component of the stress-energy tensor with itself must take the form

$$T(z)T(w) = \frac{c/2}{(z-w)^4} + \frac{2}{(z-w)^2}T(w) + \frac{1}{z-w}\partial_w T(w), \tag{1.34}$$

and analogously for the antiholomorphic component. The constant c is called the *central charge*, it cannot be fixed by symmetry requirements only and it is indeed theory dependent. The presence of the central charge term in Eq. (1.34) means that the energy-momentum tensor does not transform as a primary operator, and indeed under a conformal transformation

$$T(z) \to \left(\frac{\partial w}{\partial z}\right)^2 T(w) + \frac{c}{12}\{w,z\}, \tag{1.35}$$

where $\{w,z\}$ is the Schwartzian derivative. The central charge is also known as the *conformal anomaly*, since it is related to the breaking of conformal symmetry when a macroscopic scale is introduced in the system, for example through boundary conditions. The most typical situation is when the theory is defined on a cylinder with a compactified dimension of length L. The stress-energy tensor on the cylinder can be related to the one on the plane through (1.35), and if we assume $\langle T_{\text{plane}}\rangle = 0$, then the central charge will be proportional to the total energy on the cylinder, $\langle T_{\text{cyl}}\rangle = -c\pi^2/(6L^2)$.

We can define a mode expansion of the stress-energy tensor, by expanding in Laurent series

$$T(z) = \sum_{n\in\mathbb{Z}} z^{-n-2}L_n, \qquad \overline{T}(\bar{z}) = \sum_{n\in\mathbb{Z}} \bar{z}^{-n-2}\bar{L}_n, \tag{1.36}$$

which can be inverted by

$$L_n = \oint \frac{\mathrm{d}z}{2\pi\mathrm{i}} z^{n+1}T(z), \qquad \bar{L}_n = \oint \frac{\mathrm{d}\bar{z}}{2\pi\mathrm{i}} \bar{z}^{n+1}\overline{T}(\bar{z}). \tag{1.37}$$

The algebra of their commutators turns out to be exactly the one of the classical algebra, Eq. (1.21), a part for some terms proportional to the conformal anomaly,

$$\big[L_n, L_m\big] = (n-m)L_{n+m} + \frac{c}{12}(n^3-n)\delta_{n+m,0}, \tag{1.38a}$$

$$\big[\bar{L}_n, \bar{L}_m\big] = (n-m)\bar{L}_{n+m} + \frac{\bar{c}}{12}(n^3-n)\delta_{n+m,0}, \tag{1.38b}$$

$$\big[L_n, \bar{L}_m\big] = 0. \tag{1.38c}$$

These commutators describe two copies of an infinite dimensional algebra, called the *Virasoro algebra*. The modes L_n and $\bar{L}_n$ generate the conformal transformations on the Hilbert space, and in particular, as for the classical algebra, $L_0 + \bar{L}_0$ generates dilatation (and it is therefore proportional to the Hamiltonian) and $\mathrm{i}(L_0 - \bar{L}_0)$ generates rotations (and correspond to the linear momentum).

The modes of the stress-energy tensor play the role of ladder operators on the states of the conformal theory. The Hilbert space, albeit very intricate, shows some peculiar features common to all CFT. The vacuum $|0\rangle$ is defined by requesting that it is annihilated by all modes with index $n \geqslant -1$,

$$L_n |0\rangle = 0, \qquad \bar{L}_n |0\rangle = 0, \qquad n \geqslant -1. \tag{1.39}$$

This implies that the vacuum is invariant under any conformal transformation, and that the vacuum expectation values of $T(z)$ and $\overline{T}(\bar{z})$ vanish. When we act on the vacuum with primary fields $|h, \bar{h}\rangle \equiv \Phi(0,0)\,|0\rangle$ we get eigenstates of the dilatation operator, and hence of the Hamiltonian. These states are called *highest weight states*,

$$L_0 |h, \bar{h}\rangle = h\,|h, \bar{h}\rangle\,, \qquad \bar{L}_0 |h, \bar{h}\rangle = \bar{h}\,|h, \bar{h}\rangle\,. \tag{1.40}$$

The eigenvalue of the dilatation operator $\Delta = h + \bar{h}$ is called the *conformal dimension*, while the eigenvalue of the momentum operator is the *spin* of the field, $s = h - \bar{h}$. While, in virtue of the Virasoro algebra, $L_n |h, \bar{h}\rangle = 0$ and $\bar{L}_n |h, \bar{h}\rangle = 0$ for $n > 0$, the modes of the stress-energy tensor with $n < 0$ can be successively applied on a highest weight state to build a whole family of *descendant states* above it

$$|n_1, \ldots, n_k; h, \bar{h}\rangle = L_{-n_1} L_{-n_2} \ldots L_{-n_k} |h, \bar{h}\rangle\,, \qquad n_j \geqslant 1. \tag{1.41}$$

Again using the Virasoro algebra (1.38) it is easy to see that they are still eigenstates of the dilatation and rotation generators, $L_0 |\{n_j\}; h, \bar{h}\rangle = (h + N)\,|\{n_j\}; h, \bar{h}\rangle$, and their conformal weight is increased with respect to the primary of an integer $N = \sum_j n_j$. The descendant states are all eigenstates of the Hamiltonian and are organized in levels, labeled by the integer N. Every *conformal family*, generated by a highest weight state and its descendants, is closed under the action of the generators of the conformal transformations, and therefore correspond to a realization of the Virasoro algebra. The corresponding subspace of the Hilbert space is usually called a *Verma module*. Primaries and descendants are all the eigenstates of the Hamiltonian and form a basis for the full Hilbert space.

We have seen that primary operators Φ are in one-to-one correspondence with highest weight states $|h, \bar{h}\rangle$. In the same way, for any descendant state we can define the corresponding descendant field, as the one that creates the state when applied to the vacuum. Take for instance the state $L_{-n} |h, \bar{h}\rangle$, its corresponding descendant filed is $(L_{-n}\Phi)(z, \bar{z})$. It can be seen that correlation functions involving descendant fields can be obtained by applying a specific set of differential operators to the correlation functions of their corresponding primaries.

The structure of the Hilbert space described so far is typical of every CFT, but specific theories can have different features. For example, the *minimal models* are characterized by having a finite number of Verma modules, which makes the structure of the Hilbert space particularly regular. On the contrary, in general the number of realizations of the Virasoro algebra is infinite. For example, the set of primaries of the free massless scalar boson is in one-to-one correspondence with the real numbers. However, if we compactify the target space of the boson on a circle of radius R, thus identifying $\phi \sim \phi + 2\pi R$, the set of primaries is still infinite, but discrete.

1.3.3 Partition function on the torus and modular invariance

Up to now we restricted ourselves to the basic case of CFT defined on the cylinder, which we saw is mapped with a conformal transformation to the plane, or better to the Riemann sphere, which is the simplest Riemann surface with genus zero. In principle any CFT can be defined on any higher genus Riemann surface, and indeed these geometries naturally arise in perturbative string theory, in the computation of multiloop scattering amplitudes. Although this kind of computations seems quite unnatural in the context of critical systems, we will see in Sec. 1.4 that a similar situation appears also in the computation of Rényi entropies of one-dimensional systems at criticality, which are obtained from the partition function of the model on a class of very peculiar Riemann surfaces. The study of CFT on these surfaces is therefore very important, and many results are available. The best understood case is the simplest one beyond the trivial genus-0 Riemann sphere, namely the genus-1 torus. We give here some basic elements about the form that the partition function takes in general on the torus and of the important modular invariance. Some more technical elements of modular invariance on higher genus Riemann surfaces will be discussed in App. 2.C of Chap. 2.

The torus can be recovered from the cylinder, by imposing periodic boundary conditions on the 'time' direction as well as on the 'spatial' direction. This is equivalent to selecting two linearly independent complex numbers, say τ_1 and τ_2, and consider the complex plane modulo τ_1 and τ_2. The two vectors define a primitive cell on the plane, whose opposite sides are therefore identified. Conformal symmetry allows to fix $\tau_2 = 1$, and the remaining parameter $\tau_1 \equiv \tau$ is called the *modular parameter* (or simply the period) of the torus. Although all local properties of the operators on the torus are the same as the same operators on the cylinder, global properties may change. For example, since with a conformal transformation we can map the torus on an anulus (with identified edges) in the complex plane, only rotations and dilatation (generated by L_0 and $\bar{L}_0$) survive on the torus as global symmetries. Also boundary conditions may be affected: the periodicity of the torus is reflected by invariance with respect to translations of the period τ in the action functional of the path integral formulation. The boundary conditions of the fields must respect this periodicity by leaving the action invariant. Notice that they are not bound to be periodic, a real fermion field for example can have either periodic (P) or antiperiodic (A) boundary conditions along the 'space' and 'time' directions, thus giving rise to four possible sectors, (A,A), (A,P), (P,A) and (P,P), called *spin structures*.

The partition function of the model on the torus can be computed by tracing the operator obtained from consecutive application of the transfer matrix in the direction of the modular parameter τ. Translations along the 'time' and 'space' directions are generated respectively by the Hamiltonian and the linear momentum, which on the cylinder, are given respectively by $H = (L_0)_{\text{cyl}} + (\bar{L}_0)_{\text{cyl}}$ and $P = \mathrm{i}((L_0)_{\text{cyl}} - (\bar{L}_0)_{\text{cyl}})$, with $(L_0)_{\text{cyl}} = L_0 - c/24$, thus giving for the partition function

$$\begin{aligned} Z(\tau) &= \operatorname{Tr} \exp\left\{-H \operatorname{Im}\tau - \mathrm{i} P \operatorname{Re}\tau\right\} \\ &= \operatorname{Tr} \exp\left\{2\pi\mathrm{i}\left[\tau\big(L_0 - c/24\big) + \tau^*\big(\bar{L}_0 - \bar{c}/24\big)\right]\right\}. \end{aligned} \tag{1.42}$$

One usually defines the parameters $q = \exp(2\pi\mathrm{i}\tau)$ and $\bar{q} = \exp(-2\pi\mathrm{i}\tau^*)$, and the torus partition function is written as

$$Z(\tau) = q^{c/24}\bar{q}^{\bar{c}/24} \operatorname{Tr}\left(q^{L_0}\bar{q}^{\bar{L}_0}\right). \tag{1.43}$$

On higher genus Riemann surfaces, and in particular on the torus, we may request an additional symmetry, *modular invariance*, to our theory. Let τ_1 and τ_2 be the periods of

the lattice describing the torus. Modular invariance is the invariance of the Hamiltonian under a different choice of the periods to describe the same lattice,

$$\begin{pmatrix}\tau_1'\\ \tau_2'\end{pmatrix} = \begin{pmatrix}a & b\\ c & d\end{pmatrix}\cdot\begin{pmatrix}\tau_1\\ \tau_2\end{pmatrix}, \qquad a,b,c,d\in\mathbb{Z}, \qquad ad-bc=1. \tag{1.44}$$

We also want the transformation to be invertible, and the inverse must of course have integer coefficients. The resulting matrix belongs to the group $SL(2,\mathbb{Z})$. For theories defined on higher genus Riemann surfaces the matrices implementing the reparametrization of the lattice must also be symplectic. This property is automatically satisfied by the elements in $SL(2,\mathbb{Z})$ for the case of the torus, while it be further investigated in App. 2.C for generic genus. Under the modular transformation (1.44), the modular parameter τ transforms as follows,

$$\tau \to \frac{a\tau+b}{c\tau+d}. \tag{1.45}$$

Since changing the sign of all parameters does not change the transformation of τ, the *modular group* is actually $SL(2,\mathbb{Z})/\mathbb{Z}_2$. The usual choices for the two generators of the modular group are $\tau\to\tau+1$, and $\tau\to-1/\tau$.

The requirement of modular invariance strongly constraint the partition function of the theory. In particular, the partition function of a conformal system with fixed boundary conditions of the fields along the two directions of the torus, may not be invariant under modular transformations. Without the requirement of modular invariance, we could pick a particular choice of the allowed boundary conditions and in doing so we could obtain a perfectly well-defined theory on the torus. On the contrary, modular invariance forces us to consider particular invariant combinations of the different sectors originating from the different choices of the boundary conditions. Both modular invariant and non modular invariant theories can have perfectly sense. For example, as we will discuss in Chaps. 4 and 5, the (A,A) spin structure of the free Dirac fermion is a $c=1$ CFT describing the continuum limit of the tight binding model, and it is not modular invariant. On the other hand, considering the appropriate combination of all the spin structures, we can build a modular invariant combination, which is another $c=1$ CFT, which reproduces the scaling limit of the XX spin chain. We will see that this difference have important consequences on the entanglement properties of the two theories.

1.4 Entanglement and Conformal Field Theories

In this section we introduce the main quantities and definitions that will be used throughout the thesis. In Sec. 1.4.1 we introduce the replica trick for the entanglement entropy and its application in QFT. We will also review some of the few exact results available in the context of CFT. In Sec. 1.4.2 we will extend the replica trick to the entanglement negativity and finally in Sec. 1.4.3 we will review the main characteristics of the Riemann surfaces involved in the QFT computations of such quantities.

1.4.1 Entanglement entropy, Rényi entropies and twist fields

Given a system in its ground state $|\Psi\rangle$, as already discussed in the Introduction, a very useful measure of entanglement is the entanglement entropy. When the Hilbert space of the full system can be factorized as $\mathcal{H}=\mathcal{H}_A\otimes\mathcal{H}_B$, the A's reduced density matrix reads $\rho_A=\mathrm{Tr}_B\,\rho$, being $\rho=|\Psi\rangle\langle\Psi|$ the density matrix of the entire system in a pure state.

The Von Neumann entropy associated to ρ_A is the entanglement entropy [8–10]

$$S_A = -\operatorname{Tr}(\rho_A \log \rho_A)\,. \tag{1.46}$$

Introducing S_B in an analogous way, we have $S_B = S_A$ because ρ describes a pure state.

In quantum field theory the entanglement entropy (1.46) is usually computed by employing the replica trick, which consists in two steps: first one computes $\operatorname{Tr}\rho_A^n$ for any integer $n \geqslant 2$ (when $n = 1$ the normalization condition $\operatorname{Tr}\rho_A = 1$ is recovered) and then analytically continues the resulting expression to any complex n. This allows to obtain the entanglement entropy as $S_A = -\lim_{n\to 1} \partial_n \operatorname{Tr}\rho_A^n$. The Rényi entropies are defined as follows

$$S_A^{(n)} = \frac{1}{1-n} \log \operatorname{Tr}\rho_A^n\,. \tag{1.47}$$

Given the normalization condition, the replica trick tells us that

$$S_A = \lim_{n\to 1} S_A^{(n)}. \tag{1.48}$$

Let us stress that $S_A^{(n)}$ contain much more information than the limit (1.48), since one can extract the full spectrum of ρ_A from them [205].

In this work we will mainly consider one dimensional critical systems when A and B correspond to a spatial bipartition. The simplest and most important example is the entanglement entropy of an interval A of length ℓ in an infinite line, which is given by [20, 27, 206]

$$S_A = \frac{c}{3} \log \frac{\ell}{a} + c_1'\,, \tag{1.49}$$

where c is the central charge of the corresponding CFT, a is some UV cutoff and c_1' is a non universal constant.

In full generality, let us consider a subsystem $A = \cup_{i=1}^N A_i$ made of N disjoint intervals. Let us denote by $A_i = [u_i, v_i]$ the endpoints of the i-th interval with $i = 1, \dots, N$. By employing the method of [27, 206], $\operatorname{Tr}\rho_A^n$ can be computed as a $2N$ point function of twist fields

$$\operatorname{Tr}\rho_A^n = \langle \prod_{i=1}^{N} \mathcal{T}_n(u_i)\bar{\mathcal{T}}_n(v_i) \rangle\,. \tag{1.50}$$

In CFT, the twist fields transform as primaries (even if they are not primaries). In the case of four and higher point correlation functions, the global conformal invariance does not fix the precise dependence on u_i and v_i, because one can construct invariant ratios involving these points. In particular, let us consider the conformal map such that $u_1 \to 0$, $u_N \to 1$ and $v_N \to \infty$, namely

$$w_N(z) = \frac{(u_1 - z)(u_N - v_N)}{(u_1 - u_N)(z - v_N)}\,. \tag{1.51}$$

The remaining u_i's and v_j's are sent into the $2N-3$ four-point ratios $x_1 = w_N(v_1)$, $x_2 = w_N(u_2)$, $x_3 = w_N(v_2)$, …, $x_{2N-3} = w_N(v_{N-1})$ which are invariant under $SL(2,\mathbb{C})$ transformations. The map (1.51) preserves the ordering: $0 < x_1 < x_2 < \cdots < x_{2N-3} < 1$. We denote by $\boldsymbol{x}$ the vector whose elements are the four-point ratios $x_1, \dots, x_{2N-3}$. Global conformal invariance allows to write the $2N$ point function (1.50) as [206]

$$\operatorname{Tr}\rho_A^n = c_n^N \left| \frac{\prod_{i<j}(u_j - u_i)(v_j - v_i)}{\prod_{i,j}(v_j - u_i)} \right|^{2\Delta_n} \mathcal{F}_{N,n}(\boldsymbol{x})\,, \tag{1.52}$$

where $i, j = 1, \dots, N$. The function $\mathcal{F}_{N,n}(\boldsymbol{x})$ encodes the full operator content of the model and therefore it must be computed through its dynamical details. Since $\operatorname{Tr}\rho_A = 1$, we have $\mathcal{F}_{N,1}(\boldsymbol{x}) = 1$.

As widely argued in [27, 206], in the case of one interval $A = [u, v]$ in an infinite line, $\operatorname{Tr}\rho_A^n$ is completely fixed by global conformal invariance, since it can be written as the two point function of twist fields on the complex plane, i.e.

$$\operatorname{Tr}\rho_A^n = \langle \mathcal{T}_n(u)\bar{\mathcal{T}}_n(v)\rangle = \frac{c_n}{|u-v|^{2\Delta_n}}. \tag{1.53}$$

The twist field $\mathcal{T}_n$ and $\bar{\mathcal{T}}_n$ behave like primary operators and they have the same scaling dimension

$$\Delta_n = \frac{c}{12}\left(n - \frac{1}{n}\right). \tag{1.54}$$

The constant c_n is non universal and such that $c_1 = 1$ because of the normalization condition.

To be more concrete, and to easily extend these arguments to case of the negativity, from now on let us focus on two intervals. The Rényi entropies of an arbitrary number of intervals will be investigated in details in Chap. 2. For $N = 2$ intervals there is only one four-point ratio $0 < x < 1$

$$x = \frac{(u_1 - v_1)(u_2 - v_2)}{(u_1 - u_2)(v_1 - v_2)}. \tag{1.55}$$

A crucial role in the derivation of analytic expressions for the function $\mathcal{F}_{2,n}(x)$ is played by the methods developed in [207–214] to study CFT on higher genus Riemann surfaces. The results are expressed in terms of Riemann theta functions [215–217] and it is still an open problem to compute their analytic continuation in n for the most general case, in order to get the entanglement entropy S_A. These CFT predictions are supported by numerical studies performed through various methods [218–225]. When A is a single interval, $\operatorname{Tr}\rho_A^n$ and S_A are sensible only to the central charge of the CFT, as clear from Eq. (1.53). Instead, these computations showed that when the subsystem A consists of $N \geqslant 2$ disjoint intervals on the infinite line, the Rényi entropies encode all the data of the CFT.

Eq. (1.52) specialised to the case $N = 2$ reads

$$\operatorname{Tr}\rho_A^n \;=\; c_n^2 \left(\frac{(u_2 - u_1)(v_2 - v_1)}{(v_1 - u_1)(v_2 - u_2)(v_2 - u_1)(u_2 - v_1)}\right)^{2\Delta_n} \mathcal{F}_n(x), \tag{1.56}$$

where, to make contact with the existing literature and to lighten the notation we introduced $\mathcal{F}_n(x) \equiv \mathcal{F}_{2,n}(x)$. The function $\mathcal{F}_n$ has been studied in several papers [46, 79, 196, 218–220, 223–229] (see [74, 75, 77–80, 97, 98, 100, 230, 231] for the holographic viewpoint and [47, 49, 51, 53–55, 102] for higher dimensional conformal field theories). One of the most important examples of exactly known $\mathcal{F}_n(x)$ is the free boson compactified on a circle of radius R_{circle}. In this case, the function $\mathcal{F}_n(x)$ (parametrized in terms of $\eta = R_{\text{circle}}^2/2$) is [226]

$$\mathcal{F}_n(x) = \frac{\Theta\big(\mathbf{0}|\eta\tau\big)\,\Theta\big(\mathbf{0}|\tau/\eta\big)}{[\Theta\big(\mathbf{0}|\tau\big)]^2}, \tag{1.57}$$

where τ is an $(n-1)\times(n-1)$ matrix with elements [226]

$$\tau_{i,j}(x) \;=\; \mathrm{i}\,\frac{2}{n}\sum_{k=1}^{n-1} \sin(\pi k/n)\,\frac{{}_2F_1(k/n, 1-k/n; 1; 1-x)}{{}_2F_1(k/n, 1-k/n; 1; x)}\,\cos[2\pi(k/n)(i-j)]. \tag{1.58}$$

The matrix $\tau(x)$ is called the period matrix and its geometrical interpretation in terms of Riemann surfaces will be discussed in Sec. 1.4.3. We remark that, since $x \in (0,1)$, the period matrix $\tau(x)$ is purely imaginary. Θ is the Riemann theta function [215–217]

$$\Theta(\boldsymbol{z}|M) \equiv \sum_{\boldsymbol{m}\in\mathbb{Z}^{n-1}} e^{\mathrm{i}\pi\,\boldsymbol{m}^{\mathrm{t}}\cdot M\cdot\boldsymbol{m}+2\pi\mathrm{i}\,\boldsymbol{m}^{\mathrm{t}}\cdot\boldsymbol{z}}, \tag{1.59}$$

which is a function of the $(n-1)$ dimensional complex vector $\boldsymbol{z}$ and of the $(n-1)\times(n-1)$ matrix M which must be symmetric and with positive imaginary part.

When the compactification radius takes the value $\eta = 1/2$, the theory corresponds to the scaling limit of the XX spin chain, which is the so called Dirac point. In this case, using theta functions identities it is possible to rewrite Eq. (1.57) as follows

$$\mathcal{F}_n^{\mathrm{Dirac}}(x) = \frac{1}{2^{n-1}\,|\Theta(\boldsymbol{0}|\tau)|^2} \sum_{\boldsymbol{\varepsilon},\boldsymbol{\delta}} \left|\Theta\begin{bmatrix}\boldsymbol{\varepsilon}\\ \boldsymbol{\delta}\end{bmatrix}(\boldsymbol{0}|\tau)\right|^2, \tag{1.60}$$

where the period matrix τ is the same as in Eq. (1.58). In this case Θ is the Riemann theta function with characteristic defined as [215–217]

$$\Theta[\boldsymbol{e}](\boldsymbol{z}|M) \equiv \sum_{\boldsymbol{m}\in\mathbb{Z}^{n-1}} e^{\mathrm{i}\pi(\boldsymbol{m}+\boldsymbol{\varepsilon})^{\mathrm{t}}\cdot M\cdot(\boldsymbol{m}+\boldsymbol{\varepsilon})+2\pi\mathrm{i}\,(\boldsymbol{m}+\boldsymbol{\varepsilon})^{\mathrm{t}}\cdot(\boldsymbol{z}+\boldsymbol{\delta})}, \qquad \boldsymbol{e} \equiv \begin{pmatrix}\boldsymbol{\varepsilon}\\ \boldsymbol{\delta}\end{pmatrix}, \tag{1.61}$$

where $\boldsymbol{z}$ and M are analogous to the ones in (1.59), and $\boldsymbol{\varepsilon}, \boldsymbol{\delta}$ are vectors with entries 0 and 1/2. The sum in $(\boldsymbol{\varepsilon}, \boldsymbol{\delta})$ in (1.60) is intended over all the 2^{n-1} vectors $\boldsymbol{\varepsilon}$ and $\boldsymbol{\delta}$ with these entries. The parity of (1.61) as function of $\boldsymbol{z}$ is given by the parity of the characteristic, which is the parity of the integer number $4\boldsymbol{\varepsilon}\cdot\boldsymbol{\delta}$

$$\Theta[\boldsymbol{e}](-\boldsymbol{z}|\Omega) = (-1)^{4\boldsymbol{\varepsilon}\cdot\boldsymbol{\delta}}\,\Theta[\boldsymbol{e}](\boldsymbol{z}|\Omega)\,. \tag{1.62}$$

There are $2^{2(n-1)}$ characteristics: $2^{n-2}(2^{n-1}+1)$ are even and $2^{n-2}(2^{n-1}-1)$ are odd. In our following analysis only the trivial vector $\boldsymbol{z} = \boldsymbol{0}$ occurs and therefore all the Riemann theta functions occurring in this thesis with odd characteristic vanish identically. We will adopt the shortcut notation: $\Theta[\boldsymbol{e}](M) \equiv \Theta[\boldsymbol{e}](\boldsymbol{0}|M)$ and $\Theta(M) \equiv \Theta(\boldsymbol{0}|M)$ when the characteristic is vanishing.

For the critical Ising model, the scaling function $\mathcal{F}_n(x)$ is also known [196]

$$\mathcal{F}_n^{\mathrm{Ising}}(x) = \frac{1}{2^{n-1}\,|\Theta(\boldsymbol{0}|\tau)|} \sum_{\boldsymbol{\varepsilon},\boldsymbol{\delta}} \left|\Theta\begin{bmatrix}\boldsymbol{\varepsilon}\\ \boldsymbol{\delta}\end{bmatrix}(\boldsymbol{0}|\tau)\right|, \tag{1.63}$$

where again the period matrix τ is the same as in Eq. (1.58). More details will be given in Sec. 2.7.1.

1.4.2 The replica trick for the negativity

In this section we introduce the computation of the entanglement negativity through the replica trick. In the framework of the replica approach, field theoretical computations are possible, with a generalization of the techniques described in Sec. 1.4.1

We again consider a bipartite Hilbert space, according to two regions A and B, and we consider the reduced density matrix ρ_A, which is in general mixed. Let us further split subsystem A in two subsystems A_1 and A_2, which can be either adjacent or separated.

Notice that, when $A = A_1 \cup A_2$ is composed of two disjoint regions A_1 and A_2, the entanglement entropy quantifies only the entanglement between A and the remainder of the system B, but not the entanglement between A_1 and A_2. In this case it is customary to introduce the mutual information

$$I_{A_1,A_2} \equiv S_{A_1} + S_{A_2} - S_{A_1 \cup A_2} \,, \tag{1.64}$$

and, analogously, the Rényi mutual information

$$I^{(n)}_{A_1,A_2} \equiv \frac{1}{n-1} \ln \left(\frac{\operatorname{Tr} \rho_A^n}{\operatorname{Tr} \rho_{A_1}^n \operatorname{Tr} \rho_{A_2}^n} \right). \tag{1.65}$$

However, let us stress again that these are not measures of the entanglement between A_1 and A_2, but quantify the amount of *global correlations between the two subsystems*, see e.g. [15].

However, we are here interested in the entanglement between A_1 and A_2. In the Introduction we discussed how the negativity provides a proper measure of entanglement in a bipartite mixed state [117–120, 162, 179]. Let us recall here its definition. One first introduces the partial transpose with respect to the A_2's degrees of freedom. Let us denote by $|e_i^{(1)}\rangle$ and $|e_j^{(2)}\rangle$ two arbitrary bases in the Hilbert spaces corresponding to A_1 and A_2. The partial transpose of ρ_A with respect to A_2 degrees of freedom is defined as

$$\langle e_i^{(1)} e_j^{(2)} | \rho_A^{T_2} | e_k^{(1)} e_l^{(2)} \rangle = \langle e_i^{(1)} e_l^{(2)} | \rho_A | e_k^{(1)} e_j^{(2)} \rangle, \tag{1.66}$$

and then the *logarithmic* negativity as

$$\mathcal{E} \equiv \ln ||\rho_A^{T_2}|| = \ln \operatorname{Tr} |\rho_A^{T_2}| \,, \tag{1.67}$$

where the trace norm $||\rho_A^{T_2}||$ is the sum of the absolute values of the eigenvalues of $\rho_A^{T_2}$. Notice that the negativity is symmetric under exchange of A_1 and A_2, as any good measure of the relative entanglement should be.

The QFT approach to the logarithmic negativity $\mathcal{E}$ is based on a replica trick [134, 135]. Let us consider the traces $\operatorname{Tr}(\rho_A^{T_2})^n$ of integer powers of $\rho_A^{T_2}$. For n even and odd, denoted by n_e and n_o respectively, we have

$$\operatorname{Tr}(\rho_A^{T_2})^{n_e} = \sum_i \lambda_i^{n_e} = \sum_{\lambda_i > 0} |\lambda_i|^{n_e} + \sum_{\lambda_i < 0} |\lambda_i|^{n_e} \,, \tag{1.68a}$$

$$\operatorname{Tr}(\rho_A^{T_2})^{n_o} = \sum_i \lambda_i^{n_o} = \sum_{\lambda_i > 0} |\lambda_i|^{n_o} - \sum_{\lambda_i < 0} |\lambda_i|^{n_o} \,, \tag{1.68b}$$

where λ_i are the eigenvalues of $\rho_A^{T_2}$. Clearly, the functional dependence of $\operatorname{Tr}(\rho_A^{T_2})^n$ on $|\lambda_i|$ depends on the parity of n. Setting $n_e = 1$ in (1.68a), we formally obtain $\operatorname{Tr}|\rho_A^{T_2}|$, whose logarithm gives the logarithmic negativity $\mathcal{E}$. Instead, if we set $n_o = 1$ in (1.68b), we just get the normalization $\operatorname{Tr} \rho_A^{T_2} = 1$. Thus, the analytic continuations from even and odd values of n are different and the trace norm that we are interested in is obtained by performing the analytic continuation of the even sequence (1.68a) at $n_e \to 1$. By introducing

$$\mathcal{E}^{(n)} \equiv \ln \left[\operatorname{Tr} \left(\rho_A^{T_2} \right)^n \right], \tag{1.69}$$

we have that $\mathcal{E}^{(1)} = 0$ identically and the logarithmic negativity $\mathcal{E}$ is given by the following replica limit

$$\mathcal{E} = \lim_{n_e \to 1} \mathcal{E}^{(n_e)} \,. \tag{1.70}$$

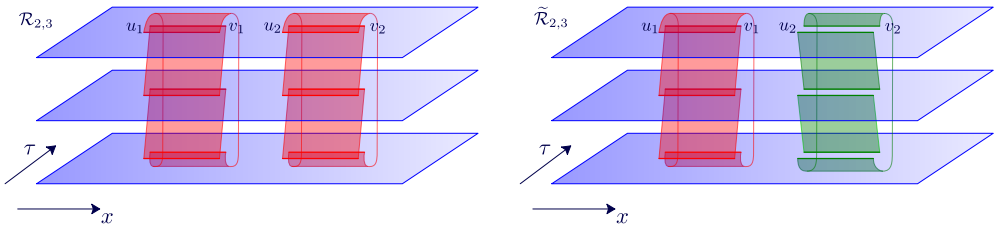

Figure 1.1: The path integral representation of $\mathrm{Tr}\,\rho_A^n$ involves a Riemann surface $\mathcal{R}_{N,n}$, which is shown in the left panel for $N = 2$ and $n = 3$. In the right panel we show a graphical representation of the Riemann surface $\widetilde{\mathcal{R}}_{N,n}$ (again for $N = 2$ and $n = 3$), which enters in the computation of $\mathrm{Tr}\left(\rho_A^{T_2}\right)^n$. The main difference lies in te fact that the sheets are glued along the transpose interval A_2 in the reversed order.

For future convenience we also introduce the ratios

$$R_n \equiv \frac{\mathrm{Tr}(\rho_A^{T_2})^n}{\mathrm{Tr}\;\rho_A^n} \quad \Rightarrow \quad \ln(R_n) = \mathcal{E}^{(n)} + (n-1)S^{(n)}_{A_1\cup A_2} \quad \text{and} \quad \mathcal{E} = \lim_{n_e\to 1} \ln(R_{n_e})\,. \tag{1.71}$$

Finally, let us notice that although this replica approach has been introduced in the context of CFT [134, 135], it has been later applied and generalized to many other circumstances [136, 141–143, 145, 146, 232, 233].

1.4.3 Path integral representations

In this section we briefly discuss the path integral formalism to compute $\mathrm{Tr}\,\rho_A^n$ and $\mathrm{Tr}\left(\rho_A^{T_2}\right)^n$ in QFT. We also review some of the key properties of the Riemann surfaces involved, mainly focusing on the case of two intervals. For the case of the Rényi entropies of any number of disjoint intervals, much more details will be given in Chap. 2

Let us again consider a subsystem $A = \cup_{i=1}^N [u_i, v_i]$ made of N disjoint intervals. The path integral representation of ρ_A has been largely discussed in [20, 27, 206]. Tracing over the spatial complement B leaves open cuts, one for each interval, along the line characterized by a fixed value of the Euclidean time. Thus, the path integral giving ρ_A involves fields which live on this sheet with open cuts, whose configurations are fixed on the upper and lower edges of the cuts.

To compute $\mathrm{Tr}\,\rho_A^n$, we take n copies of the path integral representing ρ_A and combine them as follows. We impose that the value of a field on the upper part of the cut on a sheet is equal to the value of the same field on the lower part of the corresponding cut on the subsequent sheet. This condition is applied in a cyclic way. Then, we integrate over the field configurations along the cuts. Correspondingly, the n sheets must be sewed in the same way and this procedure defines the n-sheeted Riemann surface $\mathcal{R}_{N,n}$. The endpoints u_i and v_i $(i = 1, \ldots, N)$ are branch points where the n sheets meet. The Riemann surface $\mathcal{R}_{N,n}$ is depicted in the left panel of Fig. 1.1 for $N = 2$ intervals and $n = 3$ copies. Another representation of the same surface is shown in Fig. 1.2. Denoting by $\mathcal{Z}_{N,n}$ the partition function of the model on the Riemann surface $\mathcal{R}_{N,n}$, we can compute $\mathrm{Tr}\,\rho_A^n$ as [27]

$$\mathrm{Tr}\,\rho_A^n = \frac{\mathcal{Z}_{N,n}}{\mathcal{Z}_1^n}\,, \tag{1.72}$$

where $\mathcal{Z}_1$ is the partition function of the model defined on a single copy and without cuts. Notice that (1.72) implies $\mathrm{Tr}\,\rho_A = 1$. From (1.72), one easily gets the Rényi

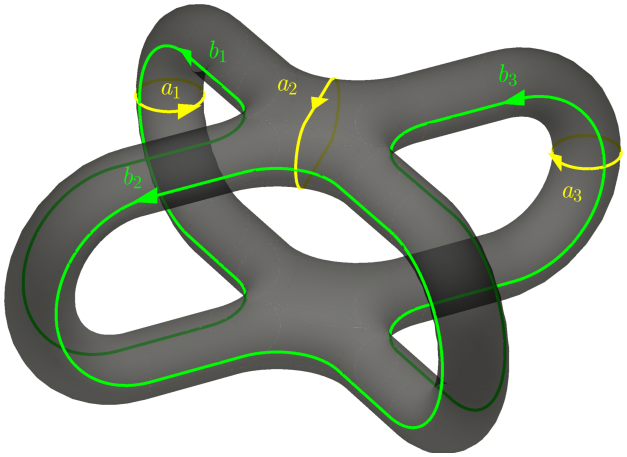

Figure 1.2: Another representation of the Riemann surface $\mathcal{R}_{2,4}$ for $N = 2$ intervals and $n = 4$ sheets (see also the left panel of Fig. 1.1). A single sheet can be seen as a sphere with two open cuts corresponding to the two intervals A_1 and A_2, or equivalently as a cylinder. The n cylinders the are sewn together cyclically. From the figure it is evident that the surface has genus $g = (n-1)(N-1) = 3$. We also depicted the basis cycles $\{a_r, b_r\,;\, r = 1, 2, 3\}$ discussed in the text.

entropies (1.47). If the analytic continuation of (1.72) to $\mathrm{Re}\, n > 1$ exists and it is unique, the entanglement entropy is obtained as the replica limit (1.48).

The Riemann surface $\mathcal{R}_{N,n}$ is defined by the following algebraic curve in $\mathbb{C}^2$ (parameterised by the complex variables z and y) [226]

$$y^n = \prod_{i=1}^{N}(z-u_i)\Big[\prod_{i=1}^{N}(z-v_i)\Big]^{n-1}. \tag{1.73}$$

It is an n sheeted cover of the complex plane and it has been studied in detail in [234]. By going around the u_i's clockwise, one goes from the j-th to the $(j+1)$-th sheet, while going around the v_i's clockwise, one moves to the $(j-1)$-th one.

In order to find the genus of $\mathcal{R}_{N,n}$ [208], let us consider a single sheet and triangulate it through V vertices, E edges and F faces, such that $2N$ vertices are located at the branch points u_i and v_i. The replication of the same triangulation on all sheets generates a triangulation of the Riemann surface $\mathcal{R}_{N,n}$ made by V' vertices, E' edges and F' faces. Notice that, since the branch points belong to all the n sheets, they are not replicated. This observation tells us that $V' = n(V-2N)+2N$, while $E' = nE$ and $F' = nF$ because all the edges and the faces are replicated. Then, the genus g of $\mathcal{R}_{N,n}$ is found by plugging these expressions into the relation $V' - E' + F' = 2 - 2g$ and employing the fact that $V - E + F = 2$, since each sheet has the topology of the sphere. The result is

$$g = (N-1)(n-1)\,. \tag{1.74}$$

We remark that we are not considering the most general genus g Riemann surface, which is characterized by $3g-3$ complex parameters, but only the class of Riemann surfaces obtained through the described replication procedure. As already anticipated, from now on we specialise to the case of two intervals, when $\mathcal{R}_n \equiv \mathcal{R}_{2,n}$ has genus $g = n-1$. The

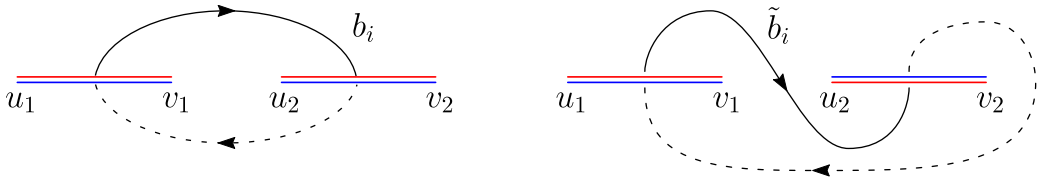

Figure 1.3: Cycles of type b for $\mathcal{R}_n$ (left) and $\widetilde{\mathcal{R}}_n$ (right). The solid line represents the part of the cycle belonging to the i-th sheet, while the dashed curve is the remaining part of the cycle, which lies in the $(i+1)$-th sheet. As for the cycles of type a, which are the same for $\mathcal{R}_n$ and $\widetilde{\mathcal{R}}_n$, we refer to Fig. 8 of [235].

algebraic curve relative to $\mathcal{R}_n$ is

$$y^n = (z-u_1)(z-u_2)\big[(z-v_1)(z-v_2)\big]^{n-1}, \tag{1.75}$$

and its genus is $g = n-1$.

In the computation of the partition function on higher genus Riemann surfaces, one has to properly choose a canonical homology basis (i.e. a set of $2g$ closed oriented curves on the surface, the a and b cycles, which satisfy some specific intersection rules) and a set of $n-1$ holomorphic differentials. By integrating such differentials along the b cycles one gets the period matrix of the Riemann surface. For a genus g Riemann surface, the period matrix is a $g \times g$ complex symmetric matrix with positive definite imaginary part [207–210, 212–214]. In Chap. 2 we will perform a detailed analysis about some possible choices of the homology basis for $\mathcal{R}_{N,n}$ and we will discuss in full details how to compute the period matrix for a given basis. In particular, the matrix in Eq. (1.58) is the period matrix of $\mathcal{R}_n$ corresponding to a specific homology basis $\{a_r, b_r\,;\, 1 \leqslant r \leqslant n-1\}$, that will be discussed in details in Sec. 2.4.2 [3]. Let us here briefly summarise the choice of the b cycles, since it is the main difference with the case of the negativity. In the left panel of Fig. 1.3 we show the j-th b cycle, which belongs to the j-th sheet and to the $(j+1)$-th sheet. Instead, the construction of a_j (which intersects b_j only once) is more involved and therefore we refer to Fig. 2.7.

The Riemann theta function with characteristic (1.61) occurs in the computation of fermionic models on higher genus Riemann surfaces [207–210, 212–214]. The characteristic $\boldsymbol{\epsilon}$ specifies the set of boundary conditions along the a and b cycles of the canonical homology basis and this provides the so called *spin structures* of the model. The vector $\boldsymbol{\varepsilon}$ is determined by the boundary conditions along the a cycles ($\varepsilon_k = 0$ for antiperiodic b.c. around a_k and $\varepsilon_k = 1/2$ for periodic b.c.), while $\boldsymbol{\delta}$ is provided by the boundary conditions along the b cycles ($\delta_k = 0$ for antiperiodic b.c. around b_k and $\delta_k = 1/2$ for periodic b.c.).

We now discuss a different Riemann surface, which is involved in the computation of the moments of $\rho_A^{T_2}$. Consider the Riemann surface $\widetilde{\mathcal{R}}_n$ defined by the following algebraic curve,

$$y^n = (z-u_1)(z-v_2)\big[(z-v_1)(z-u_2)\big]^{n-1}. \tag{1.76}$$

It is the same equation of (1.75), but with the exchange $u_2 \leftrightarrow v_2$. From the point of view of a single sheet, this operation corresponds to the exchange of the lower and upper part of the cut along A_2. When the sheets are sewed together cyclically, the result is the one

[3] In that Sec. 2.4.2, these cycles are denoted with a hat, $\hat{a}_j$ and $\hat{b}_j$. Here we removed the hat to lighten the notation.

depicted in the right panel of Fig. 1.1 Therefore, while around u_1 and v_1 the surface $\widetilde{\mathcal{R}}_n$ has the same properties as $\mathcal{R}_n$, by encircling u_2 clockwise we move from the j-th sheet to the $(j-1)$-th sheet, while by encircling v_2 clockwise the $(j+1)$-th sheet is reached. Since the exchange $u_2 \leftrightarrow v_2$ sends $x \to x/(x-1)$, the period matrix $\tilde{\tau}(x)$ of $\widetilde{\mathcal{R}}_n$ for $x \in (0,1)$ is given by [135]

$$\tilde{\tau}(x) = \tau\big(x/(x-1)\big) = \mathcal{R} + \mathrm{i}\,\mathcal{I}, \tag{1.77}$$

where the elements of τ have been defined in (1.58) and the real and imaginary parts of $\tilde{\tau}(x)$ are $\mathcal{R}$ and $\mathcal{I}$ respectively. The surfaces $\mathcal{R}_n$ and $\widetilde{\mathcal{R}}_n$ are in general different, only for $n = 2$ they are the same torus, as can be immediately seen from (1.75) and (1.76). In terms of period matrix, it can be seen [135] that sending $x \to x/(x-1)$ is equivalent to the transformation $\tau \to \tau + 1$, which is a modular transformation of the torus $\mathcal{R}_2$ (see Eq. (1.45)). Therefore the moduli τ and $\tilde{\tau} = \tau + 1$ describe the same torus. As for the cycles of $\widetilde{\mathcal{R}}_n$ providing the canonical homology basis $\{\tilde{a}_r, \tilde{b}_r\,;\, 1 \leqslant r \leqslant n-1\}$ which gives the period matrix (1.77), we find that $\tilde{a}_r$ is the same as a_r (we remind that $\widetilde{\mathcal{R}}_n$ and $\mathcal{R}_n$ differ only for the way the sheets are joined along A_2), while the generic cycle $\tilde{b}_r$ is obtained by deforming the cycle b_r as shown in Fig. 1.3.

Let us now make an example to show how the Riemann surface $\widetilde{\mathcal{R}}_n$ can enter some specific computation. In Refs. [134, 135], it has been shown that for the 1+1 dimensional quantum field theory of the compactified boson the partial transposition of the path integral representation of ρ_A corresponds to the exchange of the lower and upper edge of the cut along A_2. Therefore the traces $\mathrm{Tr}(\rho_A^{T_2})^n$ can be computed as the partition function of the theory on $\widetilde{\mathcal{R}}_n$. We recall that $\widetilde{\mathcal{R}}_n$ differs from $\mathcal{R}_n$ only by the exchange $u_2 \leftrightarrow v_2$, and this immediately translates in terms of correlation functions of twist fields. As we already reported in Sec. 1.4.1, $\mathrm{Tr}\,\rho_A^n$ for the union of two disjoint intervals $A = [u_1, v_1] \cup [u_2, v_2]$ is given by the correlator $\langle \mathcal{T}_n(u_1)\bar{\mathcal{T}}_n(v_1)\mathcal{T}_n(u_2)\bar{\mathcal{T}}_n(v_2)\rangle$. Now let us take the partial transpose with respect to the interval A_2. The quantity $\mathrm{Tr}\left(\rho_A^{T_2}\right)^n$ can be computed from the correlator above where the twist fields $\mathcal{T}_n$ and $\bar{\mathcal{T}}_n$ at the endpoints of A_2 are exchanged while the remaining ones stay untouched, giving $\mathrm{Tr}(\rho_A^{T_2})^n = \langle \mathcal{T}_n(u_1)\bar{\mathcal{T}}_n(v_1)\bar{\mathcal{T}}_n(u_2)\mathcal{T}_n(v_2)\rangle$. The configurations including adjacent intervals can be obtained as a limit of the previous one, where the distances between the proper intervals vanish. After this limit, $\mathcal{T}_n^2$ or $\bar{\mathcal{T}}_n^2$ occur at the joining point between a transposed interval and the adjacent one that has not been transposed. For example, if we send $u_2 \to v_1$, we find $\mathrm{Tr}(\rho_A^{T_2})^n = \langle \mathcal{T}_n(u_1)\bar{\mathcal{T}}_n^2(v_1)\mathcal{T}_n(v_2)\rangle$ Thus, the ratio (1.71) can be computed through the corresponding correlators of twist fields. To compute this kind of correlation functions in CFT, we need the scaling dimension of $\mathcal{T}_n^2$ and $\bar{\mathcal{T}}_n^2$ which depends on the parity of n as [134, 135]

$$\Delta_n^{(2)} \equiv \begin{cases} \Delta_n & \text{odd } n\,, \\ 2\Delta_{n/2} & \text{even } n\,, \end{cases} \tag{1.78}$$

where Δ_n has been defined in (1.53). Since the moments of the partial transpose correspond to a four-point function of twist fields, they admit the universal scaling form

$$\mathrm{Tr}\left(\rho_A^{T_2}\right)^n = c_n^2 \left(\frac{(u_2-u_1)(v_2-v_1)}{(v_1-u_1)(v_2-u_2)(v_2-u_1)(u_2-v_1)} \right)^{2\Delta_n} \mathcal{G}_n(x), \tag{1.79}$$

with c_n the same non-universal constant appearing in Eq. (1.56) and $\mathcal{G}_n(x)$ a new universal scaling function. Exploiting the fact that the above moments correspond to the exchange of two twist fields, the expression for $\mathrm{Tr}\left(\rho_A^{T_2}\right)^n$ can be obtained from the one of $\mathrm{Tr}\,\rho_A^n$ by

simply exchanging $u_2 \leftrightarrow v_2$. This means that $\mathcal{G}_n(x)$ and $\mathcal{F}_n(x)$ are related as [134, 135]

$$\mathcal{G}_n(x) = (1-x)^{4\Delta_n} \mathcal{F}_n\left(\frac{x}{x-1}\right). \tag{1.80}$$

but some care is needed to take the analytic continuation of the function $\mathcal{F}_n(y)$ to negative argument y. The result (1.57) is indeed valid only for $0 < x < 1$. For generic $x \in \mathbb{C}$, it is found [135] that

$$\mathcal{F}(x) = \frac{\Theta(T)}{|\Theta(\tau)|^2}, \qquad T = \begin{pmatrix} \mathrm{i}\mathcal{I}\eta & \mathcal{R} \\ \mathcal{R} & \mathrm{i}\mathcal{I}/\eta \end{pmatrix}. \tag{1.81}$$

When $0 < x < 1$, the period matrix $\tau(x)$ in (1.58) is purely imaginary. Then $\mathcal{R} = 0$ and the Riemann theta function in (1.81) factorizes, giving back the result (1.57). On the contrary, since for $0 < x < 1$ we have $-\infty < x/(x-1) < 0$, then $\tilde{\tau}(x)$ develops a real part and in (1.80) the full expression (1.81) must be used. More details on the real part of $\tilde{\tau}(x)$ will be given in Chap. 5 and in particular in App. 5.B.1. The CFT prediction for the ratio in Eq. (1.71) is

$$R_n(x) = (1-x)^{4\Delta_n} \frac{\mathcal{F}_n\big(x/(x-1)\big)}{\mathcal{F}_n(x)}, \tag{1.82}$$

in which the universal constants c_n as well as the dimensional part of the traces canceled out leaving a universal scale invariant quantity.

The result of the compactified boson (1.82) is automatically valid also for the (modular invariant) Dirac theory and for the Ising model, which indeed can be bosonized. Therefore, in order to obtain the moments of $\rho_A^{T_2}$, we can simply replace $x \to x/(x-1)$ in Eq. (1.60) and Eq. (1.63) respectively. However, the same result does not hold for other models, such as the free Dirac fermion. Let us stress that what we call *free* Dirac fermion is not the same Dirac fermion considered so far (and whose Rényi entropies are obtained from Eq. (1.60)). The latter is the modular invariant theory of two Majorana fermions which can be bosonized and corresponds to the compactified boson at $\eta = 1/2$, and describes the scaling limit of the XX model. On the other hand, the *free* Dirac fermion is still made of two Majorana fermions, but with fixed antiperiodic boundary conditions along all basis cycle. This theory describes the continuum limit of the tight binding model (whose Hamiltonian is reported in Eq. (5.1)), and it is not a modular invariant theory. We refer the reader to [228] for a detailed comparison between these two theories. Throughout the thesis, were it is not obvious from the context we will refer to the two theories as *modular invariant* Dirac fermion and *free* Dirac fermion. For the free Dirac fermion, the function $\mathcal{F}_n(x)$ is well known and it is identically one, $\mathcal{F}_n(x) = 1$ [46]. The simple replacement $x \to x/(x-1)$ would still give the same constant result, and this would turn out (after the trivial continuation $n_e \to 1$) in a vanishing entanglement negativity. A detailed analysis indeed shows that the traces $\mathrm{Tr}\,(\rho_A^{T_2})^n$ are not computed as partition functions on $\widetilde{\mathcal{R}}_n$, but as a particular sum of different partition functions with specific boundary conditions along the basis cycles (and therefore with specific spin structures). This calculation will be addressed in full details in Chap. 5.

1.5 Organization of the thesis

The thesis is organized as follows.

In Chap. 2 we begin the study of the entanglement properties of disjoint regions in 1+1 dimension by studying the Rényi entropies of N disjoint intervals in some simple CFT

(the free compactified boson and the Ising model). They are computed as the $2N$ point function of twist fields, by employing the partition function of the model on the Riemann surfaces $\mathcal{R}_{N,n}$. The results are written in terms of Riemann theta functions. The prediction for the free boson in the decompactification regime is checked against exact results for the harmonic chain. We also perform a numerical interpolation of the values of the Rényi entropies computed analytically, and with that we extrapolate an estimate of the entanglement entropy. The match between the result for the decompactified boson and the exact computations on the harmonic chain are very satisfactory. Finally, we check the theoretical results found for the Ising model by means of MPS, where we also identify the representation of the twist fields. The computations agree with the CFT result once the finite size corrections have been taken into account. The chapter is mainly based on the following work:

[235] A. Coser, L. Tagliacozzo, and E. Tonni, *"On Rényi entropies of disjoint intervals in conformal field theory"*, J. Stat. Mech. P01008 (2014).

The material in Sec. 2.6 and App. 2.E, as well as some analogous analysis for the logarithmic negativity, can be found in the following paper:

[236] C. De Nobili, A. Coser, and E. Tonni, *"Entanglement entropy and negativity of disjoint intervals in CFT: Some numerical extrapolations"*, J. Stat. Mech. P06021 (2015).

In Chap. 3 we start the exploration of the entanglement properties between disjoint regions in mixed states by means of the entanglement negativity. In particular, in this chapter we study the time evolution of the logarithmic negativity after a global quantum quench. In a 1+1 dimensional conformal invariant field theory, we consider the negativity between two intervals which can be either adjacent or disjoint. We show that the negativity follows the quasi-particle interpretation for the spreading of entanglement. We check and generalise our findings with a systematic analysis of the negativity after a quantum quench in the harmonic chain, highlighting two peculiar lattice effects: the late birth and the sudden death of entanglement. The chapter is based on the following article:

[237] A. Coser, E. Tonni,and P. Calabrese, *"Entanglement negativity after a global quantum quench"*, J. Stat. Mech. P12017 (2014).

In Chap. 4 we switch to the study of entanglement negativity in fermionic systems. In this chapter we partly abandon the field theoretical models and we mainly focus on spin systems. Indeed, we consider the partial transpose of the spin reduced density matrix of two disjoint blocks in spin chains admitting a representation in terms of free fermions, such as XY chains. We exploit the solution of the model in terms of Majorana fermions and show that such partial transpose in the spin variables is a linear combination of four Gaussian fermionic operators. This representation allows to explicitly construct and evaluate the integer moments of the partial transpose. We numerically study critical XX and Ising chains and we show that the asymptotic results for large blocks agree with CFT predictions if corrections to the scaling are properly taken into account. The material on which this chapter is based is found in:

[238] A. Coser, E. Tonni,and P. Calabrese, *"Partial transpose of two disjoint blocks in XY spin chains"*, J. Stat. Mech. P08005 (2015).

In Chap. 5 we come back to the physics in the continuum. Using results from Chap. 4 for the free spinless fermion, we perform a direct calculation based on coherent state path integral. In this way, we find an analytic form for the moments of the partial transpose of the reduced density matrix of two intervals for the free massless Dirac fermion. This moments are written in terms of Riemann theta functions. We also show that the moments of arbitrary order are equal to the same quantities for the compactified boson at the self-dual point $\eta = 1$. These equalities imply the non trivial result that also the negativity of the free fermion and the self-dual boson are equal. Finally, we use the same techniques to recover the known formulas for the Rényi entropies and the moment of the partial transpose of the modular invariant Dirac fermion and the Ising model. Using the techniques introduced in Chap. 4, we give numerical evidence of all our conclusions. This chapter is mainly based on the following work:

[239] A. Coser, E. Tonni, and P. Calabrese, *"Towards entanglement negativity of two disjoint intervals for a one dimensional free fermion"*, arXiv:1508.00811.

The analysis of Sec. 5.4, as well as the related Apps. 5.E and 5.D, contain unpublished material.

Chapter 2

Rényi entropies for multiple disjoint intervals

2.1 Introduction

In this chapter we begin the study of entanglement of disjoint regions by considering a subsystem $A = \cup_{i=1}^{N} A_i$ made of N disjoint intervals. Denoting by $A_i = [u_i, v_i]$ the i-th interval with $i = 1, \dots, N$, in Fig. 2.1 we depict a configuration with $N = 4$ disjoint intervals. The main goal is to exactly compute for some simple CFT (free compactified boson and Ising model) the Rényi entropies of the reduced density matrix ρ_A, when the full system is in its ground state. Unfortunately, the functional dependence of the result on the replica index n will turn out to be quite cumbersome, and we could not perform the analytic continuation to $n \to 1$ to obtain the entanglement entropy S_A. It is worth stressing that in the case of several disjoint intervals, the Rényi entropies and the entanglement entropy S_A measure the entanglement of the union of the intervals with the rest of the system B. They are not a measure of the entanglement among the intervals, whose union is in a mixed state. In order to study the entanglement for mixed states, one needs to consider other quantities, as for example the negativity, which will be addressed in the next chapters in different settings.

For two intervals the moments of the reduced density matrix $\mathrm{Tr}\,\rho_A^n$ have been computed for the free boson compactified on a circle [226] and for the Ising model [196]. For three or more intervals, few analytic results are available in the literature. For instance, the Rényi entropies of $N > 2$ disjoint intervals for the free Dirac fermion in two dimensions has been computed in [46, 47, 49]. As already mentioned at the end of Sec. 1.4.3, the free Dirac fermion studied in these works is not the same we analyze in this chapter. It can be seen as the continuum limit of a free spinless fermion on a lattice, and it is not a modular invariant theory. On any Riemann surface, the partition function of the model will only have the sector with fully antiperiodic boundary conditions. The Dirac fermion which we are going to consider in Sec. 2.3.4 is instead a modular invariant theory obtained by fermionization of the compact boson at $\eta = 1/2$. The partition function on a Riemann surface is therefore a specific invariant combination of the partition functions with all the possible boundary conditions along the nontrivial cycles (see Eq. (2.48) and the related discussion).

The layout of the chapter is as follows. In Sec. 2.2 we introduce some UV finite quantities that will be considered in the following sections. In Sec. 2.3 we compute the

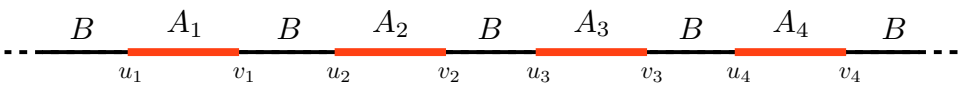

Figure 2.1: A typical configuration of disjoint intervals in the infinite line. We consider the entanglement between $A = \cup_{i=1}^{N} A_i$ (in this figure $N = 4$) and its complement B.

Rényi entropies for the free compactified boson in the generic case of N intervals and n sheets, which allows us to write the same quantity also for the Ising model. In 2.4 we discuss how the known case of two intervals is recovered. In Sec. 2.5 we check the CFT predictions for the Rényi entropies of the free boson in the decompactification regime against exact results obtained for the harmonic chain with periodic boundary conditions. In Sec. 2.6 we perform some numerical extrapolations from the known data for the Rényi entropies of the decompactified boson, to estimate its entanglement entropy. The result is again checked with the one of the harmonic chain. In Sec. 2.7 numerical results obtained with MPS for the Ising model with periodic boundary conditions are employed to check the corresponding CFT prediction through a finite size scaling analysis. In the Appendices, we collect further details and results.

2.2 Some cutoff independent quantities

By employing the method of [27, 206] and reviewed in Sec. 1.4, $\operatorname{Tr}\rho_A^n$ can be computed as a $2N$ point function of twist fields. In CFT, the dependence on the positions in a $2N$ point function of primary operators with $N \geqslant 2$ is not uniquely determined by the global conformal invariance. Indeed, we have that $\operatorname{Tr}\rho_A^n$ can be written as in Eq. (1.52), where we recall that $\mathcal{F}_{N,n}(\boldsymbol{x})$ is a model dependent function of the $2N-3$ invariant ratios $0 < x_1 < \cdots < x_{2N-3} < 1$ (see Fig. 2.2 for $N = 3$).

The expression (1.52) is UV divergent. Such divergence is introduced dividing any length occurring in the formula ($u_j - u_i$, $v_j - u_i$, etc.) by the UV cutoff ϵ. Since the ratios $\boldsymbol{x}$ are left unchanged, the whole dependence on ϵ of (1.52) comes from the ratio of lengths within the absolute value, which gives $\epsilon^{2N\Delta_n}$. It is useful to introduce some quantities which are independent of the UV cutoff. For $N = 2$, we can construct the combination of Rényi entropies already introduced in Eq. (1.65)

$$I^{(n)}_{A_1,A_2} \equiv S^{(n)}_{A_1} + S^{(n)}_{A_2} - S^{(n)}_{A_1\cup A_2} = \frac{1}{n-1} \log\left(\frac{\operatorname{Tr}\rho^n_{A_1\cup A_2}}{\operatorname{Tr}\rho^n_{A_1}\operatorname{Tr}\rho^n_{A_2}}\right). \tag{2.1}$$

The limit $n \to 1$ of this quantity gives the mutual information I_{A_1,A_2}

$$I_{A_1,A_2} \equiv S_{A_1} + S_{A_2} - S_{A_1\cup A_2} = \lim_{n\to 1} I^{(n)}_{A_1,A_2}\,, \tag{2.2}$$

which is independent of the UV cutoff as well. The subadditivity of the entanglement entropy tells us that $I_{A_1,A_2} \geqslant 0$, while the strong subadditivity implies that it increases when one of the intervals is enlarged.

For $N > 2$ we can find easily two ways to construct quantities such that the short distance divergence cancels. Let us consider first the following ratio

$$R_{N,n} \equiv \prod_{p=1}^{N} \prod_{\sigma_{N,p}} \left(\operatorname{Tr}\rho^n_{\sigma_{N,p}}\right)^{(-1)^{N-p}}, \tag{2.3}$$

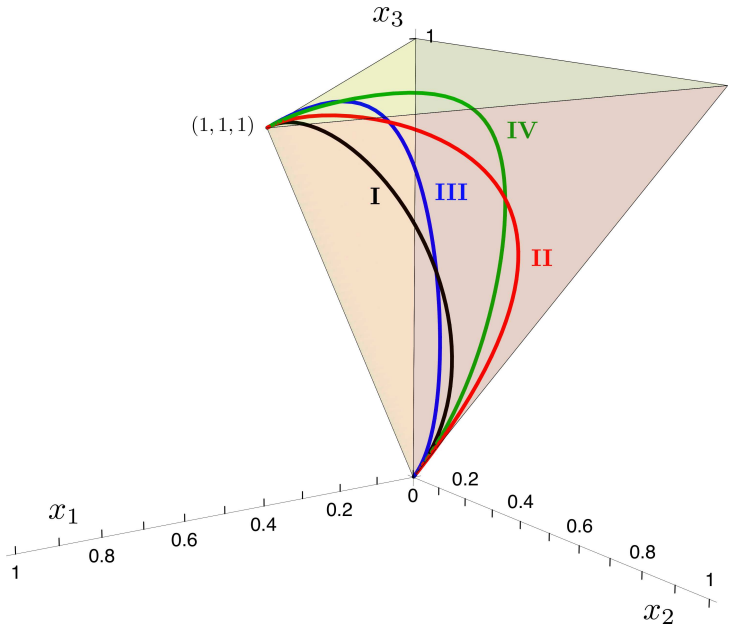

Figure 2.2: The domain $0 < x_1 < x_2 < x_3 < 1$ of the function $\mathcal{F}_{3,n}(\boldsymbol{x})$. The lines within this domain are the configurations defined in (2.79).

where we denoted by $\sigma_{N,p}$ a generic choice of $1 \leqslant p \leqslant N$ intervals among the N ones we are dealing with. Since $\operatorname{Tr} \rho^n_{\sigma_{N,p}}$ goes like $\epsilon^{2p\Delta_n}$, one finds that (2.3) is independent of ϵ by employing that $\sum_{p=1}^{N} (-1)^{N-p} \binom{N}{p} p = 0$. In the simplest cases of $N = 2$ and $N = 3$, the ratio (2.3) reads

$$R_{2,n} = \frac{\operatorname{Tr} \rho^n_{\{1,2\}}}{\operatorname{Tr} \rho^n_{\{1\}} \operatorname{Tr} \rho^n_{\{2\}}}, \qquad R_{3,n} = \frac{\operatorname{Tr} \rho^n_{\{1,2,3\}} \left(\operatorname{Tr} \rho^n_{\{1\}} \operatorname{Tr} \rho^n_{\{2\}} \operatorname{Tr} \rho^n_{\{3\}} \right)}{\operatorname{Tr} \rho^n_{\{1,2\}} \operatorname{Tr} \rho^n_{\{1,3\}} \operatorname{Tr} \rho^n_{\{2,3\}}}, \qquad \dots \tag{2.4}$$

Let us stress here that this ratio $R_{N,n}$ is quite different from the ratio defined in (1.71) and they must not be confused. In order to generalize (2.1) for $N \geqslant 2$, one introduces

$$I^{(n)}_{A_1,\dots,A_N} \equiv \frac{(-1)^N}{n-1} \log R_{N,n}\,, \tag{2.5}$$

and its limit $n \to 1$, as done in (2.2) for $N = 2$, i.e.

$$I_{A_1,\dots,A_N} \equiv \lim_{n \to 1} I^{(n)}_{A_1,\dots,A_N}\,. \tag{2.6}$$

For the simplest cases of $N = 3$ and $N = 4$, one finds respectively

$$I_{A_1,A_2,A_3} = S_{A_1} + S_{A_2} + S_{A_3} - S_{A_1 \cup A_2} - S_{A_1 \cup A_3} - S_{A_2 \cup A_3} + S_{A_1 \cup A_2 \cup A_3}\,, \tag{2.7a}$$

$$I_{A_1,A_2,A_3,A_4} = \sum_{i=1}^{4} S_{A_i} - \sum_{\substack{i,j=1 \\ i<j}}^{4} S_{A_i \cup A_j} + \sum_{\substack{i,j,k=1 \\ i<j<k}}^{4} S_{A_i \cup A_j \cup A_k} - S_{A_1 \cup A_2 \cup A_3 \cup A_4}\,. \tag{2.7b}$$

The quantity I_{A_1,A_2,A_3} is called tripartite information [49] and it provides a way to establish whether the mutual information is extensive ($I_{A_1,A_2,A_3}=0$) or not. In a general quantum field theory there is no definite sign for I_{A_1,A_2,A_3}, but for theories with a holographic dual it has been shown that $I_{A_1,A_2,A_3}\leqslant 0$ [80].

Another cutoff independent ratio is given by

$$\tilde{R}_{N,n} \equiv \frac{\operatorname{Tr}\rho_A^n}{\prod_{i=1}^N \operatorname{Tr}\rho_{A_i}^n}\,. \tag{2.8}$$

When $N=2$ we have $R_{2,n}=\tilde{R}_{2,n}$ but (2.3) and (2.8) are different for $N>2$. From the definitions (2.3) and (2.8), we observe that, when one of the intervals collapses to the empty set, i.e. $A_k\to\emptyset$ for some $k\in\{1,\dots,N\}$, we have that $R_{N,n}\to 1$ and $\tilde{R}_{N,n}\to\tilde{R}_{N-1,n}$, where $\tilde{R}_{N-1,n}$ is defined through $A\setminus A_k$.

For two dimensional conformal field theories at zero temperature we can write $R_{N,n}$ and $\tilde{R}_{N,n}$ more explicitly. In particular, plugging (1.53) and (1.52) into (2.8), it is straightforward to observe that c_n simplifies and we are left with

$$\tilde{R}_{N,n}(\boldsymbol{x}) = \left|\prod_{i<j}\frac{(u_i-u_j)(v_i-v_j)}{(u_i-v_j)(u_j-v_i)}\right|^{2\Delta_n}\mathcal{F}_{N,n}(\boldsymbol{x}) \equiv |p_N(\boldsymbol{x})|^{2\Delta_n}\,\mathcal{F}_{N,n}(\boldsymbol{x})\,, \tag{2.9}$$

where the product within the absolute value, that we denote by p_N, can be written in terms of $\boldsymbol{x}$. Thus, (2.9) tells us that $\mathcal{F}_{N,n}(\boldsymbol{x})$ can be easily obtained from $\tilde{R}_{N,n}(\boldsymbol{x})$. When $N=2$ we have $p_2(x)=-1/(1-x)$, while for $N=3$ we find

$$p_3(\boldsymbol{x}) \equiv -\frac{(x_3-x_1)(1-x_2)\,x_2}{(x_2-x_1)(1-x_1)(1-x_3)\,x_3}\,. \tag{2.10}$$

For higher values of N, the expression of $p_N(\boldsymbol{x})$ is more complicated.

As for $R_{N,n}$ in (2.3), considering the choice of intervals given by $\sigma_{N,p}$, we have

$$\operatorname{Tr}\rho_{\sigma_{N,p}}^n = c_n^p\,\big|P_p(\sigma_{N,p})\big|^{2\Delta_n}\,\mathcal{F}_{p,n}(\boldsymbol{x}^{\sigma_{N,p}})\,, \tag{2.11}$$

where

$$P_p(\sigma_{N,p}) \equiv \left.\frac{\prod_{i<j}(u_j-u_i)(v_j-v_i)}{\prod_{i,j}(v_j-u_i)}\right|_{i,j\,\in\,\sigma_{N,p}}\,, \tag{2.12}$$

and $\boldsymbol{x}^{\sigma_{N,p}}$ denotes the $2p-3$ harmonic ratios that can be constructed through the $2p$ endpoints of the intervals of A specified by $\sigma_{N,p}$. Notice that (2.11) becomes (1.52) when $p=N$ and (1.53) for $p=1$ because $\mathcal{F}_{N,1}=1$ by definition and $P_1(\sigma_{N,1})=1/(v_j-u_j)$, being j the interval specified by $\sigma_{N,1}$. Moreover, since (2.12) can be written in terms of the $2N-3$ elements of $\boldsymbol{x}$, we have that $R_{N,n}=R_{N,n}(\boldsymbol{x})$ (see App. 2.A for more details). Plugging (2.11) into (2.3), one finds that for $N>2$ all the factors $P_p(\sigma_{N,p})$ cancel (this simplification is explained in App. 2.A) and therefore we have

$$R_{N,n}(\boldsymbol{x}) = \prod_{p=2}^{N}\prod_{\sigma_{N,p}}\big[\mathcal{F}_{p,n}(\boldsymbol{x}^{\sigma_{N,p}})\big]^{(-1)^{N-p}}. \tag{2.13}$$

In order to cancel those parameters which occur only through multiplicative factors, we find it useful to normalize the quantities we introduced by themselves computed for a fixed configuration. Thus, for (2.3) and (2.6) we have respectively

$$R_{N,n}^{\text{norm}} \equiv \frac{R_{N,n}}{R_{N,n}\big|_{\text{fixed configuration}}}\,, \qquad I_N^{\text{sub}} \equiv I_N - I_N\big|_{\text{fixed configuration}}\,, \tag{2.14}$$

where we adopted the shorthand notation $I_N \equiv I_{A_1,\dots,A_N}$. In conformal field theories, for the scale invariant quantities depending on the harmonic ratios $\boldsymbol{x}$, the fixed configuration is characterized by fixed values $\boldsymbol{x}_{\text{fixed}}$. For instance, we have

$$R^{\text{norm}}_{N,n}(\boldsymbol{x}) = \frac{R_{N,n}(\boldsymbol{x})}{R_{N,n}(\boldsymbol{x}_{\text{fixed}})}\,, \qquad \mathcal{F}^{\text{norm}}_{N,n}(\boldsymbol{x}) = \frac{\mathcal{F}_{N,n}(\boldsymbol{x})}{\mathcal{F}_{N,n}(\boldsymbol{x}_{\text{fixed}})}\,. \tag{2.15}$$

In Sec. 2.5 this normalization is adopted to study the free boson on the infinite line.

2.3 Free compactified boson

In this section we consider the real free boson $\phi(z, z^*)$ on the Riemann surface $\mathcal{R}_{N,n}$ and compactified on a circle of radius R_{circle}. Its action reads

$$S[\phi] \propto \int_{\mathcal{R}_{N,n}} \partial_z\phi\, \partial_{z^*}\phi\, d^2z\,. \tag{2.16}$$

The worldsheet is $\mathcal{R}_{N,n}$ and the target space is $\mathbb{R}/(2\pi R_{\text{cirlce}}\,\mathbb{Z})$. This model has $c = 1$ and its partition function for a generic compact Riemann surface of genus g has been largely discussed in the literature (see e.g. [207, 209, 210, 212–214]).

Instead of working with a single field ϕ on $\mathcal{R}_{N,n}$, one could equivalently consider n independent copies of the model with a field ϕ_j on the j-th sheet [45, 46]. These n fields are coupled through their boundary conditions along the cuts A_i on the real axis in a cyclic way (see Fig. 2.3)

$$\phi_j(x, 0^+) = \phi_{j+1}(x, 0^-)\,, \qquad x \in A\,, \qquad j \in \{1, \dots, n\}\,, \qquad n+1 \equiv 1\,. \tag{2.17}$$

This approach has been adopted in [226] for the $N = 2$ case, employing the results of [208]. In principle one should properly generalize the construction of [226] to $N > 2$. For $n = 2$ this computation has been done in [207]. Here, instead, in order to address the case $n > 2$, we compute (1.52) for the model (2.16) more directly, borrowing heavily from the literature about the free compactified boson on higher genus Riemann surfaces, whose partition function has been constructed in terms of the period matrix of the underlying Riemann surface.

2.3.1 The period matrix

As discussed in Sec. 1.4.3, the n-sheeted Riemann surface $\mathcal{R}_{N,n}$ obtained by considering N intervals $A_i = [u_i, v_i]$ $(i = 1, \dots, N)$ is defined by the following complex curve in $\mathbb{C}^2$ [234]

$$y^n = u(z)v(z)^{n-1}\,, \qquad u(z) = \prod_{\gamma=1}^{N} (z - x_{2\gamma-2})\,, \qquad v(z) = \prod_{\gamma=1}^{N-1} (z - x_{2\gamma-1})\,. \tag{2.18}$$

The complex coordinates y and z parameterize $\mathbb{C}^2$ and in $u(z)$ we introduced $x_0 \equiv 0$ and $x_{2N-2} \equiv 1$ for notational convenience. For $n = 2$, the curve (2.18) is hyperelliptic. The genus of $\mathcal{R}_{N,n}$ is (1.74) and it can be found also by applying the Riemann-Hurwitz formula for the curve (2.18).

The period matrix of the curve (2.18) has been computed in [234] by considering the following non normalized basis of holomorphic differentials

$$\omega_{\alpha,j} = \frac{z^{\alpha-1}\, v(z)^{j-1}}{y^j}\, dz\,, \qquad \alpha = 1, \dots, N-1\,, \qquad j = 1, \dots, n-1\,, \tag{2.19}$$

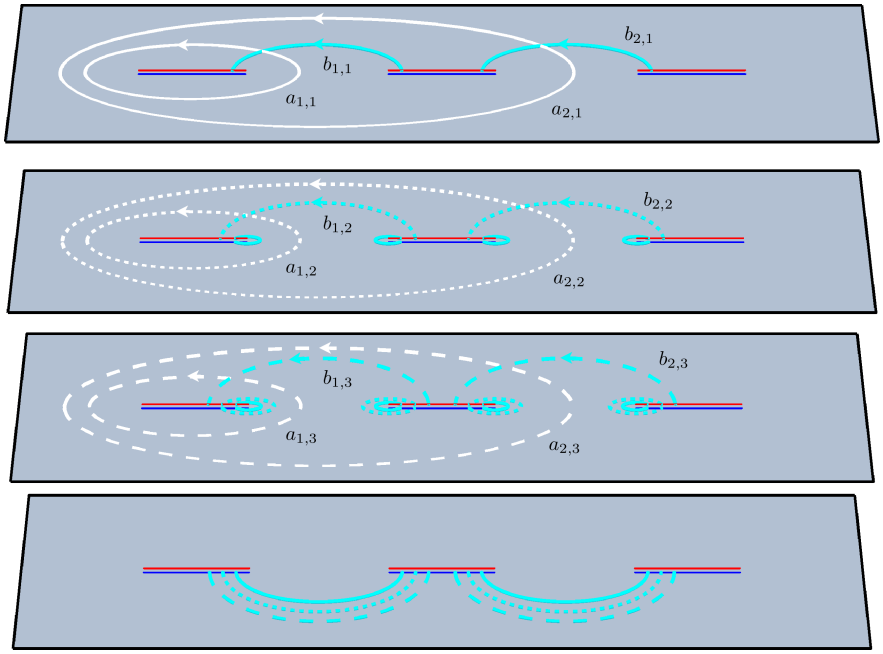

Figure 2.3: The canonical homology basis $\{a_{\alpha,j}, b_{\alpha,j}\}$ for $N = 3$ intervals of equal length and $n = 4$ sheets. The sheets are ordered starting from the top. For each cut, the upper part (red) is identified with the lower part (blue) of the corresponding cut on the next sheet in a cyclic way, according to (2.17).

where $y = y(z)$ through (2.18). The set of one forms defined in (2.19) contains g elements. In (2.19) we employed a double index notation: a greek index for the intervals and a latin one for the sheets. We make this choice to facilitate the comparison with [226], slightly changing the notation with respect to the previous section. These two indices can be combined either as $r = \alpha + (N-1)(j-1)$ [234] or $r = j + (n-1)(\alpha-1)$ [228] in order to have an index $r = 1, \dots, g$. Hereafter we assume the first choice. Notice that for the cases of $(N, n) = (2, n)$ and $(N, n) = (N, 2)$ we do not need to introduce this distinction.

The period matrix of the Riemann surface is defined in terms of a canonical homology basis, namely a set of $2g$ closed oriented curves $\{a_r, b_r\}$ which cannot be contracted to a point and whose intersections satisfy certain simple relations. In particular, defining the intersection number $h \circ \tilde{h}$ between two oriented curves h and $\tilde{h}$ on the Riemann surface as the number of intersection points, with the orientation taken into account (through the tangent vectors at the intersection point and the right hand rule), for a canonical homology basis we have $a_r \circ a_s = b_r \circ b_s = 0$ and $a_r \circ b_s = -\, b_r \circ a_s = \delta_{rs}$. By employing the double index notation mentioned above, we choose the canonical homology basis $\{a_{\alpha,j}, b_{\alpha,j}\}$ adopted in [234], which is depicted in Fig. 2.3 and in Fig. 2.4 for the special case of $N = 3$ intervals and $n = 4$ sheets.

Once the canonical homology basis has been chosen, we introduce the $g \times g$ matrices

$$\mathcal{A}^{\beta,\alpha}_{k,j} = \oint_{a_{\alpha,j}} \omega_{\beta,k} \,, \qquad \mathcal{B}^{\beta,\alpha}_{k,j} = \oint_{b_{\alpha,j}} \omega_{\beta,k} \,, \tag{2.20}$$

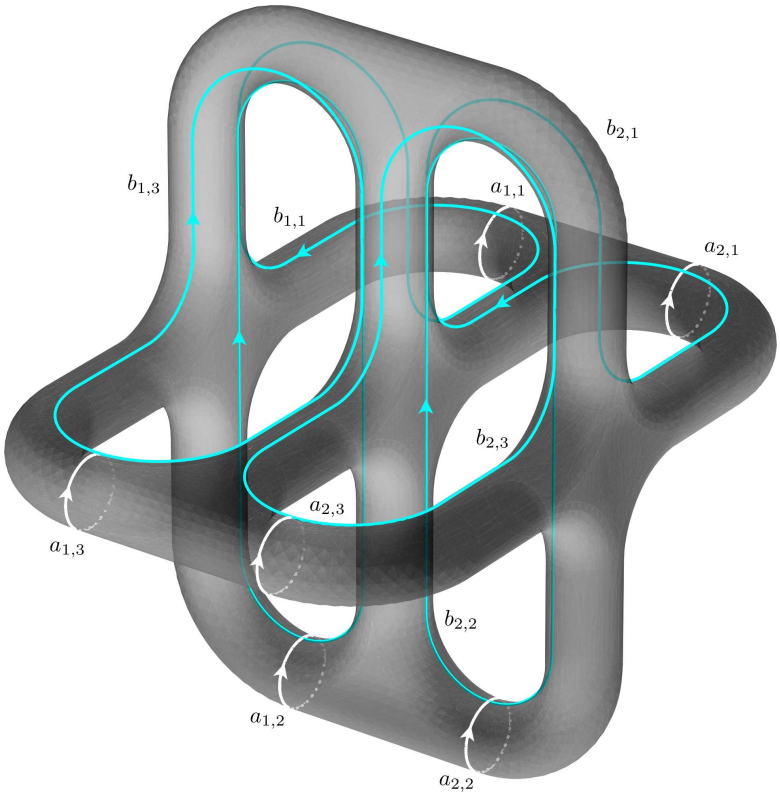

Figure 2.4: The Riemann surface $\mathcal{R}_{3,4}$ with the canonical homology basis $\{a_{\alpha,j}, b_{\alpha,j}\}$, represented also in Fig. 2.3.

where latin and greek indices run as in (2.19). Given the convention adopted above, $\mathcal{A}^{\beta,\alpha}_{k,j}$ provides the element $\mathcal{A}_{rs}$ of the $g \times g$ matrix $\mathcal{A}$ by setting $r = \beta + (N-1)(k-1)$ and $s = \alpha + (N-1)(j-1)$ (similarly for $\mathcal{B}$), namely the row index is determined by the one form and the column index by the cycle. This connection among indices is important because the matrices $\mathcal{A}$ and $\mathcal{B}$ are not symmetric.

From the one forms (2.19) and the matrix $\mathcal{A}$ in (2.20), one constructs the normalized basis of one forms $\nu_r = \sum_{s=1}^{g} \mathcal{A}^{-1}_{rs}\omega_s$, which provides the *period matrix* τ as follows

$$\oint_{a_r} \nu_s = \delta_{rs}\,, \qquad \oint_{b_r} \nu_s = \tau_{rs}\,, \qquad r,s = 1,\dots,g\,. \tag{2.21}$$

The period matrix τ is a $g \times g$ complex and symmetric matrix with positive definite imaginary part, i.e. it belongs to the Siegel upper half space. Substituting the expression of ν_s into the definition of τ in (2.21) and employing the definition of the matrix $\mathcal{B}$ in (2.20), it is straightforward to observe that

$$\tau = \mathcal{A}^{-1} \cdot \mathcal{B} \equiv \mathcal{R} + \mathrm{i}\,\mathcal{I}\,, \tag{2.22}$$

where $\mathcal{R}$ and $\mathcal{I}$ are respectively the real and the imaginary part of the period matrix.

In order to compute the period matrix (2.22), let us introduce the set of auxiliary cycles $\{a^{\text{aux}}_{\alpha,j}, b^{\text{aux}}_{\alpha,j}\}$, which is represented in Figs. 2.28 and 2.29. It is clear that this set

is not a canonical homology basis. Indeed, some cycles intersect more than one cycle. Nevertheless, we can use them to decompose the cycles of the basis $\{a_{\alpha,j}, b_{\alpha,j}\}$ as

$$a_{\alpha,j} = \sum_{\gamma=1}^{\alpha} a^{\text{aux}}_{\gamma,j} \,, \qquad b_{\alpha,j} = \sum_{l=j}^{n-1} b^{\text{aux}}_{\alpha,l} \,. \tag{2.23}$$

Integrating the one forms (2.19) along the auxiliary cycles as shown in (2.20) for the basis $\{a_{\alpha,j}, b_{\alpha,j}\}$, one defines the matrices $\mathcal{A}^{\text{aux}}$ and $\mathcal{B}^{\text{aux}}$. The advantage of the auxiliary cycles is that the integrals $(\mathcal{A}^{\text{aux}})^{\beta,\alpha}_{k,j}$ and $(\mathcal{B}^{\text{aux}})^{\beta,\alpha}_{k,j}$ on the j-th sheet are obtained multiplying the corresponding ones on the first sheet by a phase [208]

$$(\mathcal{A}^{\text{aux}})^{\beta,\alpha}_{k,j} = \rho_n^{k(j-1)} (\mathcal{A}^{\text{aux}})^{\beta,\alpha}_{k,1} \,, \quad (\mathcal{B}^{\text{aux}})^{\beta,\alpha}_{k,j} = \rho_n^{k(j-1)} (\mathcal{B}^{\text{aux}})^{\beta,\alpha}_{k,1} \,, \quad \rho_n \equiv e^{2\pi \mathrm{i}/n} \,. \tag{2.24}$$

Because of the relation (2.23) among the cycles of the canonical homology basis and the auxiliary ones, the matrices $\mathcal{A}$ and $\mathcal{B}$ in (2.20) are related to $\mathcal{A}^{\text{aux}}$ and $\mathcal{B}^{\text{aux}}$ as

$$\mathcal{A}^{\beta,\alpha}_{k,j} = \sum_{\gamma=1}^{\alpha} (\mathcal{A}^{\text{aux}})^{\beta,\gamma}_{k,j} = \rho_n^{k(j-1)} \sum_{\gamma=1}^{\alpha} (\mathcal{A}^{\text{aux}})^{\beta,\gamma}_{k,1} \,, \tag{2.25a}$$

$$\mathcal{B}^{\beta,\alpha}_{k,j} = \sum_{l=j}^{n-1} (\mathcal{B}^{\text{aux}})^{\beta,\alpha}_{k,l} = \sum_{l=j}^{n-1} \rho_n^{k(l-1)} (\mathcal{B}^{\text{aux}})^{\beta,\alpha}_{k,1} = \frac{\rho_n^{kj} - 1}{\rho_n^k (1 - \rho_n^k)} \, (\mathcal{B}^{\text{aux}})^{\beta,\alpha}_{k,1} \,, \tag{2.25b}$$

where the relations (2.24) have been used. Thus, from (2.25) we learn that we just need $(\mathcal{A}^{\text{aux}})^{\beta,\alpha}_{k,1}$ and $(\mathcal{B}^{\text{aux}})^{\beta,\alpha}_{k,1}$ to construct the matrices $\mathcal{A}$ and $\mathcal{B}$.

By carefully considering the phases in the integrand along the cycles, we find

$$(\mathcal{A}^{\text{aux}})^{\beta,\alpha}_{k,1} = \oint_{a^{\text{aux}}_{\alpha,1}} \omega_{\beta,k} = (-1)^{N-\alpha} (\rho_n^{-k} - 1) \, \mathscr{I}_{\beta,k}\big|^{x_{2\alpha-1}}_{x_{2\alpha-2}} \,, \tag{2.26a}$$

$$(\mathcal{B}^{\text{aux}})^{\beta,\alpha}_{k,1} = \oint_{b^{\text{aux}}_{\alpha,1}} \omega_{\beta,k} = (-1)^{N-\alpha} \rho_n^{k/2} (\rho_n^{-k} - 1) \, \mathscr{I}_{\beta,k}\big|^{x_{2\alpha}}_{x_{2\alpha-1}} \,, \tag{2.26b}$$

where we introduced the following integral

$$\mathscr{I}_{\beta,k}\big|^b_a \equiv \int_0^1 \frac{(b-a) \left[(b-a)t + a\right]^{\beta - 1 - k/n} \, dt}{\prod_{\gamma=2}^{N} \left|(b-a)t - (x_{2\gamma-2} - a)\right|^{k/n} \prod_{\gamma=1}^{N-1} \left|(b-a)t - (x_{2\gamma-1} - a)\right|^{1-k/n}} \,. \tag{2.27}$$

We numerically evaluate the integrals needed to get the $g \times g$ matrices $\mathcal{A}$ and $\mathcal{B}$ as explained above and then construct the period matrix $\tau = \mathcal{A}^{-1} \cdot \mathcal{B}$, as in (2.22).

In App. 2.B we write the integrals occurring in (2.26) in terms of Lauricella functions, which are generalizations of the hypergeometric functions [241]. As a check of our expressions, we employed the formulas for the number of real components of the period matrix found in [228].

Both the matrices in (2.25) share the following structure

$$\mathcal{H}^{\beta,\alpha}_{k,j} = h(k,j) (\mathcal{H}_k)_{\beta\alpha} \,, \qquad (\mathcal{H}_k)_{\beta\alpha} \equiv \mathcal{H}^{\beta,\alpha}_{k,1} \,, \tag{2.28}$$

where we denoted by $\mathcal{H}$ a $g \times g$ matrix whose indices run as explained in the beginning of this subsection, h is a generic function and we also introduced the $(N-1) \times (N-1)$

matrices $\mathcal{H}_k$ labelled by $k = 1, \dots, n-1$. Considering the block diagonal matrix made by the $\mathcal{H}_k$'s, one finds that (2.28) can be written as

$$\mathcal{H} = \mathcal{H}_{\mathrm{d}} \cdot (\mathscr{M}_{\mathcal{H}} \otimes \mathbb{I}_{N-1}) \,, \qquad \mathcal{H}_{\mathrm{d}} \equiv \mathrm{diag}(\dots, \mathcal{H}_k \,, \dots) \,, \qquad (\mathscr{M}_{\mathcal{H}})_{kj} \equiv h(k,j) \,, \tag{2.29}$$

where we denote by $\mathbb{I}_p$ the $p \times p$ identity matrix. For the determinant of (2.29), we find

$$\det(\mathcal{H}) = \big(\det(\mathscr{M}_{\mathcal{H}})\big)^{n-1} \prod_{k=1}^{n-1} \det(\mathcal{H}_k) \,. \tag{2.30}$$

Thus, (2.25) can be expressed as in (2.29) with

$$(\mathscr{M}_{\mathcal{A}})_{kj} \equiv \rho_n^{k(j-1)} \,, \qquad (\mathcal{A}_k)_{\beta\alpha} \equiv \mathcal{A}_{k,1}^{\beta,\alpha} = (\rho_n^{-k} - 1) \sum_{\gamma=1}^{\alpha} (-1)^{N-\gamma} \mathscr{I}_{\beta,k} \big|_{x_{2\gamma-2}}^{x_{2\gamma-1}} \,, \tag{2.31a}$$

$$(\mathscr{M}_{\mathcal{B}})_{kj} \equiv \frac{\rho_n^{kj} - 1}{\rho_n^k (1 - \rho_n^{-k})} \,, \quad (\mathcal{B}_k)_{\beta\alpha} \equiv \mathcal{B}_{k,1}^{\beta,\alpha} = (-1)^{N-\alpha} \rho_n^{-k/2} (1 - \rho_n^{-k}) \, \mathscr{I}_{\beta,k} \big|_{x_{2\alpha-1}}^{x_{2\alpha}} \,, \tag{2.31b}$$

where (2.26) has been employed. The period matrix (2.22) becomes [234]

$$\tau = (\mathscr{M}_{\mathcal{A}} \otimes \mathbb{I}_{N-1})^{-1} \cdot \mathrm{diag}(\mathcal{A}_1^{-1} \cdot \mathcal{B}_1, \mathcal{A}_2^{-1} \cdot \mathcal{B}_2, \dots, \mathcal{A}_{n-1}^{-1} \cdot \mathcal{B}_{n-1}) \cdot (\mathscr{M}_{\mathcal{B}} \otimes \mathbb{I}_{N-1}) \,. \tag{2.32}$$

Notice that $\det(\mathscr{M}_{\mathcal{A}}) = \det(\mathscr{M}_{\mathcal{B}})$ and this implies

$$\det(\tau) = \det\big(\mathrm{diag}(\mathcal{A}_1^{-1} \cdot \mathcal{B}_1, \dots, \mathcal{A}_{n-1}^{-1} \cdot \mathcal{B}_{n-1})\big) = \prod_{k=1}^{n-1} \frac{\det(\mathcal{B}_k)}{\det(\mathcal{A}_k)} \,. \tag{2.33}$$

Moreover, since $\det(\mathscr{M}_{\mathcal{A}}) \neq 1$, from the relation (2.30) we have $\det(\mathcal{A}) \neq \prod_{k=1}^{n-1} \det(\mathcal{A}_k)$ and $\det(\mathcal{B}) \neq \prod_{k=1}^{n-1} \det(\mathcal{B}_k)$.

2.3.2 The partition function

In order to write the partition function of the free boson on $\mathcal{R}_{N,n}$, we need the Riemann theta function introduced in (1.59) specialized to the $\boldsymbol{z} = 0$ case, which is [215, 216]

$$\Theta(\boldsymbol{0}|\Omega) = \sum_{\boldsymbol{m} \in \mathbb{Z}^p} \exp(\mathrm{i}\pi \, \boldsymbol{m}^{\mathrm{t}} \cdot \Omega \cdot \boldsymbol{m}) \,, \tag{2.34}$$

where Ω is a $p \times p$ complex, symmetric matrix with positive imaginary part. We recall that the Riemann theta function $\Theta(\boldsymbol{z}|\Omega)$ is defined as a periodic function of a complex vector $\boldsymbol{z} \in \mathbb{C}^p$, but in our problem the special case $\boldsymbol{z} = \boldsymbol{0}$ occurs.

As mentioned at the beginning of this section, we do not explicitly extend the construction of [207, 208, 226] to the case $N \geqslant 2$ and $n \geqslant 2$. Given the form of the result for $N = 2$ intervals and $n \geqslant 2$ sheets [219, 226], we assume its straightforward generalization to $N > 2$. Let us recall that $\mathcal{F}_{2,n}(x)$ can be obtained as the properly normalized partition function of the model (2.16) on $\mathcal{R}_{2,n}$, once the four endpoints of the two intervals have been mapped to 0, x, 1 and ∞ ($0 < x < 1$) [226]. Thus, for $N > 2$ we compute $\mathcal{F}_{N,n}(\boldsymbol{x})$ in (1.52) as the normalized partition function of (2.16) on $\mathcal{R}_{N,n}$, once (1.51) has been applied.

By employing the results of [207, 209, 210, 212–214], for the free compactified boson we can write $\mathcal{F}_{N,n}(\boldsymbol{x}) = \mathcal{F}_{N,n}^{\mathrm{qu}} \, \mathcal{F}_{N,n}^{\mathrm{cl}}(\eta)$, where this splitting comes from the separation of

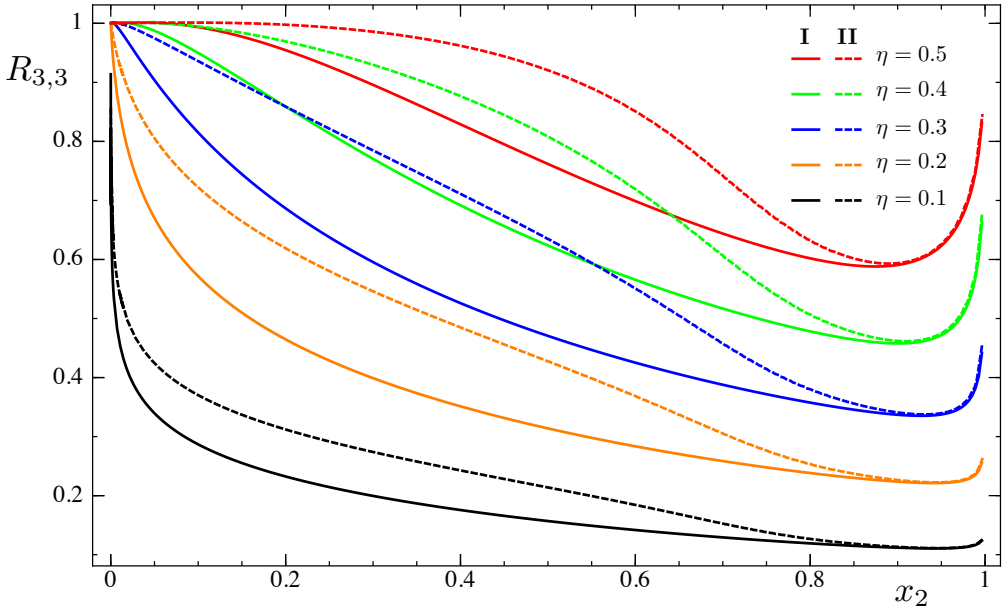

Figure 2.5: The function $R_{3,3}(\boldsymbol{x})$ for the free compactified boson, obtained from (2.13) and (2.41), computed for two configurations of intervals defined in Sec. 2.5 (see Fig. 2.2).

the field as the sum of a classical solution and the quantum fluctuation around it. The classical part is made by the sum over all possible windings around the circular target space and therefore it encodes its compactified nature. This tells us that $\mathcal{F}^{\rm cl}_{N,n}$ contains all the dependence on the compactification radius through the parameter $\eta \propto R^2_{\rm circle}$. We refer the reader to the explicit constructions of [207, 208, 226] for the details.

Given the period matrix τ for $\mathcal{R}_{N,n}$ computed in Sec. 2.3.1, the quantum and the classical part in $\mathcal{F}_{N,n}(\boldsymbol{x}) = \mathcal{F}^{\rm qu}_{N,n}\,\mathcal{F}^{\rm cl}_{N,n}(\eta)$ read [207, 209, 210, 214]

$$\mathcal{F}^{\rm qu}_{N,n} = \frac{1}{|\Theta(\boldsymbol{0}|\tau)|^2}\,, \qquad \mathcal{F}^{\rm cl}_{N,n}(\eta) = \sum_{\boldsymbol{p},\tilde{\boldsymbol{p}}} \exp[\mathrm{i}\pi(\boldsymbol{p}^{\rm t}\cdot\tau\cdot\boldsymbol{p} - \tilde{\boldsymbol{p}}^{\rm t}\cdot\tau\cdot\tilde{\boldsymbol{p}})]\,, \tag{2.35}$$

where

$$\boldsymbol{p} = \frac{\boldsymbol{m}}{\sqrt{2\eta}} + \frac{\boldsymbol{n}\sqrt{2\eta}}{2}\,, \qquad \tilde{\boldsymbol{p}} = \frac{\boldsymbol{m}}{\sqrt{2\eta}} - \frac{\boldsymbol{n}\sqrt{2\eta}}{2}\,, \qquad \boldsymbol{m},\boldsymbol{n} \in \mathbb{Z}^g\,. \tag{2.36}$$

Expanding the argument of the exponential in (2.35), one finds that the classical part can be written in terms of the Riemann theta function as

$$\mathcal{F}^{\rm cl}_{N,n}(\eta) = \Theta(\boldsymbol{0}|T_\eta)\,, \tag{2.37}$$

where T_η is the following $2g \times 2g$ symmetric matrix

$$T_\eta = \begin{pmatrix} \mathrm{i}\,\eta\,\mathcal{I} & \mathcal{R} \\ \mathcal{R} & \mathrm{i}\,\mathcal{I}/\eta \end{pmatrix}. \tag{2.38}$$

Being $\mathcal{I}$ positive definite and $\eta > 0$, also the imaginary part of T_η is positive definite. From (2.37) and (2.38), it is straightforward to observe that $\mathcal{F}^{\rm cl}_{N,n}(\eta) = \mathcal{F}^{\rm cl}_{N,n}(1/\eta)$. Thus,

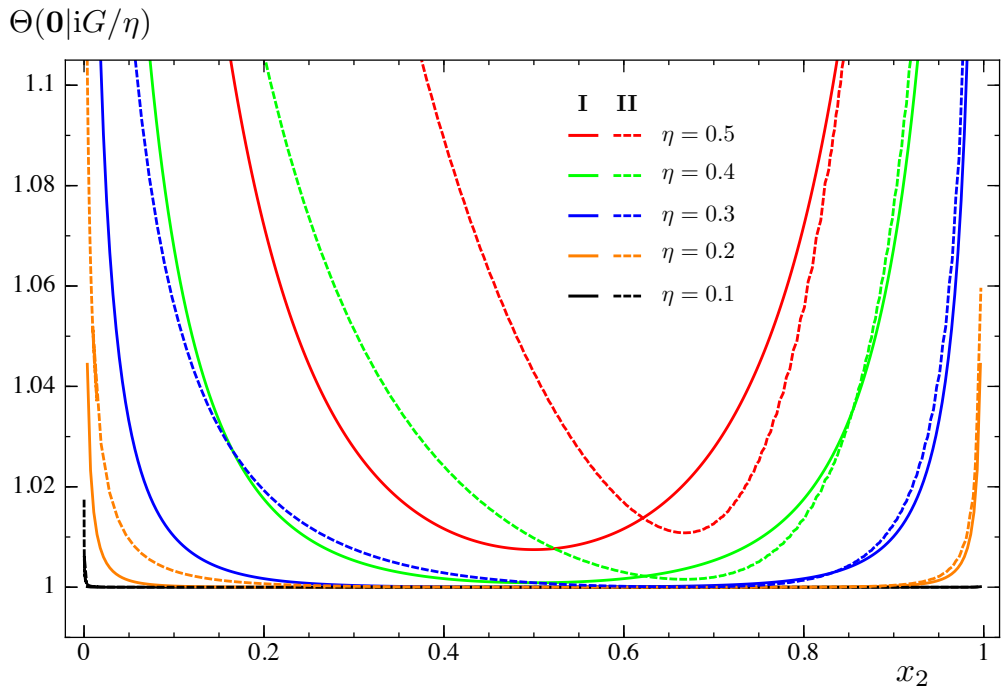

Figure 2.6: The function $\Theta(\mathbf{0}|\mathrm{i}G/\eta)$ with $N = 3$, $n = 3$ and for the configurations I and II shown in Fig. 2.2. For small η (the decompactification regime) this term can be neglected (see (2.39) and (2.41)).

since all the dependence of $\mathcal{F}_{N,n}(\boldsymbol{x})$ on η is contained in $\mathcal{F}^{\mathrm{cl}}_{N,n}$, we find that $\mathcal{F}_{N,n}(\boldsymbol{x})$ is invariant under $\eta \leftrightarrow 1/\eta$.

By employing the Poisson summation formula (only for half of the sums), the classical part (2.37) can be written as

$$\mathcal{F}^{\mathrm{cl}}_{N,n}(\eta) = \eta^{g/2}\,\frac{\Theta(\mathbf{0}|\mathrm{i}\eta G)}{\sqrt{\det(\mathcal{I})}} = \eta^{-g/2}\,\frac{\Theta(\mathbf{0}|\mathrm{i}G/\eta)}{\sqrt{\det(\mathcal{I})}}\,, \tag{2.39}$$

where the $2g \times 2g$ matrix G reads

$$G = \begin{pmatrix} \mathcal{I} + \mathcal{R}\cdot\mathcal{I}^{-1}\cdot\mathcal{R} & \mathcal{R}\cdot\mathcal{I}^{-1} \\ \mathcal{I}^{-1}\cdot\mathcal{R} & \mathcal{I}^{-1} \end{pmatrix}. \tag{2.40}$$

This matrix is real, independent of η and symmetric, being $\mathcal{R}$ and $\mathcal{I}$ symmetric matrices. Combining (2.35), (2.37) and (2.39), we find $\mathcal{F}_{N,n}(\boldsymbol{x})$ for the free compactified boson

$$\mathcal{F}_{N,n}(\boldsymbol{x}) = \frac{\Theta(\mathbf{0}|T_\eta)}{|\Theta(\mathbf{0}|\tau)|^2} = \frac{\eta^{g/2}\,\Theta(\mathbf{0}|\mathrm{i}\eta G)}{\sqrt{\det(\mathcal{I})}\,|\Theta(\mathbf{0}|\tau)|^2} = \frac{\eta^{-g/2}\,\Theta(\mathbf{0}|\mathrm{i}G/\eta)}{\sqrt{\det(\mathcal{I})}\,|\Theta(\mathbf{0}|\tau)|^2}\,. \tag{2.41}$$

The term $|\Theta(\mathbf{0}|\tau)|$ in the denominator can be rewritten by applying the Thomae type formula for the complex curves (2.18) [234, 242]

$$\Theta(\mathbf{0}|\tau)^8 = \frac{\prod_{k=1}^{n-1}[\det(\mathcal{A}_k)]^4}{(2\pi\mathrm{i})^{4g}} \left(\prod_{\substack{i,j=0 \\ i<j}}^{N-1} (x_{2j} - x_{2i}) \prod_{\substack{r,s=0 \\ r<s}}^{N-2} (x_{2s+1} - x_{2r+1}) \right)^{2(n-1)}, \tag{2.42}$$

where the $(N-1)\times(N-1)$ matrices $\mathcal{A}_k$ have been defined in (2.31). Plugging (2.41) into (1.52), one finds $\mathrm{Tr}\,\rho_A^n$ for the free compactified boson in terms of the compactification radius and of the endpoints of the intervals. Once $\mathcal{F}_{N,n}(\boldsymbol{x})$ has been found, $\tilde{R}_{N,n}(\boldsymbol{x})$ and $R_{N,n}(\boldsymbol{x})$ are obtained through (2.9) and (2.13) respectively.

In [196] the expansion where all the lengths of the intervals are small with respect to the other characteristic lengths of the systems has been studied. This means that $x_{2i+1}-x_{2i}$ are small compared to the distances $x_{2j+2}-x_{2j+1}$, where $i,j=0,\dots,N-2$ (we recall that $x_0=0$ and $x_{2N-2}=1$). Analytic expressions have been found for $N=2$ [196] and one could extend this analysis to $N>2$ by employing (2.41). We leave this analysis for future work. We checked numerically that $\mathcal{F}_{N,n}(\mathbf{0})=1$, which generalizes the known result $\mathcal{F}_{2,n}(0)=1$ [226].

In App. 2.C we discuss the invariance of (2.41) under a cyclic change in the ordering of the sheets, an inversion and the exchange $A\leftrightarrow B$, writing explicitly these transformations in terms of symplectic matrices.

2.3.3 The decompactification regime

When $\eta\to\infty$ the target space of the free boson becomes the infinite line. This regime is important because it can be obtained as the continuum limit of the harmonic chain. Notice that the results of this subsection can be obtained also for $\eta\to 0$ because of the $\eta\leftrightarrow 1/\eta$ invariance.

Since $\Theta(\mathbf{0}|\mathrm{i}\eta G)\to 1$ when $\eta\to\infty$ (or equivalently $\Theta(\mathbf{0}|\mathrm{i}G/\eta)\to 1$ when $\eta\to 0$ as shown in Fig. 2.6), we find that (2.41) becomes

$$\mathcal{F}_{N,n}^{\eta\to\infty}(\boldsymbol{x})=\frac{\eta^{g/2}}{\sqrt{\det(\mathcal{I})}\,|\Theta(\mathbf{0}|\tau)|^2}\equiv\eta^{g/2}\,\widehat{\mathcal{F}}_{N,n}(\boldsymbol{x})\,. \tag{2.43}$$

Writing $|\Theta(\mathbf{0}|\tau)|$ through (2.42), one can improve the numerical evaluation of (2.43). Plugging (2.43) into (2.13), we find that in the decompactification regime $R_{N,n}$ becomes

$$R_{N,n}^{\eta\to\infty}(\boldsymbol{x})=\eta^{(-1)^N(n-1)/2}\prod_{p=2}^{N}\prod_{\sigma_{N,p}}\big[\widehat{\mathcal{F}}_{p,n}(\boldsymbol{x}^{\sigma_{N,p}})\big]^{(-1)^{N-p}}\,. \tag{2.44}$$

In this case it is very useful to consider the normalization (2.15) through a fixed configuration of intervals characterized by $\boldsymbol{x}_{\text{fixed}}$ because the dependence on η simplifies in the ratio. Indeed, from (2.44) we find

$$\lim_{\eta\to\infty}R_{N,n}^{\text{norm}}(\boldsymbol{x})=\frac{R_{N,n}^{\eta\to\infty}(\boldsymbol{x})}{R_{N,n}^{\eta\to\infty}(\boldsymbol{x}_{\text{fixed}})}=\prod_{p=2}^{N}\prod_{\sigma_{N,p}}\left[\frac{\widehat{\mathcal{F}}_{p,n}(\boldsymbol{x}^{\sigma_{N,p}})}{\widehat{\mathcal{F}}_{p,n}(\boldsymbol{x}_{\text{fixed}}^{\sigma_{N,p}})}\right]^{(-1)^{N-p}}\,, \tag{2.45}$$

and similarly, from (2.43), we have

$$\lim_{\eta\to\infty}\mathcal{F}_{N,n}^{\text{norm}}(\boldsymbol{x})=\frac{\mathcal{F}_{N,n}^{\eta\to\infty}(\boldsymbol{x})}{\mathcal{F}_{N,n}^{\eta\to\infty}(\boldsymbol{x}_{\text{fixed}})}=\frac{\widehat{\mathcal{F}}_{N,n}(\boldsymbol{x})}{\widehat{\mathcal{F}}_{N,n}(\boldsymbol{x}_{\text{fixed}})}\,. \tag{2.46}$$

In Sec. 2.5 we compare (2.45) and (2.46) to the corresponding results for the harmonic chain with periodic boundary conditions.

2.3.4 The Dirac model

It is well known that the partition function of the compactified massless free boson describes various systems at criticality. For example, the modular invariant Dirac fermion corresponds to the case $\eta = 1/2$. Given (2.41), we can write $\mathrm{Tr}\,\rho_A^n$ for this model by applying the results of [209–211, 214]. We need the Riemann theta function with characteristic $\boldsymbol{e}^{\mathrm{t}} = (\boldsymbol{\varepsilon}^{\mathrm{t}}, \boldsymbol{\delta}^{\mathrm{t}})$ defined in Eq. (1.61), again specialized to $\boldsymbol{z} = 0$, namely

$$\Theta[\boldsymbol{e}](\boldsymbol{0}|\Omega) = \sum_{\boldsymbol{m}\,\in\,\mathbb{Z}^p} \exp\left[\mathrm{i}\pi(\boldsymbol{m}+\boldsymbol{\varepsilon})^{\mathrm{t}}\cdot\Omega\cdot(\boldsymbol{m}+\boldsymbol{\varepsilon}) + 2\pi\mathrm{i}(\boldsymbol{m}+\boldsymbol{\varepsilon})^{\mathrm{t}}\cdot\boldsymbol{\delta}\right], \tag{2.47}$$

where $\boldsymbol{\varepsilon}$ and $\boldsymbol{\delta}$ are vectors whose entries are either 0 or 1/2. When $\boldsymbol{\varepsilon} = \boldsymbol{\delta} = \boldsymbol{0}$, we recover (2.34). We saw in Sec. 1.4 that the characteristics $\boldsymbol{e}$ are either even or odd, according to the parity of $4\boldsymbol{\varepsilon}\cdot\boldsymbol{\delta}$, and that there are $2^{p-1}(2^p+1)$ even characteristics and $2^{p-1}(2^p-1)$ odd ones.

Applying some identities for the Riemann theta functions, from (2.41) one finds

$$\mathcal{F}^{\mathrm{Dirac}}_{N,n}(\boldsymbol{x}) = \mathcal{F}_{N,n}(\boldsymbol{x})\big|_{\eta=1/2} = \frac{\sum_{\boldsymbol{e}}|\Theta[\boldsymbol{e}](\boldsymbol{0}|\tau)|^2}{2^g\,|\Theta(\boldsymbol{0}|\tau)|^2}\,, \tag{2.48}$$

where the period matrix τ has been computed in Sec. 2.3.1.

Notice that, being $\Theta[\boldsymbol{e}](\boldsymbol{0}|\Omega) = 0$ when $\boldsymbol{e}$ is odd (see Eq. (1.62)), in the sum over the characteristics in (2.48) only the even ones occur. Since (2.48) has been obtained as the special case $\eta = 1/2$ of (2.41), $\mathcal{F}^{\mathrm{Dirac}}_{N,n}(\boldsymbol{0}) = 1$. The result for the *free* Dirac fermion [46] corresponds to keep only $\boldsymbol{e} = \boldsymbol{0}$ in the numerator of 2.48 instead of considering the sum over all the sectors of the model [228].

2.4 Recovering the two intervals case

In this section we want to recover the known results for two intervals [196, 226]. We first review the status of the two intervals case and then we show that the corresponding Rényi entropies reduce to a particular case of the expressions discussed in Sec. 2.3, as expected.

2.4.1 Two disjoint intervals for generic complex x

For generic positions of the twist fields in the complex plane, $x \in \mathbb{C}$ and the corresponding expression of $\langle \mathcal{T}_n\bar{\mathcal{T}}_n\mathcal{T}_n\bar{\mathcal{T}}_n\rangle$ is given by the r.h.s. of (1.52) with $\mathcal{F}_{2,n} = \mathcal{F}_{2,n}(x,x^*)$. For the free compactified boson, this function reads [135]

$$\mathcal{F}_{2,n}(x,x^*) = \frac{\Theta(\boldsymbol{0}|T_{\eta,2})}{\prod_{k=1}^{n-1}|F_{k/n}(x)|} = \frac{\Theta(\boldsymbol{0}|T_{\eta,2})}{|\Theta(\boldsymbol{0}|\tau_2)|^2}\,, \qquad F_{k/n}(x) \equiv {}_2F_1(k/n, 1-k/n; 1; x)\,, \tag{2.49}$$

where $T_{\eta,2}$ is the $2(n-1)\times 2(n-1)$ symmetric matrix given by

$$T_{\eta,2} = \begin{pmatrix} \mathrm{i}\,\eta\,\mathrm{Im}(\tau_2) & \mathrm{Re}(\tau_2) \\ \mathrm{Re}(\tau_2) & \mathrm{i}\,\mathrm{Im}(\tau_2)/\eta \end{pmatrix}, \tag{2.50}$$

defined in terms of the following $(n-1)\times(n-1)$ complex and symmetric matrix

$$(\tau_2)_{ij} = \frac{2}{n}\sum_{k=1}^{n-1}\sin(\pi k/n)\left[\,\mathrm{i}\,\frac{F_{k/n}(1-x)}{F_{k/n}(x)}\,\right]\cos[2\pi k/n(i-j)]\,. \tag{2.51}$$

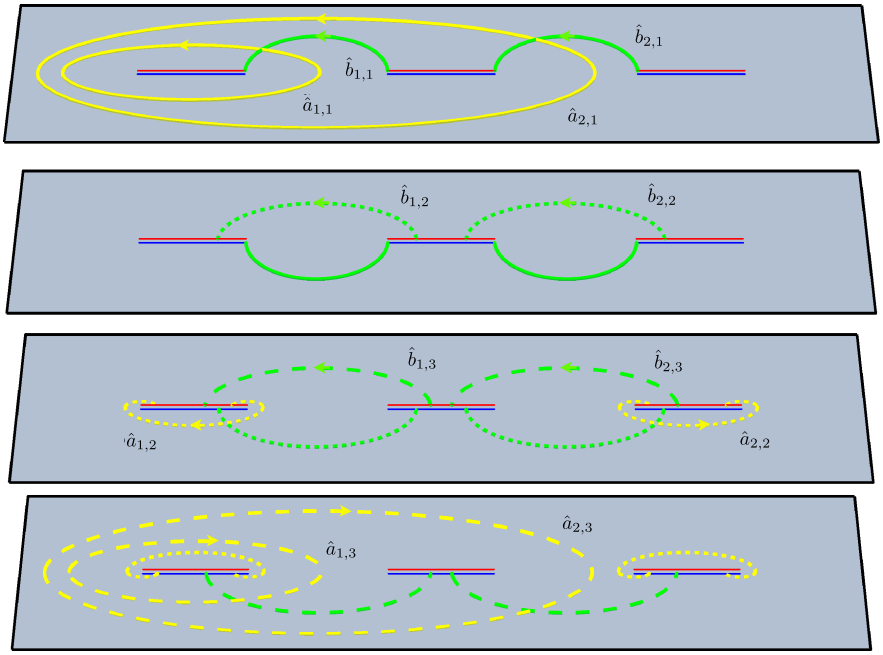

Figure 2.7: The canonical homology basis $\{\hat{a}_{\alpha,j}, \hat{b}_{\alpha,j}\}$ for $N = 3$ and $n = 4$.

The matrix $T_{\eta,2}$ in (2.49) is defined as in (2.38) with τ_2 instead of τ. In the second step of (2.49) the Thomae formula (2.42) has been employed. Notice that, because of the sum over k in (2.51), substituting $\cos[2\pi k/n(i-j)]$ with $\rho_n^{k(i-j)}$ the matrix does not change. The non vanishing of $\mathrm{Re}(\tau_2)$ is due to the fact that the term within the square brackets in (2.51) is complex for $x \in \mathbb{C}$.

As briefly explained in Sec. 2.3.4, it is straightforward to write the corresponding result for the Dirac model from (2.49). It reads

$$\mathcal{F}_{2,n}^{\text{Dirac}}(x, x^*) = \frac{\sum_{\boldsymbol{e}} |\Theta[\boldsymbol{e}](\mathbf{0}|\tau_2)|^2}{2^{n-1}\,|\Theta(\mathbf{0}|\tau_2)|^2}\,. \tag{2.52}$$

Given the period matrix (2.51), one can also find $\mathcal{F}_{2,n}^{\text{Ising}}(x, x^*)$ for the Ising model [136, 145]

$$\mathcal{F}_{2,n}^{\text{Ising}}(x, x^*) = \frac{\sum_{\boldsymbol{e}} |\Theta[\boldsymbol{e}](\mathbf{0}|\tau_2)|}{2^{n-1}\,|\Theta(\mathbf{0}|\tau_2)|}\,. \tag{2.53}$$

In order to consider the Rényi entropies, we must restrict to $x \in (0,1)$. Within this domain, $F_{k/n}(x)$ is real and this leads to a purely imaginary τ_2. Since $\mathrm{Re}(\tau_2)$ vanishes identically for $x \in (0,1)$, the matrix $T_{\eta,2}$ in (2.50) becomes block diagonal and therefore $\Theta(\mathbf{0}|T_{\eta,2}) = \Theta(\mathbf{0}|\,\mathrm{i}\eta\,\mathrm{Im}(\tau_2))\,\Theta(\mathbf{0}|\,\mathrm{i}\,\mathrm{Im}(\tau_2)/\eta)$ factorizes. Thus, the expressions given in (2.49) and (2.53) reduce to $\mathcal{F}_{2,n}(x)$ for the free compactified boson [226] and for the Ising model [196] respectively.

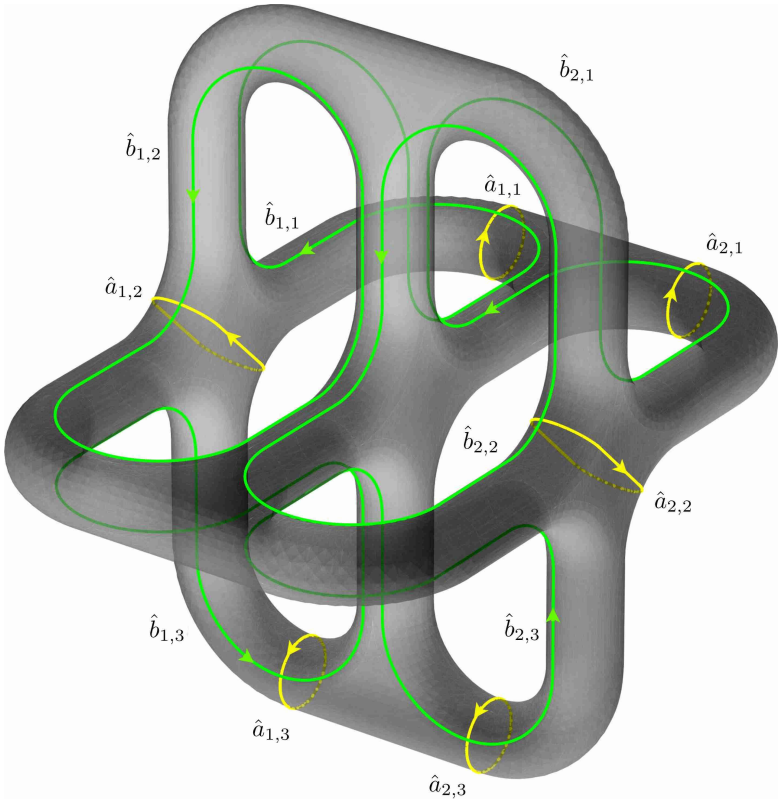

Figure 2.8: The Riemann surface $\mathcal{R}_{3,4}$ with the canonical homology basis $\{\hat{a}_{\alpha,j}, \hat{b}_{\alpha,j}\}$.

2.4.2 Another canonical homology basis

To recover the period matrix (2.51) for $x \in (0,1)$ as the two intervals case of a period matrix characterizing $N \geqslant 2$ intervals, we find it useful to introduce the canonical homology basis $\{\hat{a}_{\alpha,j}, \hat{b}_{\alpha,j}\}$ depicted in Figs. 2.7 and 2.8. This basis is considered very often in the literature on higher genus Riemann surfaces (e.g. see Fig. 1 both in [209] and [210]). Integrating the holomorphic differentials (2.19) along the cycles $\hat{\boldsymbol{a}}$ and $\hat{\boldsymbol{b}}$, as done in (2.20) for $\boldsymbol{a}$ and $\boldsymbol{b}$, one gets the matrices $\hat{\mathcal{A}}$ and $\hat{\mathcal{B}}$. To evaluate these matrices, we repeat the procedure described in Sec. 2.3.1. In particular, we first write $\{\hat{a}_{\alpha,j}, \hat{b}_{\alpha,j}\}$ through the auxiliary cycles depicted in Figs. 2.28 and 2.29, finding that

$$\hat{a}_{\alpha,j} = \sum_{\gamma=1}^{\alpha} \sum_{l=1}^{j} a^{\text{aux}}_{\gamma,l}\,, \qquad \hat{b}_{\alpha,j} = b^{\text{aux}}_{\alpha,j}\,. \tag{2.54}$$

Comparing (2.23) with (2.54), we observe that for $n = 2$ the canonical homology basis introduced here coincides with the one defined in Sec. 2.3.1. From (2.54), one can write

the matrices $\hat{\mathcal{A}}$ and $\hat{\mathcal{B}}$ as follows

$$\hat{\mathcal{A}}^{\beta,\alpha}_{k,j} = \sum_{\gamma=1}^{\alpha}\sum_{l=1}^{j}(\mathcal{A}^{\text{aux}})^{\beta,\gamma}_{k,l} = \sum_{\gamma=1}^{\alpha}\sum_{l=1}^{j}\rho_n^{k(l-1)}(\mathcal{A}^{\text{aux}})^{\beta,\gamma}_{k,1} = \frac{1-\rho_n^{jk}}{1-\rho_n^{k}}\sum_{\gamma=1}^{\alpha}(\mathcal{A}^{\text{aux}})^{\beta,\gamma}_{k,1}\,, \tag{2.55a}$$

$$\hat{\mathcal{B}}^{\beta,\alpha}_{k,j} = (\mathcal{B}^{\text{aux}})^{\beta,\alpha}_{k,j} = \rho_n^{k(j-1)}(\mathcal{B}^{\text{aux}})^{\beta,\alpha}_{k,1}\,, \tag{2.55b}$$

where (2.24) has been used. Now the elements of $\hat{\mathcal{A}}$ and $\hat{\mathcal{B}}$ are expressed in terms of the integrals in (2.26), which can be numerically evaluated. Once $\hat{\mathcal{A}}$ and $\hat{\mathcal{B}}$ have been computed, the period matrix with respect to the basis $\{\hat{a}_{\alpha,j},\hat{b}_{\alpha,j}\}$ is $\hat{\tau}=\hat{\mathcal{A}}^{-1}\cdot\hat{\mathcal{B}}$.

Since the matrices $\hat{\mathcal{A}}$ and $\hat{\mathcal{B}}$ have the structure (2.28), like $\mathcal{A}$ and $\mathcal{B}$ in Sec. 2.3.1, we can write them as in (2.29) with

$$(\mathscr{M}_{\hat{\mathcal{A}}})_{kj} \equiv \frac{1-\rho_n^{kj}}{1-\rho_n^{k}}\,, \quad (\hat{\mathcal{A}}_k)_{\beta\alpha} \equiv \hat{\mathcal{A}}^{\beta,\alpha}_{k,1} = (\rho_n^{-k}-1)\sum_{\gamma=1}^{\alpha}(-1)^{N-\gamma}\mathscr{I}_{\beta,k}\big|_{x_{2\gamma-2}}^{x_{2\gamma-1}} \tag{2.56a}$$

$$(\mathscr{M}_{\hat{\mathcal{B}}})_{kj} \equiv \rho_n^{k(j-1)}\,, \quad (\hat{\mathcal{B}}_k)_{\beta\alpha} \equiv \hat{\mathcal{B}}^{\beta,\alpha}_{k,1} = (-1)^{N-\alpha}\rho_n^{k/2}(\rho_n^{-k}-1)\,\mathscr{I}_{\beta,k}\big|_{x_{2\alpha-1}}^{x_{2\alpha}}\,. \tag{2.56b}$$

where 2.26 has been employed and $\mathscr{I}_{\beta,k}\big|_b^a$ are the integrals (2.27). Notice that $\hat{\mathcal{A}}_k=\mathcal{A}_k$, while $(\hat{\mathcal{B}}_k)_{\beta\alpha}=(\mathcal{B}^{\text{aux}})^{\beta,\alpha}_{k,1}=-\rho_n^k(\mathcal{B}_k)_{\beta\alpha}$. Thus, the period matrix $\hat{\tau}$ reads

$$\hat{\tau} = (\mathscr{M}_{\hat{\mathcal{A}}}\otimes\mathbb{I}_{N-1})^{-1}\cdot\text{diag}(\hat{\mathcal{A}}_1^{-1}\cdot\hat{\mathcal{B}}_1,\hat{\mathcal{A}}_2^{-1}\cdot\hat{\mathcal{B}}_2,\dots,\hat{\mathcal{A}}_{n-1}^{-1}\cdot\hat{\mathcal{B}}_{n-1})\cdot(\mathscr{M}_{\hat{\mathcal{B}}}\otimes\mathbb{I}_{N-1})\,. \tag{2.57}$$

Since (2.32) and (2.57) are the period matrices of the Riemann surface $\mathcal{R}_{N,n}$ with respect to different canonical homology basis, they must be related through a symplectic transformation. The relations (2.23) and (2.54) in the matrix form become respectively

$$\begin{cases} \boldsymbol{a} = A\cdot\boldsymbol{a}^{\text{aux}} \\ \boldsymbol{b} = B\cdot\boldsymbol{b}^{\text{aux}} \end{cases}, \qquad \begin{cases} \hat{\boldsymbol{a}} = \hat{A}\cdot\boldsymbol{a}^{\text{aux}} \\ \hat{\boldsymbol{b}} = \boldsymbol{b}^{\text{aux}} \end{cases}. \tag{2.58}$$

Introducing the $p\times p$ upper triangular matrix I_p^{up} made by 1's (i.e. $(I_p^{\text{up}})_{ab}=1$ if $a\leqslant b$ and zero otherwise) and also its transposed $I_p^{\text{low}}\equiv(I_p^{\text{up}})^{\text{t}}$, which is a lower triangular matrix, we can write that $A=\mathbb{I}_{n-1}\otimes I_{N-1}^{\text{low}}$, $B=I_{n-1}^{\text{up}}\otimes\mathbb{I}_{N-1}$ and $\hat{A}=I_{n-1}^{\text{low}}\otimes I_{N-1}^{\text{low}}$. We remark that the matrices $\text{diag}(A,B)$ and $\text{diag}(\hat{A},\mathbb{I}_g)$ occurring in (2.58) are not symplectic matrices because, as already noticed in Sec. 2.3.1, the auxiliary set of cycles is not a canonical homology basis. From (2.58) it is straightforward to find the relation between the two canonical homology basis, namely

$$\begin{cases} \hat{\boldsymbol{a}} = \hat{A}\cdot A^{-1}\cdot\boldsymbol{a} \\ \hat{\boldsymbol{b}} = B^{-1}\cdot\boldsymbol{b} \end{cases}, \qquad M\equiv\begin{pmatrix}\hat{A}\cdot A^{-1} & 0_g\\ 0_g & B^{-1}\end{pmatrix}\in Sp(2g,\mathbb{Z})\,, \tag{2.59}$$

which can be constructed by using that $(I_p^{\text{up}})^{-1}_{ab}=\delta_{a,b}-\delta_{a+1,b}$ and the properties of the tensor product, finding $\hat{A}\cdot A^{-1}=I_{n-1}^{\text{low}}\otimes\mathbb{I}_{N-1}$ and $B^{-1}=(I_{n-1}^{\text{up}})^{-1}\otimes\mathbb{I}_{N-1}$. Notice that (2.59) belongs to the symplectic modular group, as expected from the fact that it encodes the change between canonical homology basis.

2.4.3 The case $N=2$

Specializing the expressions given in the previous subsection to the $N=2$ case, the greek indices assume only a single value; therefore they can be suppressed. The matrices (2.55a)

and (2.55b) become respectively

$$\hat{\mathcal{A}}_{kj} \equiv \hat{\mathcal{A}}^{1,1}_{k,j} = \frac{1-\rho_n^{jk}}{1-\rho_n^k}\Big[(1-\rho_n^{-k})\mathscr{I}_{1,k}\big|_0^x\Big] = \frac{1-\rho_n^{kj}}{1-\rho_n^k}\big[2\pi\mathrm{i}\,\rho_n^{-k/2}F_{k/n}(x)\big]\,, \tag{2.60a}$$

$$\hat{\mathcal{B}}_{kj} \equiv \hat{\mathcal{B}}^{1,1}_{k,j} = \rho_n^{k(j-1)}\Big[\rho_n^{k/2}(1-\rho_n^{-k})\mathscr{I}_{1,k}\big|_x^1\Big] = \rho_n^{k(j-1)}\big[2\pi\mathrm{i}\,F_{k/n}(1-x)\big]\,, \tag{2.60b}$$

where $x \in (0,1)$, the indices $j,k \in \{1,\dots,n-1\}$ and the explicit results for $(\mathcal{A}^{\mathrm{aux}})_{k,1}$ and $(\mathcal{B}^{\mathrm{aux}})_{k,1}$, from (2.26a) and (2.26b) respectively, are written within the square brackets (see (4.29) of [208] and also (2.108a) and (2.108b)). The matrices in (2.60) can be written respectively as follow

$$\hat{\mathcal{A}} = \mathrm{diag}(\dots, 2\pi\mathrm{i}\,\rho_n^{-k/2}F_{k/n}(x), \dots)\cdot\mathscr{M}_{\hat{\mathcal{A}}}\,, \tag{2.61a}$$

$$\hat{\mathcal{B}} = \mathrm{diag}(\dots, 2\pi\mathrm{i}\,F_{k/n}(1-x), \dots)\cdot\mathscr{M}_{\hat{\mathcal{B}}}\,, \tag{2.61b}$$

where $\mathscr{M}_{\hat{\mathcal{A}}}$ and $\mathscr{M}_{\hat{\mathcal{B}}}$ have been defined in (2.56). Computing $\mathscr{M}^{-1}_{\hat{\mathcal{A}}}$, whose elements read $(\mathscr{M}^{-1}_{\hat{\mathcal{A}}})_{ik} = (\rho_n^k - 1)/(n\rho_n^{ik})$, we can easily check that (2.51) becomes

$$\tau_2 = \hat{\mathcal{A}}^{-1}\cdot\hat{\mathcal{B}} = \mathscr{M}^{-1}_{\hat{\mathcal{A}}}\cdot\mathrm{diag}\bigg(\dots, \rho_n^{k/2}\,\frac{F_{k/n}(1-x)}{F_{k/n}(x)}\,, \dots\bigg)\cdot\mathscr{M}_{\hat{\mathcal{B}}}\,. \tag{2.62}$$

Thus, the matrix (2.51) for $0 < x < 1$ found in [226], is the $N = 2$ case of the period matrix $\hat{\tau}$, written with respect to the canonical homology basis introduced in the section Sec. 2.4.2

$$\hat{\tau}|_{N=2} = \tau_2\,. \tag{2.63}$$

To conclude this section, let us consider the symplectic transformation (2.59), which reduces to $\mathrm{diag}(I^{\mathrm{low}}_{n-1}, (I^{\mathrm{up}}_{n-1})^{-1})$ for $N = 2$. Its inverse reads $\mathrm{diag}((I^{\mathrm{low}}_{n-1})^{-1}, I^{\mathrm{up}}_{n-1})$ and it allows us to find the period matrix τ_2' with respect to the canonical homology basis given by the cycles $\boldsymbol{a}$ and $\boldsymbol{b}$ through (2.111), namely

$$\tau_2' = I^{\mathrm{up}}_{n-1}\cdot\tau_2\cdot I^{\mathrm{low}}_{n-1}\,. \tag{2.64}$$

Introducing the symmetric matrix $\mathscr{A}_{ij} \equiv 2/n\sum_{k=1}^{n-1}\sin(\pi k/n)\,e^{2\pi\mathrm{i}(j-i)}$ (which has been denoted by A in the App. C of [226]), after some algebra we find

$$\mathscr{A}\cdot I^{\mathrm{up}}_{n-1}\cdot\tau_2\cdot I^{\mathrm{low}}_{n-1}\cdot\mathscr{A} = \tau_2\,. \tag{2.65}$$

Combining (2.64) and (2.65), we easily get that $\tau_2' = \mathscr{A}^{-1}\cdot\tau_2\cdot\mathscr{A}^{-1}$. Then, by employing (2.115) and the fact that $\det(I^{\mathrm{up}}_{n-1}) = 1$, we get

$$\Theta(\mathbf{0}|\tau_2') = \Theta(\mathbf{0}|\mathscr{A}^{-1}\cdot\tau_2\cdot\mathscr{A}^{-1}) = \Theta(\mathbf{0}|\tau_2)\,. \tag{2.66}$$

In [226] the second equality in (2.66) has been given as a numerical observation. We have shown that it is a consequence of the relation between the two canonical homology basis considered here.

2.5 The harmonic chain

In this section we consider the Rényi entropies and the entanglement entropy for the harmonic chain with periodic boundary conditions, which have been largely studied in

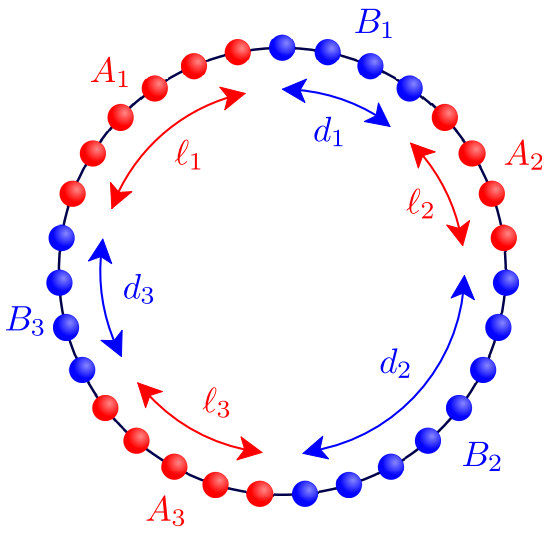

Figure 2.9: A bipartition of the periodic chain where A is made by the union of three disjoint blocks of lattice sites.

the literature [11, 12, 148–151, 243]. We compute new data for the case of disjoint blocks in order to check the CFT formulas found in Sec. 2.3 for the decompactification regime.

The Hamiltonian of the harmonic chain made by L lattice sites and with nearest neighbor interaction reads

$$H = \sum_{n=0}^{L-1} \left(\frac{1}{2M} p_n^2 + \frac{M\omega^2}{2} q_n^2 + \frac{K}{2} (q_{n+1} - q_n)^2 \right), \tag{2.67}$$

where periodic boundary conditions $q_0 = q_L$ and $p_0 = p_L$ are imposed and the variables q_n and p_m satisfy the commutation relations $[q_n, q_m] = [p_n, p_m] = 0$ and $[q_n, p_m] = \mathrm{i}\delta_{n,m}$. The Hamiltonian (2.67) contains three parameters ω, M, K but, through a canonical rescaling of the variables, it can be written in a form where these parameters occur only in a global factor and in the coupling $\frac{2K}{M\omega^2}/(1+\frac{2K}{M\omega^2})$ [147, 150]. The Hamiltonian (2.67) is the lattice discretization of a free boson with mass ω^2. When $\omega = 0$ the theory is conformal with central charge $c = 1$. Since the bosonic field is not compactified, we must compare the continuum limit of (2.67) for $\omega = 0$ with the regime $\eta \to \infty$ of the CFT expressions computed in Sec. 2.3, which has been considered in Sec. 2.3.3.

To diagonalize (2.67), first one exploits the translational invariance of the system by Fourier transforming q_n and p_n. Then the annihilation and creation operators a_k and $a_k^\dagger$ are introduced, whose algebra is $[a_k, a_{k'}] = [a_k^\dagger, a_{k'}^\dagger] = 0$ and $[a_k, a_{k'}^\dagger] = \mathrm{i}\delta_{k,k'}$. The ground state of the system $|0\rangle$ is annihilated by all the a_k's and it is a pure Gaussian state. In terms of the annihilation and creation operators, the Hamiltonian (2.67) is diagonal

$$H = \sum_{k=0}^{L-1} \omega_k \left(a_k^\dagger a_k + \frac{1}{2} \right), \tag{2.68}$$

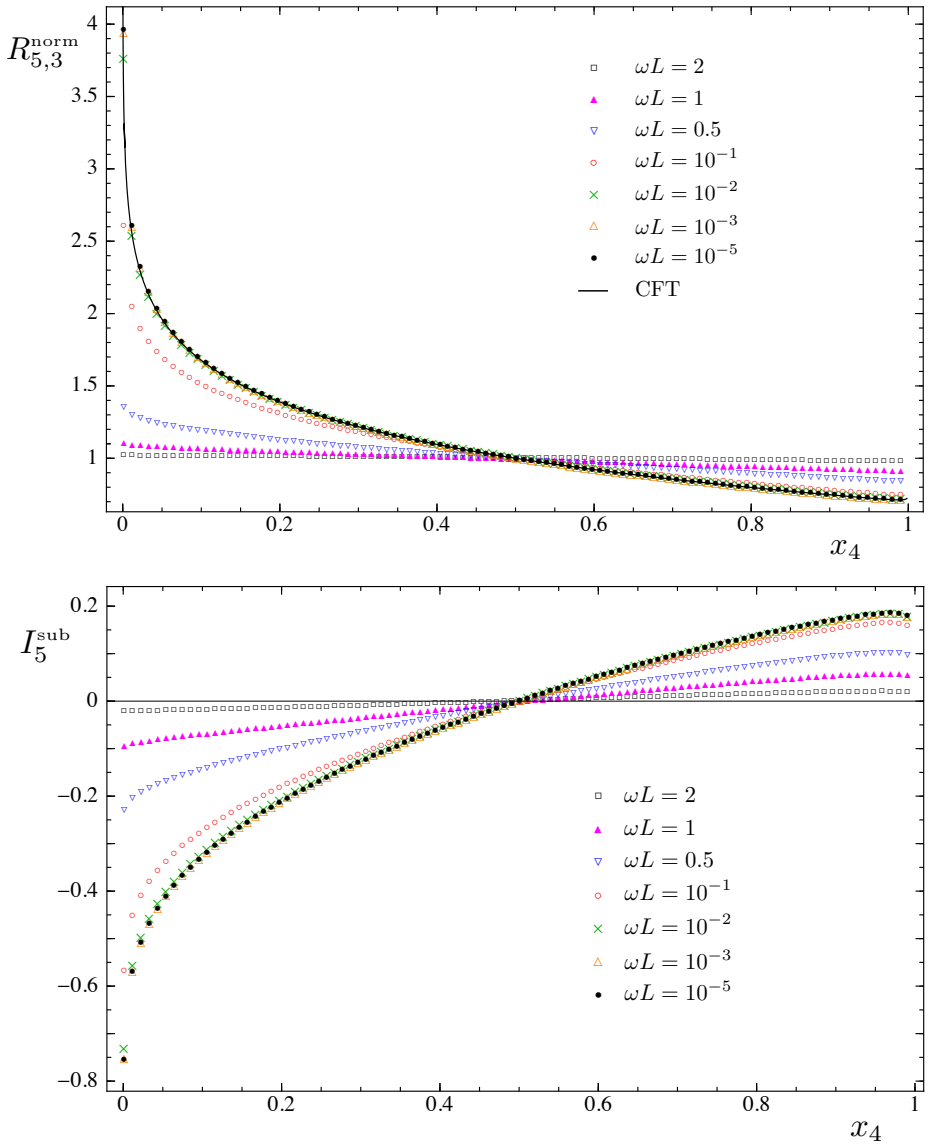

Figure 2.10: The quantities $R^{\rm norm}_{N=5,n=3}$ (top) and $I^{\rm sub}_{N=5}$ (bottom) in (2.14) computed for the harmonic chain with periodic boundary conditions by employing (2.71) and (2.72). The total length of the chain is $L = 5000$. The configuration of the intervals is (2.76) and the fixed one chosen for the normalization is (2.77). The continuos curve in the top panel is the CFT prediction (2.45) and it agrees with the lattice results for $\omega L \ll 1$. We are not able to compute the CFT prediction for the bottom panel.

where

$$\omega_k \equiv \sqrt{\omega^2 + \frac{4K}{M}\sin\left(\frac{\pi k}{L}\right)^2} \geqslant \omega\,, \qquad k = 0, \dots, L-1\,. \tag{2.69}$$

Notice that the lowest value of ω_k is obtained for $\omega_0 = \omega$.

The two point functions $\langle 0|q_i q_j|0\rangle$ and $\langle 0|p_i p_j|0\rangle$ are the elements of the correlation

matrices $\mathbb{Q}_{rs} = \langle 0|q_r q_s|0\rangle$ and $\mathbb{P}_{rs} = \langle 0|p_r p_s|0\rangle$ respectively. For the harmonic chain with periodic boundary conditions that we are considering, they read

$$\langle 0|q_i q_j|0\rangle = \frac{1}{2L}\sum_{k=0}^{L-1} \frac{1}{M\omega_k} \cos\left(\frac{2\pi k(i-j)}{L}\right), \tag{2.70a}$$

$$\langle 0|p_i p_j|0\rangle = \frac{1}{2L}\sum_{k=0}^{L-1} M\omega_k \cos\left(\frac{2\pi k(i-j)}{L}\right). \tag{2.70b}$$

When $i, j = 0, \dots, L-1$ run over the whole chain, then $\mathbb{Q}\cdot\mathbb{P} = \mathbb{I}_L/4$, which is also known as the generalized uncertainty relation. We remark that the limit $\omega \to 0$ is not well defined because the $k = 0$ term in $\langle 0|q_i q_j|0\rangle$ diverges; therefore we must keep $\omega > 0$. Thus, we set $\omega L \ll 1$ in order to stay in the conformal regime. As explained above, we can work in units $M = K = 1$ without loss of generality.

In [149–151] it has been discussed that, in order to compute the Renyi entropies and the entanglement entropy of a proper subset A (made by $\tilde{\ell}$ sites) of the harmonic chain, first we have to consider the matrices $\mathbb{Q}_A$ and $\mathbb{P}_A$, obtained by restricting the indices of the correlation matrices $\mathbb{Q}$ and $\mathbb{P}$ to the sites belonging to A. Then we compute the eigenvalues of the $\tilde{\ell}\times\tilde{\ell}$ matrix $\mathbb{Q}_A\cdot\mathbb{P}_A$. Since they are larger than (or equal to) $1/4$, we can denote them by $\{\mu_1^2, \dots, \mu_{\tilde{\ell}}^2\}$. Finally, the Renyi entropies are obtained as follows

$$\mathrm{Tr}\rho_A^n = \prod_{a=1}^{\tilde{\ell}} \left[\left(\mu_a + \frac{1}{2}\right)^n - \left(\mu_a - \frac{1}{2}\right)^n\right]^{-1}, \tag{2.71}$$

and the entanglement entropy as

$$S_A = \sum_{a=1}^{\tilde{\ell}} \left[\left(\mu_a + \frac{1}{2}\right)\log\left(\mu_a + \frac{1}{2}\right) - \left(\mu_a - \frac{1}{2}\right)\log\left(\mu_a - \frac{1}{2}\right)\right]. \tag{2.72}$$

This procedure holds also when A is the union of N disjoint intervals A_i ($i = 1, \dots, N$), which is the situation we are interested in.

Let us denote by ℓ_i the number of sites included in A_i and by d_i the number of sites in the separations between A_i and $A_{i+1 \bmod N}$, for $i = 1, \dots, N$ (see Fig. 2.9 for $N = 3$). Then, we have that $\tilde{\ell} = \sum_{i=1}^N \ell_i$ and the following consistency condition about the total length of the chain must be imposed

$$L = \sum_{i=1}^{N} (\ell_i + d_i). \tag{2.73}$$

In order to compare the CFT results found in the previous sections with the ones obtained from the harmonic chain in the continuum limit, we have to generalize the CFT formulas to the case of a finite system of total length L with periodic boundary conditions. This can be done by employing the conformal map from the cylinder to the plane, whose net effect is to replace each length y (e.g. ℓ, d, $2\ell + d$, etc.) with the corresponding chord length $(L/\pi)\sin(\pi y/L)$. Thus, for x_{2j+1} with $j = 0, \dots, N-2$ we have

$$x_{2j+1} = \frac{\sin\left(\pi\left[\sum_{i=1}^{j}(\ell_i + d_i) + \ell_{j+1}\right]/L\right)\sin(\pi\ell_N/L)}{\sin\left(\pi\sum_{i=1}^{N-1}(\ell_i + d_i)/L\right)\sin\left(\pi\left[d_{j+1} + \sum_{i=j+2}^{N-1}(\ell_i + d_i) + \ell_N\right]/L\right)}, \tag{2.74}$$

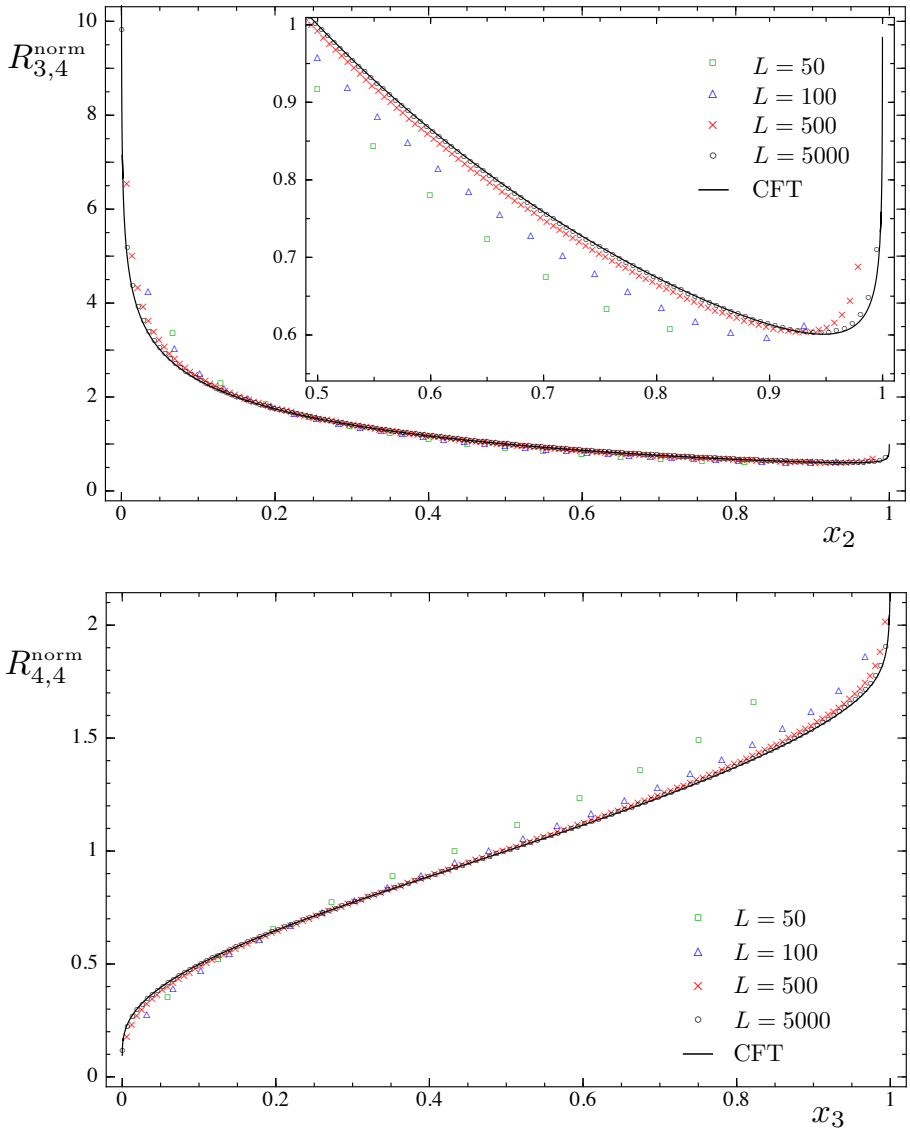

Figure 2.11: The ratio $R^{\rm norm}_{N,n}$ in (2.14) for the periodic harmonic chain with $\omega L = 10^{-3}$ and the configuration of the intervals given by (2.76), normalized through (2.77). The continuos curves are the CFT predictions (2.45). Top: $N = 3$ and $n = 4$ (in the inset we zoom on part of the region $0.5 < x_2 < 1$). Bottom: $N = 4$ and $n = 4$.

while for the harmonic ratios x_{2j}, where $j = 1, \dots, N-2$, we must consider

$$x_{2j} \;=\; \frac{\sin\left(\pi \sum_{i=1}^{j} (\ell_i + d_i)/L\right) \sin(\pi \ell_N / L)}{\sin\left(\pi \sum_{i=1}^{N-1} (\ell_i + d_i)/L\right) \sin\left(\pi \left[\sum_{i=j+2}^{N-1} (\ell_i + d_i) + \ell_N\right]/L\right)} \,. \tag{2.75}$$

Notice that d_N, which can be obtained from (2.73), does not occur in these ratios. Moreover, (2.74) and (2.75) depend only on ℓ_i/L and d_i/L, with $i = 1, \dots, N-1$.

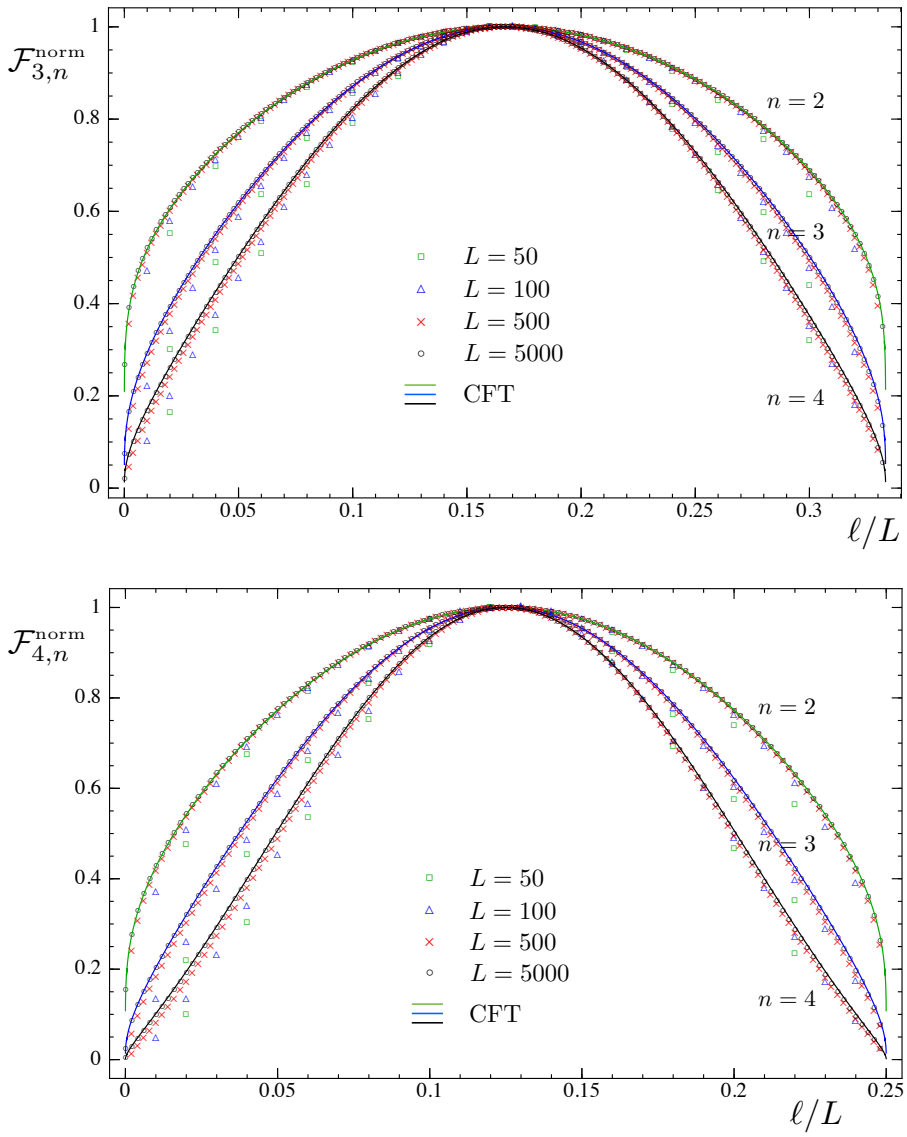

Figure 2.12: The quantity $\mathcal{F}^{\rm norm}_{N,n}$ computed for the periodic harmonic chain with $\omega L = 10^{-3}$ in the configuration of intervals (2.76), normalized through (2.77). The lattice data are obtained by using (2.8), (2.9), (2.71) and (2.72). The continuos curves are given by (2.46). The maximum value on the horizontal axis is $1/N$. We show the cases of $N = 3$ (top) and $N = 4$ (bottom) with $n = 2, 3, 4$.

We often consider the configuration where all the intervals have the same length and also the segments separating them have the same size, namely

$$\ell_1 = \cdots = \ell_N \equiv \ell\,, \qquad d_1 = \cdots = d_N \equiv d\,. \tag{2.76}$$

This configuration is parameterized by ℓ, once d has been found in terms of ℓ through the condition (2.73). As mentioned in Sec. 2.2, in order to eliminate some parameters, it

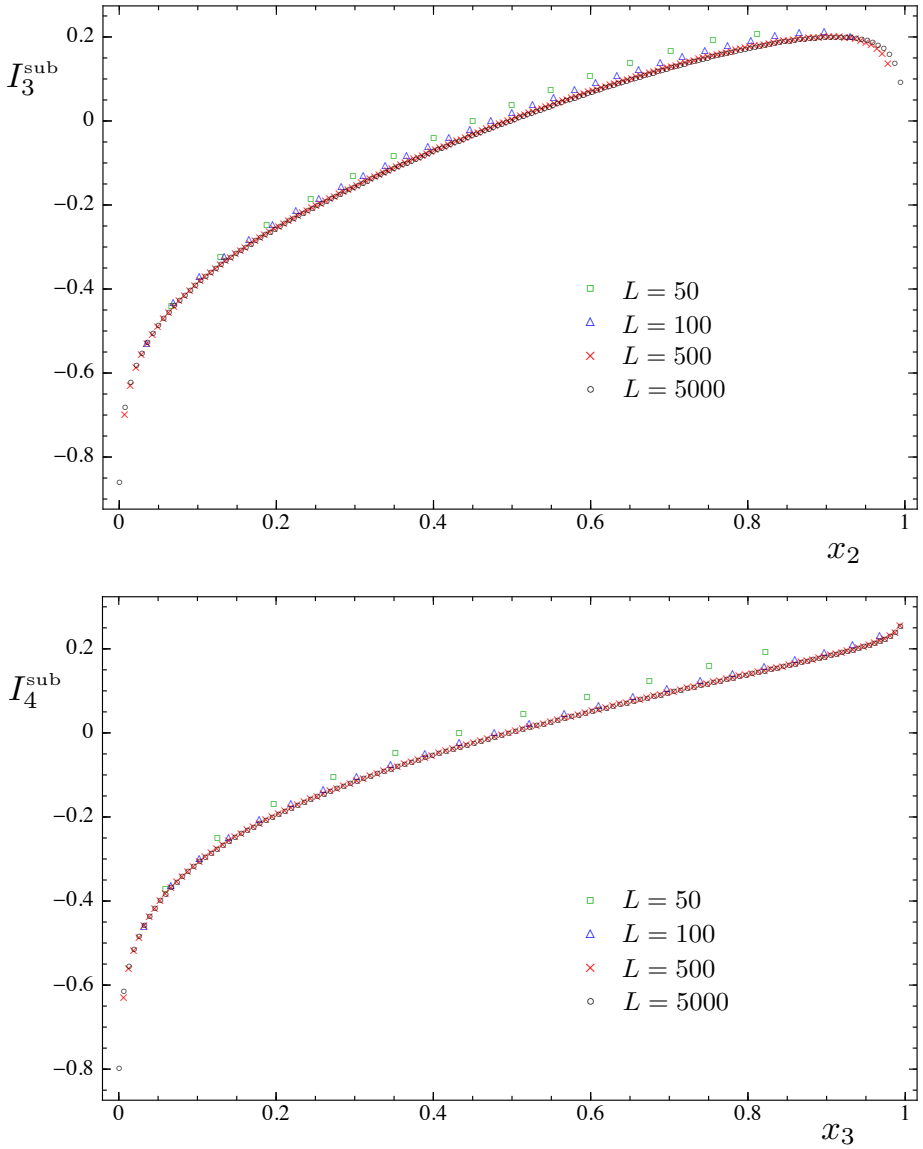

Figure 2.13: The quantity $I_N^{\rm sub}$ (see (2.14)) computed for the periodic harmonic chain with $\omega L = 10^{-3}$. The configuration of intervals is given by (2.76) and the fixed one by (2.77). We show $N = 3$ (top) and $N = 4$ (bottom).

is useful to normalize the results through a fixed configuration of intervals, as done e.g. in [134–136]. We choose the following one

$$\text{fixed configuration:} \qquad \ell_1 = \cdots = \ell_N = d_1 = \cdots = d_{N-1} = \text{int}\left(\frac{L}{2N}\right), \tag{2.77}$$

where int(...) denotes the integer part of the number within the brackets and d_N is obtained from (2.73).

In Figs. 2.10, 2.11, 2.12 and 2.13 we choose the configuration (2.76) normalized through the fixed one in (2.77). A chain made by $L = 5000$ sites gives us a very good approximation of the continuum case. We also made some checks with $L = 10000$ in order to be sure that the results do not change significantly. From Fig. 2.10 we learn that for $\omega L \sim 10^{-3}$ we are already in a regime which is suitable to check the CFT prediction of Sec. 2.3.3, therefore we keep $\omega L = 10^{-3}$ for the other plots obtained from the harmonic chain. From the exact results obtained on the lattice, it is evident that the value of η in the CFT expressions of Sec. 2.3.3 that must be fixed to find a good match is a function of ωL only. Nevertheless, as already noticed in Sec. 2.3.3, normalizing the interesting quantities through a fixed configuration as in (2.14), we can ignore this important issue because η simplifies (see 2.45 and 2.46)). The Figs. 2.11 and 2.12 show that the agreement between the exact results from the harmonic chain and the corresponding CFT predictions is very good. Instead, for the plots in Fig. 2.13 we do not have a CFT prediction because, ultimately, we are not able to compute $\partial_n \widehat{\mathcal{F}}_{N,n}(\boldsymbol{x})$ when $n \to 1$ for the function defined in (2.43).

When $N > 2$ we have many possibilities to choose the configuration of the intervals. In principle we should test all of them and not only (2.76), as above. For simplicity, we consider two other kinds of configurations defined as follows

	ℓ_1	d_1	ℓ_2	d_2	ℓ_3	d_3	$\dots$	ℓ_N	d_N
$\boldsymbol{\lambda}$	ℓ	d	$\lambda_2\ell$	d	$\lambda_3\ell$	d	$\dots$	$\lambda_N\ell$	d
$\boldsymbol{\gamma}$	ℓ	d	$\gamma_2\ell$	$\gamma_2 d$	$\gamma_3\ell$	$\gamma_3 d$	$\dots$	$\gamma_N\ell$	$\gamma_N d$

(2.78)

where λ_i and γ_i are integer numbers which can be collected as components of the vectors $\boldsymbol{\lambda}$ and $\boldsymbol{\gamma}$. Notice that the configuration (2.76) is obtained either with $\lambda_i = 1$ or with $\gamma_i = 1$, for $i = 2, \dots, N$. Once the ratios λ_i or γ_i have been chosen in (2.78), we are left with ℓ and d as free parameters. As above, d can be found as a function of ℓ through the condition (2.73) and the maximum value for ℓ corresponds to $d = 1$. The configurations in (2.78) depend only on the parameter ℓ; therefore they provide one dimensional curves in the configurations space, which is $2N - 3$ dimensional and parameterized by $0 < x_1 < x_2 < \cdots < x_{2N-3} < 1$. When $N = 3$, let us consider the configurations (2.78) with the following choices

I	$\gamma_1 = 1$	$\gamma_2 = 1$	$\gamma_3 = 1$
II	$\lambda_1 = 1$	$\lambda_2 = 2$	$\lambda_3 = 8$
III	$\gamma_1 = 1$	$\gamma_2 = 3$	$\gamma_3 = 6$
IV	$\lambda_1 = 1$	$\lambda_2 = 11$	$\lambda_3 = 11$

(2.79)

where the first one is (2.76) specialized to the case of three intervals. Plugging these configurations in (2.74) and (2.75) for $N = 3$, we can find the corresponding curves within the domain $0 < x_1 < x_2 < x_3 < 1$, as shown in Fig. 2.2. These curves can be equivalently parameterized either by ℓ/L or by one of the harmonic ratios x_i. In Fig. 2.14 we show $R^{\text{norm}}_{3,n}$ $(n = 2, 3, 4)$, finding a good agreement with the CFT prediction (2.45). In Fig. 2.15 we plot I^{sub}_3 for the harmonic chain but, as for Fig. 2.13, we do not have a CFT formula to compare with for the reason mentioned above.

2.6 The analytic continuation through a numerical extrapolation

It has already been argued several times that the analytic continuation (1.48) of the formulas found in the previous sections is very difficult, since they are written in terms

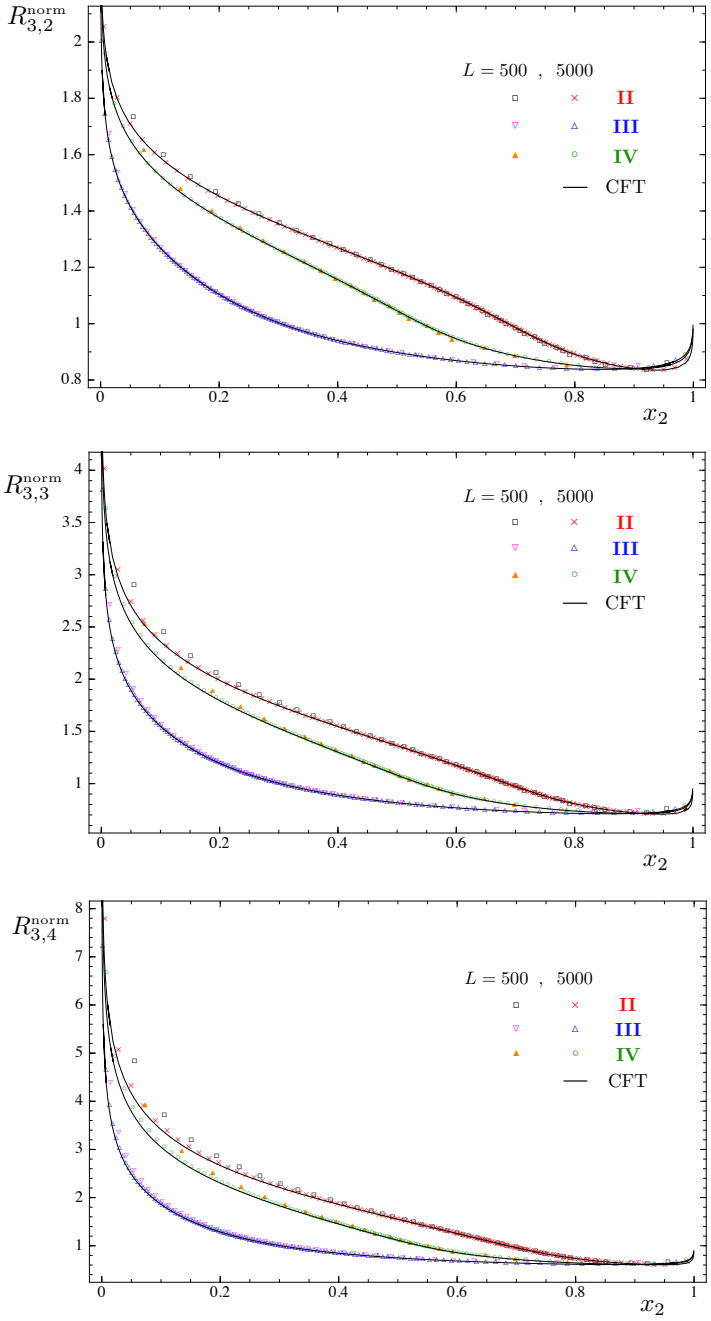

Figure 2.14: The ratio $R^{\rm norm}_{N,n}$ in (2.14) for the harmonic chain with $\omega L = 10^{-3}$. The configurations II, III and IV, which are defined in (2.79), have been normalized through (2.77). The continuous curve is the CFT prediction (2.45). We show $N = 3$ and $n = 2, 3, 4$ (top, middle, bottom).

of Riemann theta functions, which in turn are functions of matrices of dimension $g = (n-1)(N-1)$. However, we still can have predictions for the entanglement entropy and

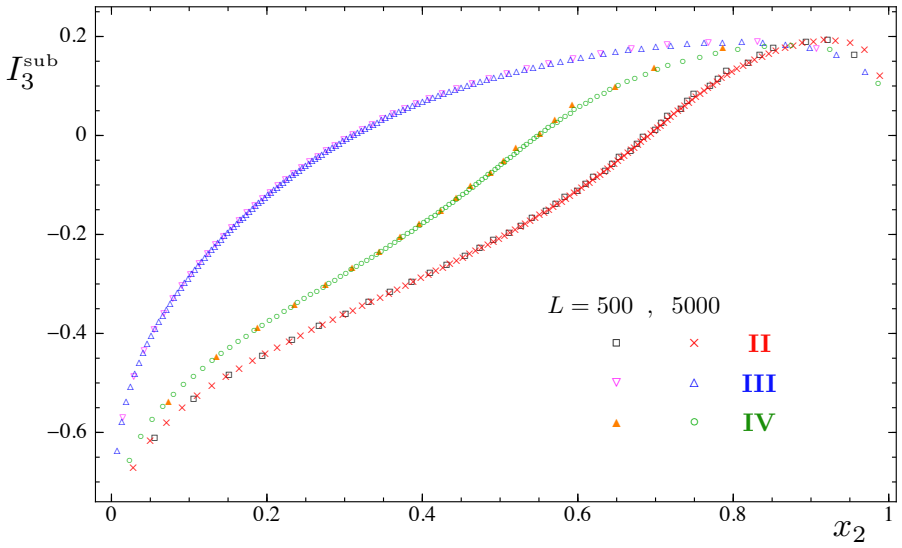

Figure 2.15: $I^{\rm sub}_{N=3}$ in (2.14) for the periodic harmonic chain with $\omega L = 10^{-3}$. The configurations are defined in (2.79) and the fixed one is given by (2.77).

the mutual information from the Rényi entropies, by resorting to numerical techniques to perform this complicated analytic continuation. In this section we employ a numerical extrapolation based on a rational interpolation of the known analytic data. This method has been first suggested in this context in Ref. [152]. In our case, we focus on the decompactified boson and we can compare the results with the numerics obtained from the harmonic chain, finding very good agreement. In [236] the same technique have been also used to study the analytic continuation of moments of the partial transpose to obtain the logarithmic negativity (see Eq. (1.70)) for the boson in the decompactification regime. In this case the analytic continuation is more troublesome and some extra care must be taken when performing the extrapolation procedure.

In the remaining part of this section we focus on the case of three disjoint intervals and perform some numerical extrapolations of the analytic results of the previous sections to $n = 1$ through rational interpolations, comparing them with the corresponding numerical data from the harmonic chain. The rational function used to interpolate the data is characterized by two positive integer parameters p and q, which are the degrees of the numerator and of the denominator respectively. As explained in App. 2.E.2, to perform a rational interpolation characterized by the pair (p, q) we need at least $p + q + 1$ known data.

In Figs. 2.16 and 2.17 we consider $I_3^{\rm sub}$ (see (2.14)) for the decompactified boson. The dots are the numerical data of the bottom panel of Fig. 2.13 and of Fig. 2.15 of the periodic harmonic chain with $L = 5000$, and different sets of data correspond to different configurations of the three intervals. We recall that the configuration considered in Fig. 2.16 is the one described in (2.76), while in Fig. 2.17 the data are labeled according to the configurations of the three intervals given in (2.79). The parameter ℓ is varied and the results are plotted as functions of the four-point ratio $x_2 \in (0, 1)$. Finally, the fixed configuration normalizing $I_3^{\rm sub}$ in (2.14) is (2.77) with $N = 3$. The coloured curves in Figs. 2.16 and 2.17 are the numerical extrapolations of the CFT formulas (2.43)

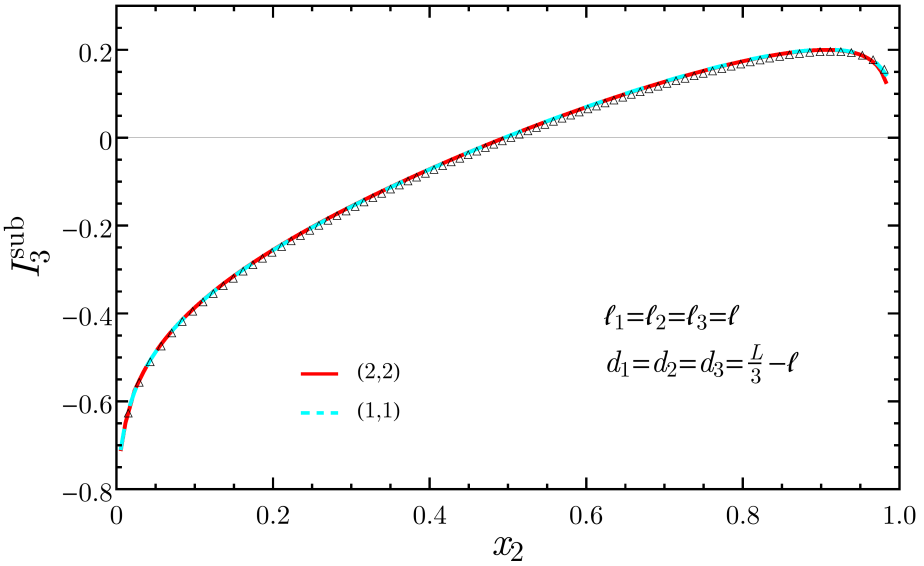

Figure 2.16: Extrapolations of $I_3^{\rm sequb}$ (see 2.14 with $N = 3$) as function of the four-point ratio x_2 for the non compact boson. The points are the data from the periodic harmonic chain with $L = 5000$ and $\omega L = 10^{-5}$. The configuration chosen here is made by equal intervals separated by equal distances, while the fixed configuration normalizing $I_3^{\rm sub}$ is given in the text. The coloured lines correspond to two different extrapolations obtained through rational interpolations with (p, q) indicated.

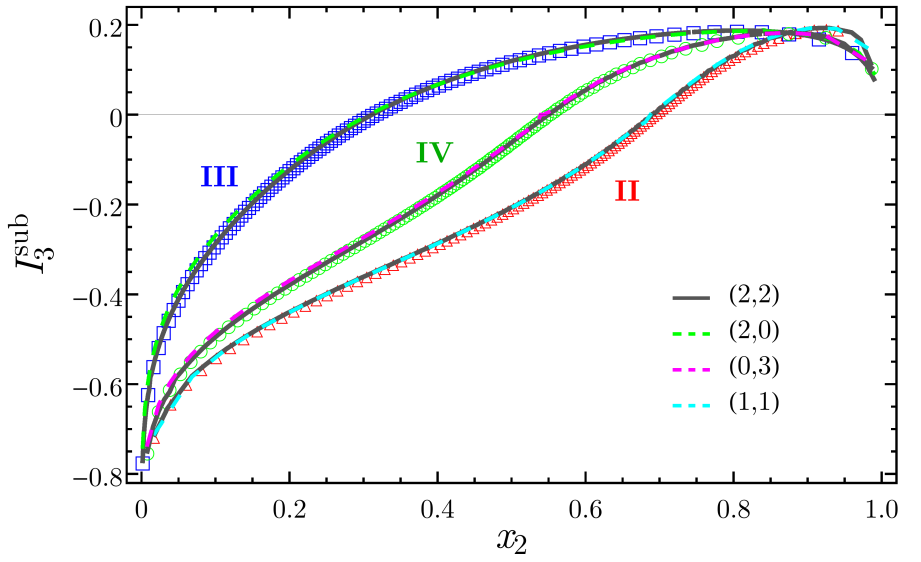

Figure 2.17: Extrapolations of $I_3^{\rm sub}$ for the non compact boson. The harmonic chain is the same one of Fig. 2.16 while the configurations of intervals are given by (2.79).

and (2.45) through the rational interpolation method. For each set of data, we show two different well-behaved rational interpolations in order to check the stability of the result (see App. 2.E for a detailed analysis of possible singular behaviors and what we mean by well-behaved). Different well-behaved rational interpolations are very similar and the agreement with the numerical data from the harmonic chain is very good, supporting the validity of the method.

An important technical difficulty that one encounters is the evaluation of the Riemann theta functions for large genus period matrices, i.e. for high values of N and n. It is worth remarking at this point that the Riemann theta functions occurring in the CFT expression (2.43) for the non compact boson contain at most $g \times g$ matrices ($g = 2(n-1)$ for $N = 3$) while for the compact boson their size is at most $2g \times 2g$ (see 2.41). From the computational viewpoint, this is an important difference because the higher is n that can be addressed, the higher is the number of different (p, q) that can be considered in the rational interpolations. Thus, the maximum n that we can deal with is related to the maximum size of the matrices in the Riemann theta functions occurring in the model. Given the computational resources at our disposal, we were able to compute Riemann theta functions containing matrices whose size is at most 12. This means that for the boson in the decompactification regime (see Eq. (2.43)), in the case of three intervals we can have access to data with $2 \leqslant n \leqslant 6$, and therefore we can use rational functions with $p + q + 1 \leqslant 5$. Nevertheless, from Figs. 2.16 and 2.17 we observe that, for this case, rational interpolations with low values of (p, q) are enough to capture the result expected from the lattice data.

In App. 2.E we give more details on the method used. In particular, in Sec. 2.E.1 we test the method on some numerical data available in the literature, while in Sec. 2.E.2 we explore some technical issues of the rational interpolation and we investigate its validity.

2.7 The Ising model

The Ising model in transverse field provides a simple scenario where we can compute the Rényi entropies of several disjoint intervals and compare them with the corresponding predictions obtained through the CFT methods. The Hamiltonian is given by

$$H = \sum_{s=1}^{L} \left(\sigma_s^x \sigma_{s+1}^x + h \sigma_s^z \right), \tag{2.80}$$

where s label the L sites of a 1D lattice $\mathcal{L}$ and the $\sigma_s^{x,z}$ are the Pauli matrices acting on the spin at site s and periodic boundary conditions are imposed. The model has two phases, one polarized along x for $\lambda < 1$ and another one polarized along z for $\lambda > 1$, which are separated by a second order phase transition at $h = 1$.

The Ising model in transverse field can be rewritten as a model of free fermions [244]. The map underlying this equivalence has been employed in [245] to compute the Rényi entropies for one block and in [222] for two disjoint blocks, where the generalization to N blocks is also discussed.

Our approach is based on the Matrix Product States (MPS), which is completely general and therefore it can be applied for every one dimensional model. We choose the MPS because they are the simplest tensor networks (see Sec. 2.7.2 for a proper definition). The same calculation can be done through other variational ansatz metohds, like the TTN or the MERA [220, 223, 246]).

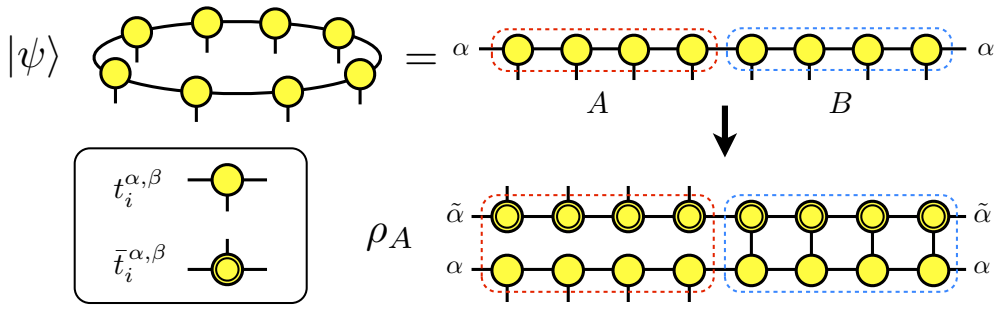

Figure 2.18: The contraction giving the MPS state $|\psi\rangle$ of a chain with $L = 8$ sites and periodic boundary conditions (points labeled by the same greek index are considered as the same point). The individual tensor $t_i^{\alpha,\beta}$, which defines the MPS state, and its complex conjugate $\bar{t}_i^{\alpha,\beta}$ are shown in the box on the left. Considering the bipartition of the chain with A made by 4 contiguous sites, we show the tensor network contraction occurring in the computation of the reduced density matrix ρ_A.

2.7.1 Rényi entropies for the Ising CFT

The continuum limit of the quantum critical point $h = 1$ corresponds to a free massless Majorana fermion, which is a CFT with $c = 1/2$.

Identifying ϕ with $-\phi$ in (2.16), the target space becomes $S^1/\mathbb{Z}_2$ and the compactification radius (orbifold radius) parameterizes the critical line of the Ashkin-Teller model, which can be seen as two Ising models coupled through a four fermions interaction. When the interaction vanishes, the partition function of the Ashkin-Teller model reduces to the square of the partition function of the Ising model. This set of $c = 1$ conformal field theories has been studied in [209–211, 214] in the case of a worldsheet given by a generic Riemann surface and the relations found within this context allow us to write $\mathrm{Tr}\,\rho_A^n$ for the Ising model in terms of Riemann theta functions with characteristic (2.47). The peculiar feature of the Ising model with respect to the other points of the Ashkin-Teller line is that we just need the period matrix τ to find the partition function on the corresponding Riemann surface.

In our case, the Riemann surface is given by (2.18) and its period matrix has been computed in Sec. 2.3.1. As anticipated in Sec. 1.4, $\mathrm{Tr}\,\rho_A^n$ for the Ising model is given by (1.52) with $c = 1/2$ and

$$\mathcal{F}_{N,n}^{\text{Ising}}(\boldsymbol{x}) = \frac{\sum_{\boldsymbol{e}} |\Theta[\boldsymbol{e}](\boldsymbol{0}|\tau)|}{2^g\,|\Theta(\boldsymbol{0}|\tau)|}\,, \tag{2.81}$$

where the period matrix τ has been discussed in Sec. 2.3.1. As already remarked in Sec. 2.3.4, the sum over the characteristics in the numerator of (2.81) contains only the even ones. We checked numerically that $\mathcal{F}_{N,n}^{\text{Ising}}(\boldsymbol{0}) = 1$. Moreover, by employing the results of Sec. 2.4 and of App. 2.C, one finds that, specializing (2.81) to $N = 2$, the expression for $\mathcal{F}_{2,n}^{\text{Ising}}(x)$ found in [196] is recovered. In App. 2.C we also discuss the invariance of (2.81) under a cyclic transformations or an inversion in the ordering of the sheets and under the exchange $A \leftrightarrow B$.

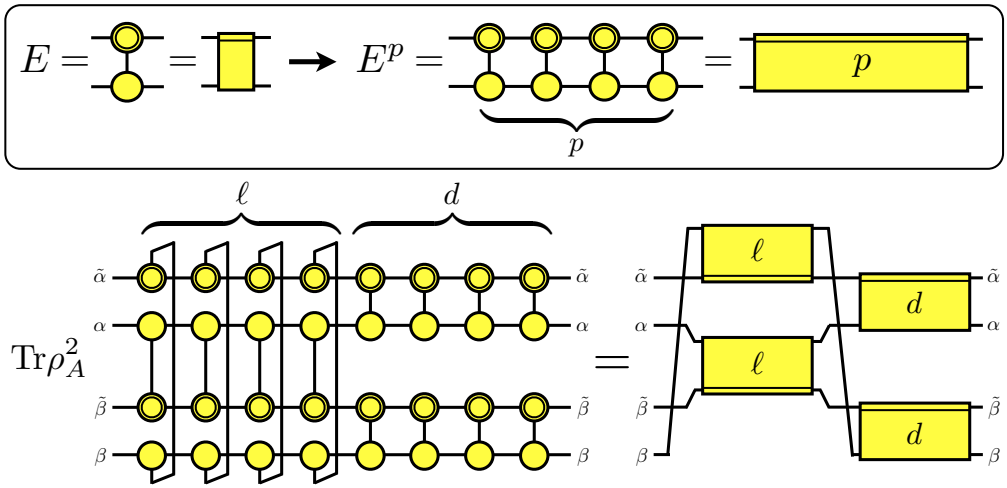

Figure 2.19: The computation of $\mathrm{Tr}\rho_A^2$ for the bipartition of Fig. 2.18, where $\ell = d = 4$. The MPS transfer matrix E and its p-th power are shown in the box as yellow rectangles. The pattern for the contractions of the indices is on the right.

2.7.2 Matrix product states: notation and examples

A pure state $|\Psi\rangle \in \mathbb{V}^{\otimes L}$ defined on the lattice $\mathcal{L}$ can be expanded in the local basis of $\mathbb{V}_s$ given by $\{|1_s\rangle, |2_s\rangle, \cdots, |\delta_s\rangle\}$ as follows

$$|\Psi\rangle = \sum_{i_1=1}^{\delta} \sum_{i_2=1}^{\delta} \cdots \sum_{i_L=1}^{\delta} T_{i_1 i_2 \cdots i_L} |i_1\rangle |i_2\rangle \cdots |i_L\rangle \ . \tag{2.82}$$

This means that $|\Psi\rangle$ is encoded in a tensor T with δ^L complex components $T_{i_1 i_2 \cdots i_L} \in \mathbb{C}$. We refer to the index $1 \leqslant i_s \leqslant \delta$, labelling a local basis for site s, as the physical index.

The tensor network approach (see e.g. the review [247]) is a powerful way to rewrite the exponentially large tensor T in (2.82) as a combination of smaller tensors. In order to simplify the notation, drawings are employed to represent the various quantities occurring in the computation. Tensors are represented by geometric shapes (circles or rectangles) having as many legs as the number of indices of the tensor. The complex conjugate of a tensor is denoted through the same geometric object delimited by a double line. A line shared by two tensors represents the contraction over the pair of indices joined by it.

The MPS are tensor networks that naturally arise in the context of the Density Matrix Renormalization Group [34, 38, 248]. They are build through a set of tensors $t_i^{\alpha,\beta}$ (one for each lattice site) with three indices (see the box in Fig. 2.18): i is the physical index mentioned above, while α and β are auxiliary indices. The tensors are contracted following the pattern shown in Fig. 2.18, where the translational invariance of the state is imposed by employing the same elementary tensor for each site. The state in Fig. 2.18 has $L = 8$ and it is given by

$$|\Psi\rangle = \sum_{i_1,\ldots,i_8=1}^{\delta} \sum_{\alpha_1,\ldots,\alpha_8=1}^{\chi} t_{i_1}^{\alpha_1\alpha_2} t_{i_2}^{\alpha_2\alpha_3} \cdots t_{i_8}^{\alpha_8\alpha_1} |i_1\rangle |i_2\rangle \cdots |i_8\rangle \ , \tag{2.83}$$

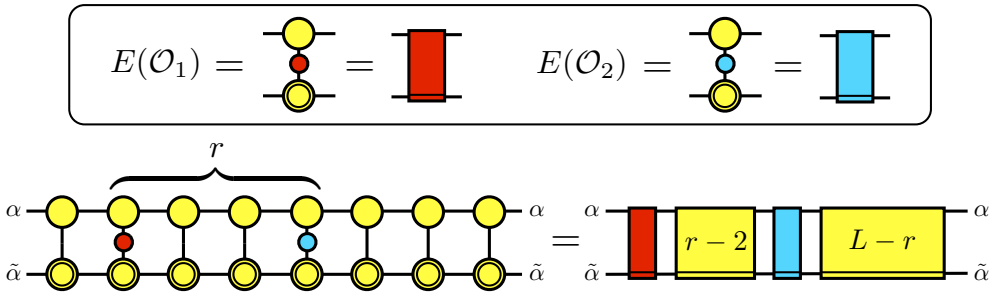

Figure 2.20: The two point correlation function $C(r)_{\mathcal{O}_1,\mathcal{O}_2}$ of the local operators $\mathcal{O}_1$ and $\mathcal{O}_2$. The corresponding generalized transfer matrices $E(\mathcal{O}_1)$ and $E(\mathcal{O}_2)$, depicted in the box, must be contracted with the proper powers of E.

where χ is the rank of the auxiliary indices, which is called bond dimension in this context. Since we are using the same tensor for each site, the state is completely determined by the components of the tensor $t_i^{\alpha\beta}$, which are $\delta\chi^2$ free parameters. In the MPS approach, the expectation value of local observables can be computed by performing $\mathcal{O}(\delta\chi^3)$ operations. The components $t_i^{\alpha\beta}$ of the tensor are obtained numerically by minimizing $\langle\Psi|H|\Psi\rangle$ for the Hamiltonian (2.80).

The bond dimension χ controls the accuracy of the results. Increasing χ, one can describe an arbitrary state of the Hilbert space [249]. In practice, a finite bond dimension which is independent of L allows to describe accurately ground states of gapped local Hamiltonians [14]. For gapless Hamiltonians described by a CFT, the bond dimension has to increase polynomially with the system size [250], namely $\chi = L^{1/\kappa}$, where κ is an universal exponent [36] which depends only on the central charge c as follows: $\kappa = 6/[c(\sqrt{12/c}+1)]$ [37, 251]. Since the Ising model has $c = 1/2$, we have $\kappa \simeq 2$.

In principle, the MPS representation of the ground state allows us to compute several observables. In practice, different computations require a different computational effort. For instance, considering the bipartition shown in Fig. 2.18, where $L = 8$ and $\ell = 4$, the reduced density matrix ρ_A in a MPS representation has at most rank χ^2 [247, 252], independently on the size of the block. This implies that it can be computed exactly by performing at most $\mathcal{O}(\delta^3\chi^6)$ operations.

The case of N disjoint blocks is more challenging. Indeed, the corresponding reduced density matrices in the MPS representation can have rank up to χ^{2N}, which means that these computations are exponentially hard in N. Some of these computations can be done by projecting the reduced density matrices on their minimal rank [220, 223]. Here we describe an alternative approach, which is based on the direct computation of the Rényi entropies.

2.7.3 Rényi entropies from MPS: the correlation functions of twist fields

In the computation of $\mathrm{Tr}\rho_A^n$, which gives the Rényi entropies through (1.47), we need the powers of the MPS transfer matrix $E^{(\alpha,\tilde{\alpha}),(\beta,\tilde{\beta})} \equiv \sum_i t_i^{\alpha,\beta}\bar{t}_i^{\tilde{\alpha},\tilde{\beta}}$. Being a mixed tensor involving both t and $\bar{t}$, we represent E as the yellow rectangle in the box of Fig. 2.19, where the double line on one side keeps track of the position of $\bar{t}$. Then, we can straightforwardly construct the p-th power E^p, which is the key ingredient to obtain $\mathrm{Tr}\rho_A^n$ for a bipartition of the chain. Indeed, when A is made by a block of length ℓ, it is computed in terms of

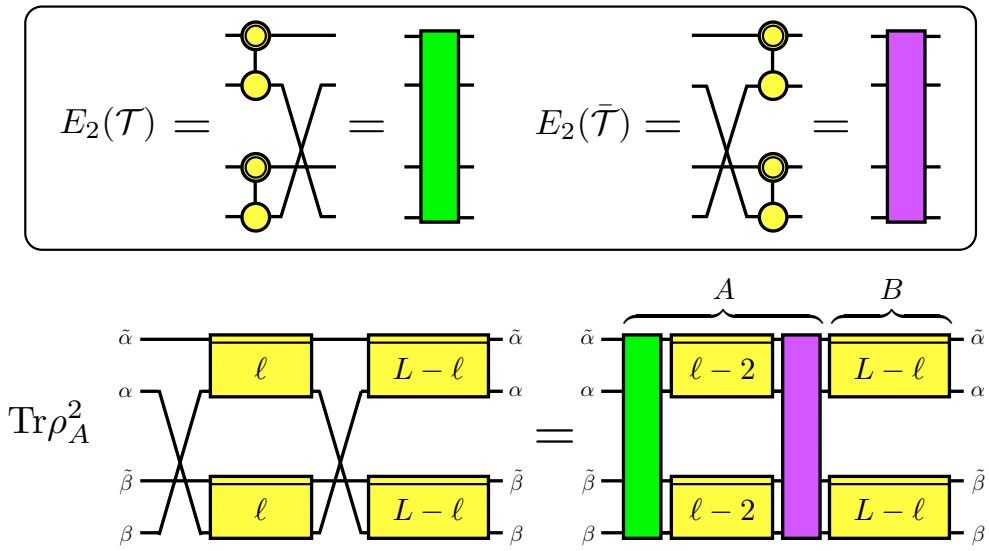

Figure 2.21: The computation of $\mathrm{Tr}\rho_A^2$ of Fig. 2.19 as the two point correlation function (see Fig. 2.20) of twist fields in the MPS formalism, i.e. through (2.86). They are operators acting on the auxiliary degrees of freedom and this allows us to define the generalized transfer matrices $E_2(\mathcal{T})$ and $E_2(\bar{\mathcal{T}})$, which must be contracted with the proper powers of E_2.

E^ℓ and E^d, where $d = L - \ell$. In Fig. 2.19 we represent the computation of $\mathrm{Tr}\rho_A^2$ for the bipartition of Fig. 2.18.

Simple manipulations allow us to write the above expression for $\mathrm{Tr}\rho_A^n$ as the two point function of twist fields. In order to see this, let us first consider the two point correlation function $C_{\mathcal{O}_1,\mathcal{O}_2}(r) \equiv \langle\psi|\mathcal{O}_1(x)\mathcal{O}_2(x+r)|\psi\rangle$ of local operators $\mathcal{O}_1$ and $\mathcal{O}_2$. For this computation we introduce the generalized transfer matrix for a generic local operator $\mathcal{O}$ as

$$E(\mathcal{O})^{(\alpha,\alpha'),(\beta,\beta')} \equiv \sum_{i,j} t_i^{\alpha,\beta} \bar{t}_j^{\tilde{\alpha},\tilde{\beta}} \mathcal{O}^{i,j} \,, \tag{2.84}$$

whose graphical representation is shown in the box of Fig. 2.20. Given (2.84), the two point correlation function becomes the following trace of the product of transfer matrices

$$C_{\mathcal{O}_1,\mathcal{O}_2}(r) = \mathrm{Tr}\big(E(\mathcal{O}_1)E^{r-2}E(\mathcal{O}_2)E^{L-r}\big) \,, \tag{2.85}$$

which is depicted in Fig. 2.20, where different colors correspond to different operators.

In a similar way, we can write $\mathrm{Tr}\rho_A^n$ for the bipartition of Fig. 2.18 as the two point correlation function of twist fields. This is done by introducing other generalized transfer matrices, namely the tensor product $E_n = E \otimes \cdots \otimes E$ of n transfer matrices and the transfer matrices $E_n(\mathcal{T})$ and $E_n(\bar{\mathcal{T}})$ associated to the twist fields (see the box in Fig. 2.21 for $n = 2$ and in Fig. 2.22 for $n = 3$). Given these matrices, $\mathrm{Tr}\rho_A^n$ reads

$$\mathrm{Tr}\rho_A^n = \mathrm{Tr}\big(E_n(\mathcal{T})E_n^{\ell-2}E_n(\bar{\mathcal{T}})E_n^{L-\ell}\big) \,. \tag{2.86}$$

Notice that (2.86) has the structure of the two point function given in 2.85, but it is not exactly the same. Indeed, since the twist fields are operators acting on the virtual bonds

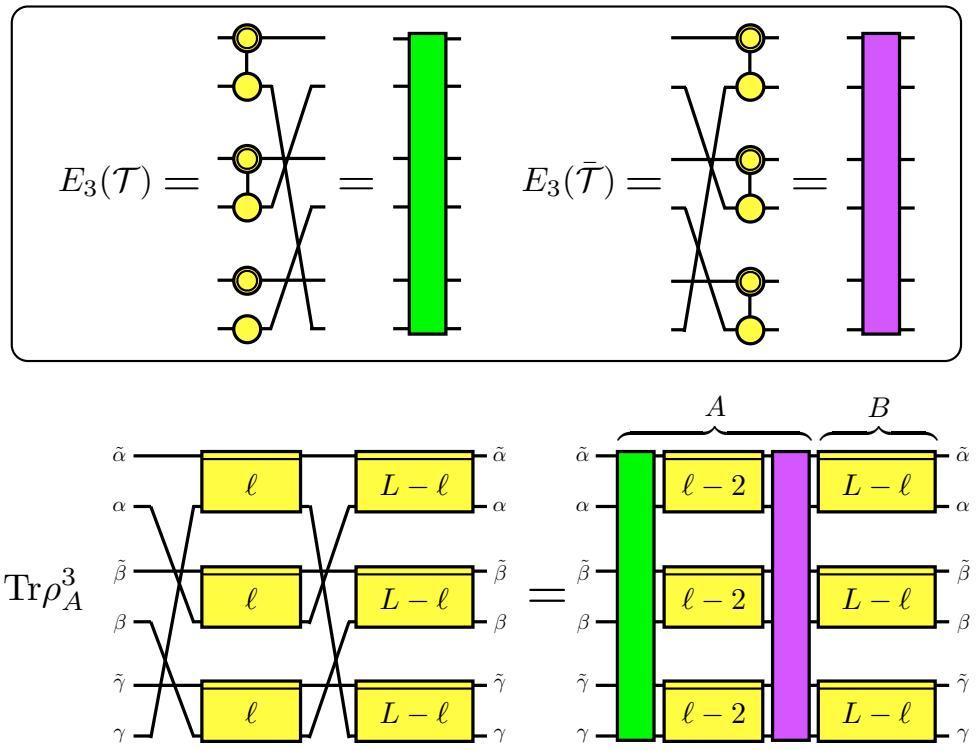

Figure 2.22: The computation of $\mathrm{Tr}\rho_A^3$ of Fig. 2.19 as the two point correlation function (see Fig. 2.20) of twist fields (2.86). In this case the twist fields act on the tensor product of three pairs of virtual indices. The generalized transfer matrices $E_3(\mathcal{T})$ and $E_3(\bar{\mathcal{T}})$ are contracted with the proper powers of $E_3 = E \otimes E \otimes E$.

rather than on the physical bonds, they are not local operators on the original spin chain. In Figs. 2.21 and 2.22 we show (2.86) for $n = 2$ and $n = 3$ respectively.

It is straightforward to generalize this construction to the case of N disjoint blocks (see Fig. 2.9 for the notation). In this case $A = \cup_{i=1}^{N} A_i$ and the generalization of (2.86) to $N \geqslant 2$ reads

$$\mathrm{Tr}\rho_A^n = \mathrm{Tr}\big(E_n(\mathcal{T})E_n^{\ell_1-2}E_n(\bar{\mathcal{T}})E_n^{d_1}\cdots E_n(\mathcal{T})E_n^{\ell_N-2}E_n(\bar{\mathcal{T}})E_n^{d_N}\big)\,, \tag{2.87}$$

where the dots replace the sequence of terms $E_n(\mathcal{T})E_n^{\ell_j-2}E_n(\bar{\mathcal{T}})E_n^{d_j}$, ordered according to the increasing value of interval index $j = 2, \ldots, N-1$. In Fig. 2.23, the MPS computation (2.87) for $N = 3$ and $n = 2$ is depicted. It is important to remark that in (2.87) the computational cost is $O(N\delta\chi^{4n+1})$, i.e. exponential in n and linear in N. Thus, for the simplest cases of $n = 2$ and $n = 3$ the cost is χ^9 and χ^{13} respectively. Because of this, in the remaining part of this section we present numerical results obtained through the exact formula (2.87) with $n = 2$ only, for configurations made by either $N = 3$ or $N = 4$ disjoint blocks.

The method that we just discussed is very general and, in principle, it can be applied for many lattice models. Nevertheless, the feasibility of the computation strongly depends on the value of the bond dimension χ, which depends on the central charge c as mentioned

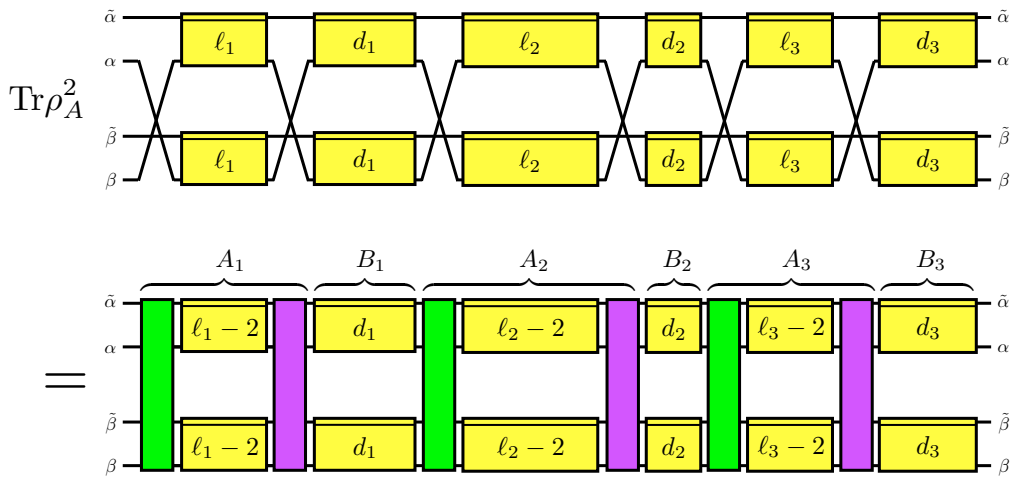

Figure 2.23: The computation of $\mathrm{Tr}\rho_A^n$ through (2.87) in the case of $N = 3$ and $n = 2$ as the six point function of twist fields.

above. Thus, having $c = 1/2$, the Ising model is the easiest model that we can deal with. A model with $c = 1$ would lead to a very high computational cost already for the Rényi entropy with $n = 2$ and this would be a very challenging computation, given the numerical resources at our disposal.

As for the approximate calculations of the Rényi entropies, a very different scenario arises. In particular, Monte Carlo techniques [218, 253–255] look very promising because they allow to obtain an approximate result for $\mathrm{Tr}\rho_A^n$ by sampling over the physical indices. Each configuration can be computed with $n\chi^3$ operations, but the number of configurations which are necessary to extract a reliable estimation of the Rényi entropies in terms of χ and n is still not understood.

2.7.4 Numerical results for $n = 2$

Let us discuss the numerical results obtained through the method discussed in Sec. 2.7.3 about $\mathrm{Tr}\,\rho_A^2$ for the Ising model with periodic boundary conditions. The length L of the chains varies within the range $30 \leqslant L \leqslant 500$. The MPS matrices have been computed by employing the variational algorithm described in [256] (see also the ones in [257, 258]). Moreover, from Fig. 2 of [37] one observes that, in order to find accurate results for the Ising model in the range of total lengths given above, we need $8 \leqslant \chi \leqslant 16$.

As for the configurations of the N disjoint blocks of sites, denoting by ℓ_i the number of sites for the block A_i and by d_i the number of sites separating A_i and $A_{i+1 \bmod N}$ with $i = 1, \ldots, N$ as in Sec. 2.5 (see Fig. 2.9 for the case $N = 3$), we find it convenient to choose the following ones

ℓ_1	d_1	ℓ_2	d_2	ℓ_3	d_3	$\ldots$	ℓ_N	d_N
ℓ	d	ℓ	d	ℓ	d	$\ldots$	ℓ	d_N

$$d = \alpha\ell\,, \tag{2.88}$$

where $d_N = L - [N + \alpha(N-1)]\ell$ is fixed by the consistency condition (2.73) on the total length of the chain. Thus, each configuration is characterized by the coefficient α and the

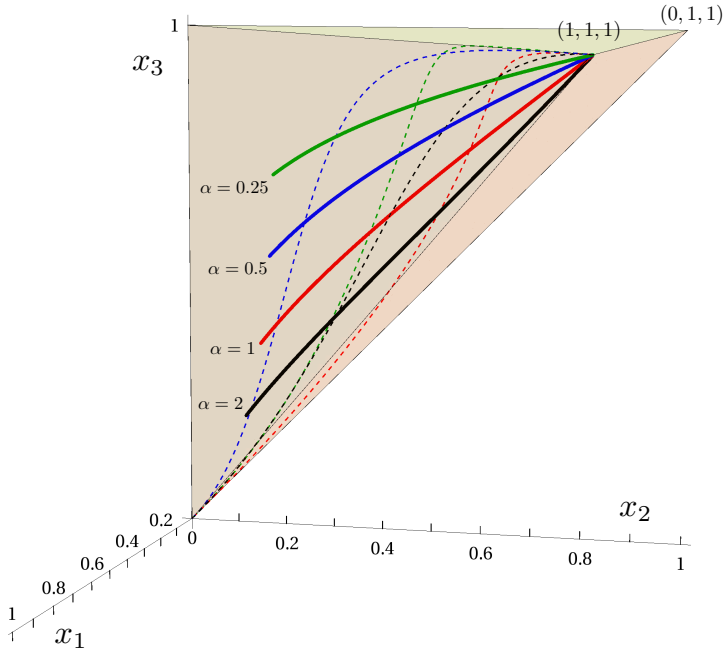

Figure 2.24: The domain $0 < x_1 < x_2 < x_3 < 1$ for $N = 3$, as in Fig. 2.2. The thick lines represents the configurations (2.88) for some choices of α. The dashed thin curves are the configurations shown in Fig. 2.2, with the same colors.

free parameter is ℓ. In the comparison with the CFT expressions discussed in Sec. 2.2 and Sec. 2.7.1, we have taken the finiteness of the system into account through (2.74) and (2.75), as already done in Sec. 2.5 for the harmonic chain. Like for (2.78) with the vectors $\boldsymbol{\lambda}$ and $\boldsymbol{\gamma}$ fixed, also for the configurations (2.88) with α fixed the harmonic ratios x_i depend only on ℓ/L, providing one dimensional curves within the $2N-3$ dimensional configuration space $0 < x_1 < x_2 < \cdots < x_{2N-3}$. Nevertheless, notice that in this case the harmonic ratios have a strictly positive lower bound, which can be computed by taking the limit $\ell \to 0$ in the expressions of x_i obtained by specializing (2.74) and (2.75) to (2.88). For instance, when $N = 3$ we have $x_1 = [\sin(\pi\ell/L)/\sin(2\pi(1+\alpha)\ell/L)]^2$, whose smallest value reads $1/[2(1+\alpha)]^2$. Always for $N = 3$, in Fig. 2.24 we show the curves corresponding to the configurations (2.88) for the numerical values of α considered in the remaining figures. Each curve can be equivalently parameterized by one the harmonic ratios and in this section we choose x_1 as the independent variable.

Given the configurations (2.88), for any fixed α different values of ℓ and L having the same ℓ/L provide the same $\boldsymbol{x}$, i.e. the same point in the configurations space. Aligning the numerical data corresponding to the same $\boldsymbol{x}$, one observes that, as ℓ increases, they approach the CFT prediction. Nevertheless, the discrepancy is quite large because the chains at our disposal are not long enough. Thus, unlike the case of the harmonic chain discussed in Sec. 2.5, for the Ising model the plots of the data do not immediately confirm the CFT expressions.

During the last few years many papers have studied the corrections to the leading scaling behavior of the Rényi entropies [136, 220, 222, 223, 259–264]. When A is a single block made by ℓ contiguous lattice sites within a periodic chain of length L, the first

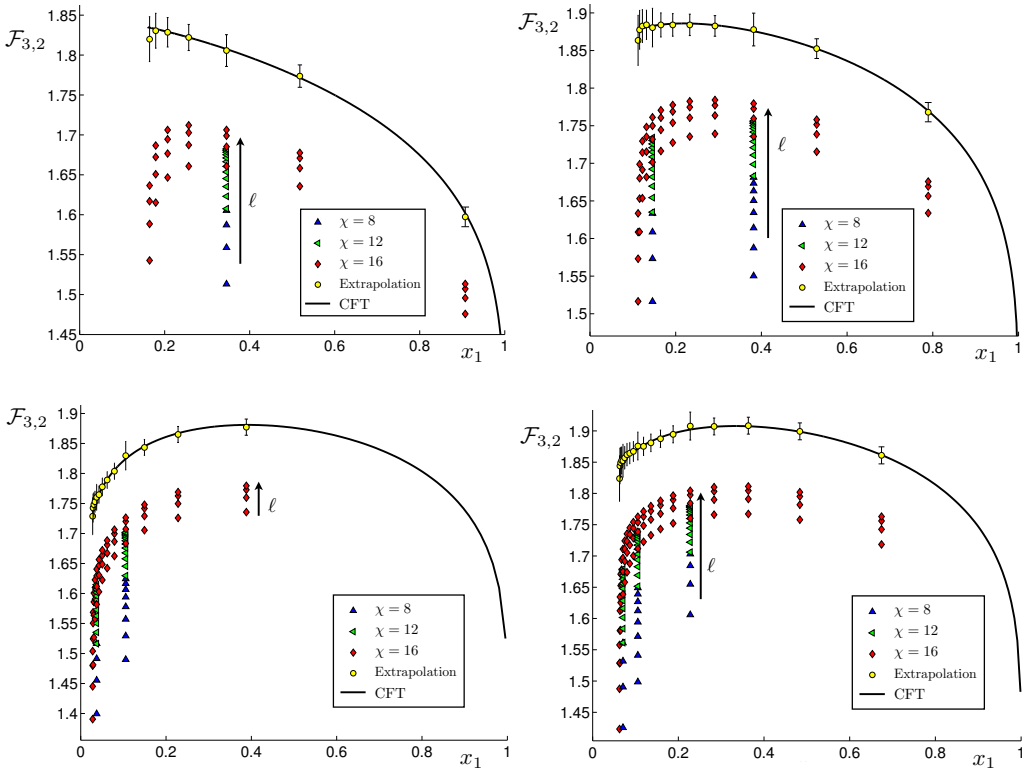

Figure 2.25: The results for $\mathcal{F}_{3,2}$ computed trough MPS ground states in terms of x_1. The configurations are (2.88) with (from the top left panel, in clockwise direction) $\alpha = 0.25$, $\alpha = 0.5$, $\alpha = 1$ and $\alpha = 2$. For a fixed $\boldsymbol{x}$, the length ℓ of the blocks increases along the black arrow. The extrapolated points are obtained as explained in Sec. 2.7.4.

deviation of $\mathrm{Tr}\,\rho_A^n$ from the corresponding value obtained through the CFT expression is proportional to $\ell^{-2\Delta/n}$, for some $\Delta < 2$. From the field theoretical point of view, this unusual scaling can be understood by assuming that the criticality is locally broken at the branch points and this allows the occurrence of relevant operators with scaling dimension $\Delta < 2$ at those points [261]. For the Ising model the relevant operator must be also parity even and this means that the first correction is proportional to $\ell^{-2/n}$. Instead, when A is made by two disjoint blocks, it has been numerically observed that the leading correction for the Ising model is proportional to $\ell^{-1/n}$ [220, 222], which agrees with $\ell^{-2\Delta/n}$ with $\Delta = 1/2$. This could be the contribution of the Majorana fermion introduced by the Jordan-Wigner string between the two blocks [222].

In the following we consider the case of A made by three and four disjoint blocks, focusing on $\mathcal{F}_{3,2}$ and $R_{3,2}$ for $N = 3$ and on $\mathcal{F}_{4,2}$ for $N = 4$. We studied the configurations (2.88) with $\alpha = p$ and $\alpha = 1/p$, where for the integer p we took $1 \leqslant p \leqslant 8$. Here we show the plots only for $\alpha \in \{0.25, 0.5, 1, 2\}$ because the ones for the remaining values of α are very similar. The results for $N = 3$ are reported in Figs. 2.25 and 2.26, while the ones for $N = 4$ are given in Fig. 2.27. Different colored shapes denote numerical data which have been obtained from ground states with different bound dimensions. Moreover, for fixed values of $\boldsymbol{x}$ and χ, the black arrow indicates the direction along which ℓ increases. For

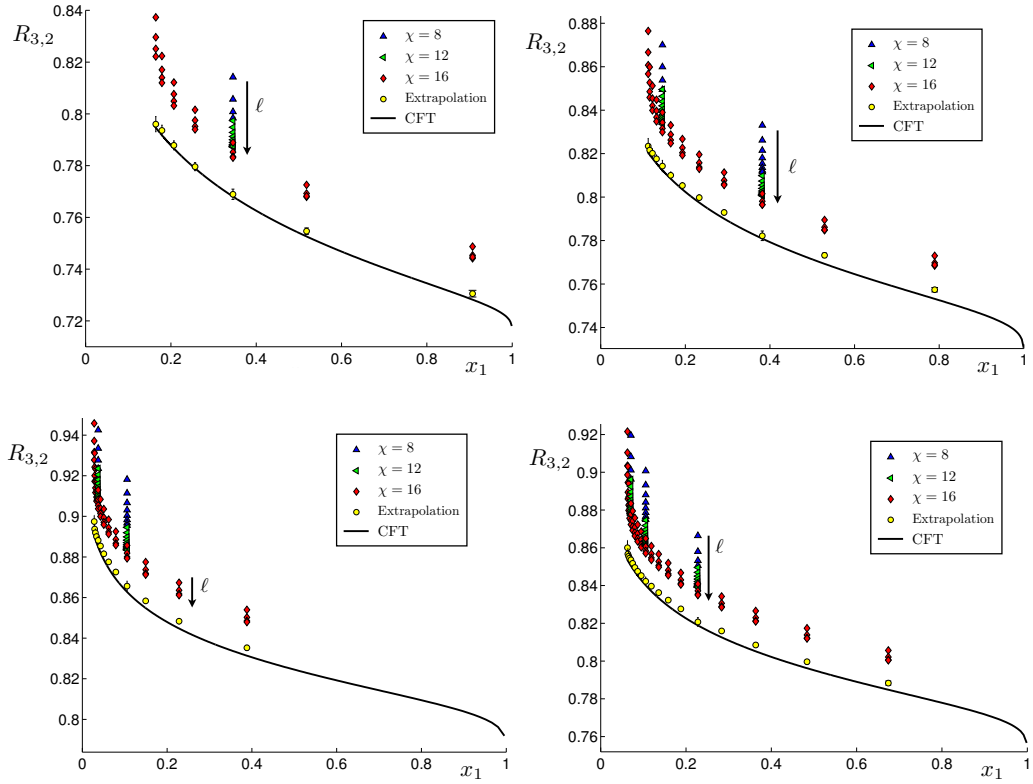

Figure 2.26: The results for $R_{3,2}$ computed trough MPS ground states in terms of x_1. The configurations are (2.88) with (from the top left panel, in clockwise direction) $\alpha = 0.25$, $\alpha = 0.5$, $\alpha = 1$ and $\alpha = 2$. For a fixed $\boldsymbol{x}$, the length ℓ of the blocks increases along the black arrow. The extrapolated points are obtained as explained in Sec. 2.7.4.

a given χ, the maximum value $L_{\max}$ of the total size of the chain has been determined according to Fig. 2 of [37]. In particular, for $\chi = 8$, $\chi = 12$ and $\chi = 16$ we used respectively $L_{\max} = 100$, $L_{\max} = 320$ and $L_{\max} = 500$.

Notice that larger values of χ and ℓ better approximate the points obtained through the CFT formulas, as expected. Nevertheless, since the discrepancy between our best numerical value and the one predicted by the CFT is quite large, a finite size scaling analysis is necessary, as discussed above. For almost every value of $\boldsymbol{x}$ that we are considering, taking the effects of the first correction into account is enough to find reasonable agreement with the CFT predictions. According to the analysis discussed in App. 2.D.1, we find that the first correction is proportional to $\ell^{-\Delta_{\text{num}}}$, where $\Delta_{\text{num}} = 0.45(5)$ for both $\mathcal{F}_{3,2}$ and $\mathcal{F}_{4,2}$, and $\Delta_{\text{num}} = 0.51(4)$ for $R_{3,2}$. We remark that these exponents have been found just from the numerical data, without assuming the CFT formulas. The result is compatible with $\Delta = 1/2$ found for two disjoint blocks [220, 222]. Thus, this result seems to be independent of the number of intervals.

Once the exponents have been determined, we can compare the numerical results with the CFT predictions. This means that, for $N = 3$ and $N = 4$, we consider

$$\mathcal{F}^{\text{lat}}_{N,2}(\boldsymbol{x}) = \mathcal{F}^{\text{ext}}_{N,2}(\boldsymbol{x}) + \frac{f_N(\boldsymbol{x})}{\ell^{\Delta_{\text{num}}}}\,, \qquad R^{\text{lat}}_{3,2}(\boldsymbol{x}) = R^{\text{ext}}_{3,2}(\boldsymbol{x}) + \frac{r(\boldsymbol{x})}{\ell^{\Delta_{\text{num}}}}\,, \tag{2.89}$$

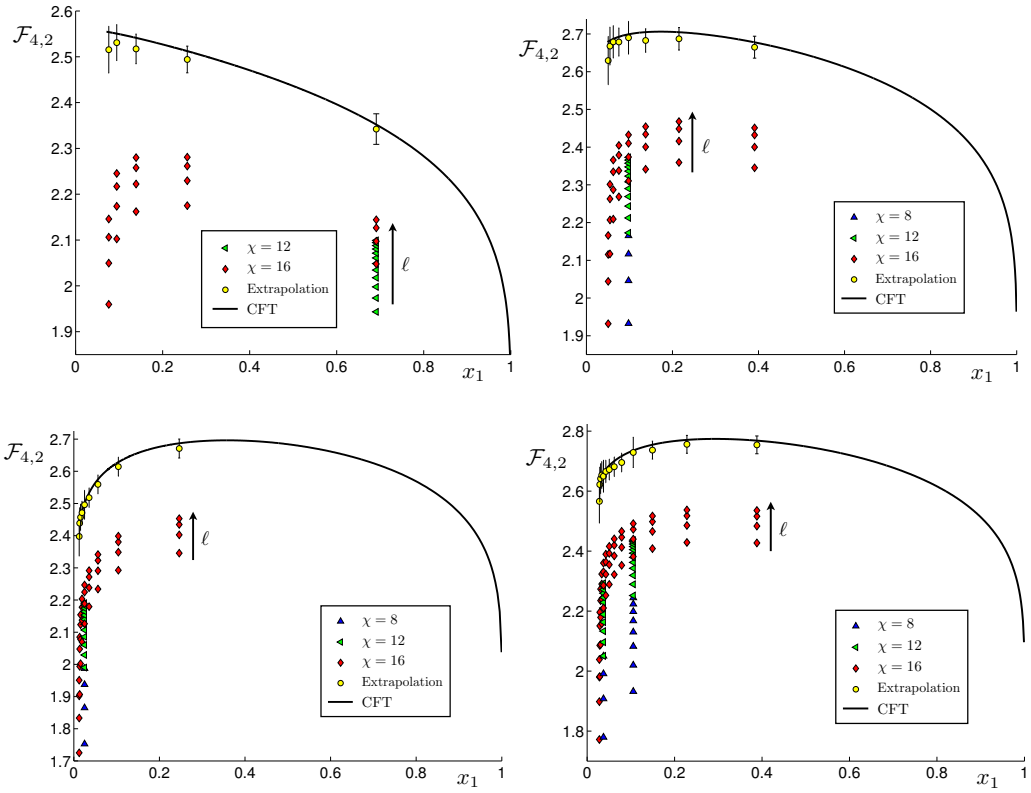

Figure 2.27: The results for $\mathcal{F}_{4,2}$ computed trough MPS ground states in terms of x_1. The configurations are (2.88) with (from the top left panel, in clockwise direction) $\alpha = 0.25$, $\alpha = 0.5$, $\alpha = 1$ and $\alpha = 2$. For a fixed $\boldsymbol{x}$, the length ℓ of the blocks increases along the black arrow. The extrapolated points are obtained as explained in Sec. 2.7.4.

where $\Delta_{\rm num}$ are the exponents given above. For any fixed $\boldsymbol{x}$, we have two parameters to fit: the coefficient of $\ell^{-\Delta_{\rm num}}$ and the extrapolated value. The latter one must be compared with the corresponding value obtained through the CFT formula. Since we have to find only two parameters through this fitting procedure, we can carry out this analysis for all the $\boldsymbol{x}$'s at our disposal, also when few numerical points occur. Because of the uncertainty on $\Delta_{\rm num}$, for any fixed $\boldsymbol{x}$ we perform the extrapolation for both the maximum and the minimum value of $\Delta_{\rm num}$. This provides the error bars indicated in Figs. 2.25, 2.26 and 2.27, where the yellow circles denote the mean values.

In App. 2.D.2 we consider more than one correction, keeping the same exponents employed for case $N = 2$ [136, 222, 223]. Unfortunately, this analysis can be performed only for those few values of $\boldsymbol{x}$ at fixed α which have many numerical points (see Figs. 2.33 and 2.34). We typically find that the second correction improves the agreement with the corresponding CFT prediction, as expected, while the third one does not, telling us that, probably, given our numerical data, we cannot catch the third correction.

In App. 2.D.3 we briefly consider the effects due to the finiteness of the bond dimension in our MPS computations. They occur because finite χ leads to a finite correlation length ξ_χ and, whenever it is smaller than the relevant length scales a deviation from the expected

power law behavior of the correction is observed [36, 37, 250, 265].

2.8 Conclusions

In this chapter we have computed the Rényi entropies of N disjoint intervals for the simple conformal field theories given by the free compactified boson and the Ising model.

For the free boson compactified on a circle of radius R_{circle}, we find that $\operatorname{Tr}\rho_A^n$ for $A = \cup_{i=1}^N A_i$ with $N \geqslant 2$ is given by (1.52) with $c = 1$ and

$$\mathcal{F}_{N,n}(\boldsymbol{x}) = \frac{\Theta(\mathbf{0}|T_\eta)}{|\Theta(\mathbf{0}|\tau)|^2}\,, \qquad T_\eta = \begin{pmatrix} \mathrm{i}\,\eta\,\mathcal{I} & \mathcal{R} \\ \mathcal{R} & \mathrm{i}\,\mathcal{I}/\eta \end{pmatrix}, \tag{2.90}$$

where $\eta \propto R^2$, the function Θ is the Riemann theta function (2.34) and $\tau = \mathcal{R} + \mathrm{i}\mathcal{I}$ is the period matrix of the Riemann surface $\mathcal{R}_{N,n}$ defined by (2.18), which has genus $g = (N-1)(n-1)$ (see e.g. Fig. 2.4, where $N = 3$ and $n = 4$). As for the Ising model, we find that $\operatorname{Tr}\rho_A^n$ is (1.52) with $c = 1/2$ and

$$\mathcal{F}_{N,n}^{\text{Ising}}(\boldsymbol{x}) = \frac{\sum_{\boldsymbol{e}} |\Theta[\boldsymbol{e}](\mathbf{0}|\tau)|}{2^g\,|\Theta(\mathbf{0}|\tau)|}\,, \tag{2.91}$$

being $\boldsymbol{e}$ the characteristics of the Riemann theta function, defined through (2.47). The period matrix of $\mathcal{R}_{N,n}$ [234] has been computed in two different canonical homology basis and, given the relation between them, one can employ either (2.32) or (2.57) in the expressions (2.90) and (2.91). The peculiar feature of the free compactified boson and of the Ising model is that, in order to write the Rényi entropies, we just need the period matrix of $\mathcal{R}_{N,n}$.

We have checked (2.90) in the decompactification regime against exact results for the harmonic chain with periodic boundary conditions, finding excellent agreement. As for the Ising model, we have performed an accurate finite size scaling analysis using MPS. In particular we have identified the twist fields within this formalism, showing that the Rényi entropies can be computed as correlation functions of twist fields also in this case. Whenever a reliable finite size scaling analysis can be performed, the numerical results confirm (2.91). The results of [196, 226] for two disjoint intervals are recovered as special cases of (2.90) and (2.91).

We have not been able to analytically continue (2.90) and (2.91), in order to find the entanglement entropy. This is still an open problem in the simplest case of two intervals for the free boson at finite η and for the Ising model. For the boson on the infinite line, we have shown numerical predictions for the tripartite information and for the corresponding quantities in the case of $N > 3$.

Appendices

2.A On the x dependence of $R_{N,n}$

In this appendix we give some details about the ratio $R_{N,n}$ defined in (2.3) in the case of two dimensional conformal field theories, when $A = \cup_{i=1}^{N} A_i$.

In the simplest case of $N = 2$ there is only one four-point ratio $x \in (0,1)$ defined through (1.51). The two quantities (2.8) and (2.3) coincide and one easily finds that

$$R_{2,n}(x) = \tilde{R}_{2,n}(x) = \frac{\mathcal{F}_{2,n}(x)}{(1-x)^{2\Delta_n}} \,. \tag{2.92}$$

When $N > 2$, first we remark that the non universal constant c_n cancels in the ratio (2.3) and this is found by employing the same combinatorial identity occurring for the cutoff independence of $R_{N,n}$, discussed in the section 2.2. Moreover in (2.3) all the factors $P_p(\sigma_{N,p})$ cancel, namely

$$\prod_{p=1}^{N} \prod_{\sigma_{N,p}} \big[P_p(\sigma_{N,p})\big]^{(-1)^{N-p}} = 1 \,. \tag{2.93}$$

This result can be obtained by writing the l.h.s. as the product of two factors

$$\prod_{p=1}^{N} \prod_{\sigma_{N,p}} \prod_{i \in \sigma_{N,p}} \frac{1}{(v_i - u_i)^{(-1)^{N-p}}} \,, \qquad \prod_{p=1}^{N} \prod_{\sigma_{N,p}} \prod_{\substack{i,j \in \sigma_{N,p} \\ i<j}} \left[\frac{(u_j - u_i)(v_j - v_i)}{(v_j - u_i)(v_i - u_j)} \right]^{(-1)^{N-p}} . \tag{2.94}$$

Then, collecting the different factors, they become respectively

$$\prod_{p=1}^{N} \prod_{i=1}^{N} \frac{1}{(v_i - u_i)^{\xi_p (-1)^{N-p}}} \,, \qquad \prod_{p=1}^{N} \prod_{\substack{i,j=1 \\ i<j}}^{N} \left[\frac{(u_j - u_i)(v_j - v_i)}{(v_j - u_i)(v_i - u_j)} \right]^{\zeta_p (-1)^{N-p}} , \tag{2.95}$$

where we denoted by $\xi_p = \binom{N-1}{p-1}$ the number of choices $\sigma_{N,p}$ containing the i-th interval and by $\zeta_p = \binom{N-2}{p-2}$ the number of $\sigma_{N,p}$'s containing both the i-th and j-th interval. By employing the combinatorial identities $\sum_{p=1}^{N} (-1)^{N-p} \xi_p = 0$ and $\sum_{p=2}^{N} (-1)^{N-p} \zeta_p = 0$ respectively, it is straightforward to conclude that the products in (2.94) are separately equal to 1. Thus, we have that $R_{N,n}(\boldsymbol{x})$ is given by (2.13).

As for the dependence on $\boldsymbol{x}$ of (2.13), let us consider the choice $\sigma_{N,p} = \{i_1, \dots, i_p\}$ of p intervals with $1 < p \leqslant N$, corresponding to the subregion $A_{i_1} \cup \cdots \cup A_{i_p}$ included in A. Then one introduces the map

$$w_{\sigma_{N,p}}(z) = \frac{(u_{i_1} - z)(u_{i_p} - v_{i_p})}{(u_{i_1} - u_{i_p})(z - v_{i_p})} \,, \tag{2.96}$$

which is constructed to send $u_{i_1} \to 0$, $u_{i_p} \to 1$ and $v_{i_p} \to \infty$. When $p = N$, the map (2.96) becomes (1.51). The function $\mathcal{F}_{p,n}(\boldsymbol{x}^{\sigma_{N,p}})$ depends on the $2p-3$ four-point ratios obtained as the images of the remaining endpoints through the map (2.96), namely

$$\mathcal{F}_{p,n}(\boldsymbol{x}^{\sigma_{N,p}}) = \mathcal{F}_{p,n}(w_{\sigma_{N,p}}(v_{i_1}), \dots, w_{\sigma_{N,p}}(v_{i_{p-1}})) \,. \tag{2.97}$$

Since the ratios $w_{\sigma_{N,s}}(u_{i_r})$ and $w_{\sigma_{N,s}}(v_{i_r})$ can be expressed in terms of the four-point ratios in $\boldsymbol{x}$ by applying (1.51), we have that $R_{N,n} = R_{N,n}(\boldsymbol{x})$. The final expression can be checked by considering the limits $x_j \to x_{j\pm1}$, whose result can be understood by using that the first operator occurring in the OPE of a twist field $\mathcal{T}_n$ with $\bar{\mathcal{T}}_n$ is the identity.

We find it useful to write explicitly $R_{N,n}(\boldsymbol{x})$ in the simplest cases. For $N = 3$

$$R_{3,n}(\boldsymbol{x}) = \frac{\mathcal{F}_{3,n}(x_1, x_2, x_3)}{\mathcal{F}_{2,n}(\frac{x_1(x_3-x_2)}{x_2(x_3-x_1)})\,\mathcal{F}_{2,n}(x_1)\,\mathcal{F}_{2,n}(\frac{x_3-x_2}{1-x_2})}\,. \tag{2.98}$$

From this expression (we recall that $\mathcal{F}_{2,n}(0) = \mathcal{F}_{2,n}(1) = 1$), we can check that $R_{3,n} \to 1$ when $x_3 \to x_2$ (i.e. $A_2 \to \emptyset$), which is obtained by using $\mathcal{F}_{3,n}(x_1, x_2, x_3) \to \mathcal{F}_{2,n}(x_1)$, that we checked numerically. In a similar way, we find that $R_{3,n} \to 1$ for $x_1 \to 0$ ($A_1 \to \emptyset$). Notice that we cannot take $A_3 \to \emptyset$ in (2.98) because the map (1.51) with $N = 3$ is not well defined in this limit. We can also consider e.g. $x_2 \to x_1$, i.e. $B_1 \to \emptyset$. In this case we verified that $\mathcal{F}_{3,n}(x_1, x_2, x_3) \to \mathcal{F}_{2,n}(x_3)$, as expected, and this implies that the corresponding limit for $R_{3,n}$ is not 1 identically. Also when $B_2 \to \emptyset$ we find that $R_{3,n}$ does not tend to 1. Indeed, $\mathcal{F}_{3,n}(x_1, x_2, x_3) \to \mathcal{F}_{2,n}(x_1/x_2)$.

When $N = 4$ the elements of $\boldsymbol{x}$ are $x_1, \ldots, x_5$ and $R_{4,n}(\boldsymbol{x})$ reads

$$R_{4,n}(\boldsymbol{x}) = \frac{\mathcal{F}_{4,n}(\boldsymbol{x})\,\prod_{i<j}\mathcal{F}_{2,n}(x^{\{i,j\}})}{\mathcal{F}_{3,n}(\boldsymbol{x}^{\{1,2,3\}})\,\mathcal{F}_{3,n}(\boldsymbol{x}^{\{1,2,4\}})\,\mathcal{F}_{3,n}(\boldsymbol{x}^{\{1,3,4\}})\,\mathcal{F}_{3,n}(\boldsymbol{x}^{\{2,3,4\}})}\,, \tag{2.99}$$

where the terms in the denominators are given by

$$\mathcal{F}_{3,n}(\boldsymbol{x}^{\{1,2,3\}}) = \mathcal{F}_{3,n}\Big(\frac{x_1(x_5-x_4)}{x_4(x_5-x_1)}, \frac{x_2(x_5-x_4)}{x_4(x_5-x_2)}, \frac{x_3(x_5-x_4)}{x_4(x_5-x_3)}\Big), \tag{2.100a}$$

$$\mathcal{F}_{3,n}(\boldsymbol{x}^{\{1,2,4\}}) = \mathcal{F}_{3,n}(x_1, x_2, x_3)\,, \tag{2.100b}$$

$$\mathcal{F}_{3,n}(\boldsymbol{x}^{\{1,3,4\}}) = \mathcal{F}_{3,n}(x_1, x_4, x_5)\,, \tag{2.100c}$$

$$\mathcal{F}_{3,n}(\boldsymbol{x}^{\{2,3,4\}}) = \mathcal{F}_{3,n}\Big(\frac{x_3-x_2}{1-x_2}, \frac{x_4-x_2}{1-x_2}, \frac{x_5-x_2}{1-x_2}\Big). \tag{2.100d}$$

As for the product in the numerator of (2.99), the arguments of the $\mathcal{F}_{2,n}$'s are not multi-component vector and they read

$$\begin{aligned} x^{\{1,2\}} &= \frac{x_1(x_3-x_2)}{x_2(x_3-x_1)}\,, & x^{\{1,3\}} &= \frac{x_1(x_5-x_4)}{x_4(x_5-x_1)}\,, & x^{\{1,4\}} &= x_1\,, \\ x^{\{2,3\}} &= \frac{(x_3-x_2)(x_5-x_4)}{(x_4-x_2)(x_5-x_3)}\,, & x^{\{2,4\}} &= \frac{x_3-x_2}{1-x_2}\,, & x^{\{3,4\}} &= \frac{x_5-x_4}{1-x_4}\,. \end{aligned} \tag{2.101}$$

The expression (2.99) allows us to check explicitly that $R_{4,n} \to 1$ when we send either $x_1 \to 0$ ($A_1 \to \emptyset$) or $x_3 \to x_2$ ($A_2 \to \emptyset$) or $x_5 \to x_4$ ($A_3 \to \emptyset$). In a similar way, we observed numerically that $\mathcal{F}_{4,n}(\boldsymbol{x}) \to \mathcal{F}_{3,n}(x_3, x_4, x_5)$ for $x_2 \to x_1$ ($B_1 \to \emptyset$) and that $\mathcal{F}_{4,n}(\boldsymbol{x}) \to \mathcal{F}_{3,n}(x_1, x_2, x_5)$ for $x_4 \to x_3$ ($B_2 \to \emptyset$). Taking the limit $x_5 \to 1$ ($B_3 \to \emptyset$), we are joining the last two intervals and we find $\mathcal{F}_{4,n}(\boldsymbol{x}) \to \mathcal{F}_{3,n}(x_1/x_4, x_2/x_4, x_3/x_4)$, as expected.

For higher N, more terms occur to deal with, but it is always possible to write explicitly $R_{N,n}(\boldsymbol{x})$ in terms of its $2N-3$ independent variables. The checks given above for the simplest cases of $N = 3$ and $N = 4$ can be generalized, finding that $R_{N,n} \to 1$ when $x_{2k-1} \to x_{2k-2}$ ($A_k \to \emptyset$), for some fixed $k \in \{1, \ldots, N-1\}$ (we recall that $x_0 =$

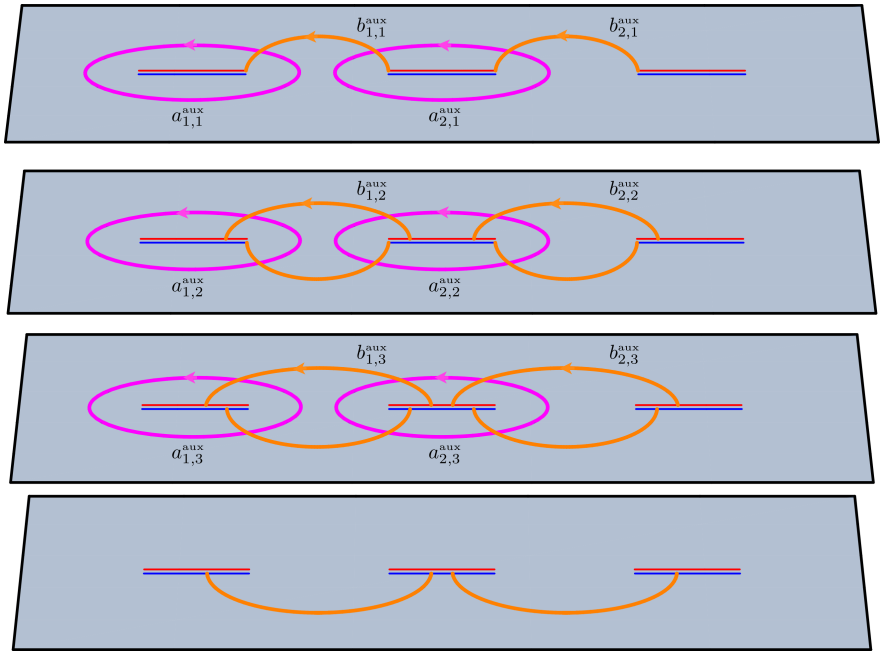

Figure 2.28: The auxiliary cycles $\{a^{\rm aux}_{\alpha,j}, b^{\rm aux}_{\alpha,j}\}$ for $N = 3$ and $n = 4$.

0). The limit $A_N \to \emptyset$ (i.e. $u_N \to v_N$) cannot be considered on $\mathcal{F}_{N,n}(\boldsymbol{x})$ because the map (1.51) is not well defined. We have to compute it before applying (1.51). As for the limit of joining intervals, for $x_{2l} \to x_{2l-1}$ ($B_l \to \emptyset$) with $l \in \{1, \dots, N-2\}$ one finds $\mathcal{F}_{N,n}(\boldsymbol{x}) \to \mathcal{F}_{N-1,n}(\boldsymbol{x} \setminus \{x_{2l-1}, x_{2l}\})$, while for $x_{2N-3} \to 1$ ($B_{N-1} \to \emptyset$) we have $\mathcal{F}_{N,n}(\boldsymbol{x}) \to \mathcal{F}_{N-1,n}(x_1/x_{2N-4}, x_2/x_{2N-4}, \dots, x_{2N-5}/x_{2N-4})$.

2.B Lauricella functions

In this appendix we show that the integrals (2.26a) and (2.26b), occurring in Sec. 2.3.1 and Sec. 2.4.2 for the computation of the period matrices, can be written in terms of the fourth Lauricella function $F_D^{(m)}$ [241], which is a generalization of the hypergeometric function ${}_2F_1$ involving several variables.

The integral representation of $F_D^{(m)}$ for $\mathrm{Re}(c) > \mathrm{Re}(a) > 0$ reads

$$\int_0^1 \frac{t^{a-1}(1-t)^{c-a-1}}{\prod_{j=1}^m (1-y_j t)^{b_j}}\, dt = \frac{\Gamma(a)\,\Gamma(c-a)}{\Gamma(c)}\, F_D^{(m)}(a, b_1, \dots, b_m; c; y_1, \dots, y_m)\,. \tag{2.102}$$

For $m = 1$ the function $F_D^{(m)}$ reduces to the hypergeometric function ${}_2F_1(a, b_1; c; y_1)$ and for $m = 2$ it becomes the Appell function $F_1(a; b_1, b_2; c; y_1, y_2)$. In our problem $m = 2N-3$ and therefore $m \geqslant 3$ for $N > 2$.

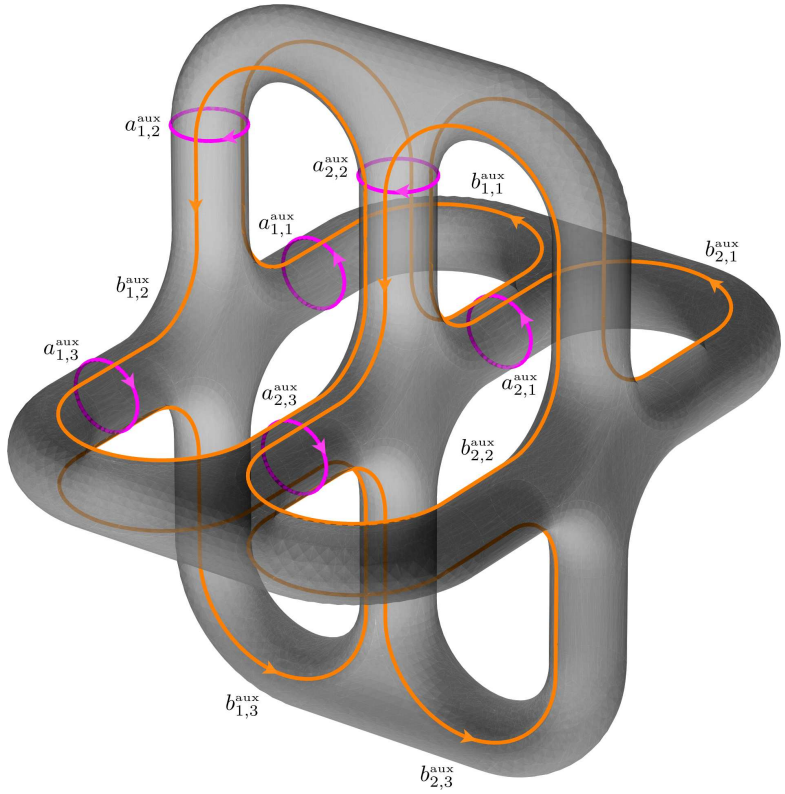

Figure 2.29: The Riemann surface $\mathcal{R}_{3,4}$ with the set of auxiliary cycles $\{a^{\rm aux}_{\alpha,j}, b^{\rm aux}_{\alpha,j}\}$ depicted also in Fig. 2.28.

In terms of the Lauricella function, the integral in (2.26a) for $\alpha = 1$ reads

$$\begin{aligned}\mathscr{I}_{\beta,k}\big|_0^{x_1} = {}& \frac{\Gamma(\beta-k/n)\,\Gamma(k/n)}{\Gamma(\beta)}\, x_1^{\beta-1} \prod_{\gamma=2}^{N-1} x_{2\gamma-2}^{-k/n} \prod_{\lambda=2}^{N-1} x_{2\lambda-1}^{k/n-1} \\ & \times F_D^{(2N-3)}\left(\beta-\frac{k}{n}, \frac{k}{n}, 1-\frac{k}{n}, \ldots, \frac{k}{n}; \beta; \frac{x_1}{x_2}, \frac{x_1}{x_3}, \ldots, \frac{x_1}{x_{2N-2}}\right),\end{aligned} \tag{2.103}$$

where we recall that $x_{2N-2} = 1$ and $1 \leqslant \beta \leqslant N-1$. Also the remaining integrals in (2.26a), which have $\alpha > 1$, can be written through $F_D^{(m)}$

$$\begin{aligned}\mathscr{I}_{\beta,k}\big|_{x_{2\alpha-2}}^{x_{2\alpha-1}} = {}& \frac{\pi}{\sin(\pi k/n)}\, x_{2\alpha-2}^{\beta-1-k/n} \prod_{\substack{\gamma=2 \\ \gamma\neq\alpha}}^{N} |x_{2\gamma-2} - x_{2\alpha-2}|^{-k/n} \prod_{\substack{\lambda=1 \\ \lambda\neq\alpha}}^{N-1} |x_{2\lambda-1} - x_{2\alpha-2}|^{k/n-1} \\ & \times F_D^{(2N-3)}\left(1-\frac{k}{n}, \frac{k}{n}+1-\beta, 1-\frac{k}{n}, \ldots, \frac{k}{n}; 1; \boldsymbol{y}^{(\alpha)}\right),\end{aligned} \tag{2.104}$$

where $\Gamma(1-k/n)\,\Gamma(k/n) = \pi \csc(\pi k/n)$ has been used and we introduced the $2N-3$

dimensional vector $\boldsymbol{y}^{(\alpha)}$, whose elements read

$$y_\zeta^{(\alpha)} \equiv \frac{x_{2\alpha-1}-x_{2\alpha-2}}{x_\zeta - x_{2\alpha-2}}\,, \qquad \zeta \in \{0,1,\dots,2N-2\} \setminus \{2\alpha-2, 2\alpha-1\}\,. \tag{2.105}$$

As for the integrals in (2.26b) for $\alpha \geqslant 1$, in terms of Lauricella functions they become

$$\begin{aligned}\mathscr{I}_{\beta,k}\big|_{x_{2\alpha-1}}^{x_{2\alpha}} = \frac{\pi}{\sin(\pi k/n)}\, x_{2\alpha-1}^{\beta-1-k/n} \prod_{\substack{\gamma=1\\ \gamma\neq\alpha}}^{N} |x_{2\gamma-2}-x_{2\alpha-2}|^{-k/n} \prod_{\substack{\gamma=1\\ \gamma\neq\alpha}}^{N-1} |x_{2\gamma-1}-x_{2\alpha-2}|^{k/n-1} \\ \times F_D^{(2N-3)}\Big(\frac{k}{n}, \frac{k}{n}+1-\beta, 1-\frac{k}{n}, \dots, \frac{k}{n}; 1;\, \boldsymbol{w}^{(\alpha)}\Big),\end{aligned} \tag{2.106}$$

where we defined the $2N-3$ dimensional vector $\boldsymbol{w}^{(\alpha)}$, whose elements are

$$w_\zeta^{(\alpha)} \equiv \frac{x_{2\alpha}-x_{2\alpha-1}}{x_\zeta - x_{2\alpha-1}}\,, \qquad \zeta \in \{0,1,\dots,2N-2\} \setminus \{2\alpha-1, 2\alpha\}\,. \tag{2.107}$$

We remark that both in (2.104) and (2.106) the dots denote the alternating occurrence of k/n and $1-k/n$, like in (2.103). For even n, the case $k/n = 1/2$ occurs and these expressions slightly simplify. In order to realize that (2.103) is (2.104) with $\alpha = 1$, it is more convenient to go back to the original integral representation and set $\alpha = 1$ there.

For $N = 2$ intervals we have only one four-point ratio $x_1 = x \in (0,1)$. Moreover, $\alpha = \beta = 1$ and therefore we have to consider only (2.103) and (2.106), which reduce respectively to

$$\mathscr{I}_{1,k}\big|_0^x = \frac{\pi}{\sin(\pi k/n)}\, F_{k/n}(x)\,, \tag{2.108a}$$

$$\mathscr{I}_{1,k}\big|_x^1 = \frac{\pi}{\sin(\pi k/n)}\, x^{-k/n}\, {}_2F_1\Big(\frac{k}{n}, \frac{k}{n}; 1; \frac{x-1}{x}\Big) = \frac{\pi}{\sin(\pi k/n)}\, F_{k/n}(1-x)\,, \tag{2.108b}$$

being $F_{k/n}$ the hypergeometric function defined in (2.49). In the last step of (2.108b) we have employed the Kummer's relation ${}_2F_1(a,b;c;y) = (1-y)^{-a}\, {}_2F_1(a,c-b;c;y/(y-1))$.

2.C Symmetries of $\mathcal{F}_{N,n}$ as symplectic transformations

In this appendix we discuss some symmetries of $\mathcal{F}_{N,n}$ through the symplectic modular transformations. In App. 2.C.1 we define the group $Sp(2g,\mathbb{Z})$ and its action on the Riemann theta functions, introducing the subset of transformations we are interested in. In App. 2.C.2 we show that $\mathcal{F}_{N,n}$ is invariant under such class of modular transformations, for both the compactified boson and the Ising model, and in App. 2.C.3 we construct the symplectic matrices implementing the cyclic transformation in the sequence of the sheets, the inversion of their order and the exchange $A \leftrightarrow B$.

2.C.1 The symplectic modular group

Let us consider the group $Sp(2g,\mathbb{Z})$ of the integer symplectic matrices, which is also known as symplectic modular group. The generic element $M \in Sp(2g,\mathbb{Z})$ is a $2g \times 2g$ matrix which satisfies

$$M = \begin{pmatrix} D & C \\ B & A \end{pmatrix}, \qquad M^{\mathrm{t}} \cdot J \cdot M = J\,, \qquad J = \begin{pmatrix} 0_g & \mathbb{I}_g \\ -\mathbb{I}_g & 0_g \end{pmatrix}, \tag{2.109}$$

where the $g \times g$ matrices A, B, C and D are made of integers, 0_g is the $g \times g$ matrix whose elements are all equal to zero and $\mathbb{I}_g$ is the identity matrix. The condition in (2.109) on M corresponds to require that $D^{\mathrm{t}} \cdot B$ and $C^{\mathrm{t}} \cdot A$ are symmetric matrices and also $D^{\mathrm{t}} \cdot A - B^{\mathrm{t}} \cdot C = \mathbb{I}_g$.

Under a symplectic transformation, the canonical basis of cycles and the normalized basis of the holomorphic one forms transform respectively as follows

$$\begin{pmatrix} \boldsymbol{a}' \\ \boldsymbol{b}' \end{pmatrix} = M \cdot \begin{pmatrix} \boldsymbol{a} \\ \boldsymbol{b} \end{pmatrix}, \qquad \boldsymbol{\nu}'^{\,\mathrm{t}} = \boldsymbol{\nu}^{\,\mathrm{t}} \cdot (C \cdot \tau + D)^{-1} . \tag{2.110}$$

From the first transformation rule, it is straightforward to observe that a canonical homology basis is sent into another canonical homology basis. Moreover, combining the transformation rules in (2.110), one finds that the period matrix τ' computed through $\boldsymbol{\nu}'$ and the cycles $\boldsymbol{b}'$ is related to τ in (2.21) as follows

$$\tau' = (A \cdot \tau + B) \cdot (C \cdot \tau + D)^{-1} . \tag{2.111}$$

The transformation rule for the absolute value of the Riemann theta function with characteristic defined in (2.47) reads [209–211, 215, 216]

$$\left|\Theta[\boldsymbol{e}'](\mathbf{0}|\tau')\right| = \sqrt{|\det(C \cdot \tau + D)|}\, \left|\Theta[\boldsymbol{e}](\mathbf{0}|\tau)\right| , \tag{2.112}$$

where the characteristic $\boldsymbol{e}'$ is given by

$$\begin{pmatrix} \boldsymbol{\varepsilon}' \\ \boldsymbol{\delta}' \end{pmatrix} = \begin{pmatrix} D & -C \\ -B & A \end{pmatrix} \cdot \begin{pmatrix} \boldsymbol{\varepsilon} \\ \boldsymbol{\delta} \end{pmatrix} + \frac{1}{2} \begin{pmatrix} (C \cdot D^{\mathrm{t}})_{\mathrm{d}} \\ (A \cdot B^{\mathrm{t}})_{\mathrm{d}} \end{pmatrix} , \tag{2.113}$$

where $(\dots)_{\mathrm{d}}$ is the vector made by the diagonal of the matrix within the brackets.

Let us consider the subset of $Sp(2g, \mathbb{Z})$ given by the following matrices

$$\begin{pmatrix} D & 0_g \\ 0_g & (D^{-1})^{\mathrm{t}} \end{pmatrix} , \qquad \begin{pmatrix} 0_g & C \\ -(C^{-1})^{\mathrm{t}} & 0_g \end{pmatrix} . \tag{2.114}$$

Under the transformations of the first kind, the cycles $\boldsymbol{a}'$ ($\boldsymbol{b}'$) are obtained through $\boldsymbol{a}$ ($\boldsymbol{b}$) cycles only; while applying the transformations of the second kind, the cycles $\boldsymbol{a}'$ ($\boldsymbol{b}'$) are combinations of the cycles $\boldsymbol{b}$ ($\boldsymbol{a}$). Moreover, for the transformations (2.114) the relation (2.113) between the characteristics becomes homogenous. In particular, the zero characteristic is mapped into itself and therefore (2.112) becomes

$$\left|\Theta(\mathbf{0}|\tau')\right| = \sqrt{|\det(C \cdot \tau + D)|}\, \left|\Theta(\mathbf{0}|\tau)\right| . \tag{2.115}$$

In the remaining part of this appendix, we will restrict to the transformations (2.114).

2.C.2 Invariance of $\mathcal{F}_{N,n}$

Let us discuss the invariance of $\mathcal{F}_{N,n}(\boldsymbol{x})$ under (2.114) for the free compactified boson. Considering the two expressions in (2.41) which are not explicitly invariant under $\eta \leftrightarrow 1/\eta$, one finds that $\sqrt{\det(\mathcal{I})}\, |\Theta(\mathbf{0}|\tau)|^2$ and $\Theta(\mathbf{0}|\mathrm{i}\eta G)$ (or $\Theta(\mathbf{0}|\mathrm{i}G/\eta)$ equivalently) are separately invariant. The invariance of $\sqrt{\det(\mathcal{I})}\, |\Theta(\mathbf{0}|\tau)|^2$ is easily obtained combining (2.115) and the following relation [211]

$$(\mathcal{I}')^{-1} = (C \cdot \tau^* + D) \cdot \mathcal{I}^{-1} \cdot (C \cdot \tau + D)^{\mathrm{t}} , \tag{2.116}$$

which can be verified starting from (2.111). This allows us to claim that the expression $\mathcal{F}_{N,n}^{\eta\to\infty}(\boldsymbol{x})$ in (2.43), which characterizes the decompactification regime, is invariant under symplectic transformations. As for the invariance $\Theta(\mathbf{0}|\mathrm{i}\eta G)$, first we find it convenient to write G in (2.40) as

$$G = \begin{pmatrix} \tau\cdot\mathcal{I}^{-1}\cdot\tau^* & \tau\cdot\mathcal{I}^{-1} - \mathrm{i}\,\mathbb{I}_g \\ \mathcal{I}^{-1}\cdot\tau^* + \mathrm{i}\,\mathbb{I}_g & \mathcal{I}^{-1} \end{pmatrix}. \tag{2.117}$$

The terms $\pm\mathrm{i}\,\mathbb{I}_g$ in the off diagonal blocks can be dropped because they cancel each others in the exponent of the general term of the series defining $\Theta(\mathbf{0}|\mathrm{i}\eta G)$. Then, we can employ the fact that $\Theta(\mathbf{0}|\mathrm{i}\eta G)$ does not change under simultaneous inversion of the sign for both the off diagonal matrices in G. Considering the exponent of the general term of the series, after some algebra one finds that

$$\begin{aligned} &\begin{pmatrix} \boldsymbol{m}^{\mathrm{t}} & \boldsymbol{n}^{\mathrm{t}} \end{pmatrix}\cdot\begin{pmatrix} \tau'\cdot(\mathcal{I}')^{-1}\cdot\tau^{*\prime} & -\tau'\cdot(\mathcal{I}')^{-1} \\ -(\mathcal{I}')^{-1}\cdot\tau^{*\prime} & (\mathcal{I}')^{-1} \end{pmatrix}\cdot\begin{pmatrix} \boldsymbol{m} \\ \boldsymbol{n} \end{pmatrix} \\ &= \begin{pmatrix} \boldsymbol{m}'^{\mathrm{t}} & \boldsymbol{n}'^{\mathrm{t}} \end{pmatrix}\cdot\begin{pmatrix} \tau\cdot\mathcal{I}^{-1}\cdot\tau^* & -\tau\cdot\mathcal{I}^{-1} \\ -\mathcal{I}^{-1}\cdot\tau^* & \mathcal{I}^{-1} \end{pmatrix}\cdot\begin{pmatrix} \boldsymbol{m}' \\ \boldsymbol{n}' \end{pmatrix}, \end{aligned} \tag{2.118}$$

where $(\mathcal{I}')^{-1}$ is defined in (2.116), τ' in (2.111) and we also introduced

$$\begin{pmatrix} \boldsymbol{m}' \\ \boldsymbol{n}' \end{pmatrix} = M^{-1}\cdot\begin{pmatrix} \boldsymbol{m} \\ \boldsymbol{n} \end{pmatrix}, \qquad M^{-1} = \begin{pmatrix} A^{\mathrm{t}} & -C^{\mathrm{t}} \\ -B^{\mathrm{t}} & D^{\mathrm{t}} \end{pmatrix}. \tag{2.119}$$

The vectors $\boldsymbol{m}'$ and $\boldsymbol{n}'$ are made of integers and they are related to $\boldsymbol{m}$ and $\boldsymbol{n}$ through the inverse M^{-1} of symplectic transformation (2.109), which is also a symplectic matrix. Since also $(\boldsymbol{m}'^{\mathrm{t}}, \boldsymbol{n}'^{\mathrm{t}})$ cover the whole $\mathbb{Z}^{2g}$, we have that $\Theta(\mathbf{0}|\mathrm{i}\eta G)$ is invariant under $Sp(2g,\mathbb{Z})$ for any η.

For the Ising model, we have that $\mathcal{F}_{N,n}^{\text{Ising}}(\boldsymbol{x})$ in (2.81) is invariant under (2.114). Indeed, from (2.112) and (2.115) it is straightforward to conclude that

$$\left|\frac{\Theta[\boldsymbol{e}'](\mathbf{0}|\tau')}{\Theta(\mathbf{0}|\tau')}\right| = \left|\frac{\Theta[\boldsymbol{e}](\mathbf{0}|\tau)}{\Theta(\mathbf{0}|\tau)}\right|. \tag{2.120}$$

Moreover, each term of the sum over the characteristics in (2.81) is sent into a different one (except for $\boldsymbol{e}^{\mathrm{t}} = (\mathbf{0}^{\mathrm{t}}, \mathbf{0}^{\mathrm{t}})$) so that the whole sum is invariant because the net effect of (2.114) is to reshuffle its terms.

2.C.3 Some explicit modular transformations

Cyclic transformation.

As a concrete example of a symmetry written in terms of a symplectic matrix, we consider first the cyclic change in the ordering of the sheets. Indeed, the choice of the first sheet is arbitrary and therefore the period matrix cannot depend on it. This symmetry has been already studied in [228]. It is useful to start from the effect of this transformation on the auxiliary cycles of Figs. 2.28 and 2.29: $a_{\alpha,j}^{\text{aux}} \to a_{\alpha,j+1}^{\text{aux}}$ and $b_{\alpha,j}^{\text{aux}} \to b_{\alpha,j+1}^{\text{aux}}$. Notice that we introduced the cycles $a_{\alpha,n}^{\text{aux}} \equiv a_{\alpha,0}^{\text{aux}}$ and $b_{\alpha,n}^{\text{aux}} \equiv b_{\alpha,0}^{\text{aux}}$, which are not shown in Figs. 2.28 and 2.29, but, given their indices, it is clear how to place them. In particular, considering this enlarged set of auxiliary cycles, we have that $\sum_{j=1}^{n} a_{\alpha,j}^{\text{aux}} = \sum_{j=1}^{n} b_{\alpha,j}^{\text{aux}} = 0$, which allow to write $a_{\alpha,n}^{\text{aux}}$ and $b_{\alpha,n}^{\text{aux}}$ in terms of the other ones. From these relations and (2.23), we find that the canonical homology basis introduced in Sec. 2.3.1 changes as follows

$$a_{\alpha,j} \to a_{\alpha,j+1} \quad j \neq n-1\,, \qquad a_{\alpha,n-1} \to -\sum_{k=1}^{n-1} a_{\alpha,k}\,, \qquad b_{\alpha,j} \to b_{\alpha,j+1} - b_{\alpha,1}\,. \tag{2.121}$$

As for the canonical homology basis defined in Sec. 2.4.2, from (2.54) we have

$$\hat{a}_{\alpha,j} \to \hat{a}_{\alpha,j+1} - \hat{a}_{\alpha,1}\,, \qquad \hat{b}_{\alpha,j} \to \hat{b}_{\alpha,j+1} \quad j \neq n-1\,, \qquad b_{\alpha,n-1} \to -\sum_{k=1}^{n-1} \hat{b}_{\alpha,k}\,. \tag{2.122}$$

Since these transformations do not affect the greek index, their rewriting in a matrix form involves $\mathbb{I}_{N-1}$. In particular, (2.121) and (2.122) become respectively

$$M_{\rm cyc} = \begin{pmatrix} D_{\rm cyc} & 0_{n-1} \\ 0_{n-1} & A_{\rm cyc} \end{pmatrix} \otimes \mathbb{I}_{N-1}\,, \qquad \hat{M}_{\rm cyc} = \begin{pmatrix} \hat{D}_{\rm cyc} & 0_{n-1} \\ 0_{n-1} & \hat{A}_{\rm cyc} \end{pmatrix} \otimes \mathbb{I}_{N-1}\,, \tag{2.123}$$

where

$$\begin{cases} (A_{\rm cyc})_{jk} = \delta_{k-j,1} - \delta_{k,1} \\ (D_{\rm cyc})_{jk} = \delta_{k-j,1} - \delta_{j,n-1} \end{cases}, \qquad \begin{cases} (\hat{A}_{\rm cyc})_{jk} = \delta_{k-j,1} - \delta_{j,n-1} = (D_{\rm cyc})_{jk} \\ (\hat{D}_{\rm cyc})_{jk} = \delta_{k-j,1} - \delta_{k,1} = (A_{\rm cyc})_{jk} \end{cases}. \tag{2.124}$$

Since $A_{\rm cyc} = (D_{\rm cyc}^{-1})^{\rm t}$, we have that $M_{\rm cyc}$ and $\hat{M}_{\rm cyc}$ belong to subset of $Sp(2g,\mathbb{Z})$ defined by the first expression in (2.114). Notice that $(D_{\rm cyc}^{-1})^{\rm t}$ is the matrix given in Eq. (3.28) of [228]. Moreover, we checked that $M_{\rm cyc}^n = \hat{M}_{\rm cyc}^n = \mathbb{I}_{2g}$ and also that $M_{\rm cyc} = M^{-1} \cdot \hat{M}_{\rm cyc} \cdot M$, being M the matrix defined in (2.59), which relates the two canonical homology basis. As for the period matrix, by applying (2.111) for the transformations (2.123), we numerically checked that $\tau'_{\rm cyc}(\boldsymbol{x}) = \tau(\boldsymbol{x})$ and $\hat{\tau}'_{\rm cyc}(\boldsymbol{x}) = \hat{\tau}(\boldsymbol{x})$, as expected.

Inversion.

Another symmetry that we can consider is obtained by taking the sheets in the inverse order. As above, we start from the action of this transformation on the auxiliary cycles, which is $a^{\rm aux}_{\alpha,j} \to -a^{\rm aux}_{\alpha,n-j+1}$ and $b^{\rm aux}_{\alpha,j} \to b^{\rm aux}_{\alpha,n-j}$ (we assume the enlarged set of auxiliary cycles introduced in App. 2.C.3), where the opposite sign has been introduced to preserve the correct intersection number. Then, plugging it into (2.23), one finds that it acts on the canonical homology basis as follows

$$a_{\alpha,1} \to \sum_{k=1}^{n-1} a_{\alpha,k}\,, \qquad a_{\alpha,j} \to -a_{\alpha,n-j+1} \quad j \neq 1\,, \qquad b_{\alpha,j} \to b_{\alpha,1} - b_{\alpha,n-j+1}\,, \tag{2.125}$$

while, from (2.54), we get that the action on the canonical homology basis introduced in Sec. 2.4.2 is simply $\hat{a}_{\alpha,j} \to \hat{a}_{\alpha,n-j}$ and $\hat{b}_{\alpha,j} \to \hat{b}_{\alpha,n-j}$. The corresponding symplectic matrices $M_{\rm inv}$ and $\hat{M}_{\rm inv}$ have the structure of (2.123) with

$$(A_{\rm inv})_{jk} = (D^{\rm t}_{\rm inv})_{jk} = \delta_{k,1} - \delta_{j+k-1,n}\,, \qquad (\hat{A}_{\rm inv})_{jk} = (\hat{D}_{\rm inv})_{jk} = \delta_{j,n-k}\,. \tag{2.126}$$

They are related as $M_{\rm inv} = M^{-1} \cdot \hat{M}_{\rm inv} \cdot M$, with M is given by (2.59), as expected. A transformation very close to the one we are considering has been already studied in [228]. In particular, their Eq. (3.29) is $A^{\rm t}_{\rm inv}$ up to a global minus sign and a cyclic transformation. Since the inversion is involutive, we have $M^2_{\rm inv} = \hat{M}^2_{\rm inv} = \mathbb{I}_{2g}$. As for the period matrix, from (2.111) we numerically find $\tau'_{\rm inv}(\boldsymbol{x}) = -\,\tau^*(\boldsymbol{x})$ and similarly, for the canonical basis of Sec. 2.4.2, we have $\hat{\tau}'_{\rm inv}(\boldsymbol{x}) = -\,\hat{\tau}^*(\boldsymbol{x})$. Since the imaginary part of the period matrix is left invariant, the inversion leaves the period matrix invariant only for $N = 2$ or $n = 2$ [228].

Exchange $A \leftrightarrow B$.

The transformations considered in Appendices 2.C.3 and 2.C.3 do not change the positions of the branch points. This means that $\boldsymbol{x}_{\rm cyc} = \boldsymbol{x}_{\rm inv} = \boldsymbol{x}$. Instead, exchanging $A = \cup_{i=1}^{N} A_1$ with its complement B, we move the intervals and this leads to a change of the four-point ratios $\boldsymbol{x}$.

A way to implement the transformation $A \leftrightarrow B$ is given by

$$\begin{cases} A_i \to B_i \\ B_i \to A_{i+1 \bmod N} \end{cases}, \qquad \begin{cases} u_i \to v_i \\ v_i \to u_{i+1 \bmod N} \end{cases}, \tag{2.127}$$

where $i = 1, \dots, N$. Applying this transformation twice, $A \to A$ and $B \to B$, but their components do not go back to themselves when $N > 2$. Indeed, we have $A_i \to A_{i+2 \bmod N}$ and $B_i \to B_{i+2 \bmod N}$. Moreover, if we give to the intervals A_i and B_i an orientation, the transformation (2.127) does not change it. Indeed, twist fields $\mathcal{T}_n$ are sent into $\bar{\mathcal{T}}_n$ and viceversa. Under (2.127), the components of the vector $\boldsymbol{x}$ change as follows

$$x_\zeta \to 1 - \frac{x_1}{x_{\zeta+1}}, \qquad \zeta = 1, \dots, 2N-3, \tag{2.128}$$

i.e. $\boldsymbol{x} \to \boldsymbol{x}_{\rm ex,1}$, where $(\boldsymbol{x}_{\rm ex,1})_\zeta \equiv 1 - x_1/x_{\zeta+1}$ (we recall that $x_{2N-2} \equiv 1$).
In order to describe the effect of (2.127) on the auxiliary cycles of Figs. 2.28 and 2.29, we find it useful to introduce, besides the $a^{\rm aux}_{\alpha,n}$ and $b^{\rm aux}_{\alpha,n}$ already defined in App. 2.C.3, also the auxiliary cycles $a^{\rm aux}_{N,j}$ and $b^{\rm aux}_{N,j}$, so that $\sum_{\alpha=1}^{N} a^{\rm aux}_{N,j} = \sum_{\alpha=1}^{N} b^{\rm aux}_{N,j} = 0$, where $j = 1, \dots, n$. Considering this enlarged set of auxiliary cycles $\{a^{\rm aux}_{\alpha,j}, b^{\rm aux}_{\alpha,j}\}$ where $\alpha = 1, \dots, N$ and $j = 1, \dots, n$, we find that (2.127) leads to $a^{\rm aux}_{\alpha,j} \to b^{\rm aux}_{\alpha,j}$ and $b^{\rm aux}_{\alpha,j} \to -a^{\rm aux}_{\alpha+1,j+1}$. By employing these relations in (2.23) and (2.54), we find respectively

$$\begin{cases} a_{\alpha,j} \to \sum_{\gamma=1}^{\alpha} (b_{\gamma,j} - b_{\gamma,j+1}) \\ b_{\alpha,j} \to \sum_{k=1}^{j} (a_{\alpha+1,k} - a_{\alpha,k}) \end{cases}, \qquad \begin{cases} \hat{a}_{\alpha,j} \to \sum_{\gamma=1}^{\alpha} \sum_{k=1}^{j} \hat{b}_{\gamma,k} \\ \hat{b}_{\alpha,j} \to -\hat{a}_{\alpha+1,j+1} + \hat{a}_{\alpha+1,j} + \hat{a}_{\alpha,j+1} - \hat{a}_{\alpha,j} \end{cases}, \tag{2.129}$$

which can be written in matrix form respectively as

$$M_{\rm ex,1} = \begin{pmatrix} 0_g & -(I^{\rm up}_{n-1})^{-1} \otimes I^{\rm low}_{N-1} \\ I^{\rm low}_{n-1} \otimes (I^{\rm up}_{N-1})^{-1} & 0_g \end{pmatrix}, \tag{2.130}$$

and

$$\hat{M}_{\rm ex,1} = \begin{pmatrix} 0_g & I^{\rm low}_{n-1} \otimes I^{\rm low}_{N-1} \\ -(I^{\rm up}_{n-1})^{-1} \otimes (I^{\rm up}_{N-1})^{-1} & 0_g \end{pmatrix}. \tag{2.131}$$

Applying (2.111) for this transformation, we find $\tau'_{\rm ex,1}(\boldsymbol{x}) = -\tau^*(\boldsymbol{x}_{\rm ex,1})$ and, for the canonical basis discussed in Sec. 2.4.2, $\hat{\tau}'_{\rm ex,1}(\boldsymbol{x}) = -\hat{\tau}^*(\boldsymbol{x}_{\rm ex,1})$. Given the transformation of the period matrix under the inversion discussed in App. 2.C.3, applying first (2.127) and then the inversion, we get $\tau'_{\rm ex,1}(\boldsymbol{x}) = \tau(\boldsymbol{x}_{\rm ex,1})$ and similarly for the other basis.

Another way to implement $A \leftrightarrow B$ is the following

$$\begin{cases} A_i \to B_{N-i \bmod N} \\ B_i \to A_{N-i \bmod N} \end{cases}, \qquad \begin{cases} u_i \to u_{N-i+1} \\ v_i \to v_{N-i \bmod N} \end{cases}, \tag{2.132}$$

which is an involution for each component A_i and B_i. This map inverts the orientation of all the intervals and it sends a twist field $\mathcal{T}_n$ into another field of the same kind, and similarly for $\bar{\mathcal{T}}_n$. The change induced on $\boldsymbol{x}$ reads

$$x_\zeta \to 1 - x_{2N-2-\zeta} \equiv (\boldsymbol{x}_{\rm ex,2})_\zeta, \qquad \zeta = 1, \dots, 2N-3. \tag{2.133}$$

When $N = 2$, both (2.128) and (2.133) give $x \to 1-x$. The transformation (2.132) acts on the enlarged set of auxiliary cycles described above as $a^{\rm aux}_{\alpha,j} \to b^{\rm aux}_{N-\alpha,j}$ and $b^{\rm aux}_{\alpha,j} \to a^{\rm aux}_{N-\alpha,j+1}$. Through (2.23) and (2.54), this allows us to find respectively

$$\begin{cases} a_{\alpha,j} \to \sum_{\gamma=N-\alpha}^{N-1} (b_{\gamma,j-1} - b_{\gamma,j}) \\ b_{\alpha,j} \to \sum_{k=j}^{n-1} (a_{N-\alpha,k} - a_{N-\alpha-1,k}) \end{cases} , \tag{2.134}$$

and

$$\begin{cases} \hat{a}_{\alpha,j} \to \sum_{\gamma=N-\alpha}^{N-1} \sum_{k=1}^{j} \hat{b}_{\gamma,k} \\ \hat{b}_{\alpha,j} \to \hat{a}_{N-\alpha,j+1} - \hat{a}_{N-\alpha,j} - \hat{a}_{N-\alpha-1,j+1} + \hat{a}_{N-\alpha-1,j} \end{cases} , \tag{2.135}$$

whose expressions in matrix form read

$$M_{\rm ex,2} = \begin{pmatrix} 0_g & -(I^{\rm low}_{n-1})^{-1} \otimes \check{I}^{\rm low}_{N-1} \\ I^{\rm up}_{n-1} \otimes (\check{I}^{\rm up}_{N-1})^{-1} & 0_g \end{pmatrix} , \tag{2.136}$$

and

$$\hat{M}_{\rm ex,2} = \begin{pmatrix} 0_g & I^{\rm low}_{n-1} \otimes \check{I}^{\rm low}_{N-1} \\ -(I^{\rm up}_{n-1})^{-1} \otimes (\check{I}^{\rm low}_{N-1})^{-1} & 0_g \end{pmatrix} , \tag{2.137}$$

where $(\check{I}_{N-1})_{\alpha\beta} \equiv 1$ if $\alpha \geqslant N - \beta$ and $(\check{I}_{N-1})_{\alpha\beta} \equiv 0$ otherwise. As for the change of the period matrix under (2.133), applying the transformation rule (2.111) for (2.136) and (2.137), we find $\tau'_{\rm ex,2}(\boldsymbol{x}) = \tau(\boldsymbol{x}_{\rm ex,2})$ and $\hat{\tau}'_{\rm ex,2}(\boldsymbol{x}) = \hat{\tau}(\boldsymbol{x}_{\rm ex,2})$ respectively.

We remark that, under the transformations considered in this subsection, the ratio within the absolute value in (1.52) is left invariant. Indeed, the cyclic transformation and the inversion do not involve the endpoints of the intervals at all. As for $A \leftrightarrow B$, in the two cases shown above, either the sets $\{u_i, i = 1, \dots, N\}$ and $\{v_i, i = 1, \dots, N\}$ are exchanged or they are mapped into themselves.

2.D Some technical issues on the numerical analysis

In this appendix we discuss some technical issues employed to extract the results of Sec. 2.7.4, performing also some additional analysis. In Appendices 2.D.1 and 2.D.2 we explain how the finite size scaling analysis has been performed by using either one correction or higher order ones, respectively. In App. 2.D.3 we briefly discuss some effects due to the finiteness of the bond dimension.

2.D.1 The exponent in the first correction

Given the large discrepancy between our numerical data for the Ising model and the corresponding CFT predictions, the finite size scaling analysis becomes crucial either to confirm or to discard them. As discussed in Sec. 2.7.4, we numerically study $\mathrm{Tr}\,\rho_A^2$ when A is made by three or four disjoint intervals by considering $\mathcal{F}_{3,2}$, $R_{3,2}$ and $\mathcal{F}_{4,2}$.

The first step in the finite size scaling analysis is the determination of the exponents of the corrections. To this aim, we start by taking only one correction into account. Since we usually have only few numerical points for a fixed value of $\boldsymbol{x}$, let us focus on those $\boldsymbol{x}$'s with several of them coming from different values of χ. For these $\boldsymbol{x}$'s, which correspond to different α's, we fit the numerical data for $\mathcal{F}_{3,2}$, $R_{3,2}$ and $\mathcal{F}_{4,2}$ by using the function $a_0 + b_0/\ell^{\Delta_{\rm num}}$, which has three parameters to determine. Changing the ranges of variation for ℓ, we can check the stability of the results and also find an estimate of the error for

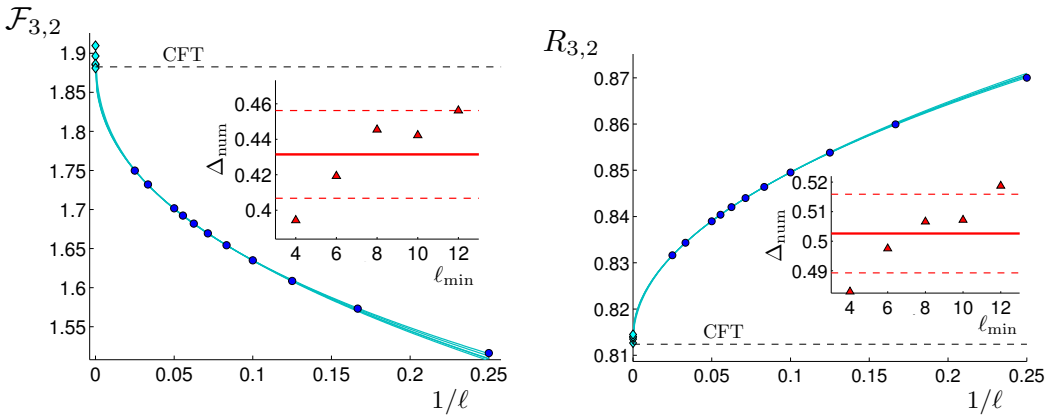

Figure 2.30: Leading corrections to the scaling of $\mathcal{F}_{3,2}$ (left) and $R_{3,2}$ (right) for the special case of $\alpha = 0.5$ and $x_1 = 0.146$ (see top right of Figs. 2.25 and 2.26), computed as explained in App. 2.D.1. In the inset we show the mean value of $\Delta_{\rm num}$ and the error bars, obtained by fitting the data with the highest values of ℓ, starting from $\ell_{\rm min}$. Each fit provides a curve in the plot. The extrapolated values are show as cyan diamonds.

the fitting process (see Fig. 2.30 for a typical example). The results for $\Delta_{\rm num}$ are shown in Fig. 2.31: starting from the top left in clockwise direction, we find $\Delta_{\rm num} = 0.45(5)$, $\Delta_{\rm num} = 0.51(4)$ and $\Delta_{\rm num} = 0.45(5)$ for $\mathcal{F}_{3,2}$, $R_{3,2}$ and $\mathcal{F}_{4,2}$ respectively. In this analysis the CFT formulas have not been used. Notice that it is non trivial that $\Delta_{\rm num}$ does not depend on $\boldsymbol{x}$. Our results are consistent with $\Delta_{\rm num} = 1/2$ found for $N = 2$ [220, 222] and they show that it holds also for $N > 2$.

The values of $\Delta_{\rm num}$ just given have been used in (2.89) to find the extrapolated points in Figs. 2.25, 2.26 and 2.27. Thus, for each $\boldsymbol{x}$, now there are two parameters to fit. Notice that we have not employed the CFT formula yet.

In Fig. 2.32 we plot the difference between the numerical data and the CFT prediction in log-log scale, in order to visualize the leading correction. All the data lie on parallel lines whose slope is close to the one expected from the two intervals case.

2.D.2 A finite size scaling analysis with higher order corrections

Instead of considering only one correction as discussed in Sec. 2.7.4 and App. 2.D.1, one can try to perform a finite size scaling analysis which includes more corrections [136, 220, 222, 223, 261, 262]. In particular, we choose the following function

$$a_0 + \frac{b_1}{\ell^{1/2}} + \frac{b_2}{\ell} + \frac{b_3}{\ell^{3/2}} \,. \tag{2.138}$$

The exponents are the ones giving agreement with the CFT predictions for $N = 2$ [136]. Since in this case we have four parameters to fit, we can carry out this analysis only for few $\boldsymbol{x}$'s at fixed α. We have considered the same configurations of Sec. 2.7.4, namely $\alpha = p$ and $\alpha = 1/p$ with $1 \leqslant p \leqslant 8$ finding the same qualitative behavior. Here we give only one representative example in Fig 2.33 for $\mathcal{F}_{3,2}$ and in Fig 2.34 for $R_{3,2}$. The error bars have been determined by choosing different minimum values for ℓ in the fitting procedure, as done for $\Delta_{\rm num}$ in App. 2.D.1.

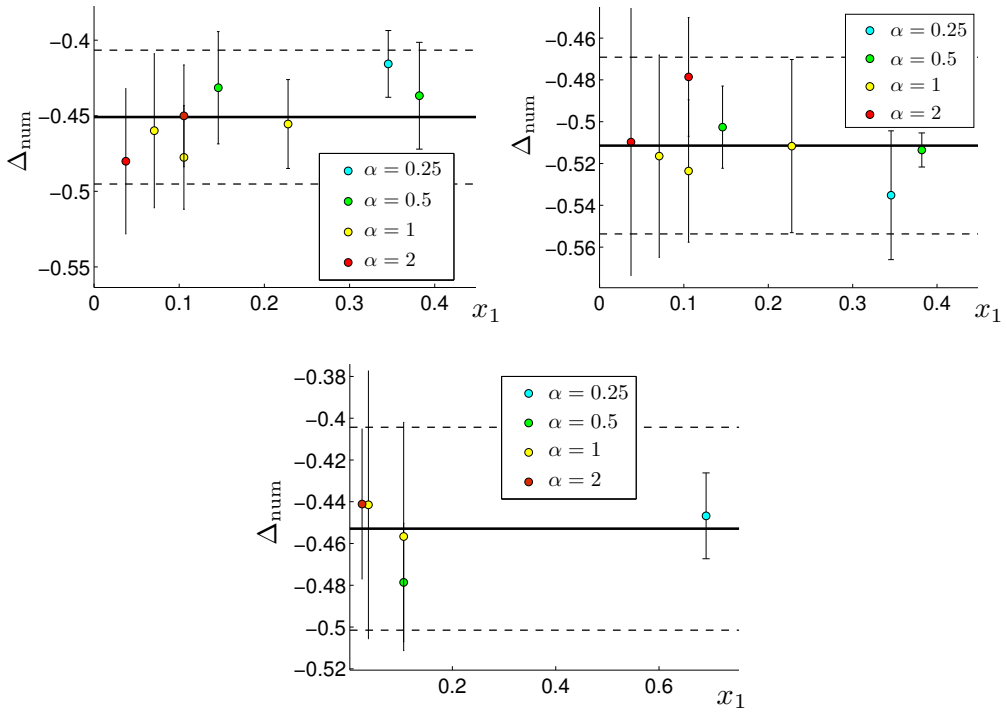

Figure 2.31: The value of the exponent $\Delta_{\rm num}$ obtained from the numerical values of $\mathcal{F}_{3,2}$, $R_{3,2}$ and $\mathcal{F}_{4,2}$ (clockwise direction, starting from the top left). The values of x_1 correspond to the ones where several numerical points are available (see Figs. 2.25, 2.26 and 2.27 respectively). The error bars are obtained by changing the number of numerical points in the fit (see Fig. 2.30).

It is instructive to analyze the contribution of the various corrections. Taking only the first correction into account (cyan circles in Figs. 2.33 and 2.34), the extrapolated points are very close to the curves predicted by the CFT. Nevertheless, they do not coincide with it, staying systematically below for $\mathcal{F}_{N,2}$ or above for $R_{N,2}$. Adding the second correction, i.e. $b_1 \neq 0$ and $b_2 \neq 0$ in (2.138), the extrapolations (green circles in Figs. 2.33 and 2.34) usually improve, as expected, getting closer to the CFT prediction and, in some case, coinciding with it. As for the third correction, we notice that it does not improve the extrapolation in almost all the cases that we studied. This probably tells us that the range of ℓ available allows us to see at most two corrections to the scaling. As for the sign of the coefficients b_1, b_2 and b_3 in (2.138), we find $(-,+,+)$ for $\mathcal{F}_{3,2}$ and $(+,-,+)$ for $R_{3,2}$. Notice that the sign of b_1 can be easily inferred from the position of the numerical points with respect to the CFT curve. For instance, since for $R_{3,2}$ they are all above the theoretical curve, we have that $b_1 > 0$ in this case.

2.D.3 On the finiteness of the bond dimension

Tensor networks, which include the MPS as a subclass, are variational approximations whose accuracy strongly depends on the bond dimension χ. In principle, one would like to have access to the regime of $\chi \to \infty$ but, being the computational cost an increasing function of χ, the results are always obtained for finite χ.

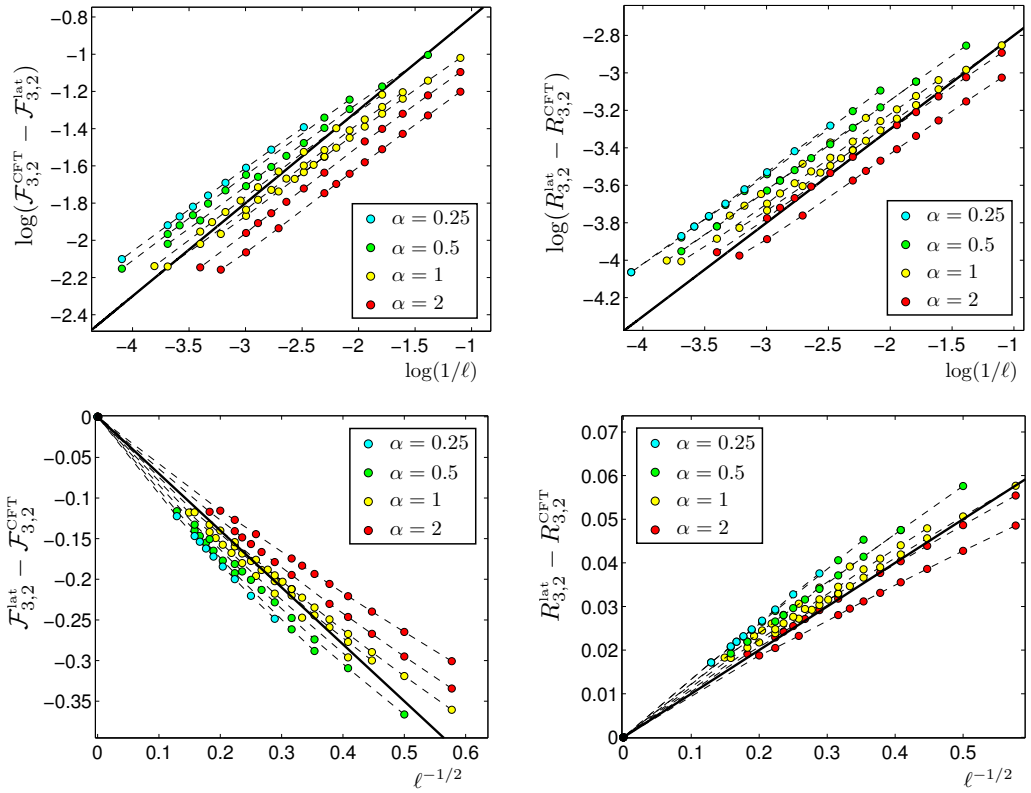

Figure 2.32: Difference between the numerical data and the CFT prediction for $\mathcal{F}_{3,2}$ (left) and $R_{3,2}$ (right). The black solid line corresponds to $\Delta = 1/2$ for the exponent of the leading correction, which is the value expected from CFT arguments. In the upper panels the results are shown in logarithmic scales in order to appreciate the fact that, joining the data having the same $\boldsymbol{x}$, we find almost straight lines having nearly the same slope.

The MPS are finitely correlated state, which means that they naturally describe systems where either the correlations do not decay or they decay exponentially at large distance [265]. The two cases are distinguished by the ratio $e_2/e_1 \leqslant 1$ between the two largest eigenvalues e_1 and e_2 of the MPS transfer matrix E. In particular, if $e_2 < e_1$, the finite correlation length of the MPS is $\xi_{\rm MPS} \equiv 1/\log(e_1/e_2)$, while, when $e_2 = e_1$, the correlation function (2.85) is constant as a function of r (long range order).

The finite size of a critical system naturally induces a finite correlation length $\xi_L \propto L$. Thus, the MPS representation can still be used to perform accurate finite size scaling analysis [250] and one would expect that a good MPS approximation has $\xi_{\rm MPS} = \xi_L$. However, it has been found that, when χ is too small, the best approximation of a critical system through a MPS with finite χ has a finite correlation length $\xi_{\rm MPS} = \xi_\chi \propto \chi^\kappa$ [36]. In order to get $\xi_{\rm MPS} = \xi_L$, one needs to increase χ. Since ξ_L enters in the scaling of the two point correlation functions for critical systems, a useful criterion is obtained by considering [37, 256]

$$\chi^* = \min\left\{\chi \,|\, \xi_\chi > L/2\right\}. \tag{2.139}$$

However, notice that this result has been found by considering the two point functions

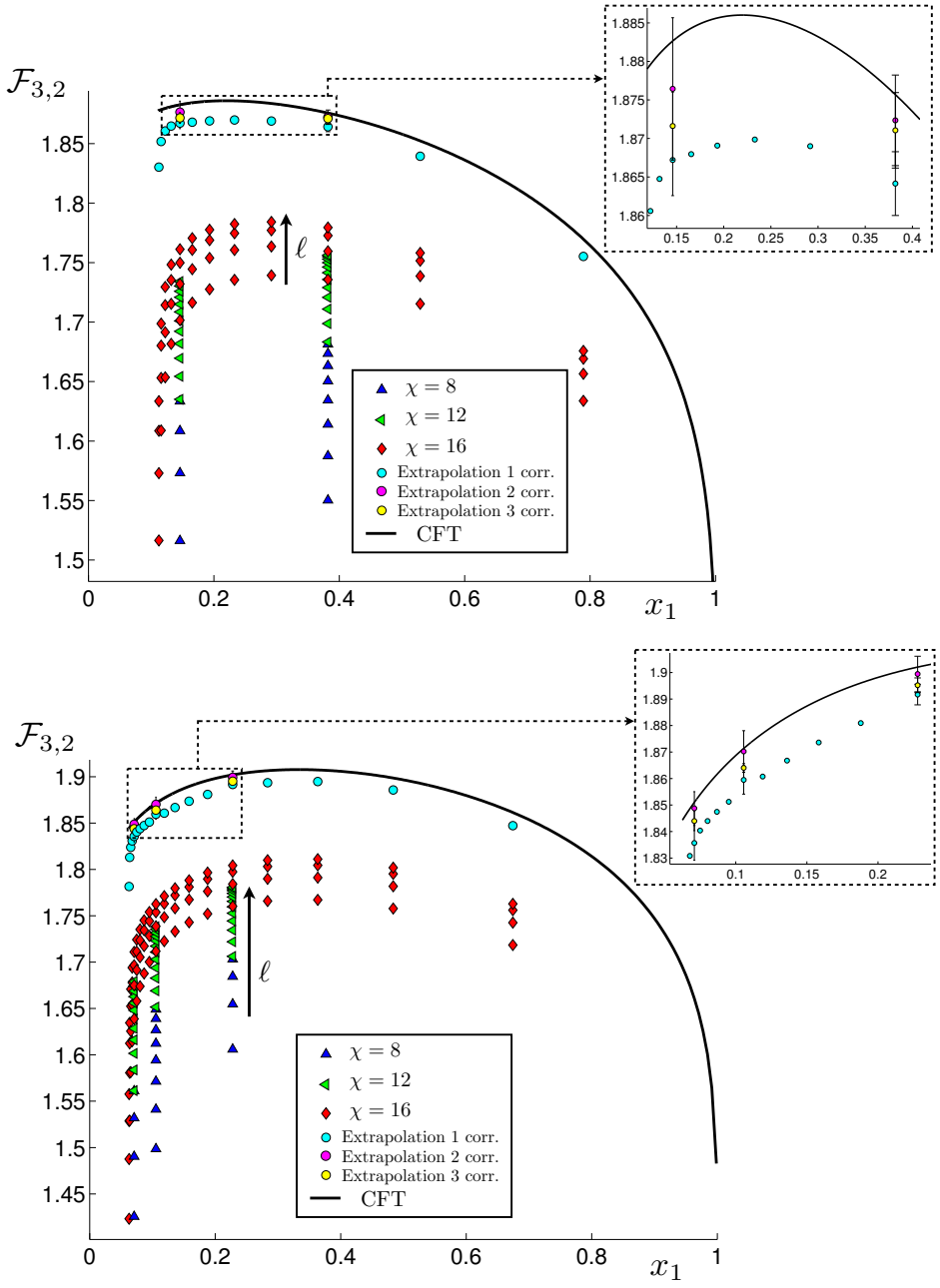

Figure 2.33: Finite size scaling analysis with higher order corrections for $\mathcal{F}_{3,2}$ for the configurations characterized by $\alpha = 0.5$ (top) and $\alpha = 1$ (bottom). The method is explained in App. 2.D.2. Three corrections can be taken into account only for those $\boldsymbol{x}$'s having several numerical points, as shown in the zoom. The third correction never improves the agreement with the CFT prediction.

of local operators, while in our problem both non local operators (whose support is of order ξ_χ) and $2N \geqslant 4$ point functions are involved. In our numerical analysis we have

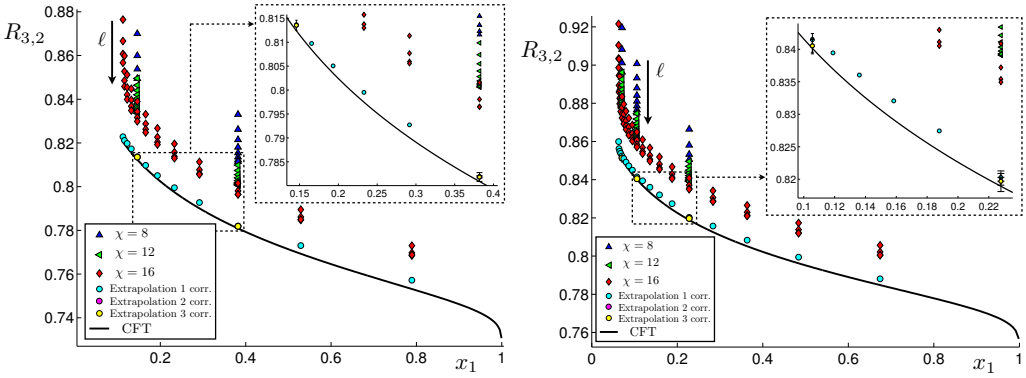

Figure 2.34: Finite size scaling analysis with higher order corrections for $R_{3,2}$ for the configurations characterized by $\alpha = 0.5$ (left) and $\alpha = 1$ (right). The method is explained in App. 2.D.2. Three corrections can be taken into account only for those $\boldsymbol{x}$'s having several numerical points, as shown in the zoom. The third correction never improves the agreement with the CFT prediction.

adopted the criterion (2.139) and, indeed, we find that sometimes it fails. For instance, this happens in Fig. 2.35 whenever a deviation from the straight lines occurs. We have taken this failure into account by discarding from the numerical analysis the points deviating from the straight lines. Being (2.139) too optimistic for our computations, the criterion

$$\chi^* = \min \{ \chi \,|\, \xi_\chi > L \} \tag{2.140}$$

should be enough to avoid deviations from the expected power law decay and should be implemented in future studies.

2.E More details on the numerical extrapolation

2.E.1 Checks with some existing data

In this appendix, we employ the numerical extrapolation based on rational interpolating functions to analytically continue the analytical results available for the Rényi entropies, and we check the result with available numerical data on the lattice. We will focus on the compactified boson and on the Ising model. The former describes the scaling limit of the XXZ chain for some values of the parameters, while the latter describes the scaling limit of the critical Ising spin chain.

We begin our analysis comparing the results of the XXZ chain and the compactified boson for $N = 2$ intervals. The Hamiltonian of the periodic XXZ spin 1/2 chain in a magnetic field h reads [266]

$$H_{\text{XXZ}} \equiv \sum_{j=1}^{L} \left(S_j^x S_{j+1}^x + S_j^y S_{j+1}^y + \Delta \, S_j^z S_{j+1}^z \right) - h \sum_{j=1}^{L} S_j^z \,, \tag{2.141}$$

where $S_j^a = \sigma_j^a / 2$, being σ_j^a the standard Pauli matrices acting on the spin at the j-th site. The chain has L sites and Δ is the anisotropy. The mutual information for this lattice model has been computed in [219] by direct diagonalization for $L \leqslant 30$. When $h = 0$ and $-1 < \Delta \leqslant 1$ the model in the continuum is described by the $c = 1$ compact boson with

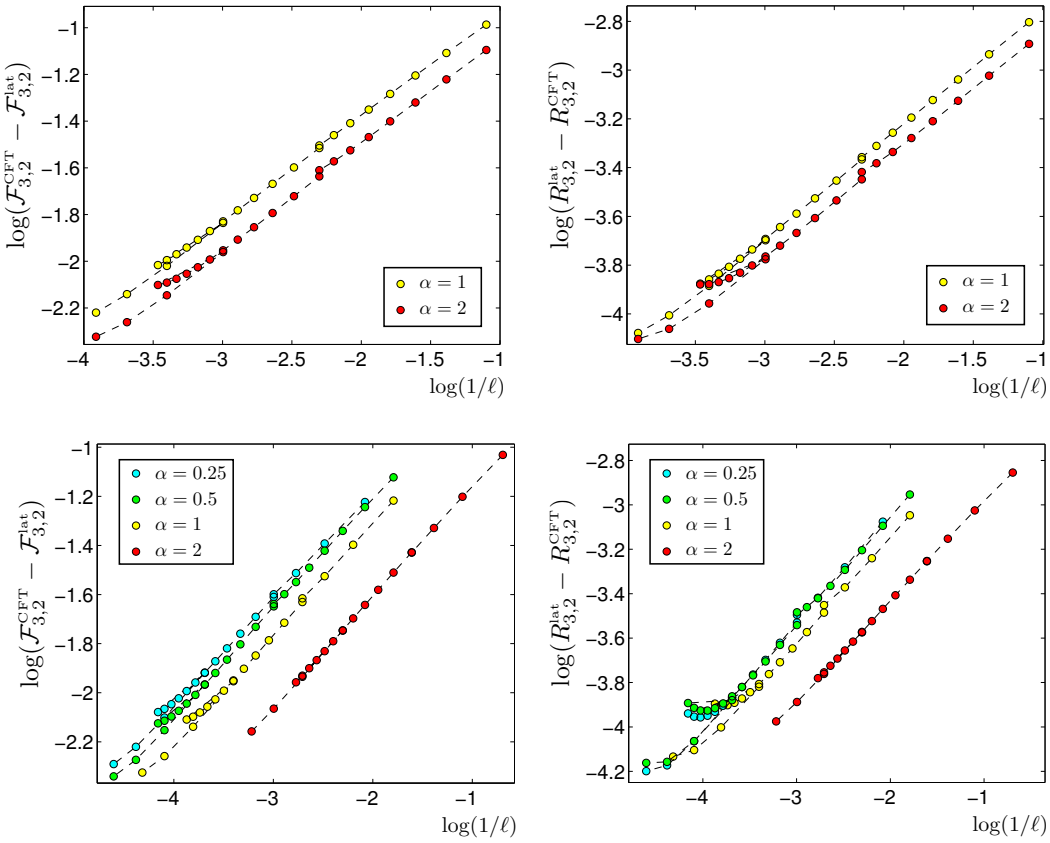

Figure 2.35: Effects of the finite bond dimension leading to deviations from the power law decays are shown for $\mathcal{F}_{3,2}$ (left) and $R_{3,2}$ (right). In the top panels $x_1 = 0.106$. For fixed ℓ, the deviation from the straight line is more evident for points with larger d ($\alpha = 2$). In the bottom panels we have: $x_1 = 0.345$ ($\alpha = 0.25$), $x_1 = 0.382$ ($\alpha = 0.5$), $x_1 = 0.228$ ($\alpha = 1$) and $x_1 = 0.037$ ($\alpha = 2$). For small values of α, regimes of large ℓ can be considered, where deviations may also occur. The points deviating from the straight line have been discarded from the numerical analysis.

$\eta = 1 - (1/\pi) \arccos \Delta$, while for $h \neq 0$ an explicit formula providing η does not exist and therefore it must be found numerically.

The mutual information of the compactified boson is not known, but we can compute analytically the Rényi mutal information as follows

$$I^{(n)}_{A_1,A_2} = -\frac{(n+1)c}{6n}\,\log(1-x) + \tilde{I}_n(x)\,, \qquad \tilde{I}_n(x) \equiv \frac{1}{n-1}\log[\mathcal{F}_{2,n}(x)]\,, \tag{2.142}$$

where we introduced $\tilde{I}_n$, and

$$\mathcal{F}_{2,n}(x) = \frac{\Theta(\eta\tau_2)\,\Theta(\tau_2/\eta)}{\Theta(\tau_2)^2}\,, \tag{2.143}$$

for any positive integer $n \geqslant 2$, with τ_2 defined in Eq. (2.51). Since the mutual information I_{A_1,A_2} is the limit $n \to 1$ of (2.142), it is given by

$$I_{A_1,A_2} = -\frac{c}{3}\,\log(1-x) + \tilde{I}_1(x)\,, \qquad \tilde{I}_1(x) \equiv \partial_n \mathcal{F}_{2,n}(x)\big|_{n=1}\,. \tag{2.144}$$

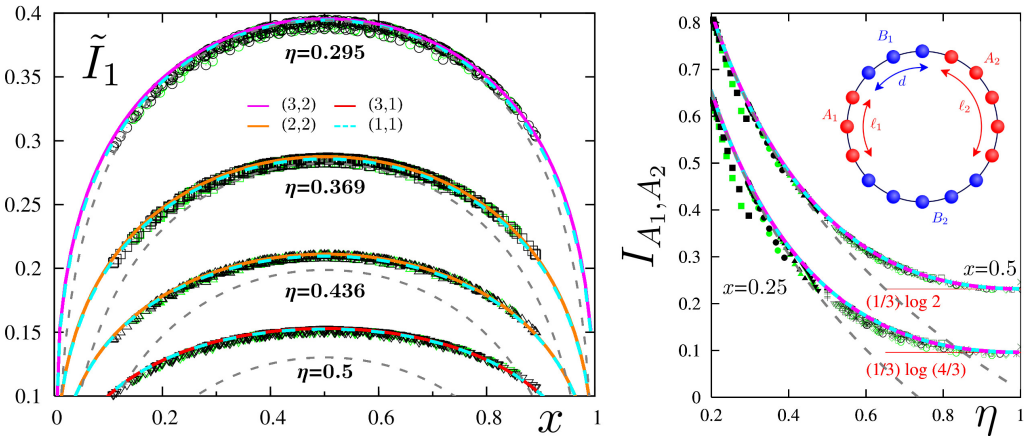

Figure 2.36: Mutual information for the XXZ model. The data points are extracted from [219] and the coloured curves are obtained from the rational interpolations of the analytic expressions (2.142) and (2.143) for the compact boson with the values of (p, q) indicated in the left panel. The dashed grey lines correspond to the decompactification regime, where the analytic continuation is known [226]. Left: $\tilde{I}_1$, defined in (2.144), as function of x for various values of η. Right: the mutual information I_{A_1,A_2} as function of η for two fixed values of x.

The corresponding analytic continuation to $n = 1$ is estimated by performing a numerical extrapolation of the known data through a rational function. We have already discussed in the text that we can have access only to a finite number of Rényis, due to the complications in numerically evaluating the Riemann theta functions for large matrices. Given the computational resources at our disposal, for the compactified boson we can obtain data for $2 \leqslant n \leqslant 11$ and therefore we could use rational functions with $p + q + 1 \leqslant 10$.

In Fig. 2.36 we compared our numerical extrapolations of the analytic expressions of [226] with the numerical data for the XXZ spin chain computed in [219] by exact diagonalization, finding a very good agreement. In the left panel $\tilde{I}_1$ is shown as function of the four-point ratio x for different values of the parameter η, while in the right panel the mutual information I_{A_1,A_2} is shown as function of η for the two fixed configurations of intervals given by $\ell_1 = \ell_2 = d_1 = d_2 = L/4$ ($x = 0.5$) and $2\ell_1 = 2\ell_2 = d_1 = d_2 = L/3$ ($x = 0.25$), being L the total length of the periodic system. All the rational interpolations in the figure exhibit a good agreement with the numerical data, despite the low values of p and q. Increasing these parameters, a better approximation is expected but the result is already stable for these values and we provided two rational interpolations for each curve as a check. Some rational interpolations may display some spurious bahaviour in some regimes of x. As discussed in detail in Sec. 2.E.2, this possibility increases with q. These results have been discarded and we showed only rational interpolations which are well-behaved in the whole domain $x \in (0, 1)$. Notice that rational interpolations that are well-behaved for some values of η and x could display some bad behaviour for other values. Thus, the values of (p, q) must be chosen case by case. In Fig. 2.36 the dashed grey lines are obtained from the analytic continuationfound in [226], which corresponds to the decompactification regime and therefore it reproduces the numerical data from the XXZ chain and from the rational interpolations only for small η, as expected.

Another important case where the Rényi entropies of two disjoint intervals have been found analytically is the Ising model [196]. The Hamiltonian of the one dimensional spin

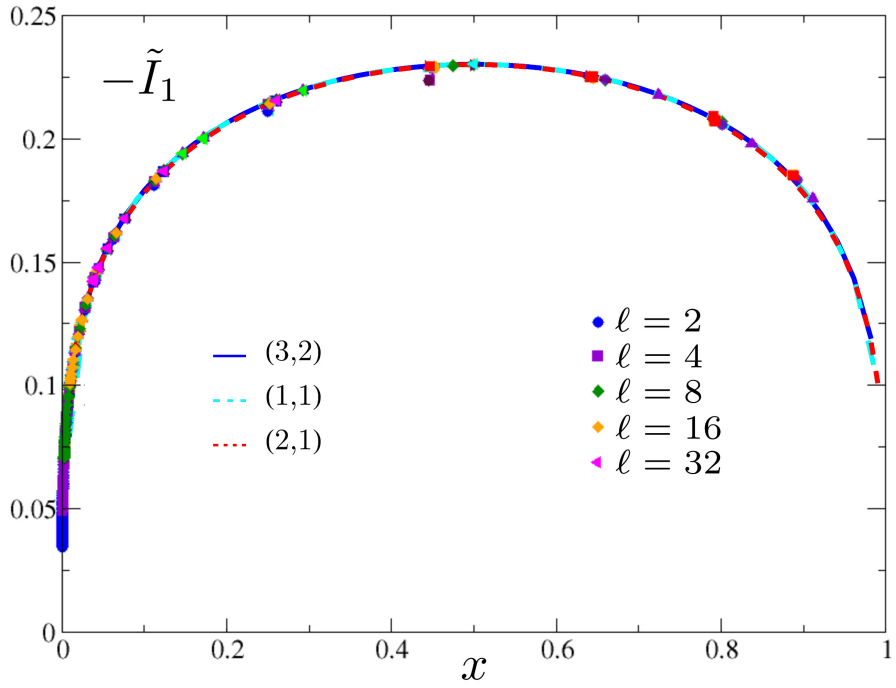

Figure 2.37: Extrapolations for $-\tilde{I}_1$, defined in (2.144), as function of x for the Ising model. The data points are extracted from [220] while the coloured curves are obtained through the rational interpolations with (p, q) indicated.

chain defining the Ising model in a transverse field is Eq. (2.80), where periodic boundary conditions are imposed. This model has a quantum critical point at $h = 1$ and in the continuum it is a free Majorana fermion with central charge $c = 1/2$. The Rényi entropies for two disjoint intervals on the Ising spin chain have been studied in [220] through a TTN algorithm [246] and in [222] through the exact solution of the model in terms of free Majorana fermions. The former method allowed to find also the mutual information.

As for the Rényi entropies for two disjoint intervals in the corresponding CFT, by employing known results about bosonization on higher genus Riemann surfaces for $c = 1$ models [207, 208, 210–214], the expression of $\mathcal{F}_{2,n}(x)$, Eq. (2.53), was found in [196]. It is a sum of Riemann theta functions evaluated for the period matrix τ_2 in (2.51). Finally, the mutual information for the Ising model is (2.144). Similarly to the case of the compact boson, also for the Ising model we are not able to compute $\tilde{I}_1(x)$ analytically and therefore we perform a numerical extrapolation through the rational interpolation method described in Sec. 2.E.2.

In Fig. 2.37 we show $-\tilde{I}_1(x)$ as function of $x \in (0, 1)$, which can be found by considering two disjoint intervals of equal length, and compare the numerical data obtained in [220] with the curve found through the numerical extrapolation performed with a rational interpolating function. Even if the Riemann theta functions in (2.53) depend on a matrix of size $g \times g$, unfortunately we cannot consider high values for n. Indeed, besides the problem of computing the Riemann theta function numerically for large period matrices, the additional obstacle occurring for the Ising model is that the number of elements in the sum (2.53) grows exponentially with n. Given our computational power, we have

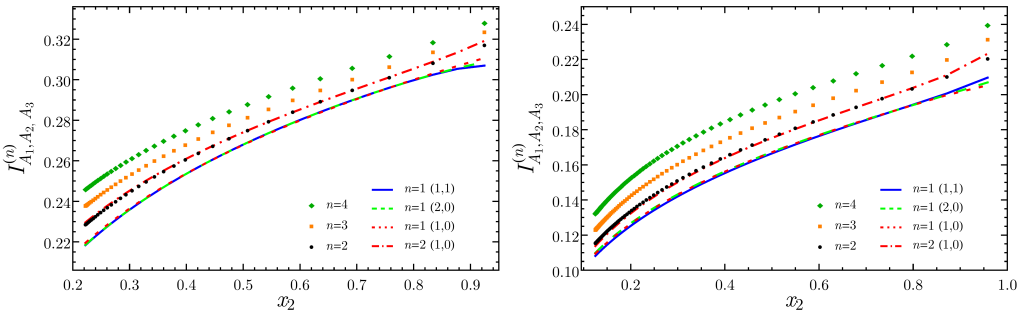

Figure 2.38: Extrapolations of I_{A_1,A_2,A_3}, defined in (2.7a), for the Ising model. Two configurations of intervals have been considered, namely (2.145) with $\alpha = 0.25$ (left) and $\alpha = 2$ (right). The dots correspond to $I^{(n)}_{A_1,A_2,A_3}$ in (2.5) with $n \in \{2,3,4\}$ while the lines are the extrapolations obtained through the rational interpolation method with the values of (p,q) indicated. The dot-dashed line is the extrapolation to $n = 2$ performed as a check of the method, while the remaining lines correspond to I_{A_1,A_2,A_3}.

computed the Rényi entropies up to $n = 7$ and in Fig. 2.37 we show the rational interpolations found by choosing three different pairs (p,q) which are well-behaved among the available ones. Since the curves coincide, the final result is quite stable and, moreover, the agreement with the numerical data found in [220] through the TTN is very good.

We conclude this appendix showing some results for I_{A_1,A_2,A_3} for the Ising model, defined in Eq. (2.7a), obtained by numerically interpolating the analytic results for $I^{(n)}_{A_1,a_2,A_3}$, Eq. (2.5). The results can be found in Fig. 2.38, where we have considered the following configurations of three intervals specified by a parameter α (see Fig. 2.9 for the notation)

$$\text{(d)} \qquad \ell_i = \ell,\ d_1 = d_2 = \alpha\ell,\ d_3 = L - (3+2\alpha)\ell\,. \tag{2.145}$$

In particular, the results in Fig. 2.38 correspond to $\alpha = 0.25$ (left panel) and $\alpha = 2$ (right panel), where the dots denote the values of $I^{(n)}_{A_1,A_2,A_3}$ for $n \in \{2,3,4\}$. Unfortunately, with the computational resources at our disposal, we could not compute Rényi entropies for higher values of n. Given the few n's available, only few rational interpolations can be employed to approximate the analytic continuation to $n = 1$ and they are depicted in Fig. 2.38 through solid and dashed lines (in general we never use $(p,q) = (0,1)$ because it is often not well-behaved).

It is interesting to observe that the three different rational interpolations provide the same extrapolation to $n = 1$ for a large range of x_2 (they differ when x_2 is close to 1). Since, to our knowledge, numerical results about I_{A_1,A_2,A_3} for the Ising model are not available in the literature, the curves in Fig. 2.38 are predictions that would be interesting to test through other methods. We remark that we are not guaranteed that this extrapolation method provides the correct analytic continuation. Nevertheless, the fact that extrapolations with different values of (p,q) give very close outputs is a strong indication that the result should be trusted, assuming that no singularities occurs for real n between 1 and the maximum value of n employed in the extrapolations. Another check of the reliability of the numerical method is the following: we have performed rational interpolations considering only $n \in \{3,4\}$ to extrapolate the value at $n = 2$, which is known analytically. Since only two points are available, only the rational interpolation with $(p,q) = (1,0)$ can be done, which is given by the dot-dashed curve in Fig. 2.38.

Despite the roughness of the extrapolation due to the few input points, the agreement with the expected values computed with the analytic expression (black dots) is very good.

2.E.2 Some technical details

In this appendix we discuss the numerical method that we have employed in sec. 2.6, which is based on rational interpolations, and the issues that may be encountered while addressing the replica limit for the entanglement entropy. Its use in this context has been first suggested in [152].

The rational interpolation method consists in constructing a rational function on the real axis which interpolates a finite set of given points labeled by a discrete variable. The extrapolation is simply obtained by evaluating the rational function obtained in the desired value of the variable.

For the quantities we are interested in, the discrete variable is an integer number n. As a working example, let us consider the case of two disjoint intervals, where the variable $x \in (0,1)$ characterizes the configuration of intervals. For any integer $n \geqslant 2$ we have a real function of x and typically we have access only to $n \leqslant n_{\max}$ for computational difficulties. The rational function interpolating the given data reads

$$W^{(n)}_{(p,q)}(x) \equiv \frac{P(x;n)}{Q(x;n)} \equiv \frac{a_0(x) + a_1(x)n + a_2(x)n^2 + \cdots + a_p(x)n^p}{b_0(x) + b_1(x)n + b_2(x)n^2 + \cdots + b_q(x)n^q}\,, \tag{2.146}$$

being $p \equiv \deg(P)$ and $q \equiv \deg(Q)$ the degrees of the numerator and of the denominator respectively as polynomials in n. The extrapolations are performed pointwise in the domain $x \in (0,1)$. Thus, for any given $x \in (0,1)$, in (2.146) we have $p+q+2$ coefficients to determine. Nevertheless, since we can divide both numerator and denominator by the same number, we can fix $b_0(x) = 1$, and the number of independent parameters to find is $p+q+1$. Once the coefficients in (2.146) have been found, the extrapolation is easily done by considering n real and setting it to the needed value. It is important to stress that, having access only to a limited number m of data points, we can only perform rational interpolations whose degrees (p,q) are such that $p+q+1 \leqslant m$. This method is implemented in *Wolfram Mathematica* through the *Function Approximations* package and the command *RationalInterpolation*.

In Fig. 2.39 we consider an explicit example where we extrapolate the $\tilde{I}_1(x)$ in (2.144) of the compact boson ($c = 1$) for a particular value of the compactification radius corresponding to $\eta = 0.295$ (see also Fig 2.36). For $n \geqslant 2$ the analytic expressions are (2.142) and (2.143) and we take into account $2 \leqslant n \leqslant 6$ only (in Fig. 2.36 we employ also $n = 7$). Given these data, we can perform rational interpolations with $p+q+1 \leqslant 5$. The blue curve in Fig. 2.39 is the extrapolation to $n = 1$ of the rational interpolation with $(p,q) = (2,2)$. We find it instructive to describe the details for a specific value of x. Let us consider, for instance, a configuration corresponding to $x = \tilde{x} \equiv 0.2101$ (see the dashed rectangle in Fig. 2.39). First one has to compute the rational interpolation with $(p,q) = (2,2)$, then the limit $n \to 1$ must be taken. For these two steps, we find respectively

$$W^{n}_{(2,2)}(\tilde{x}) = \frac{0.358 - 0.480\,n + 3.689\,n^2}{1 + 1.347\,n + 7.870\,n^2}\,, \qquad \lim_{n\to 1} W^{n}_{(2,2)}(\tilde{x}) = 0.349\,. \tag{2.147}$$

In the inset of Fig. 2.39 we show how adding more data improves the final extrapolation and how it becomes stable. Focusing again on $x = \tilde{x}$, we can start by taking only $n \in \{2,3\}$, which allow to perform a rational interpolation with $(p,q) = (1,0)$ (a line). Since rational interpolations having $p = 0$ often provide wrong predictions, we prefer

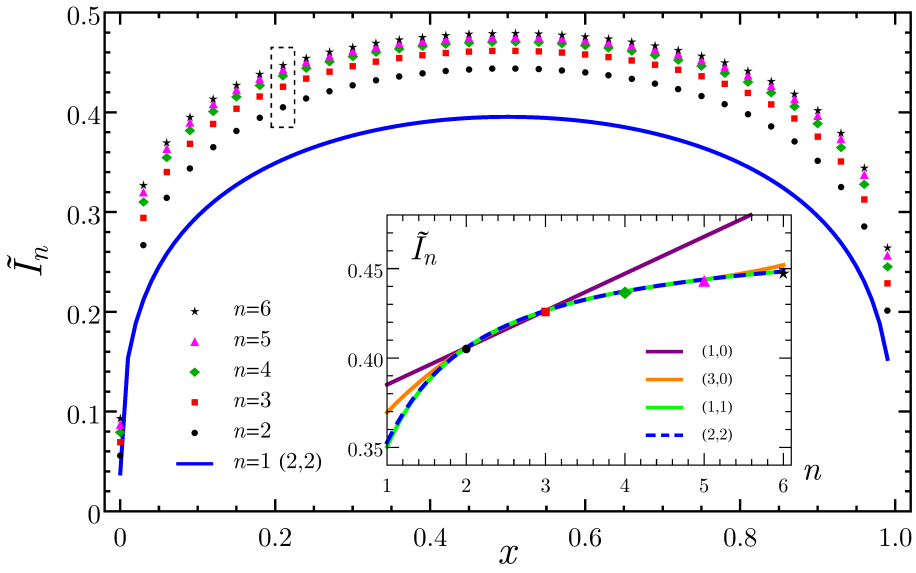

Figure 2.39: The quantity $\tilde{I}_n$ in (2.142) and the corresponding $n \to 1$ limit (2.144) for the compact boson ($c = 1$) with $\eta = 0.295$. The blue line is the extrapolation $n = 1$ of the rational interpolation with $(p, q) = (2, 2)$ obtained through the analytic expressions given by (2.143) and 2.51 with $2 \leqslant n \leqslant 6$, whose values for $\tilde{I}_n$ are shown by points for some values of the four point ratio x. In the inset, considering the configuration having $x = 0.2101$ (highlighted by the dashed rectangle in the main plot), we show $\tilde{I}_n$ as function of n for rational interpolations having different (p, q). The extrapolations having $q > 0$ capture the expected value better than the ones having $q = 0$.

to avoid them, if possible. The extrapolation to $n = 1$ corresponding to $(p, q) = (1, 0)$ cannot be trusted and therefore we consider four input data $n \in \{2, 3, 4, 5\}$ which allow to consider a rational interpolation with, for instance, $(p, q) = (3, 0)$ and also $(p, q) = (1, 1)$. These two different rational interpolations do not provide the same extrapolation to $n = 1$ and therefore we must take into account more input data. Considering $2 \leqslant n \leqslant 6$ we can choose also $(p, q) = (2, 2)$ finding that the corresponding rational interpolation basically coincides with the one with $(p, q) = (1, 1)$ (their difference is of order 10^{-3}). Thus, the extrapolation to $n = 1$ obtained with $(p, q) = (2, 2)$ is quite stable. Repeating this analysis for the whole range of $x \in (0, 1)$, one can find the blue curve in Fig. 2.39. As a further check, in Fig. 2.36 we have used $(p, q) = (3, 2)$ using more input data, finding that the final extrapolation is basically the same. Plots like the one shown in the inset of Fig. 2.39 are very useful to understand the stability of the extrapolation to $n = 1$. Increasing the values of p and q in the rational interpolations leads to more precise extrapolations, as expected. Rational interpolations with $q > 0$ provide extrapolations which are closer to the expected value with respect to the ones with $q = 0$. When q is strictly positive, q poles occur in the complex plane parameterized by $n \in \mathbb{C}$. Nevertheless, if these poles are far enough from the real interval $(1, n_{\max})$ containing all the n's employed as input data for the interpolation, the extrapolations to $n = 1$ are reliable. Increasing q, we have higher probability that one of the poles is close to the region of interpolation, spoiling the extrapolation. Plotting $W^n_{(p,q)}(x)$ as function of n is useful to realize whether this

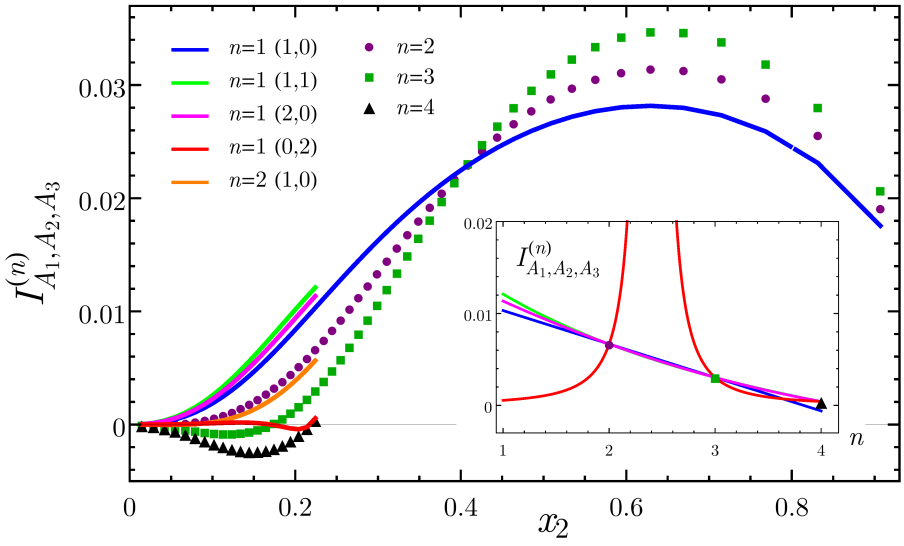

Figure 2.40: Three disjoint intervals: The quantity $I^{(n)}_{A_1,A_2,A_3}$ in (2.5) for the compact boson, computed through (2.98) and (2.41) for $n \geqslant 2$. Our limited computational power in evaluating Riemann theta functions for large matrices prevented us to consider $n = 4$ in the whole range of configurations and this limits also the possible rational interpolations that can be employed. The blu line is the extrapolation found by using only $n \in \{2, 3\}$, which should not be considered as a prediction because more n's are needed to find stable extrapolations. The orange line is a check of the method for $n = 2$: the fact that the expected points are not precisely recovered is due to low number of n's ($n \in \{3, 4\}$) available. In the inset, considering the configuration having $x_2 = 0.224$, we show $I^{(n)}_{A_1,A_2,A_3}$ as function of n for rational interpolations having different (p, q). The rational interpolation with $(p, q) = (0, 2)$ (red line) shows a bad behaviour and the extrapolation to $n = 1$ cannot be trusted; indeed, the red curve in the main plot is different from the other extrapolations.

situation occurs (see the inset of Fig. 2.40 for an explicit example).

The issue of evaluating Riemann theta functions which involve large matrices becomes important when we want to compute I_{A_1,A_2,A_3} (see 2.7a and (2.5)) for a compact boson. Indeed, $\mathcal{F}_{3,n}(\boldsymbol{x})$ in (2.98) is given by (2.41) for $N = 3$ and therefore the matrix occurring in the Riemann theta function is $2g \times 2g$ with $g = 2(n - 1)$. Given our computational power, we computed $I^{(n)}_{A_1,A_2,A_3}$ for $n \in \{2, 3\}$ for all the needed configurations of intervals, while for $n = 4$ we got results only for small intervals. In Fig. 2.40 we show our data and some numerical extrapolations. In the whole range of x_2 we performed only the rational interpolation with $(p, q) = (1, 0)$ (blue line) because only two input data are available, while for $x_2 \in (0, 0.22)$, where also $n = 4$ is available, we could employ higher values of p and q. When we have more extrapolations, unfortunately they do not overlap, indicating that we cannot trust these curves to give a prediction, even if they are quite close. Another indication that $n = 4$ is not enough to get a precise extrapolation comes from the fact that, given the data with $n \in \{3, 4\}$ and extrapolating to $n = 2$ (orange curve in Fig. 2.40) we did not recover exactly the expected values (purple circles) found with the analytic expressions. In the inset we focus on a configuration of three intervals corresponding to $x_2 = 0.224$ and show the dependence of $I^{(n)}_{A_1,A_2,A_3}$ on n for various

(p, q). While the extrapolations to $n = 1$ associated to $(1, 0)$ (for this one only $n \in \{2, 3\}$ have been used), $(1, 1)$ and $(2, 0)$ are very close, the one corresponding to $(p, q) = (0, 2)$ provides a completely different extrapolation to $n = 1$. Considering the two poles of the interpolating function in the regime of x_2 where also $n = 4$ is available, we find that they are real and at least one of them is inside the domain $n \in (1, 4)$. Thus, the function cannot be considered a good approximation of the true analytic continuation and the extrapolation cannot be trusted. This behaviour does not occur for the case considered in the inset of Fig. 2.39. Thus, it is useful to plot the n dependence of the functions obtained through the rational interpolation method in order to check the occurrence of singularities that could lead to wrong extrapolations.

In order to test the method, in some cases we have performed two further checks. Firstly we have employed as input for the extrapolations the numerical Rényi entropies obtained from the harmonic chain with the largest value of L at our disposal, rather than the analytic ones. The former naturally contains some systematic finite size errors, but the results agree with the ones obtained from the corresponding analytic expressions. Secondly, we added some randomness to the analytic expressions for the Rényi entropies to mimic some statistical errors which may arise when they are computed through approximated techniques such as Monte Carlo. The extrapolations obtained are in agreement with the expected ones up to the same amount of randomness.

It is very important to make a final remark on the validity of the method when some true singularities are present in the replica space $n \in \mathbb{C}$. When singularities in n occur (see e.g. [221, 267, 268]), the numerical method adopted here is not expected to be stable and to reproduce the correct analytical continuation. However, a more detailed analysis of the behaviour of the method in these cases would be interesting and should be addressed in the future. As for the one dimensional systems that have been considered, given the good agreement with the lattice results, a posteriori we expect that there are no singularities in the ranges of n that have been explored.

Chapter 3

Entanglement Negativity after a global quantum quench

3.1 Introduction

The non-equilibrium dynamics of isolated quantum systems is one of the most active research areas of the last years. In a global quantum quench, a system is initially prepared in the ground state $|\psi_0\rangle$ of a translationally invariant Hamiltonian H_0. The quantum quench consists in a sudden (instantaneous) change of the Hamiltonian $H_0 \to H$ at a given time that we set as $t = 0$. For example, the initial and final Hamiltonians may differ for an experimentally tunable parameter. The system is then left to evolve according to the unitary evolution induced by the new translationally invariant Hamiltonian H. Thus, the unitary evolution of $|\psi_0\rangle$ is

$$|\psi(t)\rangle = e^{-\mathrm{i}Ht}\,|\psi_0\rangle\,. \tag{3.1}$$

The density matrix associated to this pure state is $\rho(t) = |\psi(t)\rangle\langle\psi(t)|$. Key questions in quench dynamics are whether the system reaches for long time a stationary state, how to characterise it from first principles, and how this steady state is approached in time (see e.g. Refs. [269, 270] for reviews).

Nowadays a number of advanced analytical and numerical techniques have been developed to study the quench dynamics for a variety of different situations and realistic models [271–277]. However, many insights on these non-equilibrium dynamics came from the study of oversimplified theories such as 1+1 dimensional CFT. Indeed, phenomena like the light-cone spreading of correlations [106, 271], the linear increase of entanglement entropy [104] and the structure of revivals in finite systems [278] have been first discovered in CFT, later generalised to more realistic models and even verified in experiments (see [279] for the experimental measure of the light-cone spreading of correlations). In 1+1-dimensional CFT, the calculations become manageable when $|\psi_0\rangle$ is a boundary conformal state as we will explain in what follows. In this approach, analytical results have been obtained for the entanglement entropy of a single and more intervals [104], for correlation functions of primary operators [106, 271], and a few other quantities [280–285]. We will not be interested here in the time evolution of the entanglement after a local quench, a subject which has been considered instead in Refs. [96, 105, 188, 286–290] for the entanglement entropies and in [140] for the moments of the partial transpose.

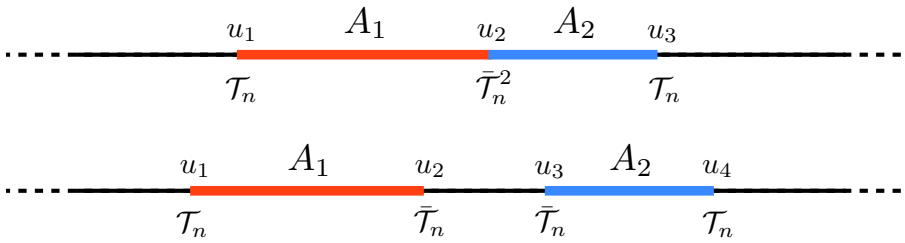

Figure 3.1: Configurations of two intervals in the infinite line that we consider: adjacent intervals (top) and disjoint intervals (bottom).

The main goal of this chapter is to shed some light on the time evolution of the entanglement *between* two different regions in an extended system following a quantum quench. In a one-dimensional setting, the two regions are two intervals, either adjacent or disjoint, as shown in Fig. 3.1. The entanglement of a bipartite system can be quantified by the entanglement entropy (1.46) or alternatively by the Rényi entanglement entropies (1.47). In this case one can introduce the mutual information (1.64) and, analogously, the Rényi mutual information (1.65). However, let us stress again that these are not measures of the entanglement between A_1 and A_2, but quantify the amount of global correlations between the two subsystems, see e.g. [15]. A proper measure of entanglement in a bipartite mixed state is the negativity $\mathcal{E}_{A_1,A_2}$, which has been defined in the Introduction, see Eq. (1.67) and for which a general quantum field theory approach is available [134, 135, 137]. In the following we will use the logarithmic negativity to quantify the entanglement evolution after the quench and we will compare the results with the ones for the mutual information. We consider this problem in the framework of CFT, closely following the approach introduced in Refs. [104, 106] for the time evolution of entanglement entropy and correlations. In order to understand the generality and the limits of this approach, we parallel the analytic CFT calculations with some exact numerical computations for the harmonic chain. The non-equilibrium evolution of the negativity in CFT, but for different quench protocols, has also been considered in Refs. [138, 139].

The chapter is organised as follows. In Sec. 3.2 we review the path integral approach to the quantum quench problem [104, 106, 271] and the known results from the time evolution of the entanglement entropy and mutual information in a CFT. In Sec. 3.3 we apply this formalism to the calculation of the negativity of two disjoint intervals after a quench to a CFT. In Sec. 3.4 we report the quasi-particle picture for the spreading of correlation and entanglement and we argue that it is valid also for the negativity. In Sec. 3.5 we report numerical calculation for the entanglement entropy, mutual information, and entanglement negativity for a quench of the frequency (mass) in the harmonic chain. We show that the results are in qualitative agreement with the CFT predictions and the differences are understood in terms of the effect of slow quasi-particles. Finally in Sec. 3.6 we draw our conclusions and we discuss some open problems.

3.2 Entanglement entropies and mutual information

In this section we briefly review the imaginary time formalism for the description of quenches in CFTs developed in Refs. [104, 106, 271]. In particular in Ref. [104], the

entanglement entropies of an arbitrary number of disjoint intervals have been already derived. It is however useful to recall how this has been done, in order to set up the calculation and notations for the negativity.

3.2.1 The path integral approach to quenches

The expectation value of a product of equal-time local operators in the time dependent state (3.1) can be written as [271]

$$\langle \mathcal{O}(t,\{r_i\})\rangle = Z^{-1}\langle\psi_0|e^{\mathrm{i}Ht-\tau_0 H}\mathcal{O}(\{r_i\})e^{-\mathrm{i}Ht-\tau_0 H}|\psi_0\rangle\,, \tag{3.2}$$

where two damping factors $e^{-\tau_0 H}$ have been added in such a way as the path integral representation of this expectation value is convergent. The normalisation factor is $Z = \langle\psi_0|e^{-2\tau_0 H}|\psi_0\rangle$. Following Ref. [271], Eq. (3.2) may be represented by a path integral in imaginary time τ

$$\frac{1}{Z}\int [d\phi(r,\tau)]\mathcal{O}(\{r_i\},0)\, e^{-\int_{\tau_1}^{\tau_2} L d\tau}\langle\psi_0|\phi(r,\tau_2)\rangle\langle\phi(r,\tau_1)|\psi_0\rangle\,, \tag{3.3}$$

where L is the (euclidean) Lagrangian corresponding to the dynamics of H. In order to match the expectation value (3.3) with the starting formula (3.2) we need to identify $\tau_1 = -\tau_0 - \mathrm{i}t$ and $\tau_2 = \tau_0 - \mathrm{i}t$. To further simplify the calculation and following Ref. [271], we consider the equivalent strip geometry between $\tau = 0$ and $\tau = 2\tau_0$, with $\mathcal{O}$ inserted at $\tau = \tau_0 + \mathrm{i}t$. The main idea of Refs. [104, 271] is to make the calculation considering τ real and only at the end of the computation to analytically continue it to the actual complex value $\tau = \tau_0 + \mathrm{i}t$.

Eq. (3.3) has the form of the equilibrium expectation value in a strip of width $2\tau_0$ with particular boundary conditions. The above expression is valid for an arbitrary field theory, but it is practically computable in the case we are interested in, i.e. a conformal invariant Hamiltonian. As detailed in Ref. [271] for a CFT, in the limit when t and the separations $|r_i - r_j|$ are much larger than the microscopic length and time scales, we can replace the boundary condition $|\psi_0\rangle$ with a boundary conformal state $|\psi_0^*\rangle$ to which $|\psi_0\rangle$ flow under the RG flow. Within this approach τ_0 is identified with the correlation length (inverse mass) of the initial state and the predictions made with this approach are expected to be valid only in the regime $t, |r_i - r_j| \gg \tau_0$. The generalisation of this approach to some other initial conditions (both in one and higher dimensions) can be found in Refs. [280, 284, 285, 291–295].

Before reporting the explicit results and technicalities for the entanglement entropies, it is worth spending few words on the regime of applicability of the above approach that often in the literature has been taken much beyond its scope, especially when comparing with results in lattice models. First of all, in a CFT all the quasi-particle excitations move with the same speed which here has been fixed to unity. This is not the case for a critical model even if its low-energy physics is described by a CFT. Indeed, while for small momenta k the dispersion relation ϵ_k has a CFT form $\epsilon_k \sim v|k|$, for larger values of the momentum k it becomes a non-trivial function. When performing a global quench, we always inject a large amount of energy into the system (unless we perform an infinitesimal quench) which populates also high-energy modes having a non-conformal scaling. Also the identification of τ_0 should be handled with a lot of care. Indeed, for small initial correlation length ξ_0 we have $\tau_0 \sim \xi_0$, but this relation should be seen only as an effective scaling for small ξ_0 in the continuum theory. However, in a given lattice model we need to have $\xi_0 \gg a$ in order to be in the field theory scaling. Thus there

is a competition between two different effects, which makes τ_0 a non-univocally defined quantity. However, this is not our main interest in the following and, when comparing with the numerical results coming from the harmonic chain, we will simply limit ourself to use τ_0 as a phenomenological fitting parameter which can depend also on the considered observable (as already noticed a few times in the literature [280, 292, 296, 297]).

3.2.2 The entanglement entropy

Let us consider a subsystem $A = \cup_{i=1}^{N} A_i$ composed by N disjoint intervals $A_i = [u_{2i-1}, u_{2i}]$ on the infinite line. We are interested in the time-dependent Rényi entropies $S_A^{(n)}(t)$ as defined in Eq. (1.47) and in the entanglement entropy obtained as a replica limit. Given that $\mathrm{Tr}\,\rho_A^n$ is equivalent to a $2N$-point function of twist fields [27, 45, 206], we have that the desired imaginary-time expectation value is

$$\mathrm{Tr}\,\rho_A^n = \langle \prod_{i=1}^{N} \mathcal{T}_n(w_{2i-1})\bar{\mathcal{T}}_n(w_{2i}) \rangle_{\mathrm{strip}}\,, \qquad w_i = u_i + \mathrm{i}\tau\,, \tag{3.4}$$

where we denoted by $w = u + \mathrm{i}\tau$ the complex coordinate on the strip ($u \in \mathbb{R}$ and $0 < \tau < 2\tau_0$). The twist fields $\mathcal{T}_n$ and $\bar{\mathcal{T}}_n$ behave under conformal transformation as primary operators whose scaling dimensions are given in Eq. (1.54).

The expectation values on the strip of width $2\tau_0$ can be obtained by employing the conformal map $z = e^{\pi w/(2\tau_0)}$, which maps the strip to the upper half plane (UHP) parameterised by complex coordinate z. Eq. (3.4) can be then written as

$$\mathrm{Tr}\,\rho_A^n = \left[\left(\frac{\pi}{2\tau_0}\right)^{2N} \prod_{i=1}^{N} |z_{2i-1} z_{2i}|\right]^{\Delta_n} \langle \prod_{i=1}^{N} \mathcal{T}_n(z_{2i-1})\bar{\mathcal{T}}_n(z_{2i}) \rangle_{\mathrm{UHP}}\,, \tag{3.5}$$

where $\langle \dots \rangle_{\mathrm{UHP}}$ are correlators on the UHP and $z_j \equiv e^{\pi w_j/(2\tau_0)}$.

The $2N$-point function of twist fields on the upper half plane occurring in (3.5) can be written as

$$\langle \prod_{i=1}^{N} \mathcal{T}_n(z_{2i-1})\bar{\mathcal{T}}_n(z_{2i}) \rangle_{\mathrm{UHP}} = \frac{c_n^N}{\prod_{a=1}^{2N} |z_a - \bar{z}_a|^{\Delta_n}} \left(\frac{\prod_{j<k}^{N} \eta_{2k,2j}\, \eta_{2k-1,2j-1}}{\prod_{j,k} \eta_{2j-1,2k}}\right)^{\Delta_n} \mathcal{F}_{N,n}(\{\eta_{j,k}\})\,, \tag{3.6}$$

where $\eta_{i,j}$ are the $\binom{2N}{2}$ cross ratios that can be constructed from the $2N$ endpoints z_j (and their images $\bar{z}_j$) of the N intervals in the UHP as follows

$$\eta_{i,j} \equiv \frac{(z_i - z_j)(\bar{z}_i - \bar{z}_j)}{(z_i - \bar{z}_j)(\bar{z}_i - z_j)}\,. \tag{3.7}$$

The function $\mathcal{F}_{N,n}(\{\eta_{j,k}\})$ in (3.6) depends on the full operator content of the model and its computation is a very difficult task, even for simple models (see Refs. [47, 79, 196, 218–220, 223–227, 229, 235, 243, 298, 299] for some specific cases in the bulk case, the references in [74, 75, 77, 78, 97, 98, 100, 228, 230, 300–302] for the holographic approach to the same problem, and [49, 51–53, 55, 303] for some higher dimensional field theoretical computations).

There is, however, some degree of arbitrariness in the way we wrote Eq. (3.6) since the product over the cross-ratios could be absorbed fully or partially in the function $\mathcal{F}_{N,n}$. However, writing it in the above form has the advantage to display the limiting behaviour for $\eta_{i,j} \to 0$ and $\eta_{i,j} \to 1$. Indeed, by employing the OPE (in the sense of Ref. [196])

$$\mathcal{T}_n(z)\bar{\mathcal{T}}_n(w) = \frac{c_n}{|z-w|^{2\Delta_n}}\,\mathbb{I} + \dots\,, \qquad w \to z\,, \tag{3.8}$$

it is easy to show that, in both limits $\eta_{i,j} \to 0$ and $\eta_{i,j} \to 1$, the leading power-law behaviour is fully encoded in the prefactor and the function $\mathcal{F}_{N,n}$ is just a constant. As we will see below, for the real time behaviour of the entanglement entropy only these two limits of the various four-point ratios matter [104, 271] and consequently we do not have to worry about the precise value of the function $\mathcal{F}_{N,n}$.

Plugging (3.6) into (3.5), we find

$$\mathrm{Tr}\,\rho_A^n \;=\; c_n^N \left[\left(\frac{\pi}{2\tau_0}\right)^{2N} \prod_{a=1}^{2N} \left|\frac{z_a}{z_a-\bar{z}_a}\right| \frac{\prod_{j<k}^{N} \eta_{2k,2j}\,\eta_{2k-1,2j-1}}{\prod_{j,k}\eta_{2j-1,2k}} \right]^{\Delta_n} \mathcal{F}_{N,n}(\{\eta_{j,k}\})\,. \tag{3.9}$$

What still remains to be done is to write the r.h.s. of (3.9) in terms of the coordinates on the strip. The a-th term of the product in (3.9) is simply

$$\frac{|z_a|}{|z_a-\bar{z}_a|} = \frac{1}{|2\sin[\pi\tau/(2\tau_0)]|}\,, \tag{3.10}$$

independently of u_a. For the cross ratios (3.7) we have that

$$\eta_{i,j} \;=\; \frac{2\sinh^2\left(\frac{\pi(u_i-u_j)}{4\tau_0}\right)}{\cosh\left(\frac{\pi(u_i-u_j)}{2\tau_0}\right) - \cos\left(\frac{\pi\tau}{\tau_0}\right)}\,. \tag{3.11}$$

This concludes the calculation on the strip of width $2\tau_0$. At this point, to obtain the real time evolution after a quench, we should analytically continue the parameter τ to the complex value

$$\tau = \tau_0 + \mathrm{i}\,t\,, \tag{3.12}$$

with $t \gg \tau_0$, as explained above. In this regime, the a-th term (3.10) gives $|z_a|/|z_a-\bar{z}_a| = e^{-\frac{\pi}{2\tau_0}t} + \dots$. As for the cross ratio (3.11), when $t \gg \tau_0$ and $|u_i-u_j| \gg \tau_0$, it becomes

$$\eta_{i,j} \;=\; \frac{e^{\pi|u_i-u_j|/(2\tau_0)}}{e^{\pi|u_i-u_j|/(2\tau_0)} + e^{\pi t/\tau_0}}\,, \tag{3.13}$$

where $\eta_{i,j} \in [0,1]$. In the limit $\tau_0 \to 0$, for the ratio (3.13) we have $\eta_{i,j} \to 0$ for $t > |u_i-u_j|/2$ and $\eta_{i,j} \to 1$ for $|u_i-u_j|/2 > t$. However, we should keep the leading behaviour for $\eta_{i,j} \to 0$ and so we find useful to write it as

$$\ln(\eta_{i,j}) \to \frac{\pi}{\tau_0} q(t,|u_i-u_j|)\,, \qquad \text{for} \quad t, |u_i-u_j| \gg \tau_0\,, \tag{3.14}$$

where

$$q(t,\ell) \;\equiv\; \frac{\ell}{2} - \max(t,\ell/2) \;=\; \begin{cases} 0 & t < \ell/2\,, \\ \ell/2 - t & t > \ell/2\,. \end{cases} \tag{3.15}$$

The time evolution of the Rényi entanglement entropies is then obtained by plugging the above analytic continuations to real time in Eq. (3.9), leading to [104]

$$S_A^{(n)} = \frac{c\pi(n+1)}{12\tau_0 n}\Bigg[Nt + \sum_{j,k=1}^{N} q(t,|u_{2j-1}-u_{2k}|) \\ - \sum_{1<j<k<N} q(t,|u_{2j}-u_{2k}|) + q(t,|u_{2j-1}-u_{2k-1}|)\Bigg]. \tag{3.16}$$

In the above equation a piece-wise constant (in time) term coming from the function $\mathcal{F}_{N,n}$ and for the various non-universal prefactors has been *intentionally* dropped because it has no physical meaning. Indeed the above formula describes only the leading term in the so-called *space-time scaling limit* [304–307] which corresponds to the limit $t \to \infty$, $|u_i - u_k| \to \infty$ with all the ratios fixed. The term we dropped is just one of the corrections to this leading behaviour and it has no meaning to consider it without taking into account all other corrections at the same order, such the dependence on the details of the initial state (which in this approach have been over-simplistically absorbed in the parameter τ_0).

Let us now specialise Eq. (3.16) to the case of one interval of length $u_2 - u_1 = \ell$ and $n = 1$ obtaining the famous formula [104]

$$S_A = \frac{\pi c}{6\tau_0}\big[t + q(t,\ell)\big] = \begin{cases} \dfrac{\pi c}{6\tau_0} t & t < \ell/2\,, \\ \dfrac{\pi c}{12\tau_0}\ell & t > \ell/2\,, \end{cases} \tag{3.17}$$

i.e. the entanglement entropy grows linearly for $t < \ell/2$ and then saturates to an extensive value in the subsystem length ℓ. Notice that the large time value of the entanglement entropy is the same as the thermodynamic entropy of a CFT at large finite temperature $T = 4\tau_0$. This fact indeed holds for all local observable leading to the remarkable phenomenon of CFT thermalisation [271] (see also [84, 86, 92, 308] for the holographic version of this phenomenon in arbitrary dimension). However, this is a specificity of the uncorrelated initial state we are considering and it has been shown that even an irrelevant boundary perturbation destroys it leading, for large time, to a generalised Gibbs ensemble where all the CFT constants of motion enter [292]. The discussion of this issue is however far beyond the goals of this paper.

In the case of two intervals A_1 and A_2 (the geometry depicted in Fig. 3.1 with $u_2 - u_1$ and $u_4 - u_3$ the lengths of the two intervals and $u_3 - u_2$ their distance) the entanglement entropy is straightforwardly written down from Eq. (3.16). Specialising to the Rényi mutual information in Eq. (1.65), we have

$$I^{(n)}_{A_1,A_2} = \frac{\pi c(n+1)}{12\tau_0 n}\big[q(t,u_3-u_1) + q(t,u_4-u_2) - q(t,u_4-u_1) - q(t,u_3-u_2)\big]. \tag{3.18}$$

Notice that, once the explicit expressions for the q's from (3.15) have been inserted in (3.18), the linear combination within the square brackets is such that only the terms involving the max's remain. For large t, we have that $I^{(n)}_{A_1:A_2}$ vanishes for all n.

Taking the limit $u_3 \to u_2$ in (3.18), we get $I^{(n)}$ for two adjacent intervals

$$I^{(n)}_{A_1,A_2} = \frac{\pi c(n+1)}{12\tau_0 n}\big[t + q(t,u_2-u_1) + q(t,u_4-u_2) - q(t,u_4-u_1)\big]. \tag{3.19}$$

It is worth mentioning that the time evolution of the entanglement entropy and mutual information has been also considered in the framework of holographic approach to CFT [81–91, 93, 94].

3.3 Entanglement negativity

In this section we present the original part of the CFT calculation of this chapter concerning the temporal evolution of the negativity between two intervals after a global quench to a conformal Hamiltonian. We consider $A = A_1 \cup A_2$, where the intervals A_1 and A_2 can be either adjacent or disjoint, as in Fig. 3.1. An important special case is when A is the entire system (i.e. $B \to \emptyset$).

As reviewed in Sec. 1.4.3, the quantity $\mathrm{Tr}\left(\rho_A^{T_2}\right)^n$ can be computed from a specific correlator of twist fields. We can apply the method of Ref. [104] to the proper correlators on the strip, which involve both $\mathcal{T}_n$ ($\bar{\mathcal{T}}_n$) and $\mathcal{T}_n^2$ ($\bar{\mathcal{T}}_n^2$). This means that we have to slightly generalize the setup described in the previous section by taking into account correlators on the strip of fields which can have different dimensions. Instead of presenting general formulas, we find more instructive to limit ourselves to discuss few cases of two intervals in which we are interested.

3.3.1 Bipartite systems

Although trivial, it is useful to first discuss the case in which $A = A_1 \cup A_2$ is the entire system and we consider the partial transpose with respect to A_2. Since the time dependent state $|\psi(t)\rangle$ is pure at any time, ρ_A corresponds to a pure state, and we can use the standard results [119, 162] that for a pure state the logarithmic negativity is the Rényi entropy with $n = 1/2$, i.e.

$$\mathcal{E}(t) = S_{A_2}^{(1/2)}(t)\,, \tag{3.20}$$

independently of the Hamiltonian governing the time evolution.

When the evolution is conformal, we can re-obtain this trivial result by using the path integral approach discussed in the previous section. We need to evaluate $\langle \mathcal{T}_n^2(w_1)\bar{\mathcal{T}}_n^2(w_2)\rangle_{\text{strip}}$ and then to analytically continue to real time. The strip two-point function is related to the one in the UHP which has the standard form

$$\langle \mathcal{T}_n^2(z_1)\bar{\mathcal{T}}_n^2(z_2)\rangle_{\text{UHP}} = \frac{c_n^{(2)}}{|(z_1-\bar{z}_1)(z_2-\bar{z}_2)\,\eta_{1,2}|^{\Delta_n^{(2)}}}\mathcal{F}(\eta_{1,2})\,, \tag{3.21}$$

where the constants $c_n^{(2)}$ are related to c_n in a known way [135], but their value is not important for what follows. Transforming the UHP to the strip, we find

$$\mathrm{Tr}(\rho_A^{T_2})^n = \langle\, \mathcal{T}_n^2(w_1)\bar{\mathcal{T}}_n^2(w_2)\,\rangle_{\text{strip}} = c_n^{(2)}\left(\frac{\pi}{2\tau_0}\right)^{2\Delta_n^{(2)}}\left|\left(\prod_{a=1}^{2}\frac{z_a}{z_a-\bar{z}_a}\right)\frac{1}{\eta_{1,2}}\right|^{\Delta_n^{(2)}}\mathcal{F}(\eta_{1,2})\,, \tag{3.22}$$

where $z_a = e^{\pi(u_a+\mathrm{i}\tau)/(2\tau_0)}$.

The time evolution of the powers of the partial transpose comes from the analytic continuation in Eq. (3.12). As usual, in the space-time scaling limit ($t \gg \tau_0$ and $u_2 - u_1 \gg \tau_0$), we should retain only the leading behaviour of the above expression and all the various constants and the function $\mathcal{F}$ can be dropped, obtaining

$$\mathcal{E}^{(n)} = -\frac{\pi\Delta_n^{(2)}}{\tau_0}\big[t + q(t, u_2-u_1)\big]\,, \qquad \Rightarrow \quad \mathcal{E} = \frac{\pi c}{4\tau_0}\big[t + q(t, u_2-u_1)\big]\,, \tag{3.23}$$

which coincides with the Rényi entropy for $n = 1/2$, as it should from (3.20).

We need to comment at this point on the asymptotic large time value of the negativity. Indeed, it is obvious that the negativity of one interval with respect to the rest of the system *does not thermalise*, being very different from the finite temperature negativity calculated in [137] (see also [121–124]). This is not a surprise since, by construction, this negativity is not a local quantity because it requires the partial transposition with respect to the infinitely large part A_2.

3.3.2 Two adjacent intervals

The conformal evolution of the entanglement negativity between two adjacent intervals after a global quench can be studied by considering the three point function $\langle \mathcal{T}_n \bar{\mathcal{T}}_n^2 \mathcal{T}_n \rangle$ on the strip which can be obtained by the mapping from the UHP of the three-point function

$$\langle \mathcal{T}_n(z_1)\bar{\mathcal{T}}_n^2(z_2)\mathcal{T}_n(z_3)\rangle_{\text{UHP}} = \frac{c_n}{\prod_{a=1}^3 |z_a - \bar{z}_a|^{\Delta_{(a)}}} \left(\frac{\eta_{1,3}^{\Delta_n^{(2)}-2\Delta_n}}{\eta_{1,2}^{\Delta_n^{(2)}}\,\eta_{2,3}^{\Delta_n^{(2)}}} \right)^{1/2} \mathcal{F}(\{\eta_{j,k}\})\,, \qquad (3.24)$$

where $\Delta_{(1)} = \Delta_{(3)} = \Delta_n$ and $\Delta_{(2)} = \Delta_n^{(2)}$ (given by (1.54) and (1.78) respectively), the harmonic ratios $\eta_{j,k}$ are defined in Eq. (3.7) and again the function $\mathcal{F}$ depends on the full operator content of the theory and it is very difficult to calculate (see Refs. [135, 235] for some explicit examples). However, as it should be already clear at this point, we do not need this function in the space-time scaling limit, but we only need to ensure that the powers in the rest of the expression have been chosen in such a way that $\mathcal{F}$ is constant in the limits $\eta_{j,k} \to 0$ or $\eta_{j,k} \to 1$. This can be easily checked by employing the following OPE

$$\mathcal{T}_n(z)\bar{\mathcal{T}}_n^2(w) = \frac{C_{\mathcal{T}_n\bar{\mathcal{T}}_n^2\bar{\mathcal{T}}_n}}{|z-w|^{\Delta_n^{(2)}}}\,\bar{\mathcal{T}}_n(z) + \dots\,, \qquad w \to z\,. \qquad (3.25)$$

Taking separately the limits $z_2 \to z_1$ and $z_2 \to z_3$ in (3.24), and using (3.25) it should be clear that $\mathcal{F}$ is constant in both the interesting limits. Then, the three-point function on the strip can be straightforwardly written by a conformal mapping, obtaining

$$\langle \mathcal{T}_n(u_1)\bar{\mathcal{T}}_n^2(u_2)\mathcal{T}_n(u_3)\rangle_{\text{strip}} = c_n \left(\frac{\pi}{2\tau_0}\right)^{\Delta} \prod_{a=1}^{3} \left|\frac{z_a}{z_a - \bar{z}_a}\right|^{\Delta_{(a)}} \left(\frac{\eta_{1,3}^{\Delta_n^{(2)}-2\Delta_n}}{\eta_{1,2}^{\Delta_n^{(2)}}\,\eta_{2,3}^{\Delta_n^{(2)}}} \right)^{1/2} \mathcal{F}(\{\eta_{j,k}\})\,, \qquad (3.26)$$

where $\Delta = 2\Delta_n + \Delta_n^{(2)}$ and $z_a = e^{\pi(u_a + \mathrm{i}\tau)/(2\tau_0)}$. The time evolution of $\mathrm{Tr}(\rho_A^{T_2})^n$ for two adjacent intervals is then obtained by the analytic continuation of the above to $\tau = \tau_0 + \mathrm{i}t$.

The CFT prediction for the temporal dependence of $\mathcal{E}^{(n)}$ in the space-time scaling regime ($t \gg \tau_0$ and $|u_j - u_i| \gg \tau_0$) is then found, as usual, by dropping the various multiplicative constants and the function $\mathcal{F}$, obtaining

$$\begin{aligned} \mathcal{E}^{(n)} = -\frac{\pi}{2\tau_0}\Big[&\big(2\Delta_n + \Delta_n^{(2)}\big)t \\ &+ \Delta_n^{(2)}\big(q(t, u_2 - u_1) + q(t, u_3 - u_2)\big) - \big(\Delta_n^{(2)} - 2\Delta_n\big)\, q(t, u_3 - u_1)\Big]. \end{aligned} \qquad (3.27)$$

Notice that, since $\Delta_2^{(2)} = 0$, for $n = 2$ the terms containing u_2 do not contribute and therefore the curve $\mathcal{E}^{(2)}(t)$ displays a change in its slope only at $t = (\ell_1 + \ell_2)/2$. This is

a consequence of the trivial fact that $\bar{\mathcal{T}}_2^2 = \mathbb{I}$ in (3.26). Finally, taking the replica limit of (3.27), we find the evolution of the logarithmic negativity for adjacent intervals

$$\mathcal{E} \;=\; \frac{\pi c}{8\tau_0}\big[\, t - q(t, u_3 - u_1) + q(t, u_2 - u_1) + q(t, u_3 - u_2)\big]\,. \tag{3.28}$$

Considering the ratio (1.71) for two adjacent intervals, since $A = A_1 \cup A_2$ is the interval $[u_1, u_3]$ in the spatial slice of the strip, Tr ρ_A^n corresponds to $[u_1, u_3]$ and (1.71), in terms of the CFT quantities, reads

$$R_n \equiv \frac{\langle \mathcal{T}_n(u_1)\bar{\mathcal{T}}_n^2(u_2)\mathcal{T}_n(u_3)\rangle_{\text{strip}}}{\langle \mathcal{T}_n(u_1)\bar{\mathcal{T}}_n(u_3)\rangle_{\text{strip}}}\,. \tag{3.29}$$

Notice that since $\mathcal{T}_2^2 = \bar{\mathcal{T}}_2^2 = \mathbb{I}$, we have that $R_2 = 1$ identically. The time dependence of R_n in the space-time scaling regime is readily obtained by combining the expressions for the numerator and the denominator in (3.29), finding

$$\ln(R_n) \;=\; \frac{\pi\Delta_n^{(2)}}{2\tau_0}\big[\, - t + q(t, u_3 - u_1) - q(t, u_2 - u_1) - q(t, u_3 - u_2)\big]\,, \tag{3.30}$$

where, once the expressions for the q's from (3.15) have been plugged in, only the terms with the max's remain within the square brackets. This expression shows why the quantities R_n are very useful when comparing these predictions with numerical calculations, indeed when comparing with Eq. (3.27) for $\mathcal{E}^{(n)}$ one immediately notices that all the dependence on Δ_n is not there.

3.3.3 Two disjoint intervals

The time evolution of logarithmic negativity between two disjoint intervals after a global quench can be computed from the analytic continuation of the four-point function $\langle \mathcal{T}_n\bar{\mathcal{T}}_n\bar{\mathcal{T}}_n\mathcal{T}_n\rangle$ on the strip (notice the order of the operators along the line which is crucial). The strip four-point function is derived from the conformal map from the same function on the UHP, which can be written as

$$\langle \mathcal{T}_n(z_1)\bar{\mathcal{T}}_n(z_2)\bar{\mathcal{T}}_n(z_3)\mathcal{T}_n(z_4)\rangle_{\text{UHP}} = \\ \frac{c_n^2}{\prod_{a=1}^4 |z_a - \bar{z}_a|^{\Delta_n}} \frac{1}{\eta_{1,2}^{\Delta_n}\,\eta_{3,4}^{\Delta_n}} \left(\frac{\eta_{1,4}\,\eta_{2,3}}{\eta_{1,3}\,\eta_{2,4}}\right)^{\Delta_n^{(2)}/2-\Delta_n} \mathcal{F}(\{\eta_{j,k}\})\,. \tag{3.31}$$

Again for the time evolution we do not need the knowledge of the function $\mathcal{F}$, but only to ensure that for $\eta_{j,k} \to 0$ and $\eta_{j,k} \to 1$ the form used above gives that $\mathcal{F}$ is constant. This can be easily checked by requiring that when the two intervals are far apart (i.e. $|z_3 - z_2| \to \infty$), the four-point function factorizes into the product of two two-point functions and that for $z_3 \to z_2$ the following OPE holds

$$\bar{\mathcal{T}}_n(z)\bar{\mathcal{T}}_n(w) = \frac{C_{\bar{\mathcal{T}}\bar{\mathcal{T}}}^{\bar{\mathcal{T}}^2}}{|z-w|^{2\Delta_n - \Delta_n^{(2)}}}\,\bar{\mathcal{T}}_n^2(z) + \dots\,, \qquad w \to z\,. \tag{3.32}$$

Mapping this four point-function on the strip, we get

$$\text{Tr}(\rho_A^{T_2})^n \;=\; c_n^2\left(\frac{\pi}{2\tau_0}\right)^{\Delta} \prod_{a=1}^4 \left|\frac{z_a}{z_a - \bar{z}_a}\right|^{\Delta_n} \frac{1}{\eta_{1,2}^{\Delta_n}\,\eta_{3,4}^{\Delta_n}} \left(\frac{\eta_{1,4}\,\eta_{2,3}}{\eta_{1,3}\,\eta_{2,4}}\right)^{\Delta_n^{(2)}/2-\Delta_n} \mathcal{F}(\{\eta_{j,k}\})\,, \tag{3.33}$$

being $\Delta = 4\Delta_n$ and $z_a = e^{\pi(u_a + \mathrm{i}\tau)/(2\tau_0)}$.

The time evolution of $\mathcal{E}^{(n)}$ in the space-time scaling regime ($t \gg \tau_0$ and $|u_j - u_i| \gg \tau_0$) is found by employing the analytic continuation (3.12). The result reads

$$\mathcal{E}^{(n)} = -\frac{\pi}{\tau_0}\Big[2\Delta_n\, t + \Delta_n\Big(q(t,u_2-u_1) + q(t,u_3-u_4)\Big) \\ - \big(\Delta_n^{(2)}/2 - \Delta_n\big)\Big(q(t,u_4-u_1) + q(t,u_3-u_2) - q(t,u_3-u_1) - q(t,u_4-u_2)\Big)\Big], \tag{3.34}$$

whose replica limit is

$$\mathcal{E} \;=\; \frac{\pi c}{8\tau_0}\big[q(t,u_3-u_1) + q(t,u_4-u_2) - q(t,u_4-u_1) - q(t,u_3-u_2)\big]\,. \tag{3.35}$$

The resulting expression for the negativity is identical to Eq. (3.18) for the Rényi mutual information apart from the prefactor. Notice that in $\mathcal{E}^{(n)}$, for small t, the expression (3.34) displays a linear regime in the initial part of the evolution, whose slope is $-2\pi\Delta_n/\tau_0$. Being $\Delta_{n=1} = 0$, this linear regime does not occur for the logarithmic negativity (1.70). We find it useful to compare (3.34) with the corresponding quantity (3.27) for adjacent intervals and observe that for $n = 2$ all the dependences on t and u_j remain when the intervals are disjoint, while for adjacent intervals the $n = 2$ is characterised by the cancellation of some variables.

The ratio R_n in Eq. (1.71) for two disjoint intervals on the strip has the easy form

$$R_n = \frac{\langle \mathcal{T}_n(u_1)\bar{\mathcal{T}}_n(u_2)\bar{\mathcal{T}}_n(u_3)\mathcal{T}_n(u_4)\rangle_{\text{strip}}}{\langle \mathcal{T}_n(u_1)\bar{\mathcal{T}}_n(u_2)\mathcal{T}_n(u_3)\bar{\mathcal{T}}_n(u_4)\rangle_{\text{strip}}} \;\simeq\; \left(\frac{\eta_{1,4}\,\eta_{2,3}}{\eta_{1,3}\,\eta_{2,4}}\right)^{\Delta_n^{(2)}/2}, \tag{3.36}$$

where we dropped the two functions $\mathcal{F}$ in numerator and denominator since they do not contribute in the the space-time scaling limit after analytic continuation in time. From this expression, we get $R_2 = 1$ identically because $\mathcal{T}_2 = \bar{\mathcal{T}}_2$. Also the time evolution of this ratio in the space-time scaling regime is particularly easy:

$$\ln R_n \;=\; \frac{\pi\Delta_n^{(2)}}{2\tau_0}\big[q(t,u_4-u_1) + q(t,u_3-u_2) - q(t,u_3-u_1) - q(t,u_4-u_2)\big]\,. \tag{3.37}$$

Plugging the explicit expressions of the q's (see (3.15)) in this expression, we find that only the terms involving the max's remain. Remarkably, also for disjoint intervals, these ratios R_n do not depend on Δ_n.

3.4 Quasi-particle interpretation and horizon effect

The time evolution of entanglement and total correlations after a quantum quench can be understood in terms of the quasi-particle interpretation for the propagation of entanglement, first suggested in [104]. According to this argument, since the initial state $|\psi_0\rangle$ has a very high energy relative to the ground state of the Hamiltonian which governs the time evolution, it acts as a source of quasi-particle excitations. Particles emitted from points further apart than the correlation length in the initial state are incoherent, but pairs of particles emitted from a given point and subsequently moving to the left or right are highly entangled and correlated. Let us suppose that a pair of quasi-particles with

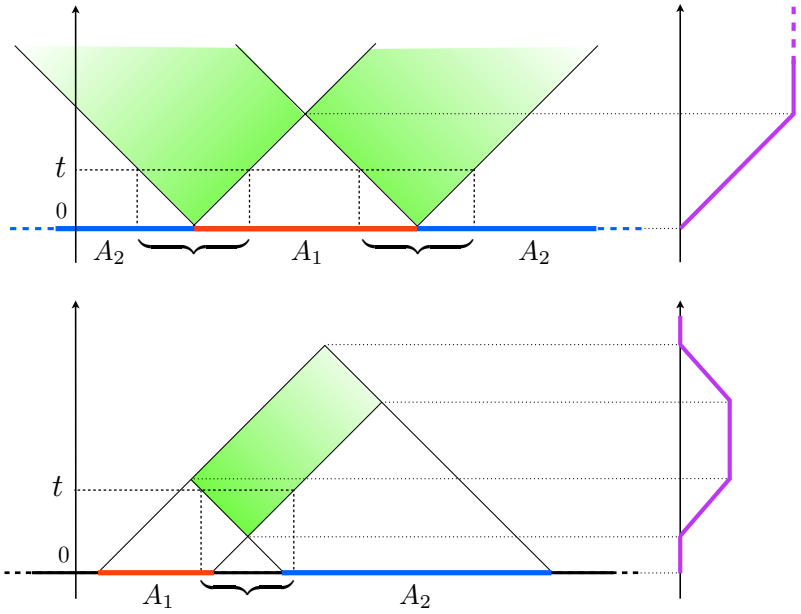

Figure 3.2: Graphical representation for the quasi-particle spreading of entanglement (for the case with all quasi-particles having the same velocity $v = 1$ as in a CFT). The quasi-particles emitted from every point at $t = 0$ and reaching one A_1 (red) and the other A_2 (blue) are responsible of the entanglement between them. The entanglement at a given time t is proportional to the section of the green shaded area, which is the intersection of the light cones starting from all the points of A_1 and A_2 (in the figure these lengths are the braces). The time-dependence of the entanglement obtained in this way are depicted as purple curves on the right for a single interval in the infinite line (top) and two disjoint intervals (bottom): they are proportional to the CFT calculations in Eqs. (3.17) and (3.35) respectively. The regions from where the corresponding quasi-particles have been emitted at $t = 0$ are obtained by projecting the intersections at time $t = 0$ (vertical dashed lines).

opposite momenta $(p, -p)$ is produced with a probability $\rho(p)$ (which depends on both the Hamiltonian governing the evolution and on the initial state). After their production, these quasi-particles move ballistically with velocity $v_p = -v_{-p}$. A quasi-particle of momentum p produced at x is therefore at $x + v_p t$ at time t. In general there is also a maximum allowed speed of propagation $v_{\max}$ (which is connected with the existence of a Lieb-Robinson bound in a lattice model [3]).

Now let us consider two regions of the system A_1 and A_2 (which can be either finite, infinite, semi-infinite, etc). According to the argument in [104], the field at some point $x_1 \in A_1$ will be entangled with that at a point $x_2 \in A_2$ if a pair of entangled particles emitted from a point x arrive simultaneously at x_1 and x_2. The entanglement and the total correlation between A_1 and A_2 are proportional to the length of the interval in x for which this can be satisfied and it can be written as [104]

$$\text{entanglement} \approx \int_{x_1\in A_1} dx_1 \int_{x_2\in A_2} dx_2 \int_{-\infty}^{\infty} dx \int dp\, \rho(p) f(p)\, \delta(x_1 - x - v_p t)\, \delta(x_2 - x + v_p t)\,, \tag{3.38}$$

where $f(p)$ is the contribution of the pair of quasi-particles to the given entanglement or

correlation measure.

When all the quasi-particles move with the same speed $|v_p| = v$ (as in the case of a CFT discussed in the previous sections where we fixed $v = 1$), the δ functions do not depend on the momentum anymore and therefore the integral over p gives just an overall normalisation (depending on the quantity we are considering), while the integral over the space coordinate can be easily done for arbitrary A_1 and A_2. In particular, in the cases of one and two intervals, one straightforwardly recovers all the CFT expressions for the entanglement entropy, mutual information and negativity such as Eqs. (3.16), (3.17), (3.18) and (3.35). A graphical interpretation of this quasi-particle picture is reported in Fig. 3.2.

Furthermore, the above argument allows us also to understand what happens in the case of a non-linear dispersion relation leading to a mode dependent velocity, which will be fundamental for the interpretation and the understanding of the numerical data reported in the next section. Indeed, assuming that a maximum speed $v_{\max}$ exists, we have that the first linear increase of the entanglement is always present, but when $v_{\max}t$ equals the half of some typical length of the configuration given by A_1 and A_2, the quasi-particles with velocity smaller than $v_{\max}$ start influencing the entanglement because we cannot ignore anymore the integral over p in Eq. (3.38). These slow quasi-particles lead to non-linear effects discussed e.g. for the entanglement entropy in Refs. [104, 304]. In particular we have that for very long times, the quasi-particles with approximately zero velocity govern the approach to the asymptotic value of the entanglement which usually is power-law as can be easily seen expanding Eq. (3.38) close to the points where $v_p = 0$.

It is important to stress at this point that, while it was already established [104, 222, 309] that the mutual information is correctly described by this quasi-particle picture, it is far from obvious that the same reasoning carries over to a complicated measure of the entanglement such as the negativity. The previous section represents a proof of this fact in the context of CFT, while the following one will confirm it also for the harmonic chain.

3.5 Numerical evaluation of the negativity and mutual information for the harmonic chain

In this section we report the numerical evaluation of the time evolution of entanglement negativity and mutual information in the harmonic chain after a global quantum quench of the frequency parameter. The quench dynamics of the Hamiltonian (2.67) has been studied already in several papers both on the lattice and in the continuum [106, 310–317]. We consider the harmonic chain because it is the only lattice model in which the partial transpose and the negativity can be obtained by means of correlation matrix techniques [147, 150].

In Sec. 2.5 we already reported the Hamiltonian and the main features of the model. In particular, from the dispersion relation (2.69), we observed that the Hamiltonian has a zero-mode for $k = 0$ and $\omega = 0$. This usually prevents a straightforward analysis of the critical behaviour, but for the global quench this will not be a problem, as we will see soon. From the dispersion relation, we straightforwardly have the velocity of each momentum mode as

$$v_k \equiv \frac{\partial \omega_k}{\partial p_k} = \frac{(K/m)\sin(p_k)}{\sqrt{\omega^2 + (4K/m)\sin^2(p_k/2)}}\,, \qquad p_k \equiv \frac{2\pi k}{L}\,, \tag{3.39}$$

and the maximum one

$$v_{\max} \equiv \max_k(v_k)\,, \tag{3.40}$$

which determines the spreading of entanglement and correlations. Notice that for $\omega = 0$, $v_{\max} = 1$ for $K = m = 1$.

In the quench protocol in which we are interested in, the system is prepared in the ground state $|\psi_0\rangle$ of the Hamiltonian

$$H(\omega_0) = \sum_{k=0}^{L-1} \omega_{0,k} \left(a^\dagger_{0,k} a_{0,k} + \frac{1}{2} \right), \tag{3.41}$$

whose dispersion relation $\omega_{0,k}$ is Eq. (2.69) with $\omega = \omega_0$. At $t = 0$ the frequency parameter is suddenly quenched from ω_0 to a different value ω and the system unitarily evolves through the new Hamiltonian (2.67), namely

$$|\psi(t)\rangle = e^{-\mathrm{i}H(\omega)t} |\psi_0\rangle , \qquad t > 0 . \tag{3.42}$$

In order to study the entanglement for the harmonic chain, we need to know the following two-point correlators

$$\begin{aligned} \mathbb{Q}_{r,s}(t) &\equiv \langle \psi_0 | q_r(t) q_s(t) | \psi_0 \rangle , \\ \mathbb{P}_{r,s}(t) &\equiv \langle \psi_0 | p_r(t) p_s(t) | \psi_0 \rangle , \\ \mathbb{M}_{r,s}(t) &\equiv \langle \psi_0 | q_r(t) p_s(t) | \psi_0 \rangle , \end{aligned} \tag{3.43}$$

where $q_r(t)$ and $p_r(t)$ are the time evolved operators in the Heisenberg picture

$$q_r(t) = e^{\mathrm{i}Ht} q_r(0) e^{-\mathrm{i}Ht} , \qquad p_r(t) = e^{\mathrm{i}Ht} p_r(0) e^{-\mathrm{i}Ht} . \tag{3.44}$$

These correlators can be written as (see also [316] for a slightly different approach)

$$\mathbb{Q}_{r,s}(t) \;=\; \frac{1}{2L} \sum_{k=0}^{L-1} Q_k(t) \cos\left[(r-s) \frac{2\pi k}{L} \right], \tag{3.45}$$

$$\mathbb{P}_{r,s}(t) \;=\; \frac{1}{2L} \sum_{k=0}^{L-1} P_k(t) \cos\left[(r-s) \frac{2\pi k}{L} \right], \tag{3.46}$$

$$\mathbb{M}_{r,s}(t) \;=\; \frac{\mathrm{i}}{2} \delta_{r,s} - \frac{1}{2L} \sum_{k=0}^{L-1} M_k(t) \cos\left[(r-s) \frac{2\pi k}{L} \right], \tag{3.47}$$

where we collected the dependence on ω, ω_0 and t into

$$Q_k(t) \;\equiv\; \frac{1}{m\omega_k} \left(\frac{\omega_k}{\omega_{0,k}} \cos^2(\omega_k t) + \frac{\omega_{0,k}}{\omega_k} \sin^2(\omega_k t) \right), \tag{3.48}$$

$$P_k(t) \;\equiv\; m\omega_k \left(\frac{\omega_k}{\omega_{0,k}} \sin^2(\omega_k t) + \frac{\omega_{0,k}}{\omega_k} \cos^2(\omega_k t) \right), \tag{3.49}$$

$$M_k(t) \;\equiv\; \left(\frac{\omega_k}{\omega_{0,k}} - \frac{\omega_{0,k}}{\omega_k} \right) \sin(\omega_k t) \cos(\omega_k t) . \tag{3.50}$$

We notice that, for $t > 0$ and $\omega = 0$ the contribution from the mode $k = 0$ is finite, indeed

$$Q_0(t) \;=\; \frac{1}{m} \left(\frac{1}{\omega_0} + \omega_0 t^2 \right), \qquad P_0(t) \;=\; m\omega_0 , \qquad M_0(t) \;=\; -\,\omega_0 t . \tag{3.51}$$

The other modes are clearly always finite, and so we can consider the global quench to a massless Hamiltonian (while, as well known, we cannot set $\omega = 0$ for the equilibrium properties).

From the correlation functions, the entanglement entropy and negativity are constructed by standard methods. Indeed, given a subsystem A of the lattice made by $\tilde{\ell}$ sites which could be either all in one interval or splitted in many disjoint intervals, the reduced density matrix for A can be studied by constructing the $\tilde{\ell} \times \tilde{\ell}$ matrices $\mathbb{Q}_A$, $\mathbb{P}_A$ and $\mathbb{M}_A$, which are the restrictions to the subsystem A of the matrices $\mathbb{Q}$, $\mathbb{P}$ and $\mathbb{M}$ respectively [11, 12, 147, 148, 150, 151]. Given $\mathbb{Q}_A$, $\mathbb{P}_A$ and $\mathbb{M}_A$, the covariance matrix γ_A associated to the subsystem A and the symplectic matrix J_A of the corresponding size are

$$\gamma_A(t) \equiv \mathrm{Re} \begin{pmatrix} \mathbb{Q}_A(t) & \mathbb{M}_A(t) \\ \mathbb{M}_A(t)^{\mathrm{t}} & \mathbb{P}_A(t) \end{pmatrix}, \qquad J_A \equiv \begin{pmatrix} \mathbf{0}_{\tilde{\ell}} & \mathbb{I}_{\tilde{\ell}} \\ -\mathbb{I}_{\tilde{\ell}} & \mathbf{0}_{\tilde{\ell}} \end{pmatrix}, \tag{3.52}$$

where $\mathbb{I}_{\tilde{\ell}}$ is the $\tilde{\ell} \times \tilde{\ell}$ identity matrix and $\mathbf{0}_{\tilde{\ell}}$ is the $\tilde{\ell} \times \tilde{\ell}$ matrix with vanishing elements. We remark that the matrix $\mathbb{M}(t)$ has a non trivial real part for $t > 0$. At this point we compute the spectrum of $\mathrm{i}J_A \cdot \gamma_A(t)$ which can be written as $\{\pm\lambda_a(t); a = 1, \dots \tilde{\ell}\}$ with $\lambda_a(t) > 0$. The time dependent Rényi entropies as function of the eigenvalues $\lambda_a(t)$ are finally written in a similar way to their ground state counterpart, Eq. (2.71)

$$\mathrm{Tr}\, \rho_A(t)^n = \prod_{a=1}^{\tilde{\ell}} \left[\left(\lambda_a(t) + \frac{1}{2} \right)^n - \left(\lambda_a(t) - \frac{1}{2} \right)^n \right]^{-1}. \tag{3.53}$$

Also the entanglement entropy is computed as in the static case, Eq. (2.72)

$$S_A(t) = \sum_{a=1}^{\tilde{\ell}} \left[\left(\lambda_a(t) + \frac{1}{2} \right) \ln \left(\lambda_a(t) + \frac{1}{2} \right) - \left(\lambda_a(t) - \frac{1}{2} \right) \ln \left(\lambda_a(t) - \frac{1}{2} \right) \right]. \tag{3.54}$$

In order to compute the negativity, we denote by $A = A_1 \cup A_2$ a subregion of the harmonic chain and we consider the partial transpose with respect to A_2. In the covariance matrix γ_A, the net effect of the partial transposition is the inversion of the signs of the momenta corresponding to the sites belonging to A_2 [147]. Thus, introducing the $\tilde{\ell} \times \tilde{\ell}$ diagonal matrix $\mathbb{R}_{A_2}$ which has -1 in correspondence of the sites of A_2 and $+1$ otherwise, we can construct

$$\gamma_A^{T_2}(t) \equiv \begin{pmatrix} \mathbb{I}_{\tilde{\ell}} & \mathbf{0}_{\tilde{\ell}} \\ \mathbf{0}_{\tilde{\ell}} & \mathbb{R}_{A_2} \end{pmatrix} \cdot \gamma_A(t) \cdot \begin{pmatrix} \mathbb{I}_{\tilde{\ell}} & \mathbf{0}_{\tilde{\ell}} \\ \mathbf{0}_{\tilde{\ell}} & \mathbb{R}_{A_2} \end{pmatrix}, \tag{3.55}$$

and compute the spectrum of $\mathrm{i}J_A \cdot \gamma_A^{T_2}(t)$, which again can be written as $\{\pm\chi_a(t); a = 1, \dots \tilde{\ell}\}$ with $\chi_a(t) > 0$. Then, the trace of the n-th power of $\rho_A^{T_2}$ is

$$\mathrm{Tr}(\rho_A^{T_2})^n = \prod_{a=1}^{\tilde{\ell}} \left[\left(\chi_a(t) + \frac{1}{2} \right)^n - \left(\chi_a(t) - \frac{1}{2} \right)^n \right]^{-1}, \tag{3.56}$$

while the trace norm reads

$$||\rho_A^{T_2}|| = \prod_{a=1}^{\tilde{\ell}} \left[\left| \chi_a(t) + \frac{1}{2} \right| - \left| \chi_a(t) - \frac{1}{2} \right| \right]^{-1} = \prod_{a=1}^{\tilde{\ell}} \max \left[1, \frac{1}{2\chi_a(t)} \right], \tag{3.57}$$

which gives the logarithmic negativity $\mathcal{E} = \ln(||\rho_A^{T_2}||)$.

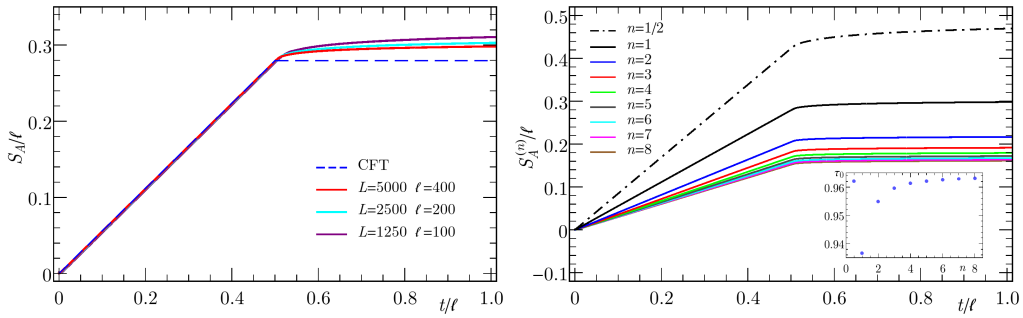

Figure 3.3: Left: Temporal evolution of the entanglement entropy for one interval of ℓ sites in a periodic harmonic chain with L sites. At $t = 0$ the mass is quenched from $\omega_0 = 1$ to $\omega = 0$. The dashed curve is the CFT prediction (3.17) with $c = 1$ and the best fitted value for τ_0. Right: Temporal evolution of the Rényi entropies and of the logarithmic negativity $\mathcal{E}_A$, which coincides with $S_A^{(1/2)}$ in this case, for a periodic chain with $L = 5000$ and $\ell = 400$. In the inset, we report the best fitted values of τ_0 for the values of n displayed in the main plot.

In what follows we will compute entanglement entropies and negativity from the above formulas by calculating the spectrum of the appropriate covariance matrix. Since the parameters K and m can be absorbed in a redefinition of the canonical variables, we fix them to $K = m = 1$ and we just consider a quench in the frequency (or mass) parameter from ω_0 to ω. The data obtained by numerically diagonalising the covariance matrix for several bi- and tripartitions of the harmonic chain are reported in the following subsections.

3.5.1 The entanglement entropy of one interval

It is instructive to start our analysis from the study of the quench dynamics of the entanglement entropy of a single interval, although this has been recently studied in Ref. [316]. Indeed, this preliminary analysis allows us to understand the regime of applicability of the CFT and the optimal quench parameters in order to observe a CFT scaling.

In Fig. 3.3, we report the time evolution of the entanglement entropy for a quench from $\omega_0 = 1$ to $\omega = 0$. We consider finite chains of length up to $L = 5000$ and several values of $\ell \ll L$ with ℓ/L kept fixed. It is evident from the figure that the behaviour of von Neumann and Rényi entropy is in good qualitative agreement with the CFT prediction (3.17) with a linear growth for $t < \ell/2$ followed by saturation for $t > \ell/2$ (we recall that for $\omega = 0$ the maximum mode velocity is $v_{\max} = 1$, cf. Eq. (3.40)). However, few comments on these results are needed. First, for $t > \ell/2$ the entanglement entropies do not saturate but they show a slow growth toward an asymptotic value. This is a well known phenomenon [104, 304] and it is due to the entanglement generated by slow quasi-particles moving with velocity $v_k < v_{\max} = 1$ as in Eq. (3.39). A second comment concerns the fitted value of τ_0: this is shown in the inset of Fig. 3.3 as function of the order of the Rényi entropy n. There is a minor dependence on n, as already anticipated and noticed in the literature [316], but overall τ_0 is very close to the initial correlation length $\xi_0 \sim \omega_0^{-1} = 1$. Finally we must comment on the chosen value of $\omega_0 = 1$. In preliminary calculations we considered several values of ω_0 which however we do not report here, but $\omega_0 = 1$ is the one for which the conformal scaling describes the data more accurately. This can be easily understood from the fact that (i) we should be in the regime $t, \ell \gg \omega_0^{-1}$ requiring

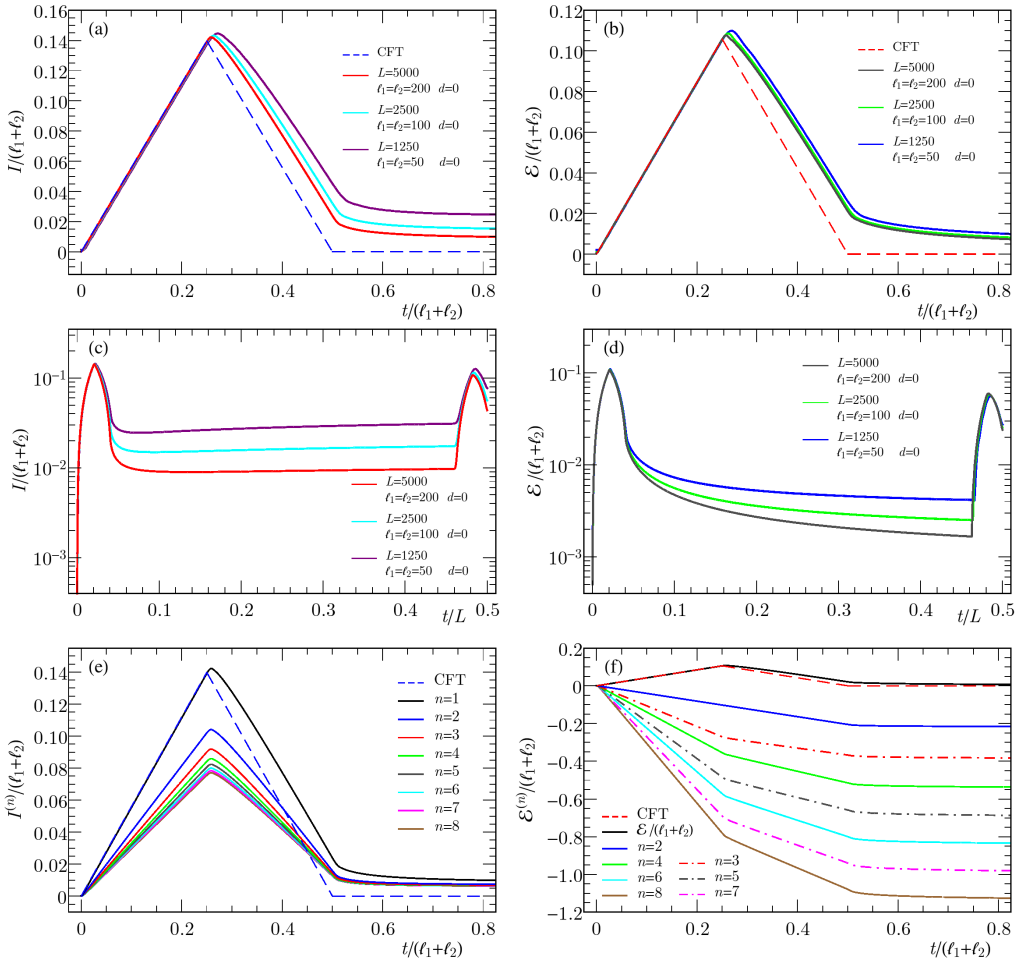

Figure 3.4: Adjacent intervals with several equal lengths $\ell_1 = \ell_2$ and for various total size L of the periodic harmonic chain. All panels show the data for $\omega_0 = 1$ and a critical evolution, $\omega = 0$. Panels (a) and (c) display the mutual information I while (b) and (d) the logarithmic negativity $\mathcal{E}$. Top and middle panels show different time scales and the revivals due to the finiteness of the system are evident in the middle panels, where a larger range of t is considered. The dashed CFT curves in (a) and (b) are given by (3.19) and (3.28) respectively. In the last two panels we show the time evolution of the Rényi mutual information $I^{(n)}$ (e) and of the replicated negativity $\mathcal{E}^{(n)}$ (f) for various values of n.

that the initial frequency should not be too small, (ii) we should be in a regime in which the continuum description is appropriate, requiring the initial correlation length not to be too small (i.e. ω_0 not too large), in order to avoid a magnification of lattice effects. The value $\omega_0 \sim 1$ appears to be the best compromise between these two effects.

The Rényi entropy with $n = 1/2$ corresponds to the logarithmic negativity, but, as expected, does not display any peculiar behaviour compared with the other values of n.

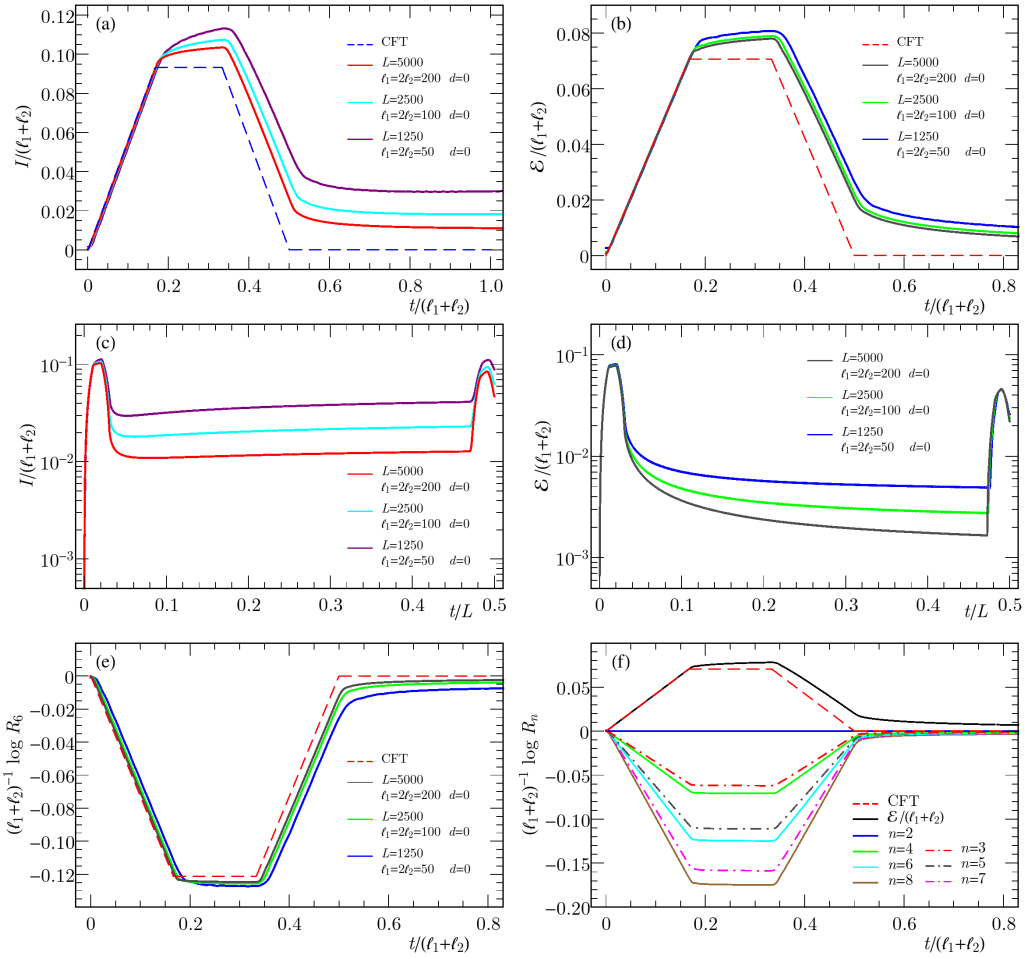

Figure 3.5: Adjacent intervals with different lengths $\ell_1 = 2\ell_2$ for different intervals lengths and total size L of the periodic harmonic chain. Critical evolution of the mutual information I (panel (a), (c)) and of the logarithmic negativity $\mathcal{E}$ (panels (b), (d)). The revivals are reported in panels (c) and (d). Notice that outside the light cone $\mathcal{E}$ always decays while I reaches a plateau (apart from some finite size effects responsible of a very slow increase) (panels (c) and (d)). Compared to Fig. 3.4 for the case of intervals with equal length, we observe a plateau starting at $t \simeq \min(\ell_1, \ell_2)/2$ with temporal width $|\ell_2 - \ell_1|/2$. The panel (e) and (f) report the ratios R_n for several values of n.

3.5.2 Two adjacent intervals

We start the study of the entanglement between two different intervals from the case of adjacent ones. In the various figures that will follow we report both the mutual information and the negativity in order to simplify the discussion of similarity and differences. As already stressed above, the principal new results of this chapter concern the evaluation of the negativity, since the time dependence of the mutual information in CFT was already established in [104] and these results were checked in a few numerical works for the Ising chain [222] and the Bose-Hubbard model [309], but, to the best of our knowledge, not for

the harmonic chain.

The numerical results for two adjacent intervals for a quench from $\omega_0 = 1$ to $\omega = 0$ are shown in Figs. 3.4 and 3.5. The main differences between the two sets of plots is that in the first one the two intervals have equal lengths, while in the second one the length of one interval is half of the other. Let us discuss these two sets of plots critically. In the top panels of Fig. 3.4, we report the time evolution of the mutual information (a) and logarithmic negativity (b) on time scales of the order of ℓ. They have a very similar behaviour characterised by an initial linear growth, followed by an almost linear dropping up to time $t = \ell_1$ when a slow power-law relaxation to the asymptotic vanishing value starts. These results are in agreement with the expectation from CFT and their behaviour is simply understood in terms of the quasi-particle picture as already explained in Sec. 3.4. Also the differences between the linear CFT behaviour and the non-linear one of the actual data is easily understood in terms of the slow quasi-particles in analogy to the entanglement entropy of a single interval in the previous subsection. No particular difference is observed in this regime between negativity and mutual information. In the two middle panels of Fig. 3.4, we again report the time evolution of the mutual information (c) and logarithmic negativity (d), but on time scales of the order of the system's size L. The main feature in this case is the presence of quantum revivals at time equal to $t \simeq (L - [\ell_1 + \ell_2])/2$. A first important difference between the mutual information and the negativity appears on these time-scales, indeed while the former reaches a plateau in a large time-window, the latter decreases monotonically until the revival. Finally, in the last two panels we also report the Rényi mutual information (e) and the replicated negativity $\mathcal{E}^{(n)}$. Their behaviour is again in qualitative agreement with the CFT predictions and the differences are easily understood in terms of slow quasi-particles. However, we mention that $\mathcal{E}^{(n)}$ with $n > 1$ does not follow the same behaviour as the mutual information or negativity and indeed it is a monotonically decreasing function of time, changing the slope in the time intervals identified above (i.e. at $t = \ell_1/2$ and at $t = \ell_1$). This is not a surprise since $\mathcal{E}^{(n)}$ is not a measure of entanglement and neither a quantifier of the correlations. However, as already stressed, the piece-wise quasi-linear behaviour is compatible with the CFT prediction apart from the effect of the slow modes.

In Fig. 3.5, we report the case of two adjacent intervals of different lengths $\ell_1 = 2\ell_2$. The main difference compared to the case of equal lengths is the appearance of a plateau after the first linear increase for both the mutual information and the negativity. This is in perfect agreement with the CFT results which indeed predict (see Eqs. (3.19) and (3.28)) a linear increase up to $t = \min(\ell_1, \ell_2)/2$, followed by a plateau for $\min(\ell_1, \ell_2)/2 < t < \max(\ell_1, \ell_2)/2$, a linear decrease for $\max(\ell_1, \ell_2)/2 < t < (\ell_1 + \ell_2)/2$, and finally zero constantly. It is evident that the differences between CFT and actual data for the harmonic chain are due to slow quasi-particles which give corrections for $t > \min(\ell_1, \ell_2)/2$. In the panel (c) and (d) of Fig. 3.5 we show the evolution of mutual information and negativity for a larger time window and, as before, the revivals are apparent at time $t = (L - \ell_1 - \ell_2)/2$. Finally in the last two panels (e) and (f) we report the behaviour of the universal ratio R_n as a function of time. Again there are no particular differences with the CFT prediction except for those ones due to slow quasi-particles. From the last panel (f), one notices that $R_2 = 1$ identically. In the quantum field theory approach, this exceptional behaviour for $n = 2$ is easily understood from the fact that $\mathcal{T}_2^2 = \bar{\mathcal{T}}_2^2 = \mathbb{I}$ (cf. Sec. 3.3.3) and it is true also on the lattice. Notice that $\ln(R_n)$ has a behaviour which closely resembles the one of the mutual information and the negativity, showing that, in this particular case, they are somehow measuring the amount of correlations or entanglement. This is an important difference compared to the quantity $\mathcal{E}^{(n)}$ in Fig. 3.4.

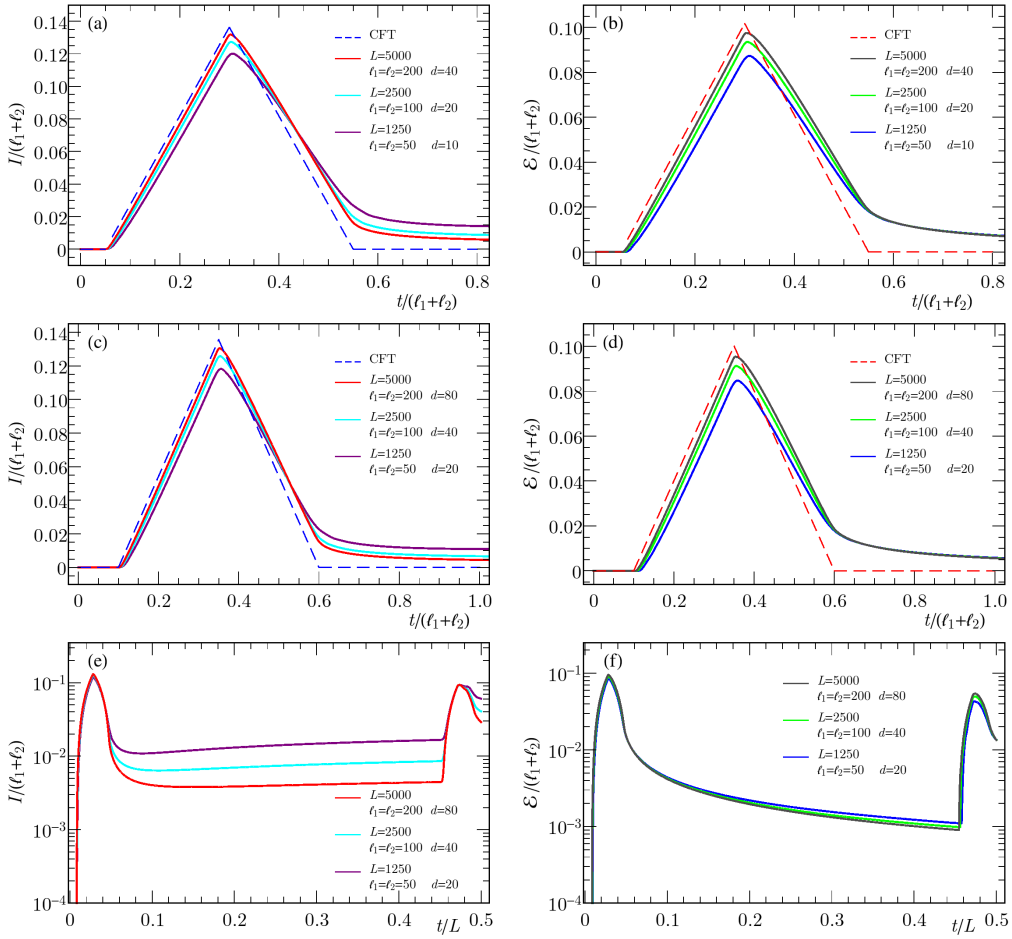

Figure 3.6: Disjoint intervals with equal lengths $\ell_1 = \ell_2$ separated by d sites, for various intervals lengths, separations d, and total size L of the periodic harmonic chain. Time evolution of the mutual information I ((a), (c) and (e)) and of the logarithmic negativity $\mathcal{E}$ ((b), (d), and (f)). The revivals at large t are evident in the bottom panels.

3.5.3 Two disjoint intervals

In this subsection we move to the case of two disjoint intervals. In Fig. 3.6 we report the numerically calculated mutual information and negativity for two disjoint intervals of equal length and for two different sets of distances between them. It is clear from the figure that the main difference compared to the case of adjacent interval is that there is an initial region for $t < d/2$ in which there is no entanglement and no correlations (we recall that the initial correlation length is $\omega_0^{-1} = 1$, so that the initial entanglement is very small). Then at time equal to $d/2$ the entanglement starts growing linearly, reaches a maximum and then decreases almost linearly. Again, this behaviour is compatible with the quasi-particle interpretation and also the power law relaxation for large times can be understood in terms of slow modes. Even in the case of disjoint intervals, we have studied the revivals. The results, which are very similar to the ones shown in the case of adjacent

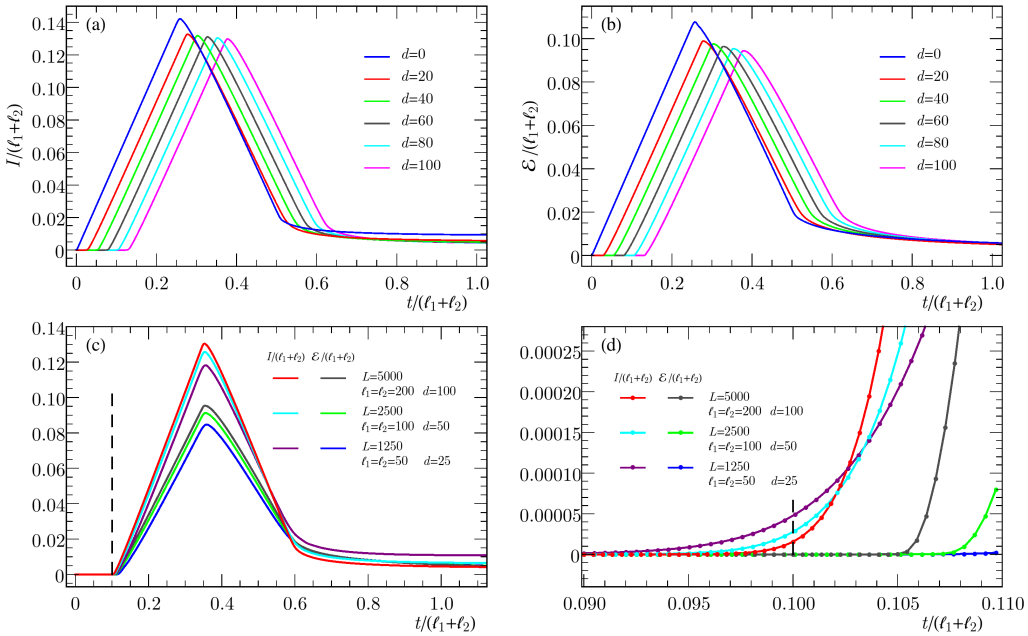

Figure 3.7: Mutual information (a) and the logarithmic negativity (b) of disjoint intervals with equal lengths $\ell_1 = \ell_2 = 200$, separated by distances d in a periodic chain with $L = 5000$. (c) Comparison between I and $\mathcal{E}$. (d) Zoom of the initial growth: a late birth effect for $\mathcal{E}$ is observed, which decreases as the continuum limit is approached. The vertical dashed line in (c) and (d) indicates the time $t = d/2$ where the growth should start in the continuum theory.

intervals, are reported in Fig. 3.6, panels (e) and (f).

Conversely, a very interesting phenomenon can be observed by looking at very short times after the entanglement starts growing. This is illustrated in Fig. 3.7, where in the top panels we show the mutual information and the negativity as function of time for different distances between the two intervals. As before, the behaviour is very reminiscent of the CFT prediction. In the panel (c) of the same figure, we show in the same plot the negativity and the mutual information for fixed d/ℓ and looking closely to the time when the entanglement starts growing it is already clear that something is happening. For this reason in the panel (d) we zoom close to the point $t = d/2$ and we highlight a very peculiar phenomenon: while the mutual information starts moving from zero slightly before $t = d/2$ the negativity starts slightly after $t = d/2$. The behaviour of the mutual information is simply the exponential tails of the correlations outside the light-cone, but the behaviour of the negativity is new. From the figure, it is evident that increasing the total system size L (at fixed ratios d/L and ℓ/L) this phenomenon disappears in such a way to recover the CFT result and the quasi-particle interpretation of the evolution in the continuum limit. As a consequence, this remarkable phenomenon is a lattice effect and so cannot have an explanation in terms of quasi-particles, but it would be interesting to understand its precise origin. In a suggestive way, and in analogy with the famous sudden death of entanglement [318] (which will be discussed below), we term this phenomenon as the *late birth of entanglement*.

In Fig. 3.8 we consider again the mutual information (a) and the negativity (b) for

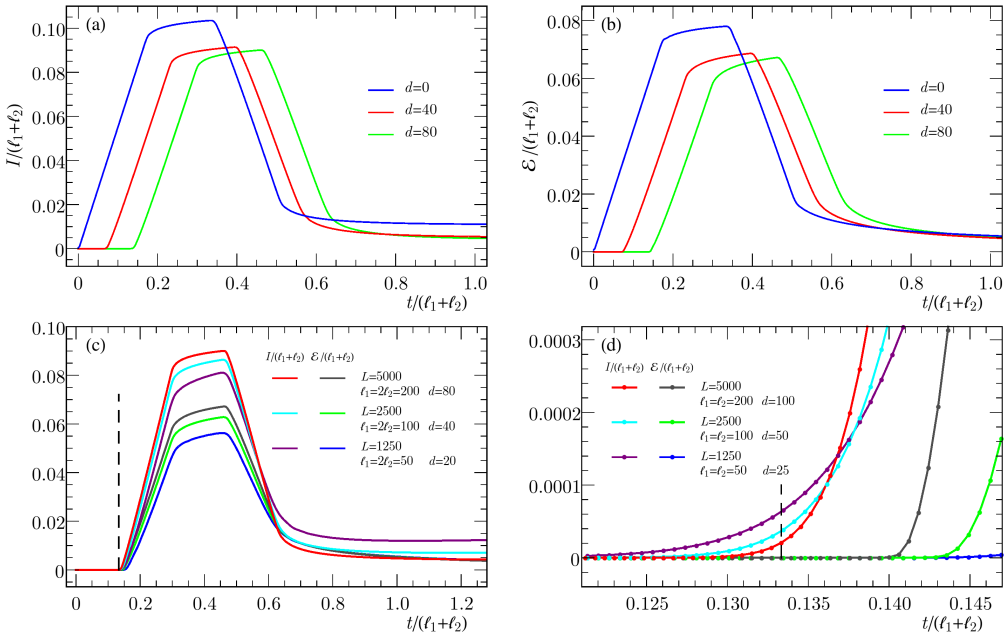

Figure 3.8: Mutual information (a) and the logarithmic negativity (b) of disjoint intervals with different lengths $\ell_1 = 2\ell_2 = 200$, separated by various distances d sites in a periodic chain with $L = 5000$. Comparison between I and $\mathcal{E}$ in (c) and zoom on the initial growth in (d), to highlight the late birth of $\mathcal{E}$. With respect to the corresponding plots in Fig. 3.7, here a plateau occurs whose temporal width is $|\ell_2 - \ell_1|/2$. The vertical dashed line in (c) and (d) indicates the time $t = d/2$ where the growth should begin, according to the quasi-particles picture.

various distances between two intervals of different lengths $\ell_1 = 2\ell_2$. The behaviour is in perfect agreement with the CFT prediction with a linear growth starting at $d/2$ up to $d/2 + \min(\ell_1, \ell_2)/2$, followed by a plateau lasting $|\ell_1 - \ell_2|/2$, then a linear decrease up to $t = (d + \ell_1 + \ell_2)/2$ and finally a power-law approach to zero. In the panel (c) we report on the same plot the negativity and the mutual information, observing again the fingerprints of the late birth, which are straightforwardly confirmed by zooming for times close to $d/2$, as done in panel (d).

3.5.4 Massive evolution

In this section we briefly discuss what happens when the time evolution is governed by a massive Hamiltonian. This is elucidated with an example in Fig. 3.9 where we report and compare critical ($\omega = 0$) and noncritical ($\omega = 0.1$) evolution of the logarithmic negativity always starting from $\omega_0 = 1$. The data are reported against $v_{\max} t$ ($v_{\max}$ is given by Eq. (3.40)). Also in this case, the data are perfectly compatible with the quasi-particle picture, but we notice an interesting effect. The slope of the negativity changes as a function of time as a consequence of the entanglement carried by slower quasi-particles which in the case of the non-critical evolution have a larger weight because of the non-monotonicity of v_k in Eq. (3.39). However, also this phenomenon does not come as a surprise and indeed it was already observed for the entanglement entropy of a single interval following a quench in the Ising/XY chain [288, 304].

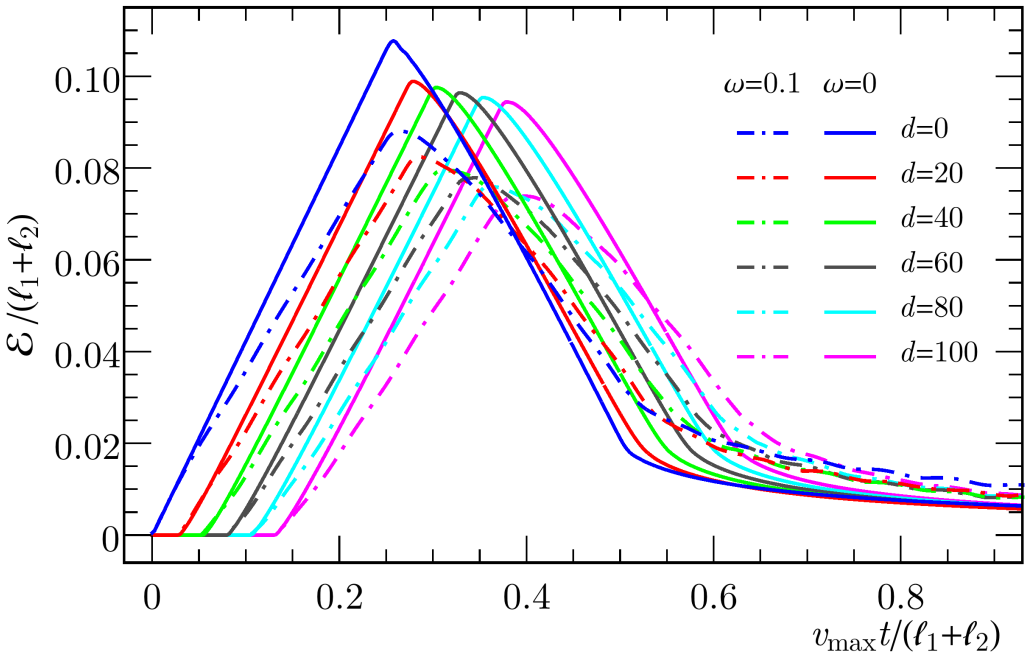

Figure 3.9: Logarithmic negativity $\mathcal{E}$ of disjoint intervals after global quenches with different evolution Hamiltonians. Here $L = 5000$, $\ell_1 = \ell_2 = 200$ and $\omega_0 = 1$, while for $t > 0$ we have $\omega = 0$ or $\omega = 0.1$. The velocity $v_{\max}$ is given by Eq. (3.40).

3.5.5 Sudden death of entanglement

A final important feature of the logarithmic negativity $\mathcal{E}$ is the so called *sudden death* of entanglement. The phenomenon has been first introduced for other entanglement measures [318], but it has been observed also for the negativity. For example, in the case of the harmonic chain at thermal equilibrium at some finite T, it consists into the exact vanishing of $\mathcal{E}$ for temperatures larger than a critical value as discussed also in [121–124, 137], where it was emphasised its lattice nature and its absence in the quantum field theory description of the continuum limit. In the case of quench, we have already seen that the entanglement and the mutual information of two intervals are vanishing for large enough time in the CFT, but this is an independent phenomenon compared to the sudden death.

In order to show the true sudden death of $\mathcal{E}$ after a global quench, we report in Fig. 3.10 the negativity and we compare it to the mutual information for several initial frequencies $\omega_0 = 10$, $\omega_0 = 30$ and $\omega_0 = 100$ and for several configurations of the intervals. It is evident that in all cases, while the mutual information stays finite at any time, the negativity $\mathcal{E}$ drops suddenly to zero after some time. Thus, the sudden death is a peculiarity of the entanglement and it is not reflected by the correlations (quantified by the mutual information) which are always a smooth function of the time. Let us now discuss how this phenomenon depends on the various parameters. First, we notice that increasing the system size and keeping the ratios between the various lengths fixed, the sudden death time increases and, when the system and the subsystems are large enough, the sudden death does not occur anymore. This agrees with the expectation that the

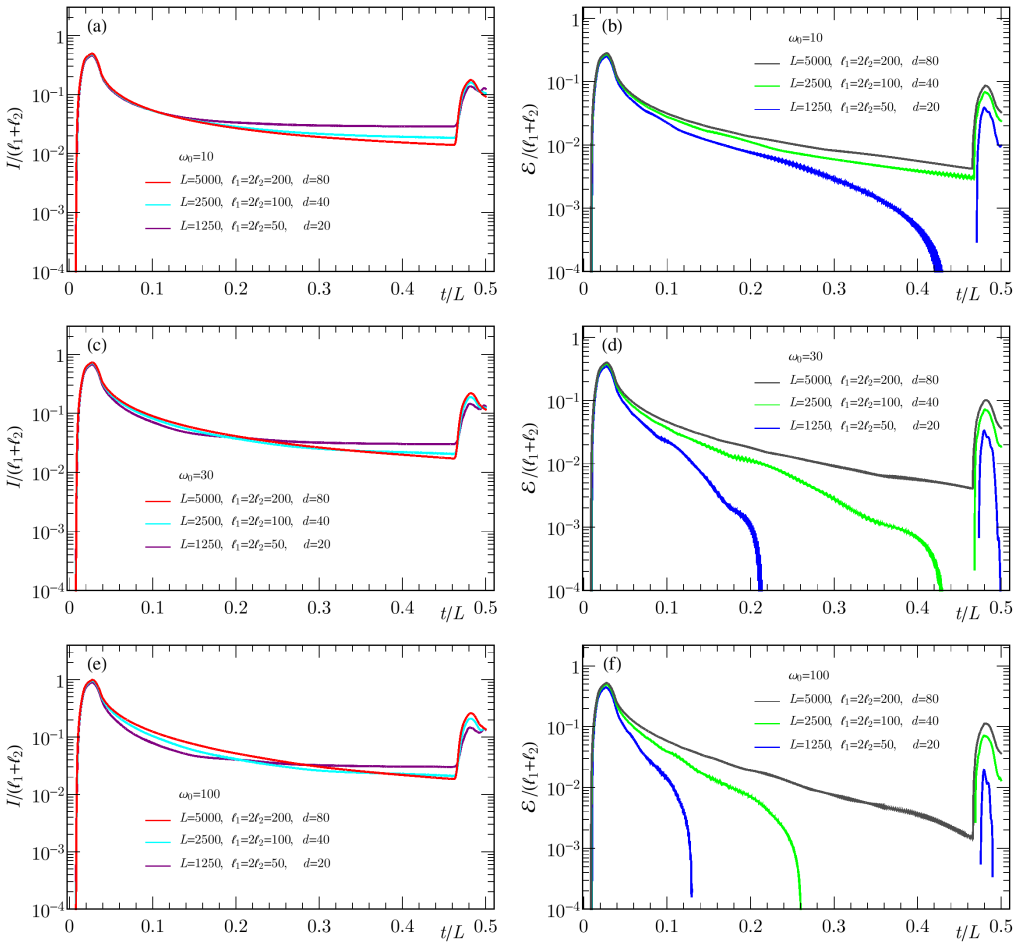

Figure 3.10: Mutual information (left panels) and logarithmic negativity (right panels) for disjoint intervals with different lengths ($\ell_1 = 2\ell_2$). Here $\omega = 0$ and different ω_0 are chosen: $\omega_0 = 10$, $\omega_0 = 30$ and $\omega_0 = 100$ (top, middle and bottom panels respectively). The sudden death of the logarithmic negativity happens for later time as L increases and as ω_0 decreases.

sudden death is a lattice effect. Second we observe that the sudden death depends also on the initial frequency ω_0: increasing ω_0, the sudden death time decreases. Finally, it is worth noticing that, when the revival takes place, the entanglement appears again, but this is not at all surprising.

3.6 Conclusions

We studied the evolution of the entanglement negativity following a quantum quench. We considered the case of a conformal evolution starting from a boundary state. First, for the sake of completeness, we reviewed the results for the entanglement entropy and the mutual information of an arbitrary number of (adjacent or disjoint) intervals within the path integral approach of Refs. [104, 106, 271]. Then we moved to the calculation of

the negativity between two adjacent and disjoint intervals which are respectively given by Eqs. (3.28) and (3.35). The applicability and generality of these results have been checked against exact numerical calculations for the same quantities in the harmonic chain. We also highlight two peculiar lattice effects: the late birth of entanglement and its sudden death. The former one consists in the fact that the negativity starts growing slightly after the time predicted by the quasi-particle picture, a delay which vanishes in the continuum limit. The latter one, instead, is well known and concerns the exact vanishing of the negativity after some given large time (but before revivals take place). We investigated how these effects depend on the quench parameters.

One of the main results of this study is that the quasi-particle picture [104] for the time dependence of the entanglement after a global quantum quench applies also to the negativity between two intervals: this is a remarkable and non-trivial property. The last conclusion should be interpreted in the sense that the quasi-particle picture for the negativity holds as far as it holds for the entanglement entropy, as both are consequences of the assumptions on the relevant singularities of the three- or four-point function of twist fields on the strip. It has recently argued in Ref. [319] that the actual presence of some of these singularities, which are denoted as "light-cone singularities", are not guaranteed by the OPEs on the UHP only. If these singularities are milder or not present in the twist field correlation functions, then the quasi-particle interpretation fails in some time regimes. The author of [319] find that such light-cone singularities are always present for rational CFT (such as the minimal models) and for the $c = 1$ CFT of the compactified boson. On the contrary, they claim that the singularities are milder, or even not present at all, when the theory is not current dominated, that is roughly when the asymptotic number of conserved currents (parametrized by an effective central charge c_{current}) is smaller than the total number of states (parametrized by c, the central charge). Strictly speaking, they consider a setup which is different from the one studied here. Indeed, they use a thermofield double entangled state (in a slightly simplified geometry), whose quench evolution has been studied in [91]. They perform a computation in the second Rényi entropy of two disjoint intervals as function of c and c_{current} and they find that the quasi-particle result is valid in all time regimes only for $c = c_{\text{current}}$. When this is not true, the result in some regimes is not universal, and the quasi-particle result provides a lower bound for the entanglement. Higher order Rényis are unfortunately unaccessible. They suspect (but give no proof) that the evolution from a boundary state cannot have more singularities than those in the thermal double, thus supporting their conclusions also for this case. Holographic CFT has $c \gg 1$, while they have few chiral states, $c_{\text{current}} \sim 1$. With explicit holographic computations, the authors show that the quasi-particle picture for the entanglement entropy and the second Rényi entropy does not hold in the thermofield double setup and, in the language of [319], entanglement *scrambles* maximally (an effect that was already observed in [85, 87, 96, 320]). In this extreme setup, the result is not the one predicted by the quasi-particle picture, but nevertheless it is again universal. With the semiclassical conformal block analysis for large-c CFT introduced in [321] and first used in this context in [98], they also show that indeed in this case light-cone singularities are totally absent. At this point it would be nice to exactly compute (analytically or numerically) the evolution of entanglement and Rényi entropies in a CFT with $c_{\text{current}} < c < \infty$, to have a direct check, both in the thermofield double setup and in the case of a boundary conformal initial state. Unfortunately, most of the well known CFT are among the ones where the quasi-particle picture holds, so no computations are available up to now. The authors provide two candidate theories to be the simplest ones, and it would be very interesting to further explore this issue in the

future.

As for the harmonic chain, it would be very interesting to obtain analytical forms for the evolution of the various entanglement measures (entropy, mutual information, and negativity) in analogy to what done in Refs. [222, 304, 322–324] for the Ising model (but only for entropy and mutual information). However, we should stress that there are still no analytic results for the entanglement entropy of bosonic models even in the ground state, in contrast with the many results available for free fermion thanks to Toeplitz matrix techniques [262, 263, 325–327]. Obtaining such analytic predictions is a prerequisite in order to tackle the quench problem.

Chapter 4

Partial transpose of two disjoint blocks in XY spin chain

4.1 Introduction

In the Introduction we described a systematic path integral approach to construct the partial transpose of the reduced density matrix, from which the negativity in 1+1 dimensional relativistic quantum field theories is obtained via a replica trick [134]. This approach has been successfully applied to the study of one-dimensional CFT in different settings, and has been tested against exact results for free bosonic systems, such as the harmonic chain. As we mentioned in the Introduction and saw explicitly in Sec. 3.5 in an out-of-equilibrium situation, for bosonic Gaussian states the spectrum of the partial transpose can be obtained from correlation matrix techniques [148–151]. Specifically, the partial transposition corresponds to a time-reversal operation leading to a partially transposed reduced density matrix which is again Gaussian [147], whose spectrum can be therefore calculated from the one of its correlation matrix. The latter is obtained by simply implementing the time-reversal operation on the correlation matrix of the reduced density matrix (see Eq. (3.55)).

In the case of free fermionic systems (such as the tight-binding model and XY spin chains) the calculation of the negativity is instead much more involved. Indeed the partial transpose of the reduced density matrix is not a Gaussian operator and standard techniques based on the correlation matrix cannot be applied. In view of the importance that exact calculations for free fermionic systems played in the understanding of the entanglement entropy [245, 262, 325, 326, 328–330], it is highly desirable to have an exact representation of the negativity also for free fermionic systems. A major step in this direction has been achieved by Eisler and Zimboras [331] who showed that the partial transpose is a linear combination of two Gaussian operators. Unfortunately, it is still not possible to extract the spectrum of the partial transpose and hence the negativity, but at least one can have access to integer powers of the partial transpose which are the main ingredient for the replica approach to negativity. Let us stress that these considerations apply only when the Wick theorem holds and this excludes interacting models (e.g. the XXZ model).

In Ref. [331] only truly fermionic systems have been considered and not spin chains that can be mapped to a fermionic system by means of a (non-local) Jordan-Wigner

transformation. Indeed, in the very interesting case of two disjoint blocks in a spin chain the density matrix of spins and fermions are not equal [220, 222, 243] and this consequently affects also the partial transposition, as already pointed out in [331]. In this chapter we give an exact representation of the partial transpose of the reduced density matrix for two disjoint blocks in the XY spin chain and from this we calculate the traces of its integer powers. These turn out to converge to the CFT predictions in the limit of large intervals.

The chapter is organised as follows. In Sec. 4.2 we describe the model and the definition of the quantities we will study. In Sec. 4.3 we review the results of Ref. [222] for the moments of the spin reduced density matrix of two disjoint blocks. In Sec. 4.4 we move to the core of this manuscript deriving an explicit representation of the partial transpose of the spin reduced density matrix as a sum of four Gaussian fermionic matrices. This allows to obtain explicit representations for the moments of the partial transpose. In Sec. 4.5 we use the above results to numerically calculate these moments up to $n = 5$ for the critical Ising model and XX chain and carefully compare them with CFT predictions by taking into account corrections to the scaling. Finally in Sec. 4.6 we draw our conclusions.

4.2 The model and the quantities of interest

In this chapter we consider the XY spin chains with Hamiltonian

$$H_{\rm XY} = -\frac{1}{2}\sum_{j=1}^{L}\left(\frac{1+\gamma}{2}\,\sigma_j^x\sigma_{j+1}^x + \frac{1-\gamma}{2}\,\sigma_j^y\sigma_{j+1}^y + h\,\sigma_j^z\right), \tag{4.1}$$

where σ_j^α are the Pauli matrices at the j-th site and we assume periodic boundary conditions $\sigma_{L+1}^\alpha = \sigma_1^\alpha$. For $\gamma = 1$ Eq. (4.1) reduces to the Hamiltonian of the Ising model in a transverse field while for $\gamma = 0$ to the one of the XX spin chain. The Hamiltonian (4.1) is a paradigmatic model for quantum phase transitions [332]. In fact, it depends on two parameters: the transverse magnetic field h and the anisotropy parameter γ. The system is critical for $h = 1$ and any γ with a transition that belongs to the Ising universality class. It is also critical for $\gamma = 0$ and $|h| < 1$ with a continuum limit given by a free compactified boson.

The Jordan-Wigner transformation

$$c_j = \Big(\prod_{m<j}\sigma_m^z\Big)\frac{\sigma_j^x - \mathrm{i}\sigma_j^z}{2}, \qquad c_j^\dagger = \Big(\prod_{m<j}\sigma_m^z\Big)\frac{\sigma_j^x + \mathrm{i}\sigma_j^z}{2}, \tag{4.2}$$

maps the spin variables into anti-commuting fermionic ones $\{c_i, c_j^\dagger\} = \delta_{ij}$. In terms of these fermionic variables the Hamiltonian (4.1) becomes

$$H_{\rm XY} = \sum_{i=1}^{L}\left(\frac{1}{2}\left[\gamma c_i^\dagger c_{i+1}^\dagger + \gamma c_{i+1}c_i + c_i^\dagger c_{i+1} + c_{i+1}^\dagger c_i\right] - h c_i^\dagger c_i\right), \tag{4.3}$$

where we neglected boundary and additive terms. This Hamiltonian is quadratic in the fermionic operators and hence can be straightforwardly diagonalised in momentum space by means of a Bogoliubov transformation.

For the study of the reduced density matrices it is very useful to introduce the Majorana fermions [245, 328]

$$a_j^x = c_j + c_j^\dagger, \qquad a_j^y = \mathrm{i}(c_j - c_j^\dagger), \tag{4.4}$$

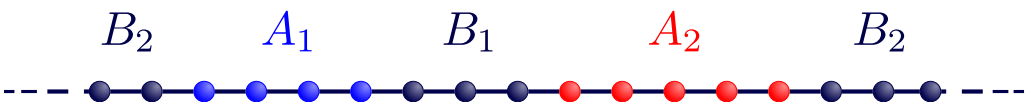

Figure 4.1: We consider the entanglement between two disjoint spin blocks A_1 and A_2 embedded in a spin chain of arbitrary length. The reminder of the system is denoted by B which is also composed of two disconnected pieces B_1 and B_2.

which satisfy the anti-commutation relations $\{a_i^\alpha, a_j^\beta\} = 2\delta_{ij}\delta_{\alpha\beta}$. The single site Majorana operators can be also written as

$$a_j^x = \Sigma_j^x, \qquad a_j^y = -\Sigma_j^y, \qquad \mathrm{i}\, a_j^x a_j^y = \Sigma_j^z. \tag{4.5}$$

The operators Σ_j^α on the single site satisfy the algebra of the Pauli matrices, but at different sites they anticommute and so they are not proper spin operators and should not be confused with the σ_j^α in (4.1). For each site, we also need to define the following unitary operator

$$U_\alpha^{(k)} = e^{\mathrm{i}\frac{\alpha}{2}\Sigma_j^k} = \cos(\alpha/2)\,\mathbb{I} + \mathrm{i}\sin(\alpha/2)\,\Sigma_j^k, \tag{4.6}$$

whose action on the Majorana operators (4.5) can be obtained from the following relation

$$U_{-\alpha}^{(k)}\,\Sigma_j^b\,U_\alpha^{(k)} = \big[\delta_{k,b} + (1-\delta_{k,b}\cos\alpha)\big]\Sigma_j^b + (\sin\alpha)\varepsilon_{kb\ell}\,\Sigma_j^\ell, \tag{4.7}$$

where $\varepsilon_{kb\ell}$ is the totally antisymmetric tensor such that $\varepsilon_{xyz} = 1$.

The main goal of this chapter is to determine the entanglement between two disjoint intervals in the XY spin chain. We consider the geometry depicted in Fig. 4.1: a spin chain is divided in two parts A and B and each of them is composed of disconnected pieces. We denote by A_1 and A_2 the two blocks in $A = A_1 \cup A_2$, B_1 is the block in B separating them, while B_2 is the remainder.

In the case of two disjoint blocks in the XY spin chain, the Rényi entropies for integer n (or equivalently the moments of the reduced density matrix ρ_A) have been explicitly constructed in Ref. [222]. However it is still not possible to find the analytic continuation to arbitrary complex values of n and consequently the entanglement entropy. This is very similar to the CFT counterpart where also one can calculate only integer moments of the reduced density matrices.

However, we are here interested in the entanglement between A_1 and A_2. A measure of this entanglement is provided by the logarithmic negativity defined and largely discussed in the Introduction.

4.3 Rényi entropies

In this section we review the results of Ref. [222], where the Rényi entropies of two disjoint blocks $A = A_1 \cup A_2$ for the XY spin chains have been computed. These results are the main ingredients to construct the integer powers of the partial transpose which will be derived in the following section. We will denote the number of spins in A_1 and A_2 with ℓ_1 and ℓ_2 respectively and the remainder of the system B contains a region separating A_1 and A_2 denoted as B_1, as pictorially depicted in Fig. 4.1.

In a general spin 1/2 chain the reduced density matrix $\rho_A = \mathrm{Tr}_B\,|\Psi\rangle\langle\Psi|$ of $A = A_1 \cup A_2$ can be computed by summing all the operators in A as follows [245, 328]

$$\rho_A = \frac{1}{2^{\ell_1+\ell_2}} \sum_{\nu_j} \Big\langle \prod_{j\in A} \sigma_j^{\nu_j} \Big\rangle \prod_{j\in A} \sigma_j^{\nu_j}, \tag{4.8}$$

where j is the index labelling the lattice sites and $\nu_j \in \{0,1,2,3\}$, with $\sigma^0 = \mathbf{1}$ the identity matrix and $\sigma^1 = \sigma^x$, $\sigma^2 = \sigma^y$ and $\sigma^3 = \sigma^z$ the Pauli matrices. The multipoints correlators in (4.8) are very difficult to compute, unless there is a representation of the state in terms of free fermions.

For the single interval case, the Jordan-Wigner string $\prod_{m<j} \sigma^z_m$ in Eq. (4.2) maps the first ℓ spins into the first ℓ fermions [245, 328] so the spin and fermionic density matrix are the same. This operator is Gaussian and it can be written as [245, 328]

$$\rho_A = \rho_A^{\mathbf{1}} \equiv \frac{1}{2^{\ell_1+\ell_2}} \sum w_{12}\, O_1 O_2, \qquad w_{12} = \langle O_2^\dagger O_1^\dagger \rangle\,, \tag{4.9}$$

where O_k (with $k \in \{1,2\}$) is a generic product of Majorana operators in A_k, namely $O_k = \prod_{j\in A_k} (a_j^x)^{\mu^x_{[j]}} (a_j^y)^{\mu^y_{[j]}}$ with $\mu^\alpha_{[j]} \in \{0,1\}$. The sum in (4.9) is performed over all possible combinations of $\mu^\alpha_{[j]}$.

In general, calculating a free fermionic density matrix is very easy. Indeed by Wick theorem they assume a Gaussian form:

$$\rho_W = \frac{\exp\left(\frac{1}{4}\boldsymbol{a}^{\mathrm{t}} \cdot W \cdot \boldsymbol{a}\right)}{\mathrm{Tr}\left[\exp\left(\frac{1}{4}\boldsymbol{a}^{\mathrm{t}} \cdot W \cdot \boldsymbol{a}\right)\right]}\,, \tag{4.10}$$

with W a complex antisymmetric matrix and the vector $\boldsymbol{A}$ contains all the a_j^x's and the a_j^y's. This density matrix is univocally identified by the correlation matrix

$$\Gamma = \mathrm{Tr}\left(\boldsymbol{a}\, \rho_W\, \boldsymbol{a}^{\mathrm{t}}\right) - \mathbb{I}, \tag{4.11}$$

which satisfies $\Gamma = \tanh(W/2)$.

Unfortunately, the same reasoning does not apply to two disjoint blocks because the fermions in the interval B_1 separating the two blocks contribute to the spin reduced density matrix of $A_1 \cup A_2$ [220, 222, 243]. It is now convenient to introduce the string of Majorana fermions along a generic subsystem C

$$P_C \equiv \prod_{j\in C} (\mathrm{i} a_j^x a_j^y). \tag{4.12}$$

In particular, the string P_{B_1} of Majorana operators appears in a crucial way[1]. Similarly, we also introduce the strings of Majorana operators along A_1 and A_2, namely P_{A_1} and P_{A_2}. These operators satisfies $P_C^{-1} = P_C$, for any $C = A_1, A_2, B_1$.

Moving back to the computation of the spin reduced density matrix (4.8) in terms of fermions, we first notice that, since the XY Hamiltonian commutes with $\prod_j \sigma^z_j$ (where j runs over the whole chain), only the expectation values of operators containing an even number of fermions are non vanishing. Thus, the numbers of fermions are either even or odd in both A_1 and A_2. This leads us to decompose the spin reduced density matrix ρ_A of $A = A_1 \cup A_2$ as [222]

$$\rho_A \;=\; \rho_{\mathrm{even}} + P_{B_1}\, \rho_{\mathrm{odd}}, \tag{4.13}$$

with

$$\rho_{\mathrm{even}} \equiv \frac{1}{2^{\ell_1+\ell_2}} \sum_{\mathrm{even}} w_{12}\, O_1 O_2, \qquad \rho_{\mathrm{odd}} \equiv \frac{\langle P_{B_1}\rangle}{2^{\ell_1+\ell_2}} \sum_{\mathrm{odd}} w^{B_1}_{12}\, O_1 O_2, \tag{4.14}$$

[1] To compare with Ref. [222], set $(S_1)_{\mathrm{there}} = (P_{A_1})_{\mathrm{here}}$ and $(S)_{\mathrm{there}} = (P_{B_1})_{\mathrm{here}}$.

where $w_{12}^{B_1} \equiv \langle O_2^\dagger P_{B_1} O_1^\dagger \rangle \,/\, \langle P_{B_1} \rangle$, and the notation $\sum_{\text{even}}$ ($\sum_{\text{odd}}$) means that the sum is restricted to operators O_1 and O_2 containing an even (odd) number of fermions. It is also convenient to rewrite (4.13) as

$$\rho_A \,=\, \frac{\mathbf{1}+P_{B_1}}{2}\,\rho_+ + \frac{\mathbf{1}-P_{B_1}}{2}\,\rho_-, \qquad \rho_\pm \equiv \rho_{\text{even}} \pm \rho_{\text{odd}}, \tag{4.15}$$

where $\mathbf{1}$ is the identity matrix and $(\mathbf{1} \pm P_{B_1})/2$ are orthogonal projectors. Moreover, the matrices $\rho_\pm$ are unitary equivalent (indeed $P_{A_2}\rho_\pm P_{A_2} = \rho_\mp$) and commute with P_{B_1} because they do not contain Majorana fermions in B_1. As a consequence, we have that

$$\rho_A^n \,=\, \frac{\mathbf{1}+P_{B_1}}{2}\,\rho_+^n + \frac{\mathbf{1}-P_{B_1}}{2}\,\rho_-^n. \tag{4.16}$$

Taking the trace of (4.16) and employing that $P_{A_2}\rho_\pm P_{A_2} = \rho_\mp$, one finds

$$\operatorname{Tr}\rho_A^n = \operatorname{Tr}\rho_\pm^n. \tag{4.17}$$

The matrices $\rho_\pm$ are fermionic but they are not Gaussian, i.e. they are not proportional to the exponential of a quadratic form, as we will discuss below.

At this point we are ready to consider the ground state of the XY chain with density matrix $\rho_W = |\Psi\rangle\langle\Psi|$, whose correlation matrix Γ is given by Eq. (4.11). The fermionic reduced density matrix of $A = A_1 \cup A_2$ is the one of Eq. (4.9) where we recall that $w_{12} = 0$ when the numbers of fermionic operators in O_1 and O_2 have different parity. In order to take into account the effect of the string P_{B_1} defined in Eq. (4.12), it is useful to introduce the auxiliary density matrix

$$\rho_A^{B_1} \equiv \frac{\operatorname{Tr}_B\left(P_{B_1}|\Psi\rangle\langle\Psi|\right)}{\langle P_{B_1}\rangle} = \frac{1}{2^{\ell_1+\ell_2}}\sum w_{12}^{B_1}\, O_1 O_2, \tag{4.18}$$

in which the normalisation $\operatorname{Tr}\rho_A^{B_1} = 1$ holds. By using that

$$P_{A_2} a_j^\alpha P_{A_2} = \begin{cases} -a_j^\alpha & j \in A_2, \\ a_j^\alpha & j \notin A_2, \end{cases} \tag{4.19}$$

one finds

$$\begin{aligned} P_{A_2}\rho_A^{\mathbf{1}} P_{A_2} &= \frac{1}{2^{\ell_1+\ell_2}}\sum (-1)^{\mu_2} w_{12}\, O_1 O_2 \\ &= \frac{1}{2^{\ell_1+\ell_2}}\sum_{\text{even}} w_{12}\, O_1 O_2 - \frac{1}{2^{\ell_1+\ell_2}}\sum_{\text{odd}} w_{12}\, O_1 O_2, \end{aligned} \tag{4.20}$$

where $\mu_2 = \sum_{j\in A_2}(\mu_{[j]}^x + \mu_{[j]}^y)$ is the total number of Majorana operators occurring in O_2. Then, from Eqs. (4.9) and (4.20) it is straightforward to get that the density matrices (4.14) become

$$\rho_{\text{even}} = \frac{\rho_A^{\mathbf{1}} + P_{A_2}\rho_A^{\mathbf{1}} P_{A_2}}{2}, \qquad \rho_{\text{odd}} = \langle P_{B_1}\rangle\,\frac{\rho_A^{B_1} - P_{A_2}\rho_A^{B_1} P_{A_2}}{2}. \tag{4.21}$$

Plugging (4.21) into (4.13), one finds that the spin reduced density matrix is a linear combination of four fermionic Gaussian operators. Since these operators do not commute, they cannot be diagonalised simultaneously and therefore we cannot find the eigenvalues of the spin reduced density matrix that would give the entanglement entropy. Nevertheless,

$\mathrm{Tr}\,\rho_A^n$ for integer n can be computed through Eq. (4.17) by providing the product rules between the four Gaussian operators occurring in (4.21) in terms of the corresponding correlation matrices, that are denoted by

$$\Gamma_1 \equiv \Gamma[\rho_A^{\mathbf{1}}], \qquad \Gamma_2 \equiv \Gamma[P_{A_2}\rho_A^{\mathbf{1}}P_{A_2}], \qquad \Gamma_3 \equiv \Gamma[\rho_A^{B_1}], \qquad \Gamma_4 \equiv \Gamma[P_{A_2}\rho_A^{B_1}P_{A_2}], \quad (4.22)$$

where $\Gamma[\rho]$ is the correlation matrix of a Gaussian density matrix ρ as in Eq. (4.11). Obviously, Γ_1 is the fermionic correlation matrix, i.e. the one of the free fermions without the Jordan-Wigner string (studied in detail in Ref. [333]).

Following Ref. [222], we can introduce the restricted correlation matrix to two fermionic sets/blocks C and D $(\Gamma_{CD})_{rs}$ which is the correlation matrix in Eq. (4.11) associated to $|\Psi\rangle\langle\Psi|$ with the restriction $r \in C$ and $s \in D$. In [222] it has been shown that the matrices Γ_2, Γ_3 and Γ_4 can be written as

$$\Gamma_1 = \Gamma_{AA}, \qquad \Gamma_3 = \Gamma_1 - \Gamma_{AB_1}\Gamma_{B_1B_1}^{-1}\Gamma_{B_1A}, \quad (4.23)$$

and

$$\Gamma_2 = M_2\Gamma_1 M_2, \qquad \Gamma_4 = M_2\Gamma_3 M_2, \qquad M_2 \equiv \begin{pmatrix} \mathbf{1}_{\ell_1} & \mathbf{0} \\ \mathbf{0} & -\mathbf{1}_{\ell_2} \end{pmatrix}. \quad (4.24)$$

These formulas provide an explicit representation of the matrices Γ_i in terms of the fermion correlation in the finite subsystem $A_1 \cup B_1 \cup A_2$.

By introducing the following notation

$$\{\dots, \Gamma, \dots, \Gamma', \dots\} \equiv \mathrm{Tr}(\dots \rho_W \dots \rho_{W'} \dots), \quad (4.25)$$

and $\{\dots, \Gamma^n, \dots\} \equiv \mathrm{Tr}(\dots \rho_W^n \dots)$ as special case, from (4.21) we have that $\mathrm{Tr}\,\rho_\pm^n$ can be written as a linear combination of traces involving the matrices Γ_k with $k \in \{1,2,3,4\}$. This finally provides $\mathrm{Tr}\rho_A^n$, which we write as follows

$$\mathrm{Tr}\rho_A^n \equiv \frac{T_n}{2^{n-1}}. \quad (4.26)$$

From (4.17) and (4.21), it is straightforward to realise that T_n is a combination of 4^n terms of the form (4.25) with coefficients given by integer powers of $\delta_{B_1} \equiv \langle P_{B_1}\rangle^2 = \det[\Gamma_{B_1B_1}]$. However, many of these 4^n terms turn out to be equal when using cyclicality of the trace and other simple algebraic manipulations.

In the following we write T_n explicitly for $2 \leqslant n \leqslant 5$, where we have computed also T_5, in addition to the other ones already reported in Ref. [222]:

- $n = 2$:

$$T_2 \;=\; \{\Gamma_1^2\} + \{\Gamma_1, \Gamma_2\} + \delta_{B_1}\Big(\{\Gamma_3^2\} - \{\Gamma_3, \Gamma_4\}\Big); \quad (4.27)$$

- $n = 3$:

$$T_3 \;=\; \{\Gamma_1^3\} + 3\,\{\Gamma_1^2, \Gamma_2\} + 3\delta_{B_1}\Big(\{\Gamma_1, \Gamma_3^2\} + \{\Gamma_2, \Gamma_3^2\} - 2\,\{\Gamma_1, \Gamma_4, \Gamma_3\}\Big); \quad (4.28)$$

- $n = 4$:

$$\begin{aligned} T_4 = {} & \{\Gamma_1^4\} + \{\Gamma_1, \Gamma_2, \Gamma_1, \Gamma_2\} + 4\,\{\Gamma_1^3, \Gamma_2\} + 2\,\{\Gamma_1^2, \Gamma_2^2\} \\ & + 2\delta_{B_1}\Big(\{\Gamma_1, \Gamma_3, \Gamma_1, \Gamma_3\} + \{\Gamma_1, \Gamma_4, \Gamma_1, \Gamma_4\} + 2\,\{\Gamma_1^2, \Gamma_3^2\} \\ & \quad + 2\,\{\Gamma_1^2, \Gamma_4^2\} + 2\,\{\Gamma_1, \Gamma_3, \Gamma_2, \Gamma_3\} + 4\,\{\Gamma_1, \Gamma_2, \Gamma_3^2\} \\ & \quad - 2\big[2\,\{\Gamma_1^2, \Gamma_3, \Gamma_4\} + \{\Gamma_1, \Gamma_3, \Gamma_1, \Gamma_4\} + \{\Gamma_1, \Gamma_2, \Gamma_3, \Gamma_4\} \\ & \quad\quad + \{\Gamma_1, \Gamma_3, \Gamma_2, \Gamma_4\} + \{\Gamma_1, \Gamma_2, \Gamma_4, \Gamma_3\}\big]\Big) \\ & + \delta_{B_1}^2\Big(\{\Gamma_3^4\} + 2\,\{\Gamma_3^2, \Gamma_4^2\} + \{\Gamma_3, \Gamma_4, \Gamma_3, \Gamma_4\} - 4\,\{\Gamma_3^3, \Gamma_4\}\Big); \end{aligned} \quad (4.29)$$

• $n = 5$

$$
\begin{aligned}
T_5 = {} & \{\Gamma_1^5\} + 5\Big(\{\Gamma_1^4,\Gamma_2\} + \{\Gamma_1^3,\Gamma_2^2\} + \{\Gamma_1^2,\Gamma_2,\Gamma_1,\Gamma_2\}\Big) \\
& + 5\delta_{B_1}\Big(\{\Gamma_1^3,\Gamma_3^2\} + \{\Gamma_1^3,\Gamma_4^2\} + 2\{\Gamma_1,\Gamma_2^2,\Gamma_3^2\} \\
& \quad + 2\{\Gamma_1^2,\Gamma_2,\Gamma_3^2\} + \{\Gamma_1,\Gamma_2,\Gamma_1,\Gamma_3^2\} + \{\Gamma_1,\Gamma_2,\Gamma_1,\Gamma_4^2\} \\
& \quad + \{\Gamma_1^2,\Gamma_3,\Gamma_1,\Gamma_3\} + \{\Gamma_1^2,\Gamma_3,\Gamma_2,\Gamma_3\} + 2\{\Gamma_1,\Gamma_3,\Gamma_1,\Gamma_3,\Gamma_2\} \\
& \quad + \{\Gamma_1,\Gamma_3,\Gamma_2^2,\Gamma_3\} + \{\Gamma_1^2,\Gamma_4,\Gamma_1,\Gamma_4\} + 2\{\Gamma_1,\Gamma_2,\Gamma_3,\Gamma_2,\Gamma_3\} \\
& \quad - 2\big[\{\Gamma_1^2,\Gamma_2,\Gamma_4,\Gamma_3\} + \{\Gamma_1^2,\Gamma_2,\Gamma_3,\Gamma_4\} + \{\Gamma_1^2,\Gamma_3,\Gamma_1,\Gamma_4\} \\
& \qquad + \{\Gamma_1^2,\Gamma_3,\Gamma_2,\Gamma_4\} + \{\Gamma_1^3,\Gamma_3,\Gamma_4\} + \{\Gamma_1,\Gamma_2,\Gamma_1,\Gamma_3,\Gamma_4\} \\
& \qquad + \{\Gamma_1,\Gamma_2,\Gamma_4,\Gamma_1,\Gamma_3\} + \{\Gamma_2,\Gamma_1,\Gamma_4,\Gamma_1,\Gamma_3\}\big]\Big) \\
& + 5\delta_{B_1}^2\Big(\{\Gamma_1,\Gamma_3^4\} + \{\Gamma_2,\Gamma_3^4\} + 2\{\Gamma_1,\Gamma_3^2,\Gamma_4^2\} + \{\Gamma_1,\Gamma_3,\Gamma_4^2,\Gamma_3\} \\
& \quad + 2\{\Gamma_1,\Gamma_3,\Gamma_4,\Gamma_3,\Gamma_4\} + \{\Gamma_1,\Gamma_4,\Gamma_3^2,\Gamma_4\} \\
& \quad - 2\big[\{\Gamma_1,\Gamma_3^3,\Gamma_4\} + \{\Gamma_1,\Gamma_3^2,\Gamma_4,\Gamma_3\} + \{\Gamma_2,\Gamma_4,\Gamma_3^3\} + \{\Gamma_2,\Gamma_3^2,\Gamma_4,\Gamma_3\}\big]\Big).
\end{aligned}
\tag{4.30}
$$

We notice that the algebraic sum of the integer coefficients occurring in any term multiplying a power $\delta_{B_1}^p$ with $p > 0$ is zero. Moreover, considering only the terms which are not multiplied by a power δ_{B_1} in T_n, the sum of their coefficients is 2^{n-1}.

4.4 Traces of integer powers of the partial transpose of the spin reduced density matrix

In this section we move to the main objective of this paper which is to give a representation of the integer powers of the partial transpose of the spin reduced density matrix of two disjoint blocks with respect to A_2. Eisler and Zimboras in Ref. [331] showed how to obtain the partial transpose of a fermionic Gaussian density matrix, a procedure which can be applied to the spin reduced density matrix in Eq. (4.15) using the linearity of the partial transpose as we are going to show. We mention that in Ref. [331] the moments of the partial transpose for two adjacent intervals were studied in details using the property that fermionic and spin reduced density matrices are equal for this special case.

Given a Gaussian density matrix ρ_W written in terms of Majorana fermions in $A = A_1 \cup A_2$, the partial transposition with respect to A_2 leaves invariant the modes in A_1 and acts only on the ones in A_2. Furthermore, the partial transposition with respect to A_2 of ρ_A in (4.13) leaves the operator P_{B_1} unchanged, therefore we have

$$
\rho_A^{T_2} = \rho_{\text{even}}^{T_2} + P_{B_1}\,\rho_{\text{odd}}^{T_2} = \frac{\mathbf{1} + P_{B_1}}{2}\,\rho_+^{T_2} + \frac{\mathbf{1} - P_{B_1}}{2}\,\rho_-^{T_2},
\tag{4.31}
$$

where

$$
\rho_\pm^{T_2} = \rho_{\text{even}}^{T_2} \pm \rho_{\text{odd}}^{T_2},
\tag{4.32}
$$

as clear from Eq. (4.15) because of the linearity of the partial transpose.

Let us consider the operator O_2 and introduce $\mu_2^y = \sum_{j\in A_2} \mu_{[j]}^y$ the number of a_r^y's in O_2. The transpose of O_2 is given by

$$
O_2^T = (-1)^{\tau(\mu_2)}(-1)^{\mu_2^y}\,O_2,
\tag{4.33}
$$

where

$$\tau(\mu_2) = \begin{cases} 0 & (\mu_2 \bmod 4) \in \{0,1\}, \\ 1 & (\mu_2 \bmod 4) \in \{2,3\}. \end{cases} \tag{4.34}$$

The factor $(-1)^{\tau(\mu_2)}$ in (4.33) originates from a rearrangement of the $a^{x,y}$'s operators after the transposition, while the factor $(-1)^{\mu_2^y}$ comes from the fact that $(a_r^y)^T = -a_r^y$ and $(a_r^x)^T = a_r^x$ for the Majorana operators occurring in O_2. This extra factor can be removed by a unitary transformation. Another transposition can be naturally defined, namely

$$O_2^{\widehat{T}} = U_{-\pi}^{(x)} O_2^T U_{\pi}^{(x)} = (-1)^{\tau(\mu_2)} O_2, \tag{4.35}$$

where the unitary $U_{\pi}^{(x)}$ is now a product of terms like (4.6) over all the sites and it changes the sign of the a_r^y's leaving the a_r^x's untouched. This is the definition introduced in [331] and we will adopt this convention throughout this manuscript. Thus, let us drop the hat in (4.35) and denote it simply by O_2^T.

Then, applying Eq. (4.35) to (4.14), we find

$$\rho_{\rm even}^{T_2} = \frac{1}{2^{\ell_1+\ell_2}} \sum_{\rm even} (-1)^{\mu_2/2}\, w_{12}\, O_1 O_2, \tag{4.36a}$$

$$\rho_{\rm odd}^{T_2} = \frac{\langle P_{B_1} \rangle}{2^{\ell_1+\ell_2}} \sum_{\rm odd} (-1)^{(\mu_2-1)/2}\, w_{12}^{B_1}\, O_1 O_2, \tag{4.36b}$$

which gives the desired fermionic representation of the partial transpose of the spin reduced density matrix.

At this point the moments of $\rho_A^{T_2}$ can be obtained following the same reasoning as for the moments of ρ_A. Indeed, since $\rho_\pm^{T_2}$ are unitarily equivalent ($P_{A_2}\rho_\pm^{T_2}P_{A_2} = \rho_\mp^{T_2}$ because $P_{A_2}\rho_{\rm even}^{T_2}P_{A_2} = \rho_{\rm even}^{T_2}$ and $P_{A_2}\rho_{\rm odd}^{T_2}P_{A_2} = -\rho_{\rm odd}^{T_2}$) and P_{B_1} commutes with them, starting from (4.31) and repeating the same observations that lead to (4.17), one gets

$$\mathrm{Tr}\left(\rho_A^{T_2}\right)^n = \mathrm{Tr}\left(\rho_\pm^{T_2}\right)^n. \tag{4.37}$$

Similarly to the case of the Rényi entropies considered in Sec. 4.3 (see Eq. (4.17)), the matrices $\rho_\pm^{T_2}$ are fermionic but not Gaussian. In the following we write them as sums of four Gaussian matrices, as done in (4.13) and (4.21) for ρ_A. In particular, by introducing

$$\tilde\rho_A^{\mathbf{1}} \equiv \frac{1}{2^{\ell_1+\ell_2}} \sum \mathrm{i}^{\mu_2} w_{12}\, O_1 O_2, \qquad \tilde\rho_A^{B_1} \equiv \frac{1}{2^{\ell_1+\ell_2}} \sum \mathrm{i}^{\mu_2}\, w_{12}^{B_1}\, O_1 O_2, \tag{4.38}$$

one has that the matrices in (4.36) become

$$\rho_{\rm even}^{T_2} = \frac{\tilde\rho_A^{\mathbf{1}} + P_{A_2}\tilde\rho_A^{\mathbf{1}}P_{A_2}}{2}, \qquad \rho_{\rm odd}^{T_2} = \langle P_{B_1} \rangle\, \frac{\tilde\rho_A^{B_1} - P_{A_2}\tilde\rho_A^{B_1}P_{A_2}}{2\mathrm{i}}, \tag{4.39}$$

telling us that $\rho_\pm^{T_2}$ in (4.32) are linear combinations of four Gaussian fermionic matrices occurring in the r.h.s.'s of (4.39). Notice that $\rho_{\rm even}^{T_2}$ and $\rho_{\rm odd}^{T_2}$ are Hermitian but the matrices defining them are not since

$$\left(\tilde\rho_A^{\mathbf{1}}\right)^\dagger = P_{A_2}\tilde\rho_A^{\mathbf{1}}P_{A_2}, \qquad \left(\tilde\rho_A^{B_1}\right)^\dagger = P_{A_2}\tilde\rho_A^{B_1}P_{A_2}. \tag{4.40}$$

In order to compute the correlation matrices associated to the four matrices in Eq. (4.39), it is convenient to introduce

$$\widetilde{M}_2 \equiv \begin{pmatrix} \mathbf{1}_{\ell_1} & \mathbf{0} \\ \mathbf{0} & \mathrm{i}\mathbf{1}_{\ell_2} \end{pmatrix}. \tag{4.41}$$

Then, the correlation matrices associated to $\tilde{\rho}_A^{\mathbf{1}}$, $P_{A_2}\tilde{\rho}_A^{\mathbf{1}}P_{A_2}$, $\tilde{\rho}_A^{B_1}$ and $P_{A_2}\tilde{\rho}_A^{B_1}P_{A_2}$ are given by

$$\widetilde{\Gamma}_k \equiv \widetilde{M}_2\Gamma_k\widetilde{M}_2, \qquad k \in \{1,2,3,4\}. \tag{4.42}$$

In analogy to Eq. (4.26), we write the moments of $\rho_A^{T_2}$ as

$$\mathrm{Tr}\left(\rho_A^{T_2}\right)^n = \frac{\widetilde{T}_n}{2^{n-1}}. \tag{4.43}$$

From Eqs. (4.32), (4.37) and (4.39), we have that $\widetilde{T}_n$ is a linear combination of 4^n terms. The net effect is that $\widetilde{T}_n$ can be written by taking T_n and replacing Γ_i with $\widetilde{\Gamma}_i$ and δ_{B_1} with $-\delta_{B_1}$. The latter rule comes from the imaginary unit in the denominator of $\rho_{\mathrm{odd}}^{T_2}$ in Eq. (4.39).

In the following we write explicitly $\widetilde{T}_n$ for $2 \leqslant n \leqslant 5$:

- $n = 2$

$$\widetilde{T}_2 \;=\; \{\widetilde{\Gamma}_1^2\} + \{\widetilde{\Gamma}_1, \widetilde{\Gamma}_2\} + \delta_{B_1}\Big(\{\widetilde{\Gamma}_3, \widetilde{\Gamma}_4\} - \{\widetilde{\Gamma}_3^2\}\Big); \tag{4.44}$$

- $n = 3$

$$\widetilde{T}_3 \;=\; \{\widetilde{\Gamma}_1^3\} + 3\,\{\widetilde{\Gamma}_1^2, \widetilde{\Gamma}_2\} + 3\delta_{B_1}\Big(2\,\{\widetilde{\Gamma}_1, \widetilde{\Gamma}_4, \widetilde{\Gamma}_3\} - \{\widetilde{\Gamma}_1, \widetilde{\Gamma}_3^2\} - \{\widetilde{\Gamma}_2, \widetilde{\Gamma}_3^2\}\Big); \tag{4.45}$$

- $n = 4$

$$\begin{aligned}
\widetilde{T}_4 = {} & \{\widetilde{\Gamma}_1^4\} + \{\widetilde{\Gamma}_1, \widetilde{\Gamma}_2, \widetilde{\Gamma}_1, \widetilde{\Gamma}_2\} + 4\,\{\widetilde{\Gamma}_1^3, \widetilde{\Gamma}_2\} + 2\,\{\widetilde{\Gamma}_1^2, \widetilde{\Gamma}_2^2\} \\
& + 2\delta_{B_1}\Big(2\,\{\widetilde{\Gamma}_3, \widetilde{\Gamma}_1, \widetilde{\Gamma}_4, \widetilde{\Gamma}_1\} + 2\,\{\widetilde{\Gamma}_1, \widetilde{\Gamma}_2, \widetilde{\Gamma}_3, \widetilde{\Gamma}_4\} + 2\,\{\widetilde{\Gamma}_1, \widetilde{\Gamma}_3, \widetilde{\Gamma}_2, \widetilde{\Gamma}_4\} \\
& \quad + 2\,\{\widetilde{\Gamma}_1, \widetilde{\Gamma}_2, \widetilde{\Gamma}_4, \widetilde{\Gamma}_3\} + 4\,\{\widetilde{\Gamma}_3, \widetilde{\Gamma}_4, \widetilde{\Gamma}_1^2\} - 2\,\{\widetilde{\Gamma}_1, \widetilde{\Gamma}_3, \widetilde{\Gamma}_2, \widetilde{\Gamma}_3\} - 4\,\{\widetilde{\Gamma}_1, \widetilde{\Gamma}_2, \widetilde{\Gamma}_3^2\} \\
& \quad - \{\widetilde{\Gamma}_1, \widetilde{\Gamma}_3, \widetilde{\Gamma}_1, \widetilde{\Gamma}_3\} - \{\widetilde{\Gamma}_1, \widetilde{\Gamma}_4, \widetilde{\Gamma}_1, \widetilde{\Gamma}_4\} - 2\,\{\widetilde{\Gamma}_1^2, \widetilde{\Gamma}_3^2\} - 2\,\{\widetilde{\Gamma}_1^2, \widetilde{\Gamma}_4^2\}\Big) \\
& + \delta_{B_1}^2\left(\{\widetilde{\Gamma}_3^4\} + 2\,\{\widetilde{\Gamma}_3^2, \widetilde{\Gamma}_4^2\} + \{\widetilde{\Gamma}_3, \widetilde{\Gamma}_4, \widetilde{\Gamma}_3, \widetilde{\Gamma}_4\} - 4\,\{\widetilde{\Gamma}_3^3, \widetilde{\Gamma}_4\}\right);
\end{aligned} \tag{4.46}$$

- $n = 5$

$$\begin{aligned}
\widetilde{T}_5 = {} & \{\widetilde{\Gamma}_1^5\} + 5\Big(\{\widetilde{\Gamma}_1^4, \widetilde{\Gamma}_2\} + \{\widetilde{\Gamma}_1^3, \widetilde{\Gamma}_2^2\} + \{\widetilde{\Gamma}_1^2, \widetilde{\Gamma}_2, \widetilde{\Gamma}_1, \widetilde{\Gamma}_2\}\Big) \\
& + 5\delta_{B_1}\Big(2\,\{\widetilde{\Gamma}_1^2, \widetilde{\Gamma}_2, \widetilde{\Gamma}_4, \widetilde{\Gamma}_3\} + 2\,\{\widetilde{\Gamma}_1^2, \widetilde{\Gamma}_2, \widetilde{\Gamma}_3, \widetilde{\Gamma}_4\} + 2\,\{\widetilde{\Gamma}_1^2, \widetilde{\Gamma}_3, \widetilde{\Gamma}_1, \widetilde{\Gamma}_4\} \\
& \quad + 2\,\{\widetilde{\Gamma}_1^2, \widetilde{\Gamma}_3, \widetilde{\Gamma}_2, \widetilde{\Gamma}_4\} + 2\,\{\widetilde{\Gamma}_1^3, \widetilde{\Gamma}_3, \widetilde{\Gamma}_4\} + 2\,\{\widetilde{\Gamma}_1, \widetilde{\Gamma}_2, \widetilde{\Gamma}_1, \widetilde{\Gamma}_3, \widetilde{\Gamma}_4\} \\
& \quad + 2\,\{\widetilde{\Gamma}_1, \widetilde{\Gamma}_2, \widetilde{\Gamma}_4, \widetilde{\Gamma}_1, \widetilde{\Gamma}_3\} + 2\,\{\widetilde{\Gamma}_1, \widetilde{\Gamma}_4, \widetilde{\Gamma}_1, \widetilde{\Gamma}_3, \widetilde{\Gamma}_2\} \\
& \quad - \{\widetilde{\Gamma}_1^3, \widetilde{\Gamma}_3^2\} - \{\widetilde{\Gamma}_1^3, \widetilde{\Gamma}_4^2\} - 2\,\{\widetilde{\Gamma}_1, \widetilde{\Gamma}_2^2, \widetilde{\Gamma}_3^2\} - 2\,\{\widetilde{\Gamma}_1^2, \widetilde{\Gamma}_2, \widetilde{\Gamma}_3^2\} \\
& \quad - \{\widetilde{\Gamma}_1, \widetilde{\Gamma}_2, \widetilde{\Gamma}_1, \widetilde{\Gamma}_3^2\} - \{\widetilde{\Gamma}_1, \widetilde{\Gamma}_2, \widetilde{\Gamma}_1, \widetilde{\Gamma}_4^2\} - \{\widetilde{\Gamma}_1^2, \widetilde{\Gamma}_3, \widetilde{\Gamma}_1, \widetilde{\Gamma}_3\} \\
& \quad - \{\widetilde{\Gamma}_1^2, \widetilde{\Gamma}_3, \widetilde{\Gamma}_2, \widetilde{\Gamma}_3\} - 2\,\{\widetilde{\Gamma}_1, \widetilde{\Gamma}_3, \widetilde{\Gamma}_1, \widetilde{\Gamma}_3, \widetilde{\Gamma}_2\} - \{\widetilde{\Gamma}_1, \widetilde{\Gamma}_3, \widetilde{\Gamma}_2^2, \widetilde{\Gamma}_3\} \\
& \quad - \{\widetilde{\Gamma}_1^2, \widetilde{\Gamma}_4, \widetilde{\Gamma}_1, \widetilde{\Gamma}_4\} - 2\,\{\widetilde{\Gamma}_1, \widetilde{\Gamma}_2, \widetilde{\Gamma}_3, \widetilde{\Gamma}_2, \widetilde{\Gamma}_3\}\Big) \\
& + 5\delta_{B_1}^2\Big(\{\widetilde{\Gamma}_1, \widetilde{\Gamma}_3^4\} + \{\widetilde{\Gamma}_2, \widetilde{\Gamma}_3^4\} + \{\widetilde{\Gamma}_1, \widetilde{\Gamma}_3, \widetilde{\Gamma}_4^2, \widetilde{\Gamma}_3\} + \{\widetilde{\Gamma}_1, \widetilde{\Gamma}_4, \widetilde{\Gamma}_3^2, \widetilde{\Gamma}_4\} \\
& \quad + 2\,\{\widetilde{\Gamma}_1, \widetilde{\Gamma}_3, \widetilde{\Gamma}_4, \widetilde{\Gamma}_3, \widetilde{\Gamma}_4\} + 2\,\{\widetilde{\Gamma}_1, \widetilde{\Gamma}_3^2, \widetilde{\Gamma}_4^2\} - 2\,\{\widetilde{\Gamma}_1, \widetilde{\Gamma}_3^3, \widetilde{\Gamma}_4\} \\
& \quad - 2\,\{\widetilde{\Gamma}_1, \widetilde{\Gamma}_3^2, \widetilde{\Gamma}_4, \widetilde{\Gamma}_3\} - 2\,\{\widetilde{\Gamma}_2, \widetilde{\Gamma}_4, \widetilde{\Gamma}_3^3\} - 2\,\{\widetilde{\Gamma}_2, \widetilde{\Gamma}_3^2, \widetilde{\Gamma}_4, \widetilde{\Gamma}_3\}\Big).
\end{aligned} \tag{4.47}$$

As for T_n, also in $\widetilde{T}_n$ the algebraic sum of the integer coefficients occurring in any term multiplying a power $\delta_{B_1}^p$ with $p > 0$ vanishes.

4.5 Numerical results for the ground state of the critical Ising and XX model

The results of the previous section for the moments of the partial transpose of the reduced density matrix of two disjoint blocks are valid for arbitrary configurations of the XY spin chain: equilibrium, non-equilibrium, finite and infinite systems, critical and non-critical values of the parameters γ and h. In this section we evaluate numerically these moments for the configurations that so far attracted most of the theoretical interest, namely the critical points of the XY Hamiltonian, whose scaling properties are described by conformal field theories. A great advantage of the present approach compared to purely numerical methods such as exact diagonalization or tensor networks techniques is that it allows to deal directly with infinite chains without any approximations, reducing the systematic errors in the estimates of asymptotic results. Indeed, all the numerical results presented in the following are obtained for infinite chains.

We will consider two particular points of the XY Hamiltonian, namely the critical Ising model for $\gamma = h = 1$ and the zero field XX spin chain (corresponding to fermions at half-filling) obtained for $\gamma = h = 0$. The scaling limit of the former is the Ising CFT with central charge $c = 1/2$, while the scaling limit of the latter is a compactified boson at the Dirac point with $c = 1$.

The CFT predictions for the moments of both reduced density matrix and its partial transpose have been derived in a series of manuscripts [134, 136, 196, 226]. For both models we consider the case of two disjoint blocks of equal length ℓ embedded in an infinite chain and placed at distance r. We numerically evaluate the moments of ρ_A and $\rho_A^{T_2}$ using the trace formulas of the previous sections for $n = 2, 3, 4, 5$ and we compute the ratio R_n defined in Eq. (1.71), whose (unknown) analytic continuation for $n_e \to 1$ would give the negativity. Notice that from Eqs. (4.26) and (4.43) we have that $R_n = \widetilde{T}_n / T_n$. In the scaling limit (i.e. $\ell, r \to \infty$ with ratio fixed) the ratio R_n converges to the CFT prediction, Eq. (1.82) (where the function $\mathcal{F}_n(x)$ is (1.63) for Ising and (1.60) for XX) written in terms of the four-point ratio x, which is

$$x = \left(\frac{\ell}{\ell + r} \right)^2 , \tag{4.48}$$

when specialised to the case of two intervals of equal length ℓ at distance r.

4.5.1 The critical Ising chain

The negativity and the moments of $\rho_A^{T_2}$ for the critical Ising chain in a transverse field have been already numerically considered in Ref. [136] by using a TTN algorithm and in Ref. [145] by Monte Carlo simulations of the two-dimensional classical problem in the same universality class. However, the finiteness of the chain length did not allow to obtain very precise extrapolations to the scaling theory for all values of n and of the four-point ratio x. We found, as generally proved [134], that R_2 is identically equal to 1. In Fig. 4.2 we report the obtained values of R_n for $n = 3, 4, 5$ as function of x for different values of ℓ. It is evident that increasing ℓ the data approach the CFT predictions (the solid curves). We can also perform an accurate scaling analysis to show that indeed the data converge to the CFT results when the corrections to the scaling are properly taken into account.

It has been argued on the basis of the general CFT arguments [261], and shown explicitly in few examples [260, 262, 263, 327, 334–336] both analytically and numerically, that $\operatorname{Tr} \rho_A^n$ displays 'unusual' corrections to the scaling which, at the leading order, are

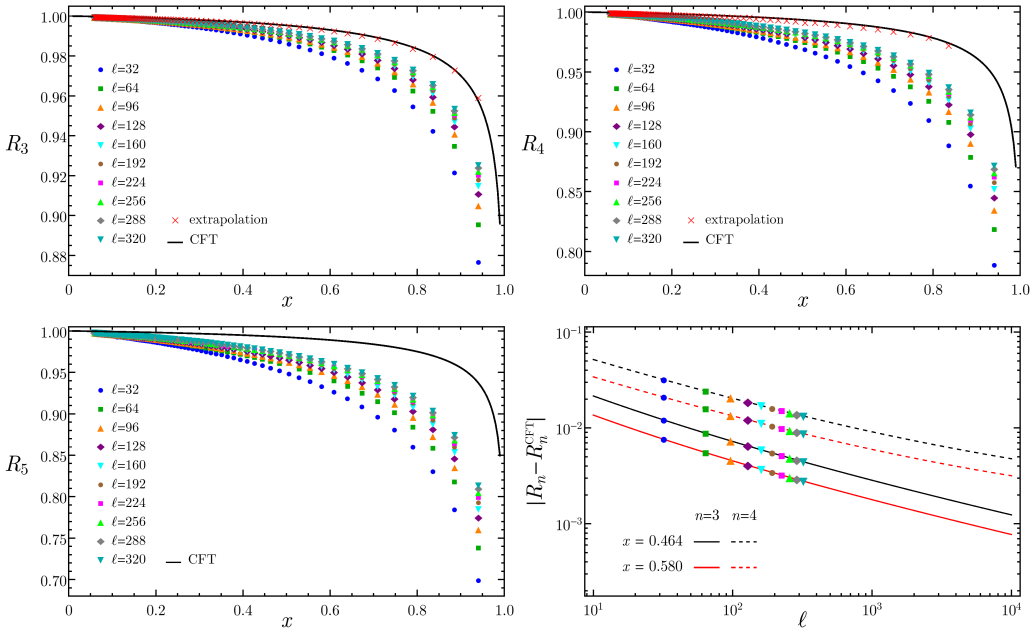

Figure 4.2: The ratio R_n between the integer moments of ρ_A and $\rho_A^{T_2}$ for two disjoint blocks of length ℓ at distance r embedded in an infinite critical Ising chain. We report the results for $n = 3, 4, 5$ as function of the four-point ratio x for various values of ℓ (and correspondingly of r). For large ℓ, the data approach the CFT predictions (solid lines). The extrapolations to $\ell \to \infty$ –done using the scaling form (4.49)– are shown as crosses and they perfectly agree with the CFT curves for $n = 3$ and 4, while for $n = 5$ the fits are unstable and the extrapolations are not shown. The last panel shows explicitly the extrapolating functions for two values of x and $n = 3, 4$.

governed by the unusual exponent $\delta_n = 2h/n$ where h is the smallest scaling dimension of a relevant operator which is inserted locally at the branch point [261]. For the Ising model it has been found that, in the case of two intervals, $h = 1/2$ [220, 222]. From the general CFT arguments in Ref. [261], we expect the same corrections to be present for $\mathrm{Tr}(\rho_A^{T_2})^n$ because they are only due to the conical singularities. Unfortunately, the corrections to the scaling in Fig. 4.2 cannot be captured by a single term, because subleading corrections become more and more important when n increases, as already pointed out in Ref. [136]. Indeed, corrections of the form $\ell^{-m/n}$ for any integer m are know to be present [222, 223, 262]. Thus the most general finite-ℓ ansatz is of the form

$$R_n = R_n^{\rm CFT}(x) + \frac{r_n^{(1)}(x)}{\ell^{1/n}} + \frac{r_n^{(2)}(x)}{\ell^{2/n}} + \frac{r_n^{(3)}(x)}{\ell^{3/n}} + \cdots . \tag{4.49}$$

The variables $r_n(x)$ are used as fitting parameters in the extrapolation procedure. The number of terms that we should keep in order to have a stable fit depends both on n and on x. For each case we keep a number of terms such that the extrapolated value at $\ell \to \infty$ is stable. The results of this extrapolation procedure for $n = 3$ and $n = 4$ are explicitly reported in Fig. 4.2. In the case of $n = 4$ the extrapolated points corresponding to the last two values of x are not shown in the figure because we cannot perform a stable fit with the available data. Indeed, we should keep a large number of terms in order to have a precise enough extrapolation and this would require larger intervals size. The agreement of the

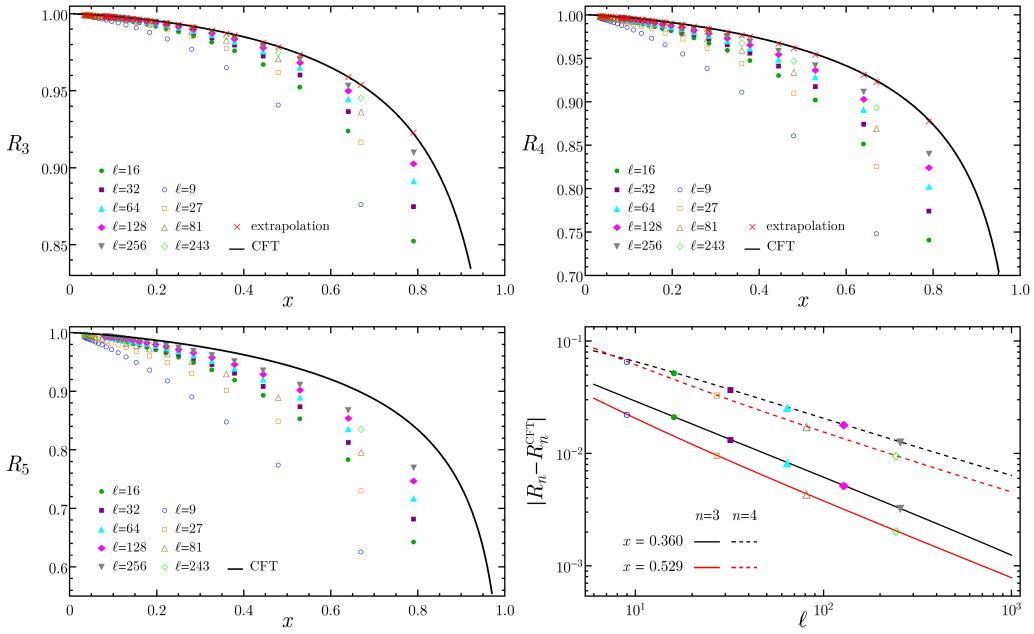

Figure 4.3: The ratio R_n between the integer moments of ρ_A and $\rho_A^{T_2}$ for two disjoint blocks of length ℓ at distance r embedded in an infinite XX chain at zero field. We report the results for $n = 3, 4, 5$ as function of the four-point ratio x for various values of ℓ (and correspondingly of r). For large ℓ, the data approach the CFT predictions (solid lines). The extrapolations to $\ell \to \infty$ –done using the scaling form (4.50)– are shown as crosses which perfectly agree with the CFT curves for $n = 3$ and 4, while for $n = 5$ the fits are unstable. The last panel shows explicitly the extrapolating functions for two values of x and $n = 3, 4$.

stable extrapolations with the CFT predictions is really excellent, at an unprecedented precision compared with fully numerical computations [136, 145]. Conversely, we find that for $n = 5$ the extrapolations are still unstable for any value of x.

4.5.2 The XX chain

We now move to the study of the powers of $\rho_A^{T_2}$ for the XX model in zero field. There are no previous numerical studies of this paradigmatic model. We again consider the ratios R_n for $n = 2, 3, 4, 5$ and we again find that R_2 is identically equal to 1, as it should be. In Fig. 4.3 we report the obtained values of R_n for $n = 3, 4, 5$ as function of x for different values of ℓ. It is evident that increasing ℓ the data approach the CFT predictions (the solid curves). We should however mention a very remarkable property. It has been observed that $\mathrm{Tr}\,\rho_A^n$ shows oscillating corrections to the scaling [222, 260, 262], which for zero magnetic field, are of the form $(-1)^\ell$. These oscillations however cancel in the ratio R_n and the corrections to the scaling are monotonous, a property which makes the extrapolation to infinite ℓ slightly simpler.

Also in this case we can perform an accurate scaling analysis to show how the data converge to the CFT results when the corrections to the scaling are properly taken into account. For the XX model, the leading correction to the scaling is governed by an exponent $\delta_n = 2/n$, which means that they are less severe than in the case of the Ising

model as it is also qualitatively clear from the figure. We then use the general finite-ℓ ansatz

$$R_n = R_n^{\rm CFT}(x) + \frac{r_n^{(1)}(x)}{\ell^{2/n}} + \frac{r_n^{(2)}(x)}{\ell^{4/n}} + \frac{r_n^{(3)}(x)}{\ell^{6/n}} + \cdots , \tag{4.50}$$

and, as in the case of the Ising model, we keep a number of fitting parameters which make stable the extrapolation at $\ell \to \infty$. The results of this procedure for $n = 3$ and 4 are explicitly reported in Fig. 4.3. The agreement of the extrapolations with the CFT predictions is excellent. Also for the XX chain we find that for $n = 5$ the fits are unstable.

4.6 Conclusions

We have shown that the partial transpose of the reduced density matrix of two disjoint spin blocks in the XY spin chain can be written as a linear combination of four Gaussian fermionic operators, fully specified by their correlation matrices (denoted as $\widetilde{\Gamma}_i$, $i = 1, 2, 3, 4$ in the text) which have been explicitly calculated in terms of the correlation matrix of the subsystem formed by the two blocks joined with the finite part between them. This construction allows to calculate the moments of the partial transpose in generic configurations of the spin chain. In this chapter we focused on the ground state of Ising and XY chain, but the approach is more general and can be used for arbitrary excited states, thermal density matrices, non-equilibrium situations etc.

The obtained representations of the moments of the partial transpose allow us to study in an exact manner infinite chains and very large subsystems, drastically reducing the systematic errors in the approach to the scaling limit. We found that for the ground state of the critical models the moments of the partial transpose agree (with high accuracy) with the recent CFT predictions after the corrections to the scaling are properly taken into account.

The main open problem left for two disjoint blocks of a spin chain is whether it is somehow possible to obtain the negativity from the correlation matrix (the problem is also present for the fermionic degrees of freedom [331]). A similar problem is also open for the entanglement entropy since integer moments are obtained in a similar fashion [222], but one has no access to the spectrum of the reduced density matrix and hence to the entanglement entropy. From the practical point of view, we discussed in Chap. 2 that if one knows a relative large number of integer moments, rational interpolations provide accurate estimates of the analytic continuations [152], and hence of the entanglement entropy. In Ref. [236] the same analysis is performed also for the negativity. However, a deeper understanding of these analytic continuations would be highly desirable.

Chapter 5

Partial transpose of two disjoint intervals for a one dimensional free fermion

5.1 Introduction

The goal of this chapter is to investigate the negativity for the one-dimensional CFT of a free fermionic model. The main result is a close analytical form for the moments of the partial transpose of two disjoint intervals for the massless free Dirac fermion reported in Eq. (5.37). The explicit form of the moments is exactly the same as for the compactified boson at the self-dual point obtained in Ref. [135].

The chapter is organised as follows. In Sec. 5.2 we build the partial transpose of the fermionic density matrix using coherent state path integral. In Sec. 5.3 we provide the analytical form for the moments of the partial transpose of two disjoint intervals and we analyse it. The method used to compute Eq. (5.37) is tested in Sec. 5.4, where we recover the known results for the modular invariant Dirac fermion and the Ising model. Finally in Sec. 5.5 we draw our conclusions and discuss some open problems. In a series of appendices we report a number of technical details.

5.2 Partial transpose of the reduced density matrix for the free fermion

In this section we provide a path integral formula for the partial transpose of the density matrix for a free fermionic field theory, after a brief review of the result of Eisler and Zimboras [331] for the partial transpose of the reduced density matrix of two disjoint blocks on the lattice.

5.2.1 Review of the lattice results

We start from the the tight binding model with Hamiltonian

$$H = \frac{1}{2}\sum_{i=1}^{L}\Big[c_i^\dagger c_{i+1} + c_{i+1}^\dagger c_i\Big], \tag{5.1}$$

where periodic boundary conditions are assumed. We only consider the model at half filling $k_F = \pi/2$. Since (5.1) is quadratic in the fermionic operators, it can be diagonalized in momentum space. The scaling limit of this model is the massless free Dirac fermion which is a CFT with $c = 1$. The local Hilbert space $\mathcal{H}_j$ of a single site is two dimensional and we can choose a basis made by the two vectors corresponding to whether the fermion occurs ($|1\rangle$) or not ($|0\rangle$). In this basis the operators c_j and $c_j^\dagger$ act as the creation and annihilation operators, $c_j |0\rangle = c_j^\dagger |1\rangle = 0$, while $c_j^\dagger |0\rangle = |1\rangle$ and $c_j |1\rangle = |0\rangle$. The tight-binding model can be mapped by a Jordan-Wigner transformation into the XX spin chain (discussed in Chap. 4)

$$H_{\mathrm{XX}} = \sum_{j=1}^{L} \Big[\sigma_j^x \sigma_{j+1}^x + \sigma_j^y \sigma_{j+1}^y \Big]. \tag{5.2}$$

Although these models are mapped one into the other, since the Jordan-Wigner transformation between them is not local, the entanglement (both entropy and negativity) of two disjoint blocks are not equal, as pointed out already in the literature [220, 243] and in Chap. 4.

We always consider the entire system to be in the ground state $|\Psi\rangle$ with density matrix $\rho = |\Psi\rangle \langle\Psi|$. As in Chap. 4, we introduce the following Majorana fermions [245, 328]

$$a_j^x = c_j + c_j^\dagger, \qquad a_j^y = \mathrm{i}(c_j - c_j^\dagger), \tag{5.3}$$

which satisfy the anticommutation relations $\{a_r^\alpha, a_s^\beta\} = 2\delta_{\alpha\beta}\delta_{rs}$.

We briefly review the results of Eisler and Zimboras [331] for the partial transpose of such fermionic Gaussian problem. With the same notations of Chap. 4, we can write the reduced density matrix as in Eq. (4.9)[1]. Since we are now interested directly in the fermionic variables, and not in the spins, there is no string in B_1 connecting the two blocks (cf. Eq. (4.12)). Given the reduced density matrix (4.9), it is still convenient to distinguish the terms having an even or odd number of fermionic operators in A_2 (we recall that the parity of operator in A_2 is the same of the operators in A_1) by introducing

$$\rho_{\mathrm{even}} = \frac{1}{2^{\ell_1+\ell_2}} \sum_{\mathrm{even}} w_{12}\, O_1 O_2, \qquad \rho_{\mathrm{odd}} = \frac{1}{2^{\ell_1+\ell_2}} \sum_{\mathrm{odd}} w_{12}\, O_1 O_2. \tag{5.4}$$

Thus $\rho_A = \rho_{\mathrm{even}} + \rho_{\mathrm{odd}}$. The partial transposition with respect to A_2 in (4.35) acts differently on the two operators in (5.4). In particular [331]

$$\rho_{\mathrm{even}}^{T_2} = \frac{1}{2^{\ell_1+\ell_2}} \sum_{\mathrm{even}} (-1)^{\mu_2/2} w_{12}\, O_1 O_2, \qquad \rho_{\mathrm{odd}}^{T_2} = \frac{1}{2^{\ell_1+\ell_2}} \sum_{\mathrm{odd}} (-1)^{(\mu_2-1)/2} w_{12}\, O_1 O_2. \tag{5.5}$$

The definition of $\tilde{\rho}_A$ (which is Gaussian, but it is not a density matrix, being not hermitian) is the same as in Sec. 4.4

$$\tilde{\rho}_A = \frac{1}{2^{\ell_1+\ell_2}} \sum \mathrm{i}^{\mu_2} w_{12}\, O_1 O_2. \tag{5.6}$$

We also naturally introduce $\tilde{\rho}_{\mathrm{even}}$ and $\tilde{\rho}_{\mathrm{odd}}$, as done in (5.4) for ρ_A. The partial transpose of ρ_A becomes

$$\rho_A^{T_2} = \tilde{\rho}_{\mathrm{even}} - \mathrm{i}\, \tilde{\rho}_{\mathrm{odd}}. \tag{5.7}$$

[1] In this chapter we remove the superscript $\mathbf{1}$, since $\rho_A = \rho_A^{\mathbf{1}}$.

The matrices $\tilde{\rho}_{\rm even}$ and $\tilde{\rho}_{\rm odd}$ in (5.7) can be written through the string P_{A_2} of the Majorana operator along A_2. Using Eq. (4.19), one finds

$$\tilde{\rho}_{\rm even} = \frac{1}{2}\big(\tilde{\rho}_A + P_{A_2}\tilde{\rho}_A P_{A_2}\big), \qquad \tilde{\rho}_{\rm odd} = \frac{1}{2}\big(\tilde{\rho}_A - P_{A_2}\tilde{\rho}_A P_{A_2}\big). \tag{5.8}$$

Thus, plugging (5.8) into (5.7), the final expression for $\rho_A^{T_2}$ is obtained [331]

$$\rho_A^{T_2} = \frac{1-\mathrm{i}}{2}\,\tilde{\rho}_A + \frac{1+\mathrm{i}}{2}\,P_{A_2}\tilde{\rho}_A P_{A_2} = \frac{1}{\sqrt{2}}\left(e^{-\mathrm{i}\frac{\pi}{4}}\tilde{\rho}_A + e^{\mathrm{i}\frac{\pi}{4}}P_{A_2}\tilde{\rho}_A P_{A_2}\right). \tag{5.9}$$

The only difference with the formulas of Chap. 4 is the absence of the string of Majorana operators (4.12) in B_1. Thus Eq. (5.9) can be obtained from Eq. (4.39) by discarding the string of Majorana operators, i.e. by replacing P_{B_1} with $\mathbf{1}$. Performing this replacement, many simplifications occur in the formulas found in Sec. 4.3 and Sec. 4.4. Making the replacement $P_{B_1} \to \mathbf{1}$ in Eqs. (4.13) and (4.14), the reduced density matrix of the two disjoint blocks becomes $\rho_A = \rho_{\rm even} + \rho_{\rm odd}$, with $\rho_{\rm even}$ and $\rho_{\rm odd}$ given in Eq. (5.4)[2]. Moreover, $\rho_A^{B_1}$ defined in Eq. (4.18) is replaced as $\rho_A^{B_1} \to \rho_A^{\mathbf{1}}$ and therefore we conclude that $\rho_A = \rho_+ = \rho_A^{\mathbf{1}}$. In the same way, we can recover the result (5.9) for the partial transpose. Once again, $\mathrm{Tr}(\rho_A^{T_2})^n$ in the fermionic variables is obtained by replacing P_{B_1} with $\mathbf{1}$ in the formulas reported in Sec. 4.4. Performing this replacement in Eq. (4.31) we get $\rho_A^{T_2} = \rho_{\rm even}^{T_2} + \rho_{\rm odd}^{T_2} = \rho_+^{T_2}$ and in Eq. (4.38) it gives $\tilde{\rho}_A^{B_1} \to \tilde{\rho}_A^{\mathbf{1}}$. These observations together with Eq. (4.39) lead to Eq. (5.9)

The computation of $\mathrm{Tr}(\rho_A^{T_2})^n$ through (5.9) provides an expression containing 2^n terms given by all the combinations of $\tilde{\rho}_0 \equiv \tilde{\rho}_A$ and $\tilde{\rho}_1 \equiv P_{A_2}\tilde{\rho}_A P_{A_2}$, which can be written as

$$\mathrm{Tr}\big(\rho_A^{T_2}\big)^n = \sum_{p_1,p_2,\dots p_n=0,1} \frac{e^{\mathrm{i}\frac{\pi}{4}\sum_i^n p_i}\, e^{-\mathrm{i}\frac{\pi}{4}\left(n-\sum_i^n p_i\right)}}{2^{n/2}}\ \mathrm{Tr}\left[\prod_{k=1}^{n}\tilde{\rho}_{p_k}\right]. \tag{5.10}$$

This formula can be further simplified noticing that the various terms in the sum are invariant under the exchange $p_i \to 1-p_i$. Using this and reorganising the terms in the sum, we can write

$$\mathrm{Tr}(\rho_A^{T_2})^n = \frac{1}{2^{n-1}}\sum_{\boldsymbol{p}} 2^{n/2}\cos\left[\frac{\pi}{4}\left(2\sum_{i=1}^{n-1}p_i - n\right)\right]\ \mathrm{Tr}\left[\tilde{\rho}_0\prod_{k=1}^{n-1}\tilde{\rho}_{p_k}\right], \tag{5.11}$$

where the vector $\boldsymbol{p}$ has $n-1$ components equal to 0 or 1 and therefore the sum contains 2^{n-1} terms.

5.2.2 Fermionic coherent states for a single site

In this subsection, we briefly review the features of the fermionic coherent states [337] which are needed to build the path integral of ρ_A and $\tilde{\rho}_A$. Here we focus on a single site (indeed, the site index will be dropped in this subsection) and in the next subsection the natural extension to many sites will be considered.

The coherent states for fermions are defined through the Grassmann anticommuting variables. If θ_1 and θ_2 are real Grassmann variables, we have that $\theta_i^2 = 0$ for $i \in \{1,2\}$ and $\theta_1\theta_2 = -\theta_2\theta_1$. Since $\theta^2 = 0$, a function $f(\theta)$ of the real Grassman variable can be

[2] To compare our notation with the one used in [331], set $(\rho_+)_{\rm there} = (\rho_{\rm even})_{\rm here}$ and $(\rho_-)_{\rm there} = (\rho_{\rm odd})_{\rm here}$.

written as $f(\theta) = f_0 + f_1\theta$. Given two real Grassmann variables one can build a complex Grassmann variable ζ as follows

$$\zeta = \frac{1}{\sqrt{2}}(\theta_1 + \mathrm{i}\,\theta_2), \qquad \zeta^* = \frac{1}{\sqrt{2}}(\theta_1 - \mathrm{i}\,\theta_2). \tag{5.12}$$

The integration over a complex Grassmann variable acts as a derivation; indeed

$$\int \mathrm{d}\zeta^*\mathrm{d}\zeta\ = 0, \quad \int \mathrm{d}\zeta^*\mathrm{d}\zeta\ \zeta = 0, \quad \int \mathrm{d}\zeta^*\mathrm{d}\zeta\ \zeta^* = 0, \quad \int \mathrm{d}\zeta^*\mathrm{d}\zeta\ \zeta\,\zeta^* = 1. \tag{5.13}$$

The coherent states are defined as follows

$$|\zeta\rangle = |0\rangle - \zeta\,|1\rangle\,, \qquad \langle\zeta| = \langle 0| + \zeta^*\,\langle 1|\,. \tag{5.14}$$

Since ζ commutes with $|0\rangle$ and anticommutes with c, $c^\dagger$ and $|1\rangle$, it is straightforward to check that $c\,|\zeta\rangle = \zeta\,|\zeta\rangle$ and $\langle\zeta|\,c^\dagger = \langle\zeta|\,\zeta^*$. Notice that the coherent states do not provide an orthonormal basis. A completeness relation and a formula for the trace of an operator O read respectively

$$\mathbb{I} = \int \mathrm{d}\zeta^*\mathrm{d}\zeta\ e^{-\zeta^*\zeta}\,|\zeta\rangle\,\langle\zeta|\,, \qquad \mathrm{Tr}\,O = \int \mathrm{d}\zeta^*\mathrm{d}\zeta\ e^{-\zeta^*\zeta}\,\langle -\zeta|\,O\,|\zeta\rangle\,. \tag{5.15}$$

Given the above rules, the matrix elements of the identity and of the operators in (4.5) on the coherent states (5.14) can be computed, finding that

$$\langle\zeta|\eta\rangle = 1 + \zeta^*\eta = \langle\eta^*| - \zeta^*\rangle\,, \tag{5.16a}$$
$$\langle\zeta|a^x|\eta\rangle = \zeta^* + \eta = \langle\eta^*|a^x|\zeta^*\rangle\,, \tag{5.16b}$$
$$\langle\zeta|a^y|\eta\rangle = -\mathrm{i}(\zeta^* - \eta) = -\,\langle\eta^*|a^y|\zeta^*\rangle\,, \tag{5.16c}$$
$$\langle\zeta|\mathrm{i}a^x a^y|\eta\rangle = 1 - \zeta^*\eta = \langle\eta^*|\mathrm{i}a^x a^y| - \zeta^*\rangle\,, \tag{5.16d}$$

where the second rewriting will be useful in the following subsection. Since $\mathrm{i}\,a^x a^y\,|\zeta\rangle = |-\zeta\rangle$, we can bring (5.16b) and (5.16c) in the same form of (5.16a) and (5.16d):

$$\langle\zeta|a^x|\eta\rangle = \langle\eta^*|\mathrm{i}a^y| - \zeta^*\rangle = -\mathrm{i}\,\langle\eta^*|\,U^{(z)}_{-\pi/2}\,a^x\,U^{(z)}_{\pi/2}\,|-\zeta^*\rangle\,, \tag{5.17a}$$
$$\langle\zeta|a^y|\eta\rangle = \langle\eta^*|\mathrm{i}a^x| - \zeta^*\rangle = \ \ \mathrm{i}\,\langle\eta^*|\,U^{(z)}_{-\pi/2}\,a^y\,U^{(z)}_{\pi/2}\,|-\zeta^*\rangle\,. \tag{5.17b}$$

Notice that the insertion of $U^{(z)}_{\pi/2}$ and its hermitian conjugate in (5.16a) and (5.16d) has no effect.

5.2.3 Partial transpose of the reduced density matrix

The coherent state $|\zeta(x)\rangle$ for a lattice is the tensor product of single site coherent states, with x runnig along the whole system or the corresponding subsystem. In the following we consider a lattice system but the final formulas can be extended to a continuous spatial dimension in a straightforward way by interpreting the discrete sums as integrals and integrations over a discrete set of variables as path integrals.

The density matrix of the whole system in the ground state is $\rho = |\Psi\rangle\,\langle\Psi|$ and its matrix element between two generic coherent states reads

$$\rho(\zeta(x),\eta(x)) \ = \ e^{-\zeta^*\eta}\,\langle\zeta(x)|\Psi\rangle\,\langle\Psi|\eta(x)\rangle\,, \tag{5.18}$$

where $\zeta^*\eta = \sum_x \zeta^*(x)\,\eta(x)$, with x labelling the whole system and $e^{-\zeta^*\eta}$ is the normalization factor (see (5.16a)). To obtain the reduced density matrix in A, one first separates the degrees of freedom in A and the ones in B and then traces over the latter ones. Denoting by $|\zeta_A(x_A)\rangle$ and $|\zeta_B(x_B)\rangle$ the coherent states on A and B respectively, we have that $|\zeta(x)\rangle = |\zeta_A(x_A)\rangle \otimes |\zeta_B(x_B)\rangle$. Adopting the notation $|\zeta(x)\rangle = |\zeta_A(x_A),\, \zeta_B(x_B)\rangle$, the matrix element of ρ_A is given by

$$\rho_A(\zeta_A(x_A), \eta_A(x_A)) \,=\, e^{-\zeta_A^*\eta_A} \int D\chi_B^*\, D\chi_B\, e^{-\chi_B^*\,\chi_B}\, \langle \zeta_A,\, -\chi_B|\Psi\rangle\, \langle \Psi|\eta_A,\, \chi_B\rangle\,, \quad (5.19)$$

where $D\chi_B^*\, D\chi_B = \prod_{x_B} \mathrm{d}\chi_B^*(x_B)\, \mathrm{d}\chi_B(x_B)$ and the minus sign comes from the trace over B, according to (5.15). In the continuum limit, the braket $\langle \Psi|\eta_A,\, \chi_B\rangle$ is the fermionic path integral on the upper half plane where the boundary conditions $\eta_A(x_A)$ and $\chi_B(x_B)$ are imposed in A and B respectively, just above the real axis. Analogously, $\langle \zeta_A,\, -\chi_B|\Psi\rangle$ is the path integral on the lower half plane. The trace over B is performed by setting the fields along B equal (but with opposite sign) and summing over all the configurations. The resulting path integral is over the whole plane with two open slits along A_1 and A_2, where the boundary conditions η_A and ζ_A are imposed respectively along the lower and the upper edge of A (left panel of Fig. 5.1).

Let us consider the partial transpose $\rho_A^{T_2}$ with respect to A_2. Remembering that the partial transposition acts only on operators in A_2, from (4.9) we can write its matrix elements as follows

$$\langle \zeta(x)|\rho_A^{T_2}|\eta(x)\rangle = \frac{1}{2^{\ell_1+\ell_2}} \sum w_{12}\; \langle \zeta_1(x_1)|O_1|\eta_1(x_1)\rangle\, \langle \zeta_2(x_2)|O_2^T|\eta_2(x_2)\rangle\,, \quad (5.20)$$

where $x_j \in A_j$, with $j \in \{1, 2\}$.

Focussing on the term corresponding to A_2 in (5.20), from (4.35), (5.16a)–(5.17b) one finds

$$\langle \zeta_2(x_2)|O_2^T|\eta_2(x_2)\rangle = (-1)^{\tau(\mu_2)}\, \mathrm{i}^{\mu_2^y - \mu_2^x}\, \langle \eta_2^*(x_2)|\, U^{(z)}_{-\pi/2}\, O_2\, U^{(z)}_{\pi/2}\, |-\zeta_2^*(x_2)\rangle\,, \quad (5.21)$$

where the unitary map $U^{(z)}_{-\pi/2}$ acts on all sites. When the number μ_2 of Majorana operators in A_2 is even, from (4.34) we have that $(-1)^{\tau(\mu_2)} = \mathrm{i}^{\mu_2}$ and therefore

$$\begin{aligned} \langle \zeta_2(x_2)|(O_2^T)_{\mathrm{even}}|\eta_2(x_2)\rangle &= (-1)^{\mu_2^y}\, \langle \eta_2^*(x_2)|\, U^{(z)}_{-\pi/2}\, (O_2)_{\mathrm{even}}\, U^{(z)}_{\pi/2}\, |-\zeta_2^*(x_2)\rangle \\ &= \langle \eta_2^*(x_2)|\, U^{(y)}_{-\pi}\, U^{(z)}_{-\pi/2}\, (O_2)_{\mathrm{even}}\, U^{(z)}_{\pi/2}\, U^{(y)}_{\pi}\, |-\zeta_2^*(x_2)\rangle\,, \end{aligned} \quad (5.22)$$

where in (5.22) the factor $(-1)^{\mu_2^y}$ has been removed through a second unitary transformation which sends $a_j^x \to -a_j^x$ leaving the a_j^y's unchanged (we recall that $U^{(z)}_{-\pi/2}$ exchanges the a_j^x's with the a_j^y's). The expression (5.22) suggests us to introduce the following unitary operator acting on A_2

$$V_2 \equiv U^{(y)}_{-\pi}\, U^{(z)}_{-\pi/2} = \prod_{j\in A_2} \exp\left(-\,\mathrm{i}\,\frac{\pi}{2}\,\frac{a_j^x - a_j^y}{\sqrt{2}}\right) = \prod_{j\in A_2} \exp\left[-\,\mathrm{i}\,\frac{\pi}{2}\left(e^{\mathrm{i}\frac{\pi}{4}} c_j^\dagger + e^{-\mathrm{i}\frac{\pi}{4}} c_j\right)\right], \quad (5.23)$$

whose net effect is to send $a_j^x \to -a_j^y$ and $a_j^y \to -a_j^x$, for $j \in A_2$.

In a similar way, we can treat the case of odd μ_2, for which $(-1)^{\tau(\mu_2)} = \mathrm{i}^{\mu_2 - 1}$ (see (4.34)). Again, from (4.35), (5.16)-(5.17a) one gets

$$\begin{aligned} \langle \zeta_2(x_2)|\big(O_2^T\big)_{\mathrm{odd}}|\eta_2(x_2)\rangle &= -\mathrm{i}\,(-1)^{\mu_2^y}\, \langle \eta_2^*(x_2)|\, U^{(z)}_{-\pi/2}\, (O_2)_{\mathrm{odd}}\, U^{(z)}_{\pi/2}\, |-\zeta_2^*(x_2)\rangle \\ &= -\mathrm{i}\, \langle \eta_2^*(x_2)|\, V_2\, (O_2)_{\mathrm{odd}}\, V_2^\dagger\, |-\zeta_2^*(x_2)\rangle\,. \end{aligned} \quad (5.24)$$

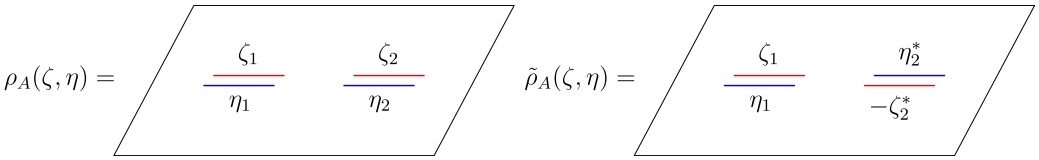

Figure 5.1: Path integral representation of ρ_A and $\tilde{\rho}_A$ in the coherent state basis.

Introducing the operator $\widetilde{O}_2$ through its matrix elements as follows

$$\langle \zeta_2(x_2)|\widetilde{O}_2|\eta_2(x_2)\rangle = \langle \eta_2^*(x_2)|\, V_2\, O_2\, V_2^\dagger\, |-\zeta_2^*(x_2)\rangle\,, \tag{5.25}$$

the expression (5.20) can be written as follows

$$\begin{aligned}\langle \zeta(x)|\rho_A^{T_2}|\eta(x)\rangle = \frac{1}{2^{\ell_1+\ell_2}}\Bigg(&\sum_{\text{even}} w_{12}\ \langle \zeta_1(x_1)|O_1|\eta_1(x_1)\rangle\, \langle \zeta_2(x_2)|\widetilde{O}_2|\eta_2(x_2)\rangle \\ &- \mathrm{i}\sum_{\text{odd}} w_{12}\ \langle \zeta_1(x_1)|O_1|\eta_1(x_1)\rangle\, \langle \zeta_2(x_2)|\widetilde{O}_2|\eta_2(x_2)\rangle\Bigg),\end{aligned} \tag{5.26}$$

where in the first (second) sum the terms have an even (odd) number of fermionic operators in A_2. In (5.26) the structure $\rho_A^{T_2} = \tilde{\rho}_{\text{even}} - \mathrm{i}\,\tilde{\rho}_{\text{odd}}$ (see (5.7)) can be recognised and this observation leads us to identify the matrix element of $\tilde{\rho}_A$ on the coherent states

$$\langle \zeta(x)|\tilde{\rho}_A|\eta(x)\rangle = \langle \zeta_1(x_1),\, \eta_2^*(x_2)|\, V_2\, \rho_A\, V_2^\dagger\, |\eta_1(x_1),\, -\zeta_2^*(x_2)\rangle\,, \tag{5.27}$$

and analogously

$$\langle \zeta(x)|P_{A_2}\tilde{\rho}_A P_{A_2}|\eta(x)\rangle = \langle \zeta_1(x_1),\, -\eta_2^*(x_2)|\, V_2\, \rho_A\, V_2^\dagger\, |\eta_1(x_1),\, \zeta_2^*(x_2)\rangle\,, \tag{5.28}$$

where from (5.16d) we can read that the action of P_{A_2} is to change the sign of ζ_2. A graphical representation of this path integral representation for $\tilde{\rho}_A$ is given in the right panel of Fig. 5.1. Hence, the final expression for the the partial transpose in the coherent state basis can be written exactly like the lattice counterpart i.e.

$$\rho_A^{T_2}(\zeta,\eta) = \frac{1}{\sqrt{2}}\Big[e^{-\mathrm{i}\frac{\pi}{4}}\tilde{\rho}_A(\zeta_1,\zeta_2;\eta_1,\eta_2) + e^{\mathrm{i}\frac{\pi}{4}}\tilde{\rho}_A(\zeta_1,-\zeta_2;\eta_1,-\eta_2)\Big], \tag{5.29}$$

where the notation is such that $\eta_i, \zeta_i \in A_i$. This explicit form of the partial transpose in the coherent state basis is the final and main result of this section.

In App. 5.A we employ the formalism of this section to check the identity $\mathrm{Tr}(\rho_A^{T_2})^2 = \mathrm{Tr}\,\rho_A^2$ (which holds for any quantum system [134, 135]) for the free fermion.

5.3 Traces of the partial transpose for the free fermion

In this section we consider the moments $\mathrm{Tr}(\rho_A^{T_2})^n$ for the free fermion. Using the path integral approach of the previous section, in Sec. 5.3.1 we derive the analytic formula for $\mathrm{Tr}(\rho_A^{T_2})^n$ given by (5.37) which is the main result of this manuscript. All the needed CFT results can be found in Sec. 1.4. In Sec. 5.3.2 we show that the moments for the free fermion are equal to the ones for the compact boson at the self-dual radius. Finally, in Sec. 5.3.3 we give some numerical checks of our results.

5.3.1 Moments of the partial transpose for the free fermionic field theory

The path integral for $\rho_A^{T_2}$ is given by (5.29) which is a sum of two different operators. The moments are then given by the sum of 2^n terms that come from the expansion of the binomial. Actually, since there is a double degeneration of these terms, the sum is only on 2^{n-1} terms. Introducing, in analogy with the lattice computation, the notation $\tilde\rho_0(\zeta,\eta) = \tilde\rho_A(\zeta,\eta)$ and $\tilde\rho_1(\zeta,\eta) = \tilde\rho_A(\zeta_1,-\zeta_2;\eta_1,-\eta_2)$, the 2^{n-1} terms in the sum for the moment of order n can be written as

$$\int \prod_{k=1}^{n} D\chi_k^* D\chi_k \, \tilde\rho_0(-\chi_n,\chi_1) \prod_{k=1}^{n-1} \tilde\rho_{p_k}(\chi_k,\chi_{k+1}), \tag{5.30}$$

with $p_i = 0, 1$. Each of these 2^{n-1} terms is a partition function of a free fermion on a Riemann surface of genus $n-1$ in which antiperiodic or periodic boundary condition are imposed along the basis cycles.

It is not difficult to realize that this surface is exactly $\widetilde{\mathcal{R}}_n$, whose main properties have been described in Sec. 1.4.3 (see the right panel of Fig. 1.1). Let us recall here that the period matrix $\tilde\tau(x)$ of $\widetilde{\mathcal{R}}_n$ for $x \in (0,1)$ is given by [135]

$$\tilde\tau(x) = \tau\big(x/(x-1)\big) = \mathcal{R} + \mathrm{i}\,\mathcal{I}, \qquad \mathcal{R} = \frac{1}{2}\,\mathcal{Q}, \tag{5.31}$$

where the elements of τ have been defined in (1.58). Here we observe that the real part $\mathcal{R}$ of the period matrix has a simple form. In (5.31) we defined the matrix $\mathcal{Q}$, which is a very simple symmetric integer matrix: it has 2 along the principal diagonal, -1 along the secondary diagonals and 0 for the remaining elements. In App. 5.B.1 we report the detailed derivation of this result. The cycles of $\widetilde{\mathcal{R}}_n$ providing the canonical homology basis $\{\tilde a_r, \tilde b_r\,;\, 1 \leqslant r \leqslant n-1\}$ which gives the period matrix (5.31), have also been discussed in Sec. 1.4.3 and depicted in Fig. 1.3. We recall here that $\tilde a_r$ is the same as a_r on $\mathcal{R}_n$, while the generic cycle $\tilde b_r$ is obtained by deforming the cycle b_r.

An important ingredient at this point is the operator P_{A_2}. For an arbitrary interval C we can write

$$P_C = (-1)^{\int_C \mathrm{d}x\, \bar\psi(x)\psi(x)} \equiv (-1)^{F_C}. \tag{5.32}$$

where F_C is the fermionic number operator in the interval C which was already introduced long ago [200]. This operator is located along the interval C and it changes the fermionic boundary conditions (from antiperiodic to periodic or viceversa) on a cycle whenever it crosses the curve C. In (5.29) for $\rho_A^{T_2}$, we have that P_{A_2} occurs both before and after $\tilde\rho_A$. This corresponds to the insertion of the operators $(-1)^{F_{A_2}}$ above and below the cut along A_2.

Each term (5.30) is a partition function on $\widetilde{\mathcal{R}}_n$ with some specific boundary conditions along the a and b cycles and it can be expressed in terms of Riemann theta functions. Explicitly, we have

$$\mathrm{Tr}\left[\tilde\rho_0 \prod_{k=1}^{n-1} \tilde\rho_{p_k}\right] = c_n^2 \left(\frac{1-x}{\ell_1\ell_2}\right)^{2\Delta_n} \left|\frac{\Theta[\boldsymbol{e}](\tilde\tau(x))}{\Theta(\tilde\tau(x))}\right|^2, \qquad \boldsymbol{e} = \begin{pmatrix} \mathbf{0} \\ \boldsymbol{\delta} \end{pmatrix}, \tag{5.33}$$

where $\mathbf{0}$ is the vector made by $n-1$ zeros. While c_n is not universal, its value for the tight-binding model at half-filling is known exactly and it is given by [325]

$$c_n = 2^{-\frac{1}{6}\left(n-\frac{1}{n}\right)} \exp\left\{ \mathrm{i}\, n \int_{-\infty}^{\infty} \mathrm{d}z\, \log\left(\frac{\Gamma\left(\frac{1}{2}+\mathrm{i}z\right)}{\Gamma\left(\frac{1}{2}-\mathrm{i}z\right)}\right) \big[\, \tanh(\pi z) - \tanh(\pi n z)\,\big] \right\}. \tag{5.34}$$

In the formula (5.33) we have still to fix the vector $\boldsymbol{\delta}$ in terms of $\boldsymbol{p}$, which is done as follows. Eq. (5.30) is evaluated on the n-sheeted Riemann surface $\widetilde{\mathcal{R}}_n$ where the i-th sheet is associated to the $\tilde{\rho}_{p_i}$. On the sheets associated to $\tilde{\rho}_1$, two operators $(-1)^{F_{A_2}}$ must be placed above and below A_2. Then, the spin structure $\boldsymbol{e}$ can be read off by counting how many times the cycles of the basis cross the curves A_2. Since the cycles $\tilde{a}_i$ do not intersect A_2 at all, we have that $\boldsymbol{\varepsilon} = \mathbf{0}$, i.e. the boundary conditions for the fermion along all the cycles $\tilde{a}_r$ are antiperiodic. Instead, for $\tilde{b}_r$ this analysis is non trivial because it intersects A_2 on the r-th sheet and on the $(r+1)$-th sheet, as one can see from the right panel of Fig. 1.3. If $\tilde{b}_r$ crosses these curves an even number of times, then $\delta_r = 0$, otherwise $\delta_r = 1/2$. It is not difficult to conclude that

$$2\delta_i = (p_i + p_{i+1}) \bmod 2, \tag{5.35}$$

whose inverse reads

$$p_i = \left(\sum_{j=i}^{n-1} 2\delta_j \right) \bmod 2 \;=\; \frac{1 - (-1)^{2\sum_{j=i}^{n-1}\delta_j}}{2}. \tag{5.36}$$

The simplest example of (5.33) is the term $\mathrm{Tr}\tilde{\rho}_0^n$ (namely $\boldsymbol{p} = \mathbf{0}$). This spin structure has antiperiodic boundary conditions along all the cycles, i.e. $\boldsymbol{\varepsilon} = \boldsymbol{\delta} = \mathbf{0}$.

Thus, $\mathrm{Tr}\left(\rho_A^{T_2}\right)^n$ can be written as a sum over all the allowed spin structures:

$$\mathrm{Tr}\left(\rho_A^{T_2}\right)^n \;=\; c_n^2 \left(\frac{1-x}{\ell_1 \ell_2}\right)^{2\Delta_n} \frac{1}{2^{n-1}} \sum_{\boldsymbol{\delta}} r_n(\boldsymbol{\delta}) \left| \frac{\Theta[\boldsymbol{e}](\tilde{\tau})}{\Theta(\tilde{\tau})} \right|^2, \qquad \boldsymbol{e} = \begin{pmatrix} \mathbf{0} \\ \boldsymbol{\delta} \end{pmatrix}. \tag{5.37}$$

The coefficient $r_n(\boldsymbol{\delta})$ is

$$r_n(\boldsymbol{\delta}) = 2^{n/2} \cos\left[\frac{\pi}{4} \left(1 + \sum_{i=1}^{n-1} (-1)^{2\sum_{j=i}^{n-1}\delta_j} \right) \right]. \tag{5.38}$$

It can be seen that $r_n(\boldsymbol{\delta}) \in \{-2^{n/2}, 0, 2^{n/2}\}$ for even n and $r_n(\boldsymbol{\delta}) \in \{-2^{(n-1)/2}, 2^{(n-1)/2}\}$ for odd n.

The analytic expression given by (5.37) and (5.38) is the main result of this chapter. When the size of the intervals is very small with respect to their distance ($\ell_1, \ell_2 \ll d$. i.e. $x \ll 1$), it is possible to expand (5.37) in powers of x, as shown in App. 5.B.2 where we find the first non trivial term of this expansion.

There is also a very interesting by-product of our analysis which is given by (5.33) providing a very deep technical insight. Indeed Eq. (5.33) shows also that *each of the* 2^{n-1} *terms in the sum over* $\boldsymbol{p}$ *in (5.11) has a well defined continuum limit* which is the partition function of the free fermion on $\widetilde{\mathcal{R}}_n$ with a particular assignment of fermionic boundary conditions, i.e. always antiperiodic along all the a cycles, while the b.c. along the b cycles are specified by $\boldsymbol{\delta}$ (we recall, antiperiodic for $\delta_i = 0$ and periodic otherwise).

Dihedral symmetry

The Riemann surfaces $\mathcal{R}_n$ and $\widetilde{\mathcal{R}}_n$ enjoy a dihedral symmetry $\mathbb{Z}_n \times \mathbb{Z}_2$, as already noticed in [228] and discussed also in Chap. 2. The symmetry $\mathbb{Z}_n$ comes from the invariance under cyclic permutation of the n sheets and the symmetry $\mathbb{Z}_2$ corresponds to take the sheets in the reversed order and to reflect all of them with respect to the real axis. The

former symmetry comes from the fact that $\mathcal{R}_n$ and $\widetilde{\mathcal{R}}_n$ are obtained through the replica construction and the latter one occurs because the endpoints of the intervals are on the real axis. Indeed, the complex equations (1.75) and (1.76), which define the Riemann surfaces $\mathcal{R}_n$ and $\widetilde{\mathcal{R}}_n$, are invariant under complex conjugation.

In [228] and in App. 2.C.3 of Chap. 2 the symplectic matrices which implement the dihedral symmetry of $\mathcal{R}_n$ have been written explicitly and in App. 5.B.3 this analysis has been extended to $\widetilde{\mathcal{R}}_n$ as well (the symmetry $\mathbb{Z}_2$ is different in the two cases). These transformations act on the period matrix and reshuffle the characteristics, but the functions and $\widetilde{\Omega}_n[\boldsymbol{e}]$ in (5.49) remain invariant. Moreover, both the transformations associated to the dihedral symmetry leave the coefficient $r_n(\boldsymbol{\delta})$ in (5.38) invariant. Thus, the terms in the sum (5.37) whose characteristics are related by one of these modular transformations are equal and the sum can be written in a simpler form by choosing a representative term for each equivalence class, whose coefficient is given by (5.38) multiplied by the number of terms of the equivalence class.

Exploiting these symmetries, one can write the explicit expressions given in Eq. (5.51) for $2 \leqslant n \leqslant 5$. Beside the goal of having more compact analytic expressions, the dihedral symmetry is very helpful also from the numerical point of view because it allows to reduce the exponentially large (in n) number of terms in (5.37).

Looking at Eq. (5.10) on the lattice, the $\mathbb{Z}_n$ symmetry corresponds to the cyclic permutation of the n factors within each trace. Instead, the $\mathbb{Z}_2$ symmetry comes from the fact that $\tilde{\rho}_0$ and $\tilde{\rho}_1$ are not separately hermitian but the hermitian conjugation exchange them, so that $\rho_A^{T_2}$ is hermitian. However, as already noticed, such exchange leaves any term of the sum unchanged. As for the continuous case, exploiting these symmetries one can simplify the formulas, and for $2 \leqslant n \leqslant 5$ one obtains the expressions (5.47).

5.3.2 Self-dual boson

In this subsection we show that the expression (5.37) for $\mathrm{Tr}\left(\rho_A^{T_2}\right)^n$ of the free Dirac fermion is equal to the one for the compactified boson at its self-dual radius.

The analytic formula for $\mathrm{Tr}\left(\rho_A^{T_2}\right)^n$ of the compactified boson for a generic value of the compactification radius has been derived in [135] by studying the partition function of the model on the Riemann surface $\widetilde{\mathcal{R}}_n$ and it has been reviewed in Sec. (1.4.3), see Eq. (1.81). At the self-dual radius $\eta = 1$, it becomes

$$\mathrm{Tr}\left(\rho_A^{T_2}\right)^n = c_n^2 \left(\frac{1-x}{\ell_1 \ell_2}\right)^{2\Delta_n} \frac{\Theta(T)}{|\Theta(\tilde{\tau})|^2}, \qquad T = \begin{pmatrix} \mathrm{i}\mathcal{I} & \mathcal{R} \\ \mathcal{R} & \mathrm{i}\mathcal{I} \end{pmatrix}, \tag{5.39}$$

where the matrices occurring in this expression have been recalled in (5.31). The Riemann theta function $\Theta(T)$ in the numerator can be written as follows

$$\Theta\begin{pmatrix} \mathrm{i}\mathcal{I} & \mathcal{R} \\ \mathcal{R} & \mathrm{i}\mathcal{I} \end{pmatrix} = \sum_{\boldsymbol{\varepsilon}} \left| \Theta\begin{bmatrix} \boldsymbol{\varepsilon} \\ \mathbf{0} \end{bmatrix}(2\tilde{\tau}) \right|^2 = \sum_{\boldsymbol{\varepsilon}} e^{2\pi \mathrm{i}\, \boldsymbol{\varepsilon}\cdot\mathcal{Q}\cdot\boldsymbol{\varepsilon}}\, \Theta\begin{bmatrix} \boldsymbol{\varepsilon} \\ \mathbf{0} \end{bmatrix}(2\tilde{\tau})^2, \tag{5.40}$$

where in the first step we have used (3.6b) of [214] and in the second one $-2\tilde{\tau}^* = 2\tilde{\tau} - 2\mathcal{Q}$. Then, by specialising the addition formula reported in [215] (pag. 4) to our case, we find

$$\Theta\begin{pmatrix} \mathrm{i}\mathcal{I} & \mathcal{R} \\ \mathcal{R} & \mathrm{i}\mathcal{I} \end{pmatrix} = \frac{1}{2^{n-1}} \sum_{\boldsymbol{\varepsilon},\boldsymbol{\delta}} (-1)^{4\boldsymbol{\varepsilon}\cdot\boldsymbol{\delta}}\, e^{2\pi \mathrm{i}\, \boldsymbol{\varepsilon}\cdot\mathcal{Q}\cdot\boldsymbol{\varepsilon}}\, \Theta\begin{bmatrix} \mathbf{0} \\ \boldsymbol{\delta} \end{bmatrix}(\tilde{\tau})^2 = \frac{1}{2^{n-1}} \sum_{\boldsymbol{\delta}} m_n(\boldsymbol{\delta})\, \Theta\begin{bmatrix} \mathbf{0} \\ \boldsymbol{\delta} \end{bmatrix}(\tilde{\tau})^2, \tag{5.41}$$

where

$$m_n(\boldsymbol{\delta}) = \sum_{\boldsymbol{\varepsilon}} (-1)^{4\boldsymbol{\varepsilon}\cdot\boldsymbol{\delta}}\, e^{2\pi \mathrm{i}\, \boldsymbol{\varepsilon}\cdot\mathcal{Q}\cdot\boldsymbol{\varepsilon}} = \sum_{\boldsymbol{\varepsilon}} e^{4i\pi\left(\boldsymbol{\varepsilon}\cdot\frac{\mathcal{Q}}{2}\cdot\boldsymbol{\varepsilon}+\boldsymbol{\varepsilon}\cdot\boldsymbol{\delta}\right)}. \tag{5.42}$$

In App. 5.C we show that $m_n(\boldsymbol{\delta})$ can be written as the partition function of a classical Ising spin system, where $\boldsymbol{\varepsilon}$ play the role of the spin variables and the $\boldsymbol{\delta}$ are the local magnetic fields. In the same appendix we also employ standard transfer matrix techniques to prove that $m_n(\boldsymbol{\delta}) = r_n(\boldsymbol{\delta})$ (see (5.38) and (5.42)).

5.3.3 Numerical checks

In order to evaluate numerically the moments of the partial transpose, we employ the techniques first developed in [222] for $\mathrm{Tr}\,\rho_A^n$ and used in Chap. 4 to compute $\mathrm{Tr}(\rho_A^{T_2})^n$ for spin systems. Indeed, being the tight-binding Hamiltonian (5.1) quadratic in the fermionic operators, the ground state reduced density matrix ρ_A is Gaussian. Moreover, $\tilde{\rho}_A$ in (5.9) is Gaussian as well and, since the string operator P_C can be written as the exponential of a quadratic operator, the density matrix $P_{A_2}\tilde{\rho}_A P_{A_2}$ is also Gaussian. Nevertheless, the sum of these two matrices in (5.9) is not Gaussian (this is indeed the main difficulty compared to bosonic models in which the partial transpose is itself Gaussian [126, 147, 150, 151]). By exploiting the fact that for Gaussian states all the information of the system is encoded in the correlation matrices, the computations can be performed in a polynomial time in terms of the total size of the subsystem. In particular, in our case the correlation matrices of $\tilde{\rho}_A$ and $P_{A_2}\tilde{\rho}_A P_{A_2}$ can be obtained from the one of ρ_A, as described in [331] and discussed in Chap. 4.

As already noticed in Sec. 5.2.1, the only difference with the formulas of Chap. 4 is the absence of the string of Majorana operators (4.12) in B_1. Thus, the formulas for the moment of the partial transpose in terms of correlation matrices can be computed both from Eq. (5.9) as well as from the formulas derived in Chap. 4, by discarding the string of Majorana operators, i.e. by replacing P_{B_1} with $\mathbf{1}$, in the same manner as what was done at the end of Sec. 5.2.1 for the reduced density matrix and its partial transpose.

At the level of the correlation matrices Γ_i discussed in Chap. 4, since $\rho_A^{B_1} \to \rho_A^{\mathbf{1}}$, it is obvious that $\Gamma_3 \to \Gamma_1$ and $\Gamma_4 \to \Gamma_2$. We conclude that the fermionic $\mathrm{Tr}\,\rho_A^n$ is found by making in Eq. (4.26) the following replacements

$$\delta_{B_1} \to 1, \qquad \Gamma_3 \to \Gamma_1, \qquad \Gamma_4 \to \Gamma_2. \tag{5.43}$$

Performing these substitutions in the explicit examples given in Sec. 4.3 for $2 \leqslant n \leqslant 5$, it is straightforward to find

$$\mathrm{Tr}\,\rho_A^n = \{\Gamma_1^n\}. \tag{5.44}$$

which is just the obvious result that the fermionic density matrix is the Gaussian operator with correlation matrix given by Γ_1. We numerically calculated $\mathrm{Tr}\,\rho_A^n$ using Eq. (5.44) (as was already done in Ref. [333]), obtaining that on the critical lines in the scaling limit it converges to

$$\mathrm{Tr}\,\rho_A^n \to \frac{c_n^2}{\left[\ell_1\ell_2(1-x)\right]^{2\Delta_n}}, \tag{5.45}$$

that corresponds to $\mathcal{F}_n(x) = 1$ identically in the general CFT formula (1.56). Indeed this result was already proven in the continuum free fermion theory [46].

We can proceed in the same way for the partial transpose. Given that $\tilde{\rho}_A^{B_1} \to \tilde{\rho}_A^{\mathbf{1}}$, it follows that we should perform the replacements $\widetilde{\Gamma}_3 \to \widetilde{\Gamma}_1$ and $\widetilde{\Gamma}_4 \to \widetilde{\Gamma}_2$ in order to get

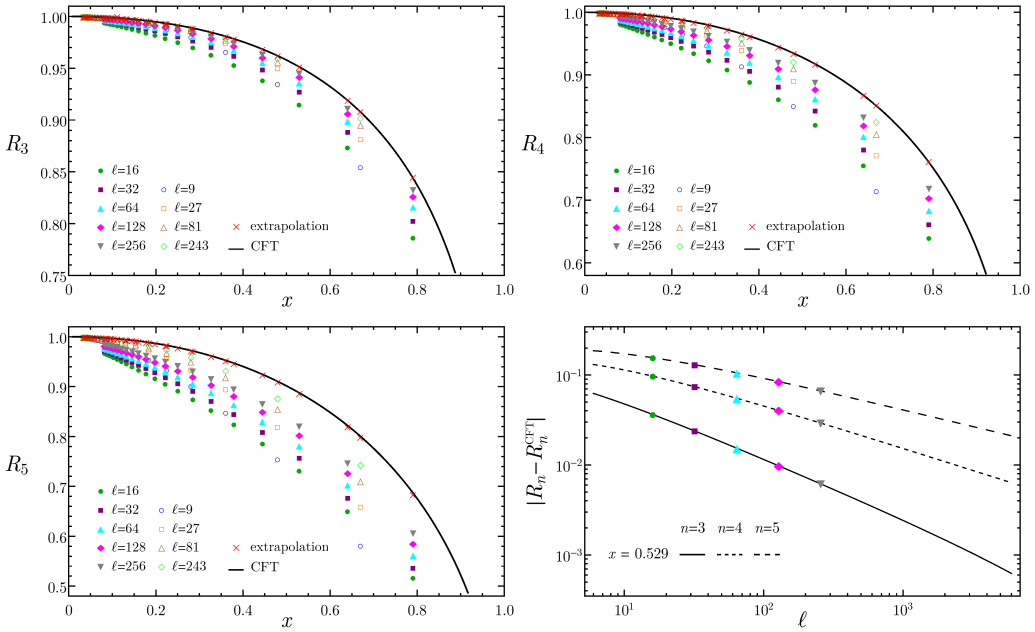

Figure 5.2: The ratio R_n between the integer moments of ρ_A and $\rho_A^{T_2}$ for two disjoint intervals of length ℓ at distance r for the tight-binding model at half-filling. We report the results for $n = 3, 4, 5$ as function of the four-point ratio x for various values of ℓ (and correspondingly of r). For large ℓ, the data approach the CFT predictions (solid lines). The extrapolations to $\ell \to \infty$ –done using the scaling form (4.50)– are shown as crosses and they perfectly agree with the CFT curves for $n = 3, 4, 5$. The last panel shows explicitly the extrapolating functions for one value of x and $n = 3, 4, 5$.

the moments of the partial transpose in terms of the correlation matrices. Summarising, the fermionic $\mathrm{Tr}(\rho_A^{T_2})^n$ are given by the formulas in Sec. 4.4 performing the replacements

$$\delta_{B_1} \to 1, \qquad \widetilde{\Gamma}_3 \to \widetilde{\Gamma}_1, \qquad \widetilde{\Gamma}_4 \to \widetilde{\Gamma}_2. \tag{5.46}$$

Performing the replacements in the formulas for $2 \leqslant n \leqslant 5$ given in Eqs. (4.44), (4.45), (4.46) and (4.47), and exploiting the symmetries described at the end of Sec. 5.3.1, we find

$$\widetilde{T}_2 = 2\,\{\widetilde{\Gamma}_1, \widetilde{\Gamma}_2\}, \tag{5.47a}$$

$$\widetilde{T}_3 = -2\,\{\widetilde{\Gamma}_1^3\} + 6\,\{\widetilde{\Gamma}_1^2, \widetilde{\Gamma}_2\}, \tag{5.47b}$$

$$\widetilde{T}_4 = -4\,\{\widetilde{\Gamma}_1^4\} + 4\,\{\widetilde{\Gamma}_1, \widetilde{\Gamma}_2, \widetilde{\Gamma}_1, \widetilde{\Gamma}_2\} + 8\,\{\widetilde{\Gamma}_1^2, \widetilde{\Gamma}_2^2\}, \tag{5.47c}$$

$$\widetilde{T}_5 = -4\,\{\widetilde{\Gamma}_1^5\} - 20\,\{\widetilde{\Gamma}_1^4, \widetilde{\Gamma}_2\} + 20\,\{\widetilde{\Gamma}_1^3, \widetilde{\Gamma}_2^2\} + 20\,\{\widetilde{\Gamma}_1^2, \widetilde{\Gamma}_2, \widetilde{\Gamma}_1, \widetilde{\Gamma}_2\}, \tag{5.47d}$$

where $\widetilde{T}_n$ is defined in Eq. (4.43). Notice that the final expressions are very compact compared to the much more cumbersome spin counterparts.

The lattice computations have been performed in an infinite chain, as in Chap. 4. Again, the disjoint blocks A_1 and A_2 have been taken with the same size $\ell_1 = \ell_2 \equiv \ell$, while the size of the block B_1 separating them is d. Thus, the four point ratio x becomes (4.48). and configurations with the same value of ℓ/d correspond to the same x. The numerical

results for the ratios $R_n = \mathrm{Tr}(\rho_A^{T_2})^n/(\mathrm{Tr}\,\rho_A^n)$ are reported in Fig. 5.2 as function of the four-point ratio x for different ℓ and for $n = 3, 4, 5$ (we checked that $R_2 = 1$ identically, as it should). The CFT formulas for R_n are computed through Eqs. (5.37) and (5.45). The explicit formulas for $2 \leq n \leq 5$ are given at the end of this section in Eq. (5.51). It is evident from Fig. 5.2 that the lattice numerical results approach the CFT predictions depicted as solid lines for all n.

In order to deal with the finite size effects, we perform an accurate scaling analysis, as in the spin case of Sec. 4.5. We recall that from general CFT arguments it has been shown that these quantities display some unusual corrections to the scaling in ℓ described by a power law term with exponent $\delta_n = 2h/n$, being h the smallest scaling dimension of a relevant operator inserted at the branch points [260–263, 327, 334–336]. For the Dirac fermion $h = 1$ and terms of the form $\ell^{-2m/n}$ are present, for any positive integer m. Because of the slow convergence of these terms (which becomes slower and slower for increasing n), typically it is necessary to include in the scaling function many of them. The finite ℓ ansatz is then given by Eq. (4.50). As for the spin case, fitting the data with (5.50), the more terms we include, the more precise the fit could be. Nevertheless, since we have access to limited values of ℓ, by using too many terms overfitting problems may be encountered, which lead to very unstable results. The number of terms to be included in (5.50) has been chosen in order to get stable fits. The results of this extrapolation procedure for $n = 3, 4, 5$ are explicitly reported in Fig. 5.2 (red crosses). The agreement of the extrapolations with the CFT predictions is excellent also for $n = 5$ as a difference compared to the spin counterpart (see Figs. 4.2 and 4.3).

We can perform some other checks. Indeed, we have given a set of more stringent relations (5.33) between each term in the sum for $\mathrm{Tr}(\rho_A^{T_2})^n$ appearing both in CFT and on the lattice. We can provide explicit numerical evidence of this term-by-term correspondence for $n = 2, 3, 4$. Referring to Eq. (5.11), let us introduce the following lattice quantities

$$\tilde{J}_n^{\mathrm{lat}} = \mathrm{Tr}\,\tilde{\rho}_0^n, \qquad \widetilde{\Omega}_n^{\mathrm{lat}}[\boldsymbol{p}]^2 = \frac{1}{\mathrm{Tr}\,\tilde{\rho}_0^n}\ \mathrm{Tr}\left[\tilde{\rho}_0 \prod_{k=1}^{n-1} \tilde{\rho}_{p_k}\right]. \tag{5.48}$$

We also introduce their CFT continuum limit:

$$\tilde{J}_n \equiv c_n^2 \left(\frac{1-x}{\ell_1 \ell_2}\right)^{2\Delta_n}, \qquad \widetilde{\Omega}_n[\boldsymbol{e}] \equiv \left|\frac{\Theta[\boldsymbol{e}](\tilde{\tau}(x))}{\Theta(\tilde{\tau}(x))}\right|. \tag{5.49}$$

These CFT values are again approached by taking configurations with increasing ℓ, keeping the ratio ℓ/d fixed. As discussed at the end of Sec. 5.3.1, many terms in the sum (5.11) are equal because of the properties of the trace (in the continuum, this degeneracy is due to the dihedral symmetry of the Riemann surface).

In order to compare the lattice data with their continuum counterpart, we again need to perform a scaling analysis, exactly as was done for the ratio R_n. The most general finite-ℓ ansatz for $\widetilde{\Omega}_n$ takes the following form

$$\widetilde{\Omega}_n^{\mathrm{lat}}[\boldsymbol{p}]^2 = \widetilde{\Omega}_n^2[\boldsymbol{e}] + \frac{\omega_n^{(1)}(x)}{\ell^{2/n}} + \frac{\omega_n^{(2)}(x)}{\ell^{4/n}} + \frac{\omega_n^{(3)}(x)}{\ell^{6/n}} + \ldots, \tag{5.50}$$

where $\boldsymbol{p}$ and $\boldsymbol{e}$ are related through (5.35) and (5.36). As for the prefactor, the ratio $\tilde{J}_n^{\mathrm{lat}}/\tilde{J}_n$ has been considered in order to eliminate the trivial dependence on ℓ which survives in the continuum limit. For this ratio a scaling function similar to (5.50) can be studied. Again, to have an accurate description of the data we keep a number of fitting parameters

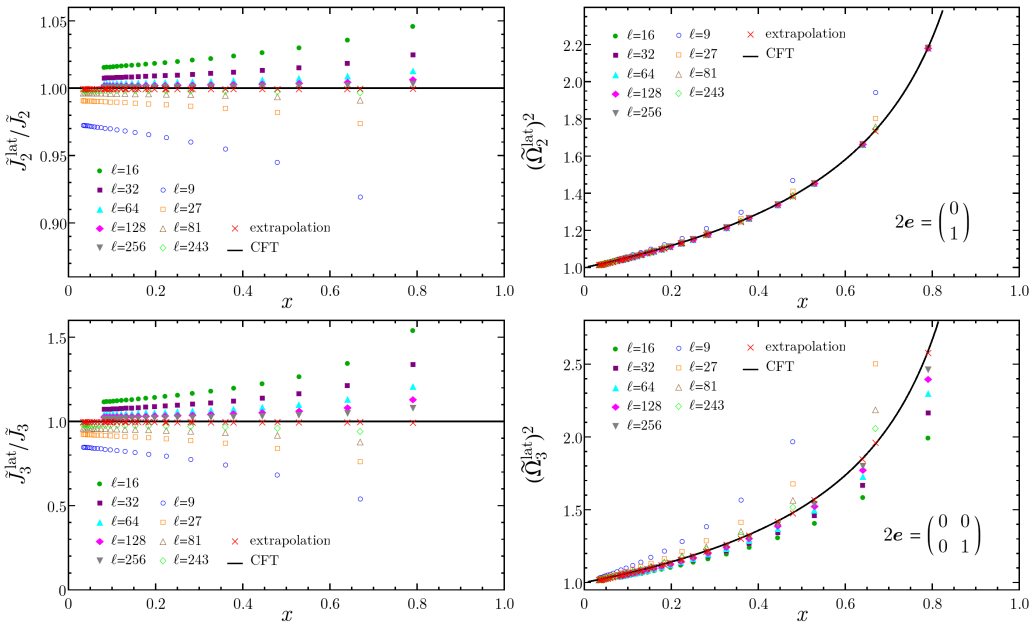

Figure 5.3: The terms occurring in $\mathrm{Tr}(\rho_A^{T_2})^n$ for the free fermion (see (5.37)), according to the correspondence (5.33). Here we show $n = 2$ (top panels) and $n = 3$ (bottom panels). For each group of identical terms, only one representative has been plotted. In the left panels, the term with $\boldsymbol{p} = \boldsymbol{0}$ has been divided by its CFT counterpart ($\boldsymbol{\delta} = \boldsymbol{0}$), in order to simplify the residual dependence on ℓ_1 and ℓ_2. The extrapolated points (red crosses) are obtained through a fit of the data according to the scaling function (5.50) and they agree with the CFT predictions (solid lines).

in (5.50) which make stable the extrapolation at $\ell \to \infty$. We find that every term $\widetilde{\Omega}_n[\boldsymbol{e}]$ follows the scaling (5.50) and the extrapolated value agrees with the corresponding CFT result. Our numerical results are shown in Fig. 5.3 for $n = 2$ (top panels) and $n = 3$ (bottom panels), while Fig. 5.4 is about the $n = 4$ case. The solid lines are the CFT predictions, which are given by (5.33).

We conclude this section by giving explicit formulas for the ratio R_n in the continuum limit in terms of the quantities defined in Eq. (5.49).

$$\frac{2R_2}{(1-x)^{4\Delta_2}} = 2\,\widetilde{\Omega}_n^2 \begin{bmatrix} 0 \\ 1/2 \end{bmatrix}, \tag{5.51a}$$

$$\frac{4R_3}{(1-x)^{4\Delta_3}} = -2 + 6\,\widetilde{\Omega}_n^2 \begin{bmatrix} 0 & 0 \\ 0 & 1/2 \end{bmatrix}, \tag{5.51b}$$

$$\frac{8R_4}{(1-x)^{4\Delta_4}} = -4 + 8\,\widetilde{\Omega}_n^2 \begin{bmatrix} 0 & 0 & 0 \\ 0 & 1/2 & 0 \end{bmatrix} + 4\,\widetilde{\Omega}_n^2 \begin{bmatrix} 0 & 0 & 0 \\ 1/2 & 1/2 & 1/2 \end{bmatrix}, \tag{5.51c}$$

$$\frac{16R_5}{(1-x)^{4\Delta_5}} = -4 + 20\,\widetilde{\Omega}_n^2 \begin{bmatrix} 0 & 0 & 0 & 0 \\ 0 & 0 & 1/2 & 0 \end{bmatrix} + 20\,\widetilde{\Omega}_n^2 \begin{bmatrix} 0 & 0 & 0 & 0 \\ 0 & 1/2 & 1/2 & 1/2 \end{bmatrix} - 20\,\widetilde{\Omega}_n^2 \begin{bmatrix} 0 & 0 & 0 & 0 \\ 0 & 0 & 0 & 1/2 \end{bmatrix}. \tag{5.51d}$$

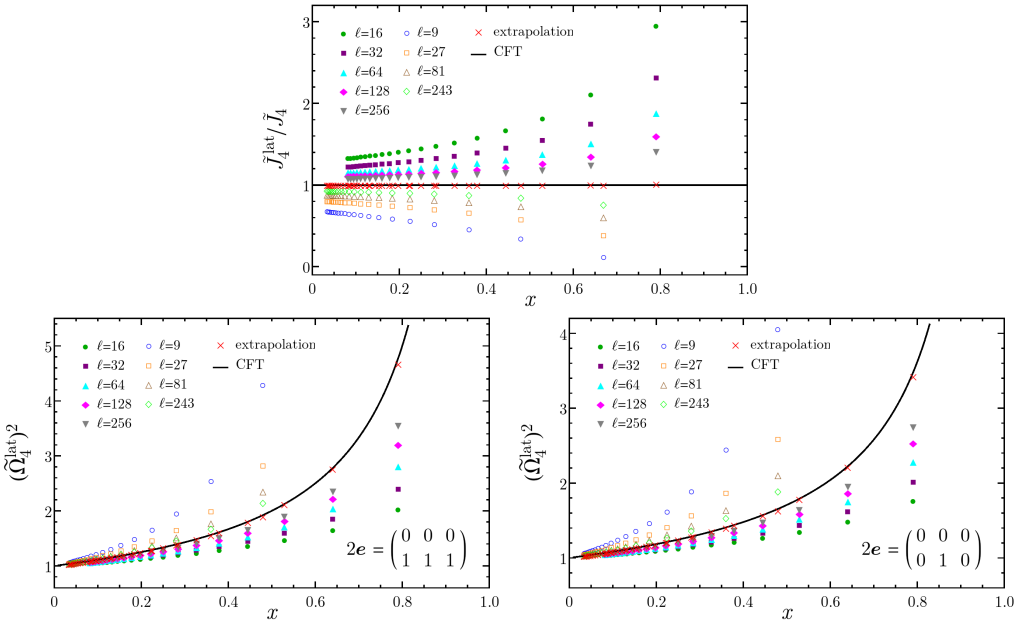

Figure 5.4: The terms occurring in $\mathrm{Tr}(\rho_A^{T_2})^4$ for the free fermion (see (5.37)), according to the correspondence (5.33). For each of the three groups of identical terms, only one representative has been plotted. In the top panel, the term with $\boldsymbol{p} = \boldsymbol{0}$ has been divided by its CFT counterpart ($\boldsymbol{\delta} = \boldsymbol{0}$), in order to simplify the residual dependence on ℓ_1 and ℓ_2. The extrapolated points (red crosses) are obtained through a fit of the data according to the scaling function (5.50) and they agree with the CFT predictions (solid lines).

5.4 Ising model and modular invariant Dirac fermion

In this section we apply the technique developed for the free fermion in Sec. 5.3 to the Ising model and to the modular invariant Dirac fermion. The CFT formulas for $\mathrm{Tr}\,\rho_A^n$ and $\mathrm{Tr}(\rho_A^{T_2})^n$ for these models are known [135, 145, 196] and they are written as modular invariant expressions given by a sum over all the possible spin structures. For $\mathrm{Tr}\,\rho_A^n$ the explicit form of $\mathcal{F}_n(x)$ for the two models is (see Eqs. (1.63) and (1.60)),

$$\mathcal{F}_n^{\rm Ising}(x) = \frac{1}{2^{n-1}} \sum_{\boldsymbol{e}} \left| \frac{\Theta[\boldsymbol{e}](\tau(x))}{\Theta(\tau(x))} \right|, \tag{5.52a}$$

$$\mathcal{F}_n^{\rm Dirac}(x) = \frac{1}{2^{n-1}} \sum_{\boldsymbol{e}} \left| \frac{\Theta[\boldsymbol{e}](\tau(x))}{\Theta(\tau(x))} \right|^2. \tag{5.52b}$$

while for $\mathrm{Tr}(\rho_A^{T_2})^n$ we simply need to replace $x \to x/(x-1)$ (see Eq. (1.80))

$$\mathcal{F}_n^{\rm Ising}\big(x/(x-1)\big) = \frac{1}{2^{n-1}} \sum_{\boldsymbol{e}} \left| \frac{\Theta[\boldsymbol{e}](\tilde{\tau}(x))}{\Theta(\tilde{\tau}(x))} \right|, \tag{5.53a}$$

$$\mathcal{F}_n^{\rm Dirac}\big(x/(x-1)\big) = \frac{1}{2^{n-1}} \sum_{\boldsymbol{e}} \left| \frac{\Theta[\boldsymbol{e}](\tilde{\tau}(x))}{\Theta(\tilde{\tau}(x))} \right|^2. \tag{5.53b}$$

Although the scaling functions for the two models are already known, both for the moments of the reduced density matrix and its partial transpose, it is instructive to rederive

them with the method of Sec. 5.3. Moreover, going through this procedure we can identify the quantities on the lattice whose continuum limit is characterised by a specific spin structure.

5.4.1 Hamiltonians on the lattice

The Ising model and the modular invariant Dirac model are the scaling limit of the Ising spin chain and the XX spin chain respectively, which are both particular cases of the XY spin chain, discussed in Chap. 4. The Hamiltonian (4.1) depends on two parameters: the transverse magnetic field h and the anisotropy parameter γ [332]. In this manuscript we focus on two special cases: the critical XX spin chain ($\gamma = h = 0$) and the critical Ising model ($\gamma = h = 1$)

$$H_{\mathrm{XX}} = -\frac{1}{4}\sum_{j=1}^{L}\left(\sigma_j^x\sigma_{j+1}^x + \sigma_j^y\sigma_{j+1}^y\right), \qquad H_{\mathrm{Ising}} = -\frac{1}{2}\sum_{j=1}^{L}\left(\sigma_j^x\sigma_{j+1}^x + \sigma_j^z\right). \tag{5.54}$$

It is possible to diagonalize both operators in (5.54) via the Jordan-Wigner transformation (4.2) which maps the spin variables into anti-commuting fermionic variables (i.e. $\{c_i, c_j^\dagger\} = \delta_{ij}$). The Hamiltonians in (5.54) can be written as

$$H_{\mathrm{XX}} = \frac{1}{2}\sum_{i=1}^{L}\left(c_i^\dagger c_{i+1} + c_{i+1}^\dagger c_i\right), \tag{5.55a}$$

$$H_{\mathrm{Ising}} = \sum_{i=1}^{L}\left(\frac{1}{2}\left[c_i^\dagger c_{i+1}^\dagger + c_{i+1}c_i + c_i^\dagger c_{i+1} + c_{i+1}^\dagger c_i\right] - c_i^\dagger c_i\right), \tag{5.55b}$$

where boundary and additive terms have been discarded. Then, the Hamiltonians in (5.55) can be easily diagonalised in momentum space by means of a Bogoliubov transformation.

5.4.2 Moments of the reduced density matrix and its partial transpose on the lattice

The moments $\mathrm{Tr}\,\rho_A^n$ of two disjoint blocks for the XY model (4.3) have been studied in [222] and $\mathrm{Tr}\left(\rho_A^{T_2}\right)^n$ in Chap. 4. In order to describe the reduced density matrix ρ_A of two disjoint blocks separated by the block B_1 for the model (4.3), beside the string P_{A_2} largely discussed in Sec. 5.2, we also need to consider the string of Majorana operators P_{B_1} along B_1 (see (4.12)). It is also important to introduce the auxiliary density matrix (4.18).

In Sec. 4.3 we showed that $\mathrm{Tr}\,\rho_A^n = \mathrm{Tr}(\rho_{\mathrm{even}} + \rho_{\mathrm{odd}})^n$, where ρ_{even} and ρ_{odd} have been defined in (4.21). Thus, $\rho_{\mathrm{even}} + \rho_{\mathrm{odd}}$ can be written as a linear combination of the following four fermionic Gaussian operators[3]

$$\rho_1 \equiv \rho_A^{\mathbf{1}} \qquad \rho_2 \equiv P_{A_2}\rho_A^{\mathbf{1}}P_{A_2} \qquad \rho_3 \equiv \langle P_{B_1}\rangle\,\rho_A^{B_1} \qquad \rho_4 \equiv -\langle P_{B_1}\rangle\,P_{A_2}\rho_A^{B_1}P_{A_2} \tag{5.56}$$

We recall that for the free fermion $\rho_A = \rho_A^{\mathbf{1}}$ and this result can be obtained by taking (4.13) and setting $P_{B_1} = \mathbf{1}$.

Thus, $\mathrm{Tr}\rho_A^n$ is an algebraic sum of 4^n terms and each of them is specified by a string $\boldsymbol{q}$ made by n elements $q_i \in \{1,2,3,4\}$. The terms with an odd number of 4's in $\boldsymbol{q}$ will occur

[3] In this section we reintroduce the superscript $\mathbf{1}$ to distinguish between the spin density matrix ρ_A and the fermionic density matrix $\rho_A^{\mathbf{1}}$.

in $\mathrm{Tr}\,\rho_A^n$ with a minus sign. Moreover, by using the cyclic property of the trace and the fact that $P_{A_2}^2 = \mathbf{1}$, it is straightforward to observe that a term characterised by $\boldsymbol{q}$ is equal to the one relative to $\boldsymbol{q}'$ obtained by exchanging $1 \leftrightarrow 2$ and $3 \leftrightarrow 4$. A term characterised by a $\boldsymbol{q}$ with an odd number of 3's and 4's will have opposite sign with respect to the one characterised by $\boldsymbol{q}'$. Hence, the terms with an odd total number of ρ_3's and ρ_4's will cancel out, while the other ones simplify and a factor 2 can be collected. Thus, we have that

$$\mathrm{Tr}\rho_A^n = \frac{1}{2^{n-1}} \sum_{\boldsymbol{q}} \mathrm{Tr}\left[\prod_{k=1}^{n} \rho_{q_k} \right], \tag{5.57}$$

where the sum must be intended over all $\boldsymbol{q}$ with an even total number of 3's and 4's and modulo the exchange $1 \leftrightarrow 2$ and $3 \leftrightarrow 4$. It is not difficult to realize that the sum contains $2^{2(n-1)}$ terms. The terms in (5.57) with an odd number of ρ_4's occurs with a minus sign. Explicit expressions of (5.57) for $2 \leqslant n \leqslant 5$ have been written in Eqs. (4.27)–(4.30) in terms of the correlators.

The analysis just sketched for $\mathrm{Tr}\,\rho_A^n$ can be performed also for $\mathrm{Tr}\left(\rho_A^{T_2}\right)^n$. In this case, considering Eqs. (4.32), (4.37) and (4.39), it is convenient to define the following four Gaussian operators

$$\tilde{\rho}_1 \equiv \tilde{\rho}_A^{\mathbf{1}} \qquad \tilde{\rho}_2 \equiv P_{A_2} \tilde{\rho}_A^{\mathbf{1}} P_{A_2} \qquad \tilde{\rho}_3 \equiv -\,\mathrm{i}\,\langle P_{B_1} \rangle\, \tilde{\rho}_A^{B_1} \qquad \tilde{\rho}_4 \equiv \mathrm{i}\,\langle P_{B_1} \rangle\, P_{A_2} \tilde{\rho}_A^{B_1} P_{A_2} \tag{5.58}$$

where $\tilde{\rho}_A^{\mathbf{1}}$ and $\tilde{\rho}_A^{B_1}$ have been defined in (4.38). We recall that all these fermionic operators are Gaussian. Since $\mathrm{Tr}\left(\rho_A^{T_2}\right)^n = \mathrm{Tr}(\rho_{\mathrm{even}}^{T_2} + \rho_{\mathrm{odd}}^{T_2})^n$, where $\rho_{\mathrm{even}}^{T_2}$ and $\rho_{\mathrm{odd}}^{T_2}$ are defined in (4.36), and can be written as linear combinations of the operators in (5.58) (see Eq. (4.39)), then one finds that $\mathrm{Tr}(\rho_A^{T_2})^n$ is a linear combination of 4^n terms and each one of them is again specified by a string $\tilde{\boldsymbol{q}}$ made by n elements $q_i \in \{1,2,3,4\}$. An important difference between (5.56) and (5.58) is the occurrence of the imaginary unit in the latter set of definitions. In this case the analysis is very similar to the previous one performed for $\mathrm{Tr}\,\rho_A^n$. In particular, a term characterised by some $\tilde{\boldsymbol{q}}$ is equal to the one specified by the $\tilde{\boldsymbol{q}}'$ obtained by exchanging $1 \leftrightarrow 2$ and $3 \leftrightarrow 4$ in $\tilde{\boldsymbol{q}}$. As in the case of the Rényi entropies, the terms with an odd total number of $\tilde{\rho}_3$'s and $\tilde{\rho}_4$'s cancel out. The latter simplification guarantees that all the non vanishing coefficients in $\mathrm{Tr}\left(\rho_A^{T_2}\right)^n$ are real. Thus, we have that

$$\mathrm{Tr}\left(\rho_A^{T_2}\right)^n = \frac{1}{2^{n-1}} \sum_{\tilde{\boldsymbol{q}}} \mathrm{Tr}\left[\prod_{k=1}^{n} \tilde{\rho}_{\tilde{q}_k} \right], \tag{5.59}$$

where again the sum contains $2^{2(n-1)}$ terms and must be intended over all $\tilde{\boldsymbol{q}}$ with an even total number of 3's and 4's and modulo the exchange $1 \leftrightarrow 2$ and $3 \leftrightarrow 4$. Explicit expressions for $\mathrm{Tr}(\rho_A^{T_2})^n$ with $2 \leqslant n \leqslant 5$ can be found in Eqs. (4.44)–(4.47). They are written through the correlators but the identification of the various terms with the ones in (5.59) is straightforward.

5.4.3 Moments of the reduced density matrix and its partial transpose in the continuum

In this section we want to identify the quantity on the lattice occurring in (5.57) and (5.59) whose continuum limit is a single term in (5.52) and (5.53) respectively with given characteristic $\boldsymbol{e}$.

In Sec. 5.2.3 we already identified the coherent state path integral representation of $\rho_1(\zeta,\eta) \equiv \rho_A^{\mathbf{1}}(\zeta,\eta)$ and $\tilde\rho_1(\zeta,\eta) \equiv \tilde\rho_A^{\mathbf{1}}(\zeta,\eta)$ (see Eqs. (5.19), (5.27) and Fig. 5.1) and the effect of the operator P_{A_2} in $\rho_2(\zeta,\eta)$ and $\tilde\rho_2(\zeta,\eta)$ (see Eq. (5.28)). The latter changes the sign of the fermion above and below the cut along A_2, and in the continuum must be identified with the operator $(-1)^{F_{A_2}}$, defined in Eq. (5.32). When n sheets are sewn together as in (5.30) (see also Fig. 1.1), the effect of this operator is to change the fermionic boundary conditions along any homology cycle that crosses the curves along which it is inserted.

To extend the analysis to the modular invariant Dirac fermion and the Ising model we also need a path integral representation of $\rho_3(\zeta,\eta)$ and $\tilde\rho_3(\zeta,\eta)$. As can be seen from the definition of $\rho_A^{B_1}$ and $\tilde\rho_A^{B_1}$ in the lattice, Eqs. (4.18) and (4.38), the main difference is the presence of the string operator P_{B_1}. In the continuum this corresponds to the insertion of the operator $(-1)^{F_{B_1}}$ between the two intervals, along B_1. In the path integral representation of $\rho_3(\zeta,\eta)$ the field above and below B_1 will appear with the opposite relative sign with respect to B_2 (compare the expression with the path integral representation of $\rho_1(\zeta,\eta)$ in Eq. (5.19))

$$\rho_3(\zeta_A,\eta_A) = e^{-\zeta_A^*\eta_A} \int D\chi_B^*\, D\chi_B\, e^{-\chi_B^*\,\chi_B}\, \langle \zeta_A;\, \chi_{B_1},\, -\chi_{B_2}|\Psi\rangle\, \langle\Psi|\eta_A;\, \chi_{B_1},\, \chi_{B_2}\rangle\,. \quad (5.60)$$

The path integral representation of $\tilde\rho_3(\zeta,\eta)$ is then obtained from (5.60) by essentially exchanging the values of the fields above and below the cut in A_2 with a relative minus sign, according to Eq. (5.27). There is also a factor $-\mathrm{i}$ coming from the definition (5.58). When joining n sheets, the fermionic boundary conditions along all the cycles which cross B_1 on a sheet of the type (5.60), will be changed from antiperiodic to periodic. Finally, the path integral representation of $\rho_4(\zeta,\eta)$ and $\tilde\rho_4(\zeta,\eta)$ contains the operator $(-1)^F$ both around the interval A_2 and along B_1. Therefore, its path integral representation of $\rho_4(\zeta,\eta)$ is given by

$$\begin{aligned}\rho_4(\zeta_A,&\eta_A) = -\rho_3(\zeta_{A_1},-\zeta_{A_2};\eta_{A_1},-\eta_{A_2}) = -e^{-\zeta_A^*\eta_A}\times \\ &\int D\chi_B^*\, D\chi_B\, e^{-\chi_B^*\,\chi_B}\, \langle \zeta_{A_1},-\zeta_{A_2};\, \chi_{B_1},\, -\chi_{B_2}|\Psi\rangle\, \langle\Psi|\eta_{A_1},-\eta_{A_2};\, \chi_{B_1},\, \chi_{B_2}\rangle\,,\end{aligned} \quad (5.61)$$

and analogously $\tilde\rho_4(\zeta_A,\eta_A) = -\tilde\rho_3(\zeta_{A_1},-\zeta_{A_2};\eta_{A_1},-\eta_{A_2})$. Summarizing, we can write the coherent state path integral representation of $\rho_+(\zeta,\eta)$ and $\rho_+^{T_2}(\zeta,\eta)$ as a sum of four terms

$$\rho_+(\zeta,\eta) = \frac{1}{2}\Big[\rho_1(\zeta,\eta) + \rho_2(\zeta,\eta) + \rho_3(\zeta,\eta) + \rho_4(\zeta,\eta)\Big], \quad (5.62a)$$

$$\rho_+^{T_2}(\zeta,\eta) = \frac{1}{2}\Big[\tilde\rho_1(\zeta,\eta) + \tilde\rho_2(\zeta,\eta) + \tilde\rho_3(\zeta,\eta) + \tilde\rho_4(\zeta,\eta)\Big]. \quad (5.62b)$$

When computing $\mathrm{Tr}\,\rho_A^n = \mathrm{Tr}\,\rho_+^n$ and $\mathrm{Tr}\,\big(\rho_A^{T_2}\big)^n = \mathrm{Tr}(\rho_+^{T_2})^n$, as in the lattice case we get sums over 4^n terms specified by the same strings $\boldsymbol{q}$ and $\boldsymbol{q}'$ of n integers $q_i \in \{1,2,3,4\}$ discussed in Sec. 5.4.2. Each of these terms has a form similar to the one of Eq. (5.30) for the free fermion,

$$\mathrm{Tr}\left[\prod_{k=1}^n \rho_{q_k}\right] = \int \prod_{k=1}^n D\chi_k^* D\chi_k\, \rho_{q_1}(-\chi_1,\chi_2) \prod_{k=2}^n \rho_{q_k}(\chi_{k-1},\chi_k), \quad (5.63a)$$

$$\mathrm{Tr}\left[\prod_{k=1}^n \tilde\rho_{\tilde q_k}\right] = \int \prod_{k=1}^n D\chi_k^* D\chi_k\, \tilde\rho_{\tilde q_1}(-\chi_1,\chi_2) \prod_{k=2}^n \tilde\rho_{\tilde q_k}(\chi_{k-1},\chi_k), \quad (5.63b)$$

and can therefore be computed from the partition function of the model on $\mathcal{R}_n$ or $\widetilde{\mathcal{R}}_n$ respectively, with the correct boundary conditions along the a and b cycles, and it can be again expressed in terms of Riemann theta functions.

Moments of the reduced density matrix

Let us first focus on $\mathrm{Tr}\,\rho_A^n$. In this case we know that any term (5.63a) can be computed from the partition function on $\mathcal{R}_n$ (left panel of Fig. 5.1). For the modular invariant Dirac fermion we find

$$\mathrm{Tr}\left[\prod_{k=1}^{n}\rho_{q_k}\right]=\frac{c_n^2}{[\ell_1\ell_2(1-x)]^{2\Delta_n}}\left|\frac{\Theta[\boldsymbol{e}](\tau(x))}{\Theta(\tau(x))}\right|^2,\qquad \boldsymbol{e}=\begin{pmatrix}\boldsymbol{\varepsilon}\\ \boldsymbol{\delta}\end{pmatrix},\tag{5.64}$$

where we recall that $c=1$ in Δ_n, and with the expression (5.34) for c_n. Similarly, for Ising we have

$$\mathrm{Tr}\left[\prod_{k=1}^{n}\rho_{q_k}\right]=\frac{(c_n^{\mathrm{Ising}})^2}{[\ell_1\ell_2(1-x)]^{2\Delta_n}}\left|\frac{\Theta[\boldsymbol{e}](\tau(x))}{\Theta(\tau(x))}\right|,\qquad \boldsymbol{e}=\begin{pmatrix}\boldsymbol{\varepsilon}\\ \boldsymbol{\delta}\end{pmatrix},\tag{5.65}$$

where $c=1/2$ in Δ_n and the expression for c_n^{Is} is the one found in [329], i.e.

$$c_n^{\mathrm{Ising}}=2^{-\frac{1}{12}\left(n-\frac{1}{n}\right)}\sqrt{c_n},\tag{5.66}$$

being c_n given by (5.34).

We now need to discuss the relation between the string $\boldsymbol{q}$ and the fermionic boundary conditions described by the characteristic $\boldsymbol{e}$. As for the sum (5.57), two terms characterised by $\boldsymbol{q}$ and $\boldsymbol{q}'$ are equal if they are related by the exchange $1\leftrightarrow 2$ and $3\leftrightarrow 4$. Due to the relative minus sign in front of ρ_3 and ρ_4, terms with an odd total number of ρ_3's and ρ_4's cancel out in the sum for $\mathrm{Tr}\,\rho_A^n$, while terms with an even total number of ρ_3's and ρ_4's survive and are pairwise equal. The final sum has therefore the same structure of (5.57). This implies that in the $2^{(n-1)}$ surviving terms the operator $(-1)^F$ is placed along non trivial closed curves. These cycles may be either around A_2 (whenever ρ_2 or ρ_4 are present) or along B_1 on two different sheets (whenever a couple of ρ_3's or ρ_4's are present). It is easy to convince oneself that the $2^{(n-1)}$ terms correspond to all the inequivalent insertions on the different sheets of the operator $(-1)^F$ around the cut in A_2 or along B_1. Since the insertions of $(-1)^F$ dictate the fermionic boundary conditions along the basis cycles, there is a bijective relation between the $\boldsymbol{q}$'s and the set of all characteristics $\boldsymbol{e}$, which are indeed $2^{2(n-1)}$. The explicit expression of this relation depends on the basis cycles that are chosen on $\mathcal{R}_n$. For each term, the string $\boldsymbol{q}$ tells us where the operator $(-1)^F$ must be inserted on $\mathcal{R}_n$ and, once the homology basis is chosen, the characteristic $\boldsymbol{e}$ can be read off by counting how many times the basis cycles cross the curves where $(-1)^F$ is inserted. Notice that, unlike the case of the moments of the partial transpose of the free Dirac fermion, since here the operator $(-1)^F$ can be placed also along B_1, the boundary conditions along the a cycles may be changed too, from antiperiodic to periodic. Explicitly, $\varepsilon_k=0$ (which means antiperiodic b.c.) if a_k crosses B_1 an even number of times in the presence of $(-1)^F$, and $\varepsilon_k=1/2$ (periodic b.c.) otherwise. Analogously, $\delta_k=0$ (antiperiodic b.c.) if b_k crosses an even number of times any edge of A_2 in the presence of $(-1)^F$, and $\delta_k=1/2$ (periodic b.c.) otherwise.

This bijection between $\boldsymbol{q}$ and $\boldsymbol{e}$ shows how each term (5.64) or (5.65) is the scaling limit of the term relative to the same $\boldsymbol{q}$ in the sum (5.57) for $\mathrm{Tr}\,\rho_A^n$ in the lattice. Recalling that

any Riemann theta function with odd characteristic vanishes identically, an important by-product of this analysis is that the scaling limit of the terms in (5.57) associated to odd characteristics according to the correspondence (5.64), (5.65), is zero identically. These terms turn out to be the ones with an odd number of ρ_4's, and hence the ones which appear in (5.57) with a global minus sign. We stress that this fact is independent of the choice of the homology cycles on $\mathcal{R}_n$. Indeed, any two basis are related by a modular transformation which leaves invariant the parity of the characteristics.

Moments of the partial transpose

The analysis for $\mathrm{Tr}\left(\rho_A^{T_2}\right)^n$ is very similar ot the one of $\mathrm{Tr}\,\rho_A^n$, but we have to remember that in this case the main ingredient is $\tilde{\rho}_1(\zeta,\eta) \equiv \tilde{\rho}_A^{\mathbf{1}}(\zeta,\eta)$, thus we have to deal with the surface $\widetilde{\mathcal{R}}_n$ (right panel of Fig. 5.1) with period matrix $\tilde{\tau}(x)$. For the modular invariant Dirac fermion we find

$$\mathrm{Tr}\left[\prod_{k=1}^{n}\tilde{\rho}_{\tilde{q}_k}\right] = c_n^2\left(\frac{1-x}{\ell_1\ell_2}\right)^{2\Delta_n}\left|\frac{\Theta[\boldsymbol{e}](\tilde{\tau}(x))}{\Theta(\tilde{\tau}(x))}\right|^2, \qquad \boldsymbol{e}=\begin{pmatrix}\boldsymbol{\varepsilon}\\ \boldsymbol{\delta}\end{pmatrix}, \tag{5.67}$$

where we recall that $c=1$ in Δ_n, and with the expression (5.34) for c_n. Similarly, for Ising we have

$$\mathrm{Tr}\left[\prod_{k=1}^{n}\tilde{\rho}_{\tilde{q}_k}\right] = (c_n^{\mathrm{Is}})^2\left(\frac{1-x}{\ell_1\ell_2}\right)^{2\Delta_n}\left|\frac{\Theta[\boldsymbol{e}](\tilde{\tau}(x))}{\Theta(\tilde{\tau}(x))}\right|, \qquad \boldsymbol{e}=\begin{pmatrix}\boldsymbol{\varepsilon}\\ \boldsymbol{\delta}\end{pmatrix}, \tag{5.68}$$

where $c=1/2$ in Δ_n and the expression for c_n^{Is} is the one of Eq. (5.66).

As for $\mathrm{Tr}\,\rho_A^n$, there is a bijective relation between $\tilde{\boldsymbol{q}}$ and $\boldsymbol{e}$, which translates in a bijective relation among the terms in the sum (5.59) and the set of all characteristics. The situation is the same as before: for each term, the string $\tilde{\boldsymbol{q}}$ contains the information on where the operator $(-1)^F$ must be inserted on $\widetilde{\mathcal{R}}_n$, and the characteristic $\boldsymbol{e}$ is read off by counting how many times the basis cycles cross it. An important difference with the case of $\mathrm{Tr}\,\rho_A^n$ is that now the cycle $\tilde{b}_r$ crosses B_1 (see Fig. 1.3), and therefore the boundary conditions along the b cycles, which are given by $\boldsymbol{\delta}$, are modified by the presence of $(-1)^F$ along B_1, and not only around the cut in A_2. Since we are dealing with two different Riemann surfaces with two different homology basis, the relation between $\boldsymbol{e}$ and the two strings $\boldsymbol{q}$ and $\tilde{\boldsymbol{q}}$ are in principle different. Also in the case of $\mathrm{Tr}\left(\rho_A^{T_2}\right)^n$ it turns out that the terms which appear in the sum (5.59) with a global minus sign correspond through (5.67) or (5.68) to terms with odd characteristic, and therefore they vanish in the scaling limit. Notice that the presence of the minus sign depends now on both how many ρ_3's and how many ρ_4's are present, due to the imaginary unit in (5.58).

Dihedral symmetry

At the end of Sec. 5.3.1 we argued that the dihedral symmetry $\mathbb{Z}_n\times\mathbb{Z}_2$ of $\widetilde{\mathcal{R}}_n$ provides some degeneracies among the terms in the sums for the moment of the partial transpose for the free fermion. The symmetry $\mathbb{Z}_n$ comes from the invariance under cyclic permutation of the n sheets and the symmetry $\mathbb{Z}_2$ corresponds to taking the sheets in reverse order and reflecting all of them with respect to the real axis. The same applies here for the modular invariant Dirac fermion and the Ising model. Beside the vanishing terms with odd characteristics in the sums (5.52), further degeneracies can be found among the non vanishing ones by exploiting the dihedral symmetry $\mathbb{Z}_n \times \mathbb{Z}_2$ on $\mathcal{R}_n$. Analogously, in

the sums (5.53) many degeneracies are found exploiting the dihedral symmetry on $\widetilde{\mathcal{R}}_n$. We recall that this symmetry has been investigated in App. 2.C.3 of Chap. 2 in terms of modular transformations acting on $\mathcal{R}_n$, and the extension to $\widetilde{\mathcal{R}}_n$ can be found in App. 5.B.3.

As for the expression (5.57) on the lattice, the $\mathbb{Z}_n$ symmetry is the cyclic permutation of the n factors within each trace The $\mathbb{Z}_2$ symmetry instead comes from the reality of each trace and the fact that every factor ρ_{q_k} within the trace is hermitian. Indeed, these observations imply that each term is equal to the one where all factors are taken in the reverse order. The dihedral symmetry has also a counterpart on the lattice terms of (5.59). Again $\mathbb{Z}_n$ comes from the cyclic permutation of the factors within each trace, while the $\mathbb{Z}_2$ symmetry is related to the reality of each term, but with some extra care. As already pointed out for the free Dirac fermion in Sec. 5.3.1, the four terms in (5.58) are not separately hermitian. The hermitian conjugation exchanges $\tilde{\rho}_1 \leftrightarrow \tilde{\rho}_2$ and $\tilde{\rho}_3 \leftrightarrow \tilde{\rho}_4$, so that $\rho_A^{T_2}$ is hermitian. However, as already noticed above Eq. (5.59), such exchange leaves any term of the sum unchanged.

In App. 5.E some details are given about the numerical analysis for the XX model and the Ising model. Some plots are shown for the various terms occurring in $\operatorname{Tr}\rho_A^n$ and $\operatorname{Tr}\left(\rho_A^{T_2}\right)^n$ for $n = 2$ (Figs. 5.5 for the modular invariant Dirac theory, and 5.7 for Ising) and $n = 3$ (Figs. 5.6 for the modular invariant Dirac theory, and 5.8 for Ising). The lattice data are computed for the XX and the Ising chains (5.54), with the same techniques used in Chap. 4 and in Sec. 5.3.3 for the free fermion. After taking into account the finite size corrections, the extrapolations of the lattice data match very nicely with the corresponding CFT predictions.

As a further check, in App. 5.D we recover the expressions of $\operatorname{Tr}\rho_A^n$ and $\operatorname{Tr}(\rho_A^{T_2})^n$ for the free fermion from the corresponding ones for the modular invariant Dirac fermion, in a fashion which resembles what was done in Sec. 5.3.3 to recover the lattice expressions (5.47) for the tight-binding model from the formulas found in Sec. 4.4 for the XX and Ising spin chains.

5.5 Conclusions

In this chapter we studied the moments of the partial transpose of the reduced density matrix $\operatorname{Tr}(\rho_A^{T_2})^n$ for two disjoint intervals in the conformal field theory of the massless Dirac fermion. Our main result is a closed analytic form for these moments of arbitrary order, i.e. Eq. (5.37). The analytic computation of the logarithmic negativity $\mathcal{E}$ through the replica limit of (5.37) for even $n_e \to 1$ is beyond our knowledge.

It turned out that these moments are identical, for arbitrary order, to those of the compactified boson at the self-dual point. This equality comes from the explicit computation and we miss a proper understanding of this fact. It was already noticed that for the moments of the reduced density matrix of two disjoint intervals $\operatorname{Tr}\rho_A^n$, the result for the free fermion [46, 333] and the one for the compactified boson at the self-dual radius [226] are equal and very easy (they are both given by (1.56) with $\mathcal{F}_n(x) = 1$). This is not the case for three or more disjoint intervals, as noticed in [228] and observed also in Chap. 2. This unexpected equivalence has been investigated in [228], where also other results have been found, based on the fact that $\tau(x)$ is purely imaginary when $x \in (0, 1)$. For the partial transpose, the period matrix $\tilde{\tau}(x)$ of $\widetilde{\mathcal{R}}_n$ in (5.31) has a non vanishing real part.

Nevertheless, here we have shown that $\mathrm{Tr}\left(\rho_A^{T_2}\right)^n$ for the free fermion is equal to the one for the self-dual boson, a property that does not follow from the analysis of [228]. The equality of all the moments obviously implies also the equality of the negativities. Since the negativity is directly measurable by means of tensor network algorithms (as e.g. done in [125, 136] for the Ising model), it would be very interesting to check numerically the identity between the negativity of the tight-binding model and the isotropic Heisenberg antiferromagnet (whose continuum limit is the self-dual boson). This is a highly non trivial prediction.

We point out that an interesting technical byproduct of this paper is a one-to-one correspondence between each of the 2^{n-1} terms appearing in the lattice formulation of the moments $\mathrm{Tr}(\rho_A^{T_2})^n$ and the partition function of the free fermion on $\widetilde{\mathcal{R}}_n$ with a particular assignment of fermionic boundary conditions. This correspondence has been explicitly checked against lattice numerical computations, as well as the overall sum. The consequence of this correspondence for the moments of both the reduce density matrix and its partial transpose in spin models with a free fermionic representation has been explored in Sec. 5.4, and the numerical analysis is reported in App.5.E.

Appendices

5.A A check for $n = 2$

In this appendix, by employing the formalism described in Sec. 5.2.2 and Sec. 5.2.3, we check the standard relation between the reduced density matrix of two disjoint intervals and its partial transpose

$$\mathrm{Tr}\left(\rho_A^{T_2}\right)^2 = \mathrm{Tr}\left(\rho_A^2\right). \tag{5.69}$$

From (5.9), it is immediate to observe that $\mathrm{Tr}\left(\rho_A^{T_2}\right)^2 = \mathrm{Tr}\left(\tilde{\rho}_A P_{A_2} \tilde{\rho}_A P_{A_2}\right)$. Then, by using (5.15), we can write

$$\begin{aligned}
&\mathrm{Tr}\left(\tilde{\rho}_A P_{A_2} \tilde{\rho}_A P_{A_2}\right) = \\
&= \int D\zeta^* D\zeta \, D\eta^* D\eta \, e^{-\zeta^*\zeta} e^{-\eta^*\eta} \, \langle -\zeta_1, -\zeta_2 | \tilde{\rho}_A | \eta_1, \eta_2 \rangle \, \langle \eta_1, \eta_2 | P_{A_2} \tilde{\rho}_A P_{A_2} | \zeta_1, \zeta_2 \rangle \\
&= \int D\zeta^* D\zeta \, D\eta^* D\eta \, e^{-\zeta^*\zeta} e^{-\eta^*\eta} \, \langle -\zeta_1, -\zeta_2 | \tilde{\rho}_A | \eta_1, \eta_2 \rangle \, \langle \eta_1, -\eta_2 | \tilde{\rho}_A | \zeta_1, -\zeta_2 \rangle \\
&= \int D\zeta^* D\zeta \, D\eta^* D\eta \, e^{-\zeta^*\zeta} e^{-\eta^*\eta} \, \langle -\zeta_1, \eta_2^* | \rho_A | \eta_1, \zeta_2^* \rangle \, \langle \eta_1, -\zeta_2^* | \rho_A | \zeta_1, \eta_2^* \rangle \\
&= \int D\zeta^* D\zeta \, D\eta^* D\eta \, e^{-\zeta_1^*\zeta_1 + \zeta_2^*\zeta_2} e^{-\eta_1^*\eta_1 + \eta_2^*\eta_2} \, \langle -\zeta_1, \eta_2 | \rho_A | \eta_1, \zeta_2 \rangle \, \langle \eta_1, -\zeta_2 | \rho_A | \zeta_1, \eta_2 \rangle \,,
\end{aligned} \tag{5.70}$$

where in the last step the change of variables $\zeta_2 \to \zeta_2^*$, $\eta_2 \to \eta_2^*$ has been employed. Then, by noticing that the relations in (5.15) can be slightly modified as follows

$$-\mathbb{I} = \int \mathrm{d}\zeta^* \mathrm{d}\zeta \, e^{\zeta^*\zeta} \, |\zeta\rangle \, \langle -\zeta| \,, \qquad -\mathrm{Tr}\, \hat{O} = \int \mathrm{d}\zeta^* \mathrm{d}\zeta \, e^{\zeta^*\zeta} \, \langle \zeta | \, \hat{O} \, | \zeta \rangle \,, \tag{5.71}$$

we can conclude that (5.70) is exactly $\mathrm{Tr}\left(\rho_A^2\right)$.

5.B On the Riemann surface $\widetilde{\mathcal{R}}_n$

In this appendix we derive with all the details some further results about the Riemann surface $\widetilde{\mathcal{R}}_n$ and its period matrix $\tilde{\tau}(x)$ in 5.31, that have already been introduced and discussed in Sec. 1.4.3.

While the period matrix $\tau(x)$ of $\mathcal{R}_n$ is purely imaginary (see (1.58)), the period matrix $\tilde{\tau}(x)$ for $\widetilde{\mathcal{R}}_n$ has a non vanishing real part. In Sec. 5.B.1 we show that $\mathrm{Re}[\tilde{\tau}(x)]$ has a very simple form. In Sec. 5.B.2 we consider the moments $\mathrm{Tr}\left(\rho_A^{T_2}\right)^n$ in the regime of small intervals $x \to 0$ and in Sec. 5.B.3 we provide a detailed discussion of the $\mathbb{Z}_2$ part of the dihedral symmetry for $\widetilde{\mathcal{R}}_n$.

5.B.1 The real and imaginary part of the period matrix $\tilde{\tau}(x)$

In this subsection we want to write explicitly the real and the imaginary part of the period matrix $\tilde{\tau}(x)$ given by (5.31). The real part $\mathrm{Re}[\tilde{\tau}(x)]$ turns out to be a simple tridiagonal matrix with half-integer entries.

Let us introduce the following ratios of hypergeometric functions, which enter in the expressions for the period matrices $\tau(x)$ and $\tilde{\tau}(x)$ (see (1.58) and (5.31))

$$\tau_r(x) \equiv \mathrm{i}\, \frac{{}_2F_1(r, 1-r; 1; 1-x)}{{}_2F_1(r, 1-r; 1; x)}, \qquad \tilde{\tau}_r(x) \equiv \tau_r\Big(\frac{x}{x-1}\Big) \equiv \tilde{\alpha}_r(x) + \mathrm{i}\tilde{\beta}_r(x), \tag{5.72}$$

where $0 < r < 1$ and $x \in (0,1)$. Moreover, we also define

$$\mathcal{A}_r(x) \equiv \frac{\Gamma(1-2r)}{\Gamma(1-r)^2}\,\frac{{}_2F_1(r,r;2r;1-x)}{{}_2F_1(r,r;1;x)}, \tag{5.73a}$$

$$\mathcal{B}_r(x) \equiv \frac{\Gamma(2r-1)}{\Gamma(r)^2}\,(1-x)^{1-2r}\,\frac{{}_2F_1(1-r,1-r;2(1-r);1-x)}{{}_2F_1(r,r;1;x)}. \tag{5.73b}$$

By employing the expressions given in (87) of [135], one finds that

$$\tilde{\alpha}_r(x) \,=\, \sin(\pi r)\big[\mathcal{A}_r(x)+\mathcal{B}_r(x)\big], \qquad \tilde{\beta}_r(x) \,=\, \cos(\pi r)\big[\mathcal{A}_r(x)-\mathcal{B}_r(x)\big]. \tag{5.74}$$

At this point we need the following identity (see e.g. Eq. (1) at pag. 108 of Ref. [338])

$$\begin{aligned} {}_2F_1(a,b;c;z) = {}& \frac{\Gamma(c)\,\Gamma(c-a-b)}{\Gamma(c-a)\,\Gamma(c-b)}\,{}_2F_1(a,b;a+b-c+1;1-z) \\ & + \frac{\Gamma(c)\,\Gamma(a+b-c)}{\Gamma(a)\,\Gamma(b)}\,(1-z)^{c-a-b}\,{}_2F_1(c-a,c-b;c-a-b+1;1-z), \end{aligned} \tag{5.75}$$

which holds for $|\arg(1-z)| < \pi$. By specialising (5.75) to the case of $(a,b,c) = (r,r,1)$ and $z = x \in (0,1)$, from (5.73) one finds that

$$\mathcal{A}_r(x) + \mathcal{B}_r(x) = 1. \tag{5.76}$$

From this expression it is clear that the x dependence disappears from the real part of $\tilde{\tau}_r(x)$ and hence from the period matrix. Indeed, using (5.74) and (5.76) in (1.58) one gets (see also 5.31)

$$\tilde{\tau}(x)_{i,j} \,=\, \frac{2}{n}\sum_{k=1}^{n-1}\sin(\pi k/n)\,\tilde{\tau}_{k/n}(x)\,\cos[2\pi(k/n)(i-j)] \,=\, \frac{1}{2}\,\big[\mathcal{Q}\big]_{i,j} + \mathrm{i}\,\big[\mathcal{I}(x)\big]_{i,j}, \tag{5.77}$$

where the sum giving the real part can be explicitly performed, finding that the matrix $\mathcal{Q}$ has integer elements which read

$$[\mathcal{Q}]_{i,j} \equiv 2\delta_{i,j} - \delta_{|i-j|,1}, \tag{5.78}$$

namely $\mathcal{Q}$ is a symmetric tridiagonal matrix, with 2 on the main diagonal and -1 on the first diagonals. On the other hand, the imaginary part can be written as follows,

$$\big[\mathcal{I}(x)\big]_{i,j} \,=\, \frac{2}{n}\sum_{k=1}^{n-1}\sin(\pi k/n)\,\tilde{\beta}_{k/n}(x)\cos[2\pi(k/n)(i-j)], \tag{5.79}$$

with

$$\tilde{\beta}_r(x) \equiv \frac{\tilde{f}_r(1-x)-\tilde{f}_{1-r}(1-x)}{(1-x)^r\,{}_2F_1(r,r;1;x)}\,\cos(\pi r), \quad \tilde{f}_r(x) \equiv \frac{\Gamma(1-2r)}{\Gamma(1-r)^2}\,x^r\,{}_2F_1(r,r;2r;x). \tag{5.80}$$

This expression for $\mathcal{I}(x)$ can be further simplified. Plugging (5.76) into the second expression of (5.74), we have

$$\tilde{\beta}_r(x) = \cos(\pi r)\big[2\mathcal{A}_r(x)-1\big]. \tag{5.81}$$

For $0 < x < 1$ we can rewrite $\mathcal{A}_r(x)$ as follows [338]

$$\mathcal{A}_r(x) = \frac{1}{2\cos(\pi r)} \left[e^{-\mathrm{i}\pi r} + e^{\mathrm{i}\pi r}\, x^{-r}\, \frac{{}_2F_1(r,r;1;1/x)}{{}_2F_1(r,r;1;x)} \right]. \tag{5.82}$$

Since $\mathcal{A}_r(x)$ is real for $0 < x < 1$, the vanishing of its imaginary part gives

$$\frac{1}{x^r} \left[\tan(\pi r)\, \mathrm{Re}\left(\frac{{}_2F_1(r,r;1;1/x)}{{}_2F_1(r,r;1;x)} \right) + \mathrm{Im}\left(\frac{{}_2F_1(r,r;1;1/x)}{{}_2F_1(r,r;1;x)} \right) \right] = \tan(\pi r). \tag{5.83}$$

On the other hand, by writing $\mathcal{A}_r(x)$ as its real part and plugging the resulting expression in (5.81), one finds

$$\tilde{\beta}_r(x) = \frac{1}{x^r} \left[\cos(\pi r)\, \mathrm{Re}\left(\frac{{}_2F_1(r,r;1;1/x)}{{}_2F_1(r,r;1;x)} \right) - \sin(\pi r)\, \mathrm{Im}\left(\frac{{}_2F_1(r,r;1;1/x)}{{}_2F_1(r,r;1;x)} \right) \right]. \tag{5.84}$$

Finally, using (5.83) we can write

$$\tilde{\beta}_r(x) = \cos(\pi r) - \frac{x^{-r}}{\sin(\pi r)}\, \mathrm{Im}\left(\frac{{}_2F_1(r,r;1;1/x)}{{}_2F_1(r,r;1;x)} \right). \tag{5.85}$$

The matrix $\mathcal{I}(x)$ can be easily written by plugging (5.85) into (5.79) and noticing that the sum over the cosine vanishes. The result reads

$$\big[\mathcal{I}(x)\big]_{i,j} = -\frac{2}{n} \sum_{k=1}^{n-1} x^{-k/n}\, \mathrm{Im}\left(\frac{{}_2F_1(k/n,k/n;1;1/x)}{{}_2F_1(k/n,k/n;1;x)} \right) \cos[2\pi(k/n)(i-j)]. \tag{5.86}$$

The result (5.78) is employed in Sec. 5.3.2 and in App. 5.B.3.

5.B.2 Short intervals regime

In this appendix we study the $\mathrm{Tr}\left(\rho_A^{T_2}\right)^n$ for the free fermion (5.37) in the limit of short intervals, i.e. when $x \to 0$.

In the expression (5.37), only Riemann theta functions with $\boldsymbol{\varepsilon} = \mathbf{0}$ occur, which are given by

$$\Theta\begin{bmatrix} \mathbf{0} \\ \boldsymbol{\delta} \end{bmatrix}\big(\tilde{\tau}(x)\big) = 1 + \sum_{\boldsymbol{m} \neq \mathbf{0}} e^{\mathrm{i}\pi(\boldsymbol{m}\cdot\mathcal{Q}\cdot\boldsymbol{m} + 2\boldsymbol{\delta}\cdot\boldsymbol{m})}\, e^{-\pi\, \boldsymbol{m}\cdot\mathcal{I}\cdot\boldsymbol{m}}, \tag{5.87}$$

where $\mathcal{Q}$ is independent of x. Expanding $\tilde{\beta}_{k/n}(x)$ in (5.80) for $x \to 0$, one finds

$$\tilde{\beta}_q(x) = -\frac{\sin(\pi q)}{\pi} \big[\log(x) + 2\gamma_E + \psi(q) + \psi(1-q) \big] + O(x). \tag{5.88}$$

Plugging this expansion into (5.79) and (5.87), one gets that the leading term is $x^{\boldsymbol{m}\cdot\mathcal{Q}\cdot\boldsymbol{m}}$. The exponent $\boldsymbol{m}\cdot\mathcal{Q}\cdot\boldsymbol{m}$ for $\boldsymbol{m} \in \mathbb{Z}^{n-1}$ has been already analyzed in [196], finding that its minimum is 1, which is obtained for the following vectors

$$\boldsymbol{m}_\pm \equiv \big(\underbrace{0, \dots, 0}_{j_1}, \overbrace{\pm 1, \dots, \pm 1}^{j_2}, 0, \dots, 0 \big), \qquad \boldsymbol{m}_\pm \neq \mathbf{0}, \qquad 0 \leqslant j_1 < j_2 \leqslant n-1, \tag{5.89}$$

namely $\boldsymbol{m}_\pm \cdot \mathcal{Q} \cdot \boldsymbol{m}_\pm = 1$. Then, by applying again the results of [196] (notice that the vectors $\boldsymbol{m}_+$ and $\boldsymbol{m}_-$ give the same contribution) to (5.87), we find

$$\Theta\begin{bmatrix}\mathbf{0}\\ \boldsymbol{\delta}\end{bmatrix}\big(\tilde{\tau}(x)\big) \;=\; 1 - \frac{x}{2n^2}\sum_{\boldsymbol{m}_+}\frac{(-1)^{2\boldsymbol{\delta}\cdot\boldsymbol{m}_+}}{\sin^2(\pi(j_2-j_1)/n)} + \ldots, \tag{5.90}$$

where the dots denote $o(x)$ terms. Thus, for the generic term occurring in the sum (5.37) we have

$$\widetilde{\Omega}_n[\boldsymbol{e}] \;=\; 1 - \frac{x}{2n^2}\sum_{\boldsymbol{m}_+}\frac{1+(-1)^{2\boldsymbol{\delta}\cdot\boldsymbol{m}_+}}{\sin^2(\pi(j_2-j_1)/n)} + \ldots, \qquad \boldsymbol{e} = \begin{pmatrix}\mathbf{0}\\ \boldsymbol{\delta}\end{pmatrix}. \tag{5.91}$$

Plugging this result into (5.37), we get the first term of the $x \to 0$ expansion of $\mathrm{Tr}\left(\rho_A^{T_2}\right)^n$, which is

$$\mathrm{Tr}\left(\rho_A^{T_2}\right)^n \;=\; \tilde{J}_n\Big[1 - \frac{x}{2^{n-1}\,n^2}\sum_{\boldsymbol{\delta}} r_n(\boldsymbol{\delta})\sum_{\boldsymbol{m}_+}\frac{1+(-1)^{2\boldsymbol{\delta}\cdot\boldsymbol{m}_+}}{\sin^2(\pi(j_2-j_1)/n)} + \ldots\Big]. \tag{5.92}$$

5.B.3 The $\mathbb{Z}_2$ part of the dihedral symmetry of $\widetilde{\mathcal{R}}_n$

In this subsection we briefly discuss the most peculiar aspect of the dihedral symmetry for the Riemann surface $\widetilde{\mathcal{R}}_n$ occurring in the computation of $\mathrm{Tr}\left(\rho_A^{T_2}\right)^n$ (see Secs. 5.3.1 and 5.3.1).

The Riemann surface $\mathcal{R}_n$ has a dihedral symmetry $\mathbb{Z}_n \times \mathbb{Z}_2$ due to the invariance under cyclic permutation of the sheets ($\mathbb{Z}_n$) and the complex conjugation ($\mathbb{Z}_2$). For a genus g Riemann surface, the modular transformations are given by the symplectic matrices $Sp(2g,\mathbb{Z})$ [207–210, 212–214]. The dihedral symmetry can be identified with a subgroup of the modular transformations acting on $\mathcal{R}_n$ which has been discussed in [228] and in Chap. 2. In particular, these peculiar modular transformations map the a cycles among themselves and the b cycles among themselves, leaving the period matrix $\tau(x)$ unchanged.

Also the surface $\widetilde{\mathcal{R}}_n$ has a dihedral symmetry $\mathbb{Z}_n \times \mathbb{Z}_2$ but, while the cyclic permutation ($\mathbb{Z}_n$) is exactly the same one discussed above for $\mathcal{R}_n$, the complex conjugation is slightly different because it mixes a and b cycles. Let us remind that the complex conjugation corresponds to reverse the order of the sheets and to reflect all of them with respect to the real axis. Considering the canonical homology basis $\{\tilde{a}_r, \tilde{b}_r; 1 \leqslant r \leqslant n-1\}$ introduced in Sec. 1.4.3 (see the right panel of Fig. 1.3) and used in Sec. 5.3.1, this transformation acts as follows

$$\begin{pmatrix}\tilde{\boldsymbol{a}}'\\ \tilde{\boldsymbol{b}}'\end{pmatrix} = M_{\mathrm{inv}} \cdot \begin{pmatrix}\tilde{\boldsymbol{a}}\\ \tilde{\boldsymbol{b}}\end{pmatrix}, \qquad M_{\mathrm{inv}} = \begin{pmatrix}\overleftrightarrow{\mathbb{I}}_{n-1} & 0\\ -\overleftrightarrow{\mathcal{Q}} & \overleftrightarrow{\mathbb{I}}_{n-1}\end{pmatrix} \in Sp\big(2(n-1),\mathbb{Z}\big), \tag{5.93}$$

where we introduced the notation of the double-headed arrow above a matrix to indicate that the columns have to be taken in the reversed order ($\mathbb{I}_k$ is the $k \times k$ identity matrix and $\mathcal{Q}$ is given by (5.78)). Under the symplectic transformation defined in (5.93), the period matrix $\tilde{\tau}$ (1.58) changes as follows

$$\tilde{\tau}' = \overleftrightarrow{\mathbb{I}} \cdot \tilde{\tau} \cdot \overleftrightarrow{\mathbb{I}} - \overleftrightarrow{\mathcal{Q}} \cdot \overleftrightarrow{\mathbb{I}} = \tilde{\tau} - \mathcal{Q} = -\mathcal{R} + \mathrm{i}\mathcal{I} = -\,\tilde{\tau}^*, \tag{5.94}$$

while for the characteristics of the Riemann theta functions we have

$$\begin{pmatrix}\boldsymbol{\varepsilon}'\\ \boldsymbol{\delta}'\end{pmatrix} = \begin{pmatrix}\overleftrightarrow{\mathbb{I}} & 0\\ \overleftrightarrow{\mathcal{Q}} & \overleftrightarrow{\mathbb{I}}\end{pmatrix} \cdot \begin{pmatrix}\boldsymbol{\varepsilon}\\ \boldsymbol{\delta}\end{pmatrix}. \tag{5.95}$$

Notice that the powers of $M_{\rm inv}$ read

$$M_{\rm inv}^{2k-1} = \begin{pmatrix} \overleftrightarrow{\mathbb{I}} & 0 \\ -(2k-1)\overleftrightarrow{\mathcal{Q}} & \overleftrightarrow{\mathbb{I}} \end{pmatrix}, \qquad M_{\rm inv}^{2k} = \begin{pmatrix} \mathbb{I} & 0 \\ -2k\mathcal{Q} & \mathbb{I} \end{pmatrix}, \tag{5.96}$$

(in particular, notice that $M_{\rm inv}^2 \neq \mathbb{I}$) so that, by applying (5.94) k times one finds

$$\tilde{\tau}^{(k)} = \tilde{\tau} - k\,\mathcal{Q}. \tag{5.97}$$

As for the change of the Riemann theta function under the modular transformation in (5.93), because of the particular form of $\mathcal{Q}$, it is easy to show that for k even it is left invariant (a part for an overall sign), while for k odd it becomes its complex conjugate, up to an overall sign. Since in our formulas the modulus of the Riemann theta function always occurs, the terms occurring in our sums over the characteristics are invariant under this transformation. Thus, $M_{\rm inv}$ can be the modular transformation representing the $\mathbb{Z}_2$ of the dihedral symmetry, even if $M_{\rm inv}^2 \neq \mathbb{I}$.

5.C Details on the computation for the self-dual boson

In this appendix we show the equality $m_n(\boldsymbol{\delta}) = r_n(\boldsymbol{\delta})$ between the coefficient $m_n(\boldsymbol{\delta})$ in (5.42), coming from the self-dual boson approach, and the coefficient $r_n(\boldsymbol{\delta})$ in (5.38) occurring in the expression obtained through the free fermion analysis.

Considering $m_n(\boldsymbol{\delta})$ in (5.42), the expression in the exponent can be written as follows

$$\boldsymbol{\varepsilon} \cdot \frac{\mathcal{Q}}{2} \cdot \boldsymbol{\varepsilon} + \boldsymbol{\varepsilon} \cdot \boldsymbol{\delta} = -\sum_{i=1}^{n-2} \varepsilon_i\, \varepsilon_{i+1} + \sum_{i=1}^{n-1} \varepsilon_i^2 + \sum_{i=1}^{n-1} \varepsilon_i \delta_i. \tag{5.98}$$

Then, defining the spin variables $\sigma_i = 4\varepsilon_i - 1 = \pm 1$ and the local magnetic fields $h_i = 4\delta_i$, we find that $m_n(\boldsymbol{\delta})$ is equal to the partition function Z_n of $n-1$ Ising spins in a binary magnetic field $h_i = 0, 2$ (a part for the first and last site), which reads

$$Z_n = e^{\frac{\mathrm{i}\pi}{4}\left(\sum_i h_i + n\right)} \sum_{\boldsymbol{\sigma}} \exp\left[\mathrm{i}\,\frac{\pi}{4}\Big(-\sum_{i=1}^{n-2} \sigma_i \sigma_{i+1} + \sum_{i=1}^{n-1} \sigma_i h_i + \sigma_1 + \sigma_{n-1} \Big)\right]. \tag{5.99}$$

Given this Ising model representation, we can compute $m_n(\boldsymbol{\delta})$ through standard transfer matrix techniques. Following [339], let us introduce the conditioned partition function with the last spin set to μ, namely

$$\begin{aligned} Z_n(\mu) = {} & e^{\frac{\mathrm{i}\pi}{4}\left(\sum_i h_i + n\right)} \times \\ & \times \sum_{\boldsymbol{\sigma}} \exp\left[\frac{\mathrm{i}\pi}{4}\Big(-\sum_{i=1}^{n-3} \sigma_i\, \sigma_{i+1} - \mu\, \sigma_{n-2} + \sum_{i=1}^{n-2} \sigma_i h_i + \mu\, h_{n-1} + \sigma_1 + \mu \Big)\right]. \end{aligned} \tag{5.100}$$

Then, by adding one spin ϵ to the partition function, it becomes

$$\begin{aligned} Z_{n+1}(\epsilon) = e^{\frac{\mathrm{i}\pi}{4}\left(\sum_i h_i + n\right)} \sum_{\mu=\pm 1} \sum_{\boldsymbol{\sigma}} \exp\Bigg[\frac{\mathrm{i}\pi}{4}\Big(& -\sum_{i=1}^{n-3} \sigma_i \sigma_{i+1} - \mu\, \sigma_{n-2} - \mu\, \epsilon \\ & + \sum_{i=1}^{n-2} \sigma_i\, h_i + \mu\, h_{n-1} + \epsilon\, h_n + \sigma_1 + \epsilon \Big)\Bigg]. \end{aligned} \tag{5.101}$$

After some algebra, one realizes that

$$Z_{n+1}(+) = (-1)^{2\delta_n}\,[Z_n(+) - Z_n(-)]\,, \qquad Z_{n+1}(-) = Z_n(+) + Z_n(-). \tag{5.102}$$

and these relations give the transfer matrix

$$\widehat{T}(\delta) = \frac{1}{\sqrt{2}} \begin{pmatrix} (-1)^{2\delta} & -(-1)^{2\delta} \\ 1 & 1 \end{pmatrix}, \qquad \delta \in \{0, 1/2\}. \tag{5.103}$$

We also need the conditioned partition functions for a single spin, which read

$$Z_2(+) = -\,e^{\frac{\mathrm{i}\pi}{2}h_1}, \qquad Z_2(-) = 1. \tag{5.104}$$

Then, the partition function for $n-1$ spins in (5.99) is given by $Z_n = Z_n(+) + Z_n(-)$,

$$Z_n = 2^{\frac{n}{2}-1} \begin{pmatrix} 1 & 1 \end{pmatrix} \prod_{k=n-1}^{2} \widehat{T}(\delta_k) \begin{pmatrix} -(-1)^{2\delta_1} \\ 1 \end{pmatrix} = 2^{\frac{n-1}{2}} \begin{pmatrix} 1 & 1 \end{pmatrix} \prod_{k=n-1}^{1} \widehat{T}(\delta_k) \begin{pmatrix} 0 \\ 1 \end{pmatrix}. \tag{5.105}$$

In order to compute the matrix product in (5.105), it is convenient to perform a change of basis which diagonalises $\widehat{T}(0)$, namely

$$T(\delta) = U^\dagger\, \widehat{T}(\delta)\, U, \qquad U = \frac{1}{2} \begin{pmatrix} 1+\mathrm{i} & -(1+\mathrm{i}) \\ 1-\mathrm{i} & 1-\mathrm{i} \end{pmatrix}. \tag{5.106}$$

From (5.103) and (5.106) we can explicitly write the transfer matrix in the new basis

$$T(0) = \frac{1}{\sqrt{2}} \begin{pmatrix} 1+\mathrm{i} & 0 \\ 0 & 1-\mathrm{i} \end{pmatrix}, \qquad T(1/2) = \frac{1}{\sqrt{2}} \begin{pmatrix} 0 & 1-\mathrm{i} \\ 1+\mathrm{i} & 0 \end{pmatrix}, \tag{5.107}$$

and therefore the partition function (5.105) can be rewritten as follows

$$Z_n = 2^{\frac{n}{2}-1} \begin{pmatrix} 1 & 1 \end{pmatrix} T(0) \prod_{k=n-1}^{1} T(\delta_k) \begin{pmatrix} 1 \\ 1 \end{pmatrix}. \tag{5.108}$$

Now, it is convenient to move all $T(0)$'s in the product of (5.108) to the left of all the $T(1/2)$'s. To do this, one observes that $T(0)T(1/2) = T(1/2)T(0)^{-1}$ and $T(1/2)T(0) = T(0)^{-1}T(1/2)$. By employing the latter rule, one finds

$$Z_n = 2^{\frac{n}{2}-1} \begin{pmatrix} 1 & 1 \end{pmatrix} T(0)^{1+\sum_i (1-2\delta_i)(-1)^{\sum_{j=i}^{n-1} 2\delta_j}}\, T(1/2)^{\sum_i 2\delta_i} \begin{pmatrix} 1 \\ 1 \end{pmatrix}. \tag{5.109}$$

The factor $1-2\delta_i$ within the sum in the exponent of $T(0)$ selects only the sites where $\delta_i = 0$, while the other factor $(-1)^{\sum_{j=i}^{n-1} 2\delta_j}$ counts all the $T(1/2)$'s on the left of site i. The exponent of $T(0)$ can be rewritten as

$$s(\boldsymbol{\delta}) = 1 + \sum_{i=1}^{n-1} (1-2\delta_i)(-1)^{\sum_{j=i}^{n-1} 2\delta_j} = 1 + \frac{1-(-1)^{\sum_i 2\delta_i}}{2} + \sum_{i=1}^{n-1} (-1)^{\sum_{j=i}^{n-1} 2\delta_j}. \tag{5.110}$$

Since $T(0)$ is diagonal, its powers can be easily performed. Moreover, since $T(1/2)^2 = \mathbb{I}_2$, every integer power of $T(1/2)$ is simply $\mathbb{I}_2$ if the exponent is even, and $T(1/2)$ otherwise.

Thus, we have

$$T(0)^{s(\boldsymbol{\delta})} = \begin{pmatrix} e^{\frac{\mathrm{i}\pi}{4}s(\boldsymbol{\delta})} & 0 \\ 0 & e^{-\frac{\mathrm{i}\pi}{4}s(\boldsymbol{\delta})} \end{pmatrix}, \tag{5.111a}$$

$$T(1/2)^{2\sum_i \delta_i} = \begin{pmatrix} [1+(-1)^{\sum_i 2\delta_i}]/2 & e^{-\frac{i\pi}{4}}[1-(-1)^{\sum_i 2\delta_i}]/2 \\ e^{\frac{i\pi}{4}}[1-(-1)^{\sum_i 2\delta_i}]/2 & [1+(-1)^{\sum_i 2\delta_i}]/2 \end{pmatrix}. \tag{5.111b}$$

Finally, (5.109) tells us that we just need to multiply this two matrices and to sum the four elements of the resulting matrix. After some of algebra, we get

$$m_n(\boldsymbol{\delta}) = 2^{n/2}\left[\frac{1+(-1)^{\sum_i 2\delta_i}}{2}\cos\left(\frac{\pi}{4}s(\boldsymbol{\delta})\right) + \frac{1-(-1)^{\sum_i 2\delta_i}}{2}\cos\left(\frac{\pi}{4}\left(s(\boldsymbol{\delta})-1\right)\right)\right]. \tag{5.112}$$

By inspection of the two cases of $\sum_i 2\delta_i$ even or odd, it is clear that (5.112) equals (5.38).

5.D The free fermion from the modular invariant Dirac fermion

The main difference between the free spinless fermion on the lattice, Eq. (5.1), and the XX model, Eq. (5.54), is the occurrence of the string of Majorana operators P_{B_1} along the sites of B_1, which separates the two blocks A_1 and A_2. Thus, by eliminating this operator from the results of the XX model leads to the corresponding ones for the free fermion. This procedure has been described in Sec. 5.3.3. Something analogous can be done on the corresponding expressions for the free fermion and the modular invariant Dirac fermion in the continuum. In this appendix we briefly illustrate this procedure for $\operatorname{Tr}\rho_A^n$ and $\operatorname{Tr}(\rho_A^{T_2})^n$.

5.D.1 Rényi entropies

Let us consider the expression of $\mathcal{F}_n(x)$ given in (5.52b) for the modular invariant Dirac fermion [196], focusing our attention only on the sum over the characteristics. In the lattice expressions (5.57) some terms are negative and their continuum limit corresponds to terms in (5.64) with odd characteristics and therefore vanishing. Motivated by this lattice comparison, let us write the sum over characteristics as follows

$$\sum_{\boldsymbol{\varepsilon},\boldsymbol{\delta}} (-1)^{4\boldsymbol{\varepsilon}\cdot\boldsymbol{\delta}}\,\Theta\begin{bmatrix}\boldsymbol{\varepsilon}\\ \boldsymbol{\delta}\end{bmatrix}(\tau)^2 \tag{5.113}$$

Replacing the string P_{B_1} with the identity operator $\mathbf{1}$ in each term of the lattice expressions for the XX model (see Eqs. (5.57) and (5.56)) corresponds in the continuum to removing the operator $(-1)^{F_{B_1}}$ which changes the boundary conditions from antiperiodic to periodic along the cycles that intersects B_1. According to the discussion in Sec. 5.4, the vector $\boldsymbol{\varepsilon}$ is determined by the a cycles and the vector $\boldsymbol{\delta}$ by the b cycles. Since on $\mathcal{R}_n$ all the a cycles intersects B_1, removing all the operators $(-1)^{F_{B_1}}$ means that we are fixing the fermionic boundary conditions along all the a cycles to be antiperiodic. Instead, since the b cycles do not intersect B_1 (see left panel of Fig. 1.3), the boundary conditions along them are not modified. This means that removing $(-1)^{F_{B_1}}$ corresponds to setting $\boldsymbol{\varepsilon} = \mathbf{0}$ in each Riemann theta function occurring in (5.113), which becomes

$$\sum_{\boldsymbol{\varepsilon},\boldsymbol{\delta}} (-1)^{4\boldsymbol{\varepsilon}\cdot\boldsymbol{\delta}}\,\Theta\begin{bmatrix}\mathbf{0}\\ \boldsymbol{\delta}\end{bmatrix}(\tau)^2 = 2^{n-1}\sum_{\boldsymbol{\delta}} \delta_{\boldsymbol{\delta},\mathbf{0}}\,\Theta\begin{bmatrix}\mathbf{0}\\ \boldsymbol{\delta}\end{bmatrix}(\tau)^2 = 2^{n-1}\,\Theta\begin{bmatrix}\mathbf{0}\\ \mathbf{0}\end{bmatrix}(\tau)^2 \tag{5.114}$$

Plugging this result into (5.52), we recover for the free fermion the result $\mathcal{F}_n(x) = 1$ found in [46]. Let us stress a peculiar and important point of this procedure. After the operator $(-1)^{F_{B_1}}$ is removed and $\boldsymbol{\varepsilon}$ is set to $\mathbf{0}$, the terms in the sum (5.113) corresponding to odd characteristics turn out to have an even characteristic (and therefore they are non vanishing). For this reason, the choice of the minus sign in front of these terms is crucial in order to obtain the correct result.

5.D.2 Traces of the partial transpose

Similar considerations can be done for $\mathrm{Tr}\left(\rho_A^{T_2}\right)^n$. The sum over the characteristics occurring in the CFT formula for the modular invariant Dirac fermion (5.53b) reads

$$\sum_{\boldsymbol{\varepsilon},\boldsymbol{\delta}} (-1)^{4\boldsymbol{\varepsilon}\cdot\boldsymbol{\delta}}\, \Theta\begin{bmatrix} \boldsymbol{\varepsilon} \\ \boldsymbol{\delta} \end{bmatrix}(\tilde{\tau})^2 \tag{5.115}$$

where, as in (5.113), we have exploited the knowledge of the lattice result to choose the correct minus sign in front of the terms with odd characteristics.

Since the cycles $\tilde{a}_r$ on $\widetilde{\mathcal{R}}_n$ intersect B_1 (see right panel of Fig. 1.3), removing all the operators $(-1)^{F_{B_1}}$ leads to $\boldsymbol{\varepsilon} = \mathbf{0}$ in each Riemann theta function occurring in (5.115), similarly to Sec. (5.D.1). Moreover, differently from Sec. 5.D.1, the removal of $(-1)^{F_{B_1}}$ affects also the boundary conditions along the b cycles of $\widetilde{R}_n$. In particular, $\boldsymbol{\delta} \to \boldsymbol{\delta}' \equiv (\boldsymbol{\delta} - \mathcal{P}\,\boldsymbol{\varepsilon}) \mod 2$, where $\mathcal{P}$ has 1's on the main diagonal, -1's on the lower diagonal and zeros elsewhere. This procedure brings (5.113) into the following form

$$\sum_{\boldsymbol{\varepsilon},\boldsymbol{\delta}} (-1)^{4\boldsymbol{\varepsilon}\cdot\boldsymbol{\delta}} \Theta\begin{bmatrix} \mathbf{0} \\ \boldsymbol{\delta}' \end{bmatrix}(\tilde{\tau})^2 = \sum_{\boldsymbol{\varepsilon},\boldsymbol{\delta}'} (-1)^{4\boldsymbol{\varepsilon}\cdot(\boldsymbol{\delta}'+\mathcal{P}\boldsymbol{\varepsilon})}\, \Theta\begin{bmatrix} \mathbf{0} \\ \boldsymbol{\delta}' \end{bmatrix}(\tilde{\tau})^2 = \sum_{\boldsymbol{\delta}'} t_n(\boldsymbol{\delta}')\, \Theta\begin{bmatrix} \mathbf{0} \\ \boldsymbol{\delta}' \end{bmatrix}(\tilde{\tau})^2 \,, \tag{5.116}$$

where in the first step we have changed the summation variable and in the second one we have introduced

$$t_n(\boldsymbol{\delta}) = \sum_{\boldsymbol{\varepsilon}} (-1)^{4(\boldsymbol{\varepsilon}\cdot\boldsymbol{\delta} + \boldsymbol{\varepsilon}\cdot\mathcal{P}\cdot\boldsymbol{\varepsilon})} \,. \tag{5.117}$$

At this point, it is not difficult to observe that $\boldsymbol{\varepsilon}\cdot\mathcal{P}\cdot\boldsymbol{\varepsilon} = \boldsymbol{\varepsilon}\cdot\mathcal{Q}/2\cdot\boldsymbol{\varepsilon}$, which leads to the conclusion that $t_n(\boldsymbol{\delta})$ is equal to $m_n(\boldsymbol{\delta})$ given in (5.42), and therefore is equal to the $r_n(\boldsymbol{\delta})$ in the formula for the moments of the partial transpose of the free fermion, Eqs. (5.37) and (5.38). Let us stress again that the choice of the minus sign in front of the terms with odd characteristics in (5.115) is crucial to obtain the correct result.

5.E Numerical checks from the Ising model and the XX chain

In this appendix we give some numerical evidence of (5.64) and (5.65) for the terms in $\mathrm{Tr}\,\rho_A^n$ and of (5.67) and (5.68) for the terms in $\mathrm{Tr}(\rho_A^{T_2})^n$.

The lattice computations are performed on the XX and on the Ising spin chain. For both models, because of the presence of the Jordan-Wigner string, in both ρ_A and $\rho_A^{T_2}$ four terms occur that cannot be simultaneously diagonalized (see (4.13) and (4.31) respectively). The four correlation matrices corresponding to this four terms can be computed from the ones relative to subsystems A and B_1 [222, 331] as explained in Secs. 4.3 and 4.4. The expressions on the lattice for $\mathrm{Tr}\,\rho_A^n$ and $\mathrm{Tr}\left(\rho_A^{T_2}\right)^n$ have been written in Eqs. (4.27)–(4.30) and (4.44)–(4.47) for $2 \leqslant n \leqslant 5$ as sums of various terms involving these matrices. Here we consider these terms separately and study their scaling limit. We compute the

correlation matrices of an infinite system, and the subsystem A is taken to be two blocks of equal size ℓ. The continuum limit is approached by increasing ℓ and the data are plotted as function of the four-point ratio x (4.48). Because of the dihedral symmetry discussed in the final part of Sec. 5.4.3, many terms are equal and here we show only one representative for each equivalence class. Despite this symmetry, the number of terms increases very fast with n, and for this reason we present the results only for $n = 2$ and $n = 3$.

In analogy with the definitions (5.49), we find it convenient to introduce a notation for the following functions

$$J_n \equiv \frac{c_n^2}{\big[\ell_1\ell_2(1-x)\big]^{2\Delta_n}}, \qquad \Omega_n[\boldsymbol{e}] \equiv \left|\frac{\Theta[\boldsymbol{e}](\tau(x))}{\Theta(\tau(x))}\right|, \tag{5.118}$$

which enter in the single terms of the sum over the spin structures in $\operatorname{Tr}\rho_A^n$. The prefactors J_n differ in the Ising and in the modular invariant Dirac model for the central charge in Δ_n and for the explicit value of the c_n. In the plots, we show the lattice analog of these quantities. In analogy to what was done in Eq. 5.48, for the terms in $\operatorname{Tr}\rho_A^n$ we plot

$$J_n^{\text{lat}} = \operatorname{Tr}\rho_1^n, \qquad \Omega_n^{\text{lat}}[\boldsymbol{q}]^2 = \frac{1}{\operatorname{Tr}\rho_1^n}\ \operatorname{Tr}\left[\prod_{k=1}^{n}\rho_{q_k}\right], \tag{5.119}$$

for the XX model, and

$$J_n^{\text{lat}} = \operatorname{Tr}\rho_1^n, \qquad \Omega_n^{\text{lat}}[\boldsymbol{q}] = \frac{1}{\operatorname{Tr}\rho_1^n}\ \operatorname{Tr}\left[\prod_{k=1}^{n}\rho_{q_k}\right], \tag{5.120}$$

for the Ising model. Analogous quantities can be defined for the terms appearing in the formula of $\operatorname{Tr}\left(\rho_A^{T_2}\right)^n$. The numerical results for the XX model are showed in Figs. 5.5 and 5.6 for $n = 2$ and $n = 3$ respectively; while in Figs. 5.7 and 5.8 the same quantities are plotted for the Ising model for $n = 2$ and $n = 3$ respectively. The points computed on the lattice clearly tend to the CFT formulas as the subsystem size increases.

A finite size scaling analysis has been performed in order to extrapolate the continuum behaviour. For the moments of the reduced density matrix of the XX chain, the scaling function is very similar to the one of the free fermion (5.50),

$$\Omega_n^{\text{lat}}[\tilde{\boldsymbol{q}}]^2 = \Omega_n^2[\boldsymbol{e}] + \frac{\omega_n^{(1)}(x)}{\ell^{2/n}} + \frac{\omega_n^{(2)}(x)}{\ell^{4/n}} + \frac{\omega_n^{(3)}(x)}{\ell^{6/n}} + \dots, \tag{5.121}$$

where $\boldsymbol{q}$ and $\boldsymbol{e}$ are related as explained in Sec. 5.4. A similar expression can be defined for J_n^{lat}/J_n (as was done in Sec. 5.3.3 we plot this ratio in order to eliminate the residual dependence on ℓ in the continuum) and for the analogous terms in the formula of the moments of the partial transpose. Once this scaling is taken into account, the extrapolated points for infinite size of the subsystem (red crosses) match with the CFT curve very nicely.

As for the Ising model, also the Majorana fermion operator with conformal weight $h = 1/2$ must be take into account [222]. This leads us to modify the scaling function as follows

$$\Omega_n^{\text{lat}}[\tilde{\boldsymbol{q}}] = \Omega_n[\boldsymbol{e}] + \frac{\omega_n^{(1)}(x)}{\ell^{1/n}} + \frac{\omega_n^{(2)}(x)}{\ell^{2/n}} + \frac{\omega_n^{(3)}(x)}{\ell^{3/n}} + \dots, \tag{5.122}$$

and analogously for J_n^{lat}/J_n and the terms in the moments of the partial transpose. From the analysis of the terms (5.120) for the Ising model, we find a very peculiar and unexpected feature. It turns out that in the sum (5.57) the only terms which follow this

scaling are those whose continuum limit corresponds to odd characteristics, and therefore vanishes. Instead, all the terms whose continuum limit corresponds to even characteristics follow a milder scaling with the same exponents occurring for the free fermion and the XX model (see (5.50) and (5.121)). This feature is present for both the terms in $\mathrm{Tr}\,\rho_A^n$ and $\mathrm{Tr}\left(\rho_A^{T_2}\right)^n$. Indeed, by simple inspection of Figs. 5.7 and 5.8, it is possible to notice that the finite size effects for the terms corresponding to odd characteristics are much more severe than those of the terms corresponding to even characteristic. In practice, it means that if we simply ignore the terms which are going to vanish in the continuum limit, we can extract the CFT result with much more precision. Indeed, with respect to the whole sums (5.57) and (5.59), the sum with only the terms corresponding to even characteristics according to (5.65) and (5.68), will present milder finite size effects.

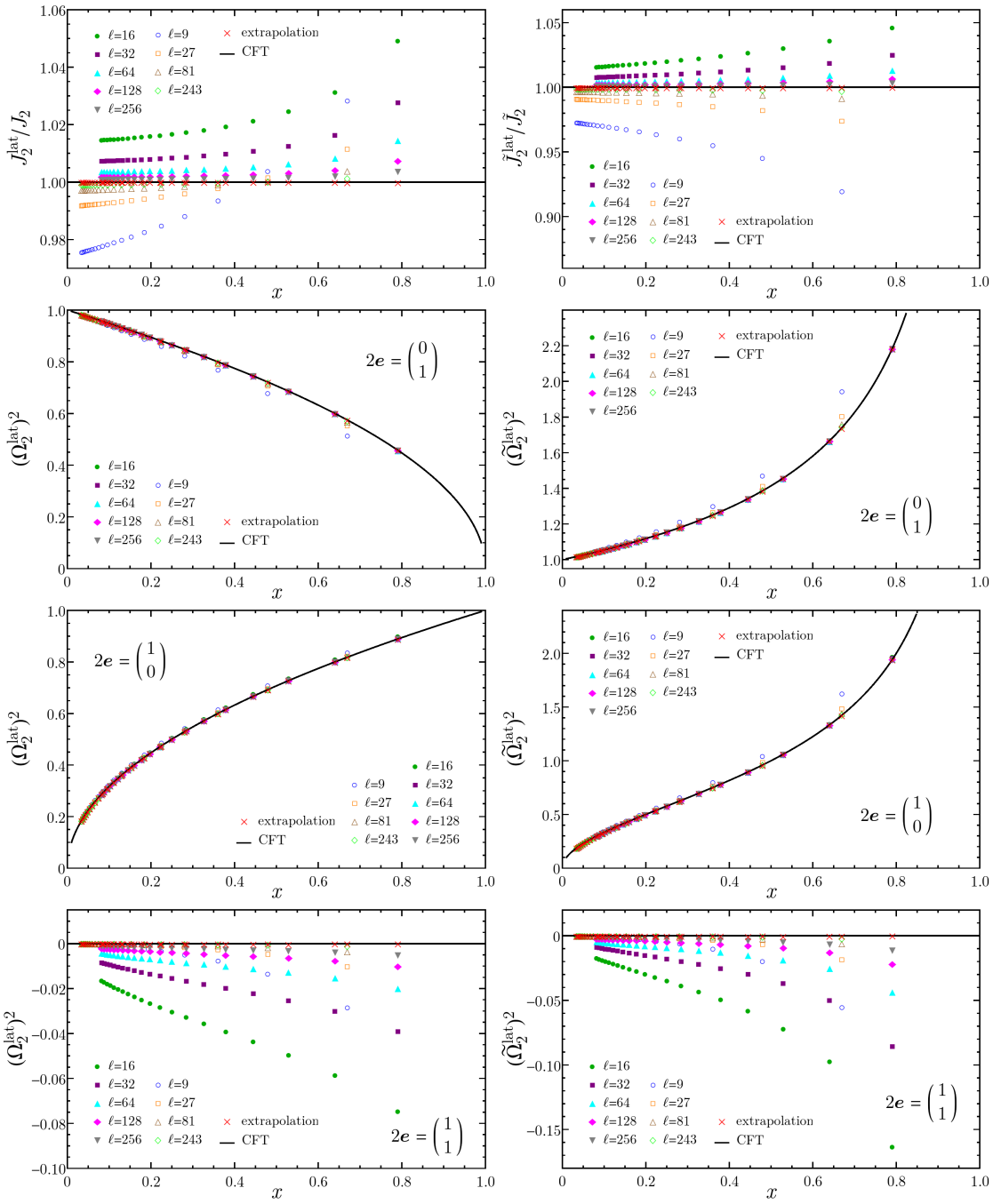

Figure 5.5: The terms occurring in $\mathrm{Tr}\,\rho_A^2$ (left panels) and $\mathrm{Tr}\left(\rho_A^{T_2}\right)^2$ (right panels) for the XX model, according to the correspondence (5.64). For each group of identical terms, only one representative has been plotted. The extrapolated points (red crosses) are obtained through a fit of the data according to the scaling function (5.121) and they agree very well with the CFT predictions (solid lines).

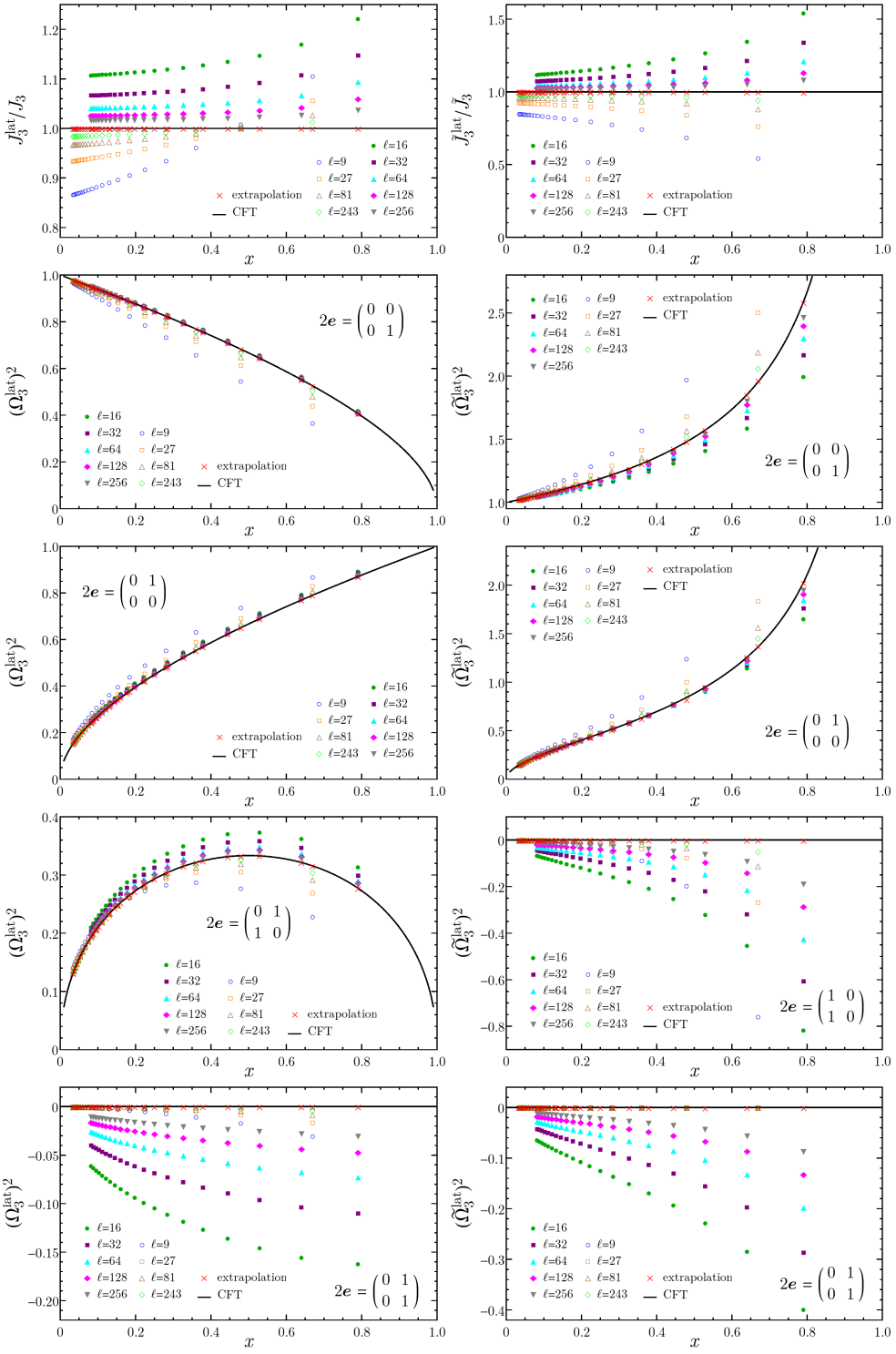

Figure 5.6: The terms in $\mathrm{Tr}\,\rho_A^3$ (left) and $\mathrm{Tr}\left(\rho_A^{T_2}\right)^3$ (right) for the XX model (see Fig. 5.5).

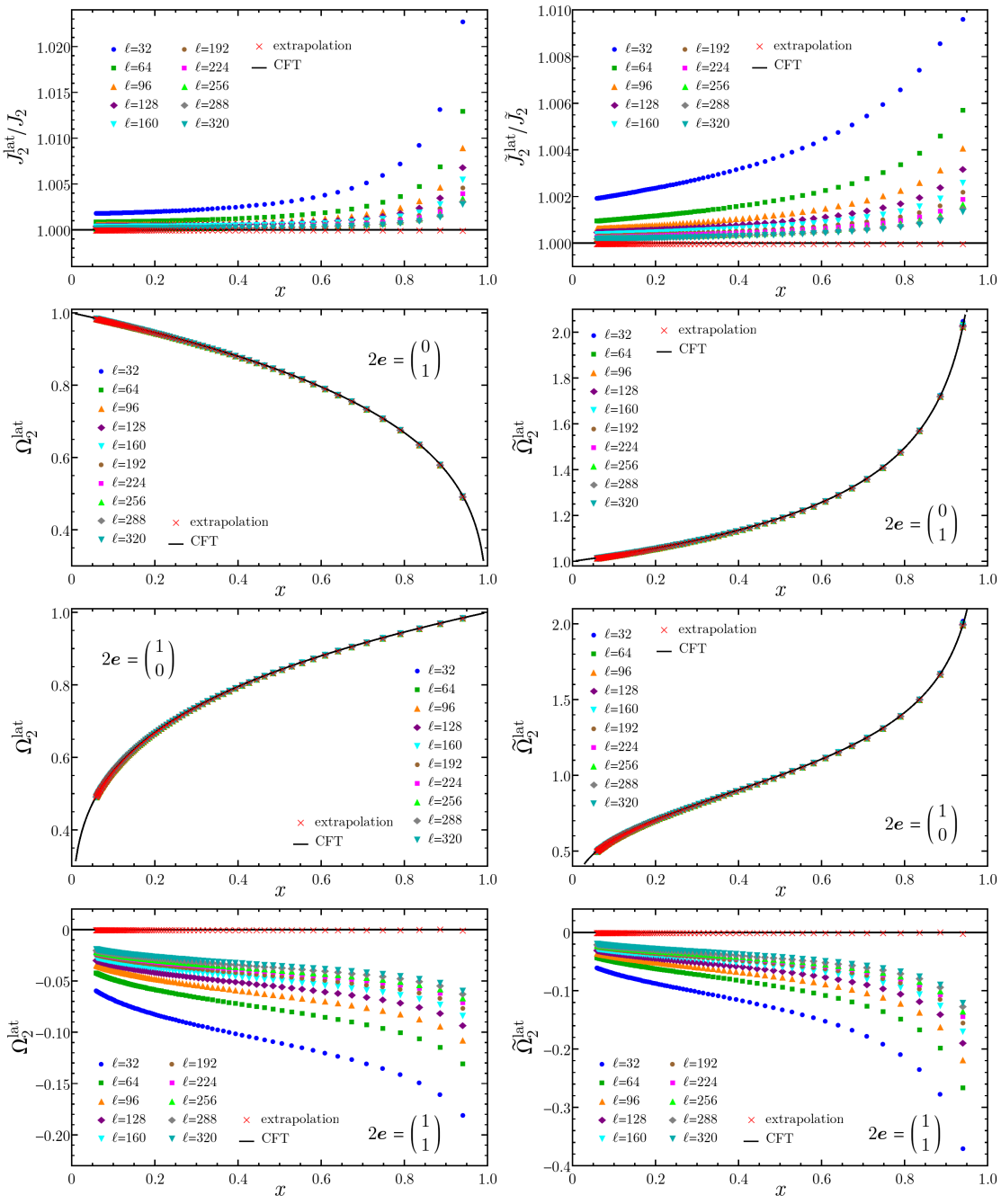

Figure 5.7: The terms occurring in $\mathrm{Tr}\,\rho_A^2$ (left panels) and $\mathrm{Tr}\left(\rho_A^{T_2}\right)^2$ (right panels) for the Ising model, according to the correspondence (5.65). For each group of identical terms, only one representative has been plotted. The extrapolated points (red crosses) are obtained through a fit of the data according to the appropriate scaling function. The expression (5.122) is used for the terms corresponding to odd characteristic, while we take the milder exponents of the scaling function (5.121) for the terms corresponding to even characteristic. They agree very well with the CFT predictions (solid lines).

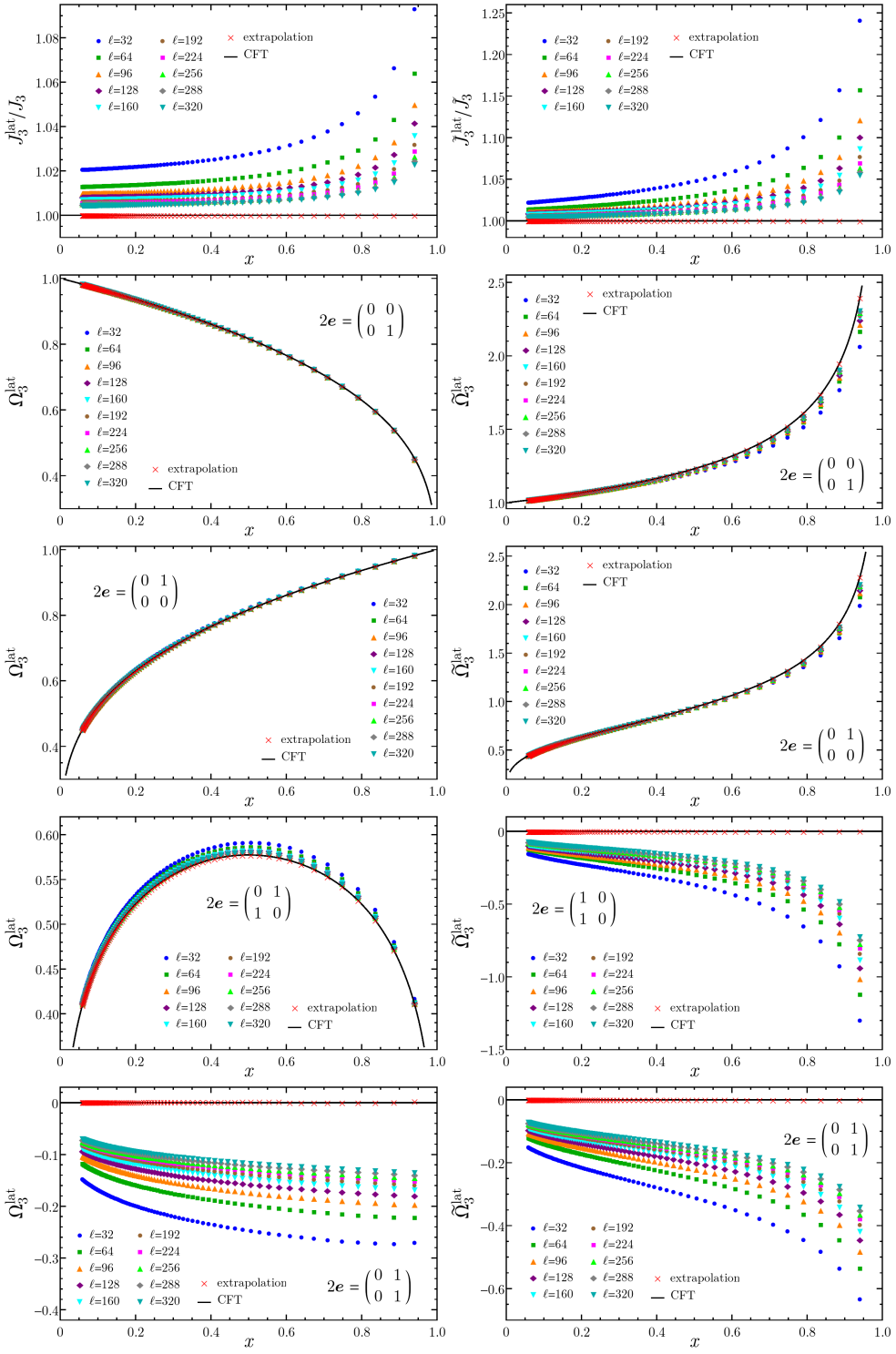

Figure 5.8: The terms in $\mathrm{Tr}\,\rho_A^3$ (left) and $\mathrm{Tr}\left(\rho_A^{T_2}\right)^3$ (right) for the Ising model (see Fig. 5.7).

Conclusions

Entanglement negativity has drawn a lot of attention in the last years as a very useful tool to quantify entanglement between separated regions or in general mixed states of quantum many-body systems. The entanglement entropy computed for disjoint regions, as is done in Chap. 2, only measures the amount of entanglement between the union of the intervals with the rest of the system. If one needs the entanglement shared by the disjoint regions, which are in general left in a mixed state after the rest is traced out, the entanglement entropy is no longer useful, and other measures must be used. The simplicity of the definition of the negativity makes it a 'computable measure of entanglement' [119], and we saw that it can be computed in QFT, at least in principle, using the replica trick [134, 135]. Exact analytical computations in QFT are available only in few simple cases, especially for one-dimensional free massless fields in CFT. The computational difficulty of the moments of the partial transpose is comparable with the one of the Rényi entropies for subsystems made of disjoint regions, and it is expressed in terms of Riemann theta functions. The negativity can also be studied in many situations numerically.

As for the entanglement entropy, an easy case from the computational viewpoint is given by the bosonic Gaussian states, whose prototypical example is the ground states of the harmonic chain. This is due to the fact that the spectrum of the reduced density matrix and of its partial transpose can be obtained by correlation matrix techniques [147–151]. This is valid also in more general situations than the ground state, as for example in thermal states or in out-of-equilibrium configurations. In Chap. 3, we used these techniques in the case of a global quench to study the evolution of the logarithmic negativity among two intervals in the harmonic chain, and we compared the results with the CFT predictions, computed from multi-point function of twist fields on the strip. In particular, we discuss the quasi-particle interpretation for the spreading of entanglement and correlations. However, there are still many open problems in the context of evolution of entanglement. The range of validity of the quasi-particle picture is surely something that should be addressed in order to settle the questions raised in Ref. [319]. Moreover, some analytical results on the evolution of the entanglement entropy and negativity in the harmonic chain would be extremely important. Unfortunately, at the moment no results are available for the entanglement entropy of bosonic models, not even in the ground state.

We saw in Chap. 4 that the situation is more complicated for fermionic Gaussian states [331], such as the ground state of the tight-binding model. Here the spectrum of the partial transpose is not directly computable, still one can obtain its moments from the correlation matrices relative to some auxiliary Gaussian reduced density matrices. It is however still an open problem to find the full negativity for two disjoint blocks of sites.

We also discussed how the same problem arises for disjoint blocks of a spin chain: the moments of the partial transpose can be computed, but the negativity is out of reach. The situation is reminiscent of the one of the Rényi entropies for disjoint regions in a spin chain [222], which is also reviewed in Chap. 4.

From the structure of the the partial transpose on the fermionic lattice it is possible to compute its path integral representation. This allows for the computation of the moments of the partial transpose in the continuum theory of a free massless Dirac fermion, which has been done in Chap. 5. Thanks to the similarity with the case of the entanglement of disjoint intervals in spin chains, the same approach was also able to reproduce the already known formulas for the Rényi entropies of the modular invariant Dirac fermion and the critical Ising model.

Many of the available CFT formulas for the moments of the partial transpose, as well as for the Rényi entropies for disjoint intervals, are expressed in terms of Riemann theta functions, which in turn are function of a period matrix of size $(n-1) \times (n-1)$ (for two intervals). This makes the analytic continuation to $n \to 1$ technically very difficult, even for very simple CFT. In Chap. 2 we discussed a numerical method based on the interpolation of the known values for integer $n > 1$ with a rational function, which was first used in this context in Ref. [152]. The resulting approximate analytic continuation is found by extrapolating to $n = 1$. In Sec. 2.6 we showed some of the results obtained for the mutual information, where we found that even if the Rényi entropies are available for few values of n, the analytic continuation can be obtained with high accuracy. Moreover, in App. 2.E we discussed some technical details and some drawbacks of the method. In Ref. [236] a similar analysis is performed also for the entanglement negativity, and it is found that in general many more values of the moments are needed in order to obtain sensible results. Moreover, the replica space for the negativity is more complicated, since there are different analytic continuations for even and odd integer values of n. To obtain the negativity one should continue the even series to $n \to 1$, and this means that high values of n are needed to get an accurate numerical extrapolation. In certain cases the computational cost of the moments of the partial transpose grows exponentially with n, and this is a serious obstacle to obtaining their values for arbitrarily high order, and therefore a precise approximation of the negativity. The analytic continuation is still an open problem, and a deeper understanding would be highly desirable.

An important open problem is the study of negativity in higher dimensions, where few results are available [141, 142]. In particular not much has been investigated in higher dimensional QFT [340], unlike for the entanglement entropy, the Rényi entropies and the mutual information where some important results have been found [51–54]. Finally, let us mention that a holographic description of negativity is still lacking, even if some steps have been made in that direction [232, 233]. A deeper analysis of this issue would open new interesting perspectives on the connections between entanglement and the holographic principle.

Acknowledgements

First of all, I am glad to thank my supervisor Erik Tonni who really helped me go through these years in SISSA. I want to thank him especially for all his patience, for being always willing to help and discuss, and for constantly motivating and supporting me even when times where difficult. I also need to thank all my other collaborators, from whom I really learned a lot. A special thank to Luca Tagliacozzo, who will always have my gratitude for all the discussions about physics and for all the precious suggestions he gave me about research and the choices I had to take.

I am happy to thank all the guys I met in SISSA who shared joys and sorrows of the PhD life. I have to admit, despite all my complaints, thanks to you SISSA has been a nice and stimulating work place. Thanks for all your patience.

While thinking to these years in Trieste, I realize I will never forget the life in via Rossetti 28, along with all the flat mates with whom I joyfully spent even a bit of my time. They really are a lot, so let me mention only Guido and Mimmo, who where with me from the beginning four years ago and are leaving now too. Thanks for all the time we spent together, and for making home a cheerful place where to come back. And good luck to the old and new resident of the "kibbutz" for the next years.

A huge thank also to my teammates of the Flying Boars. I am truly grateful for all the moments of joy, frustration, grit and satisfaction that we shared, but especially for a lot of pure and healthy fun (and a bunch of hard-fought second to last places). Sharing with you the goal of doing our best in getting better and trying to spread our sport was fundamental for my mental health in the times of difficulty. I look forward to meet you again on the fields at some great tournaments somewhere in Europe. Let it fly!

I feel I truly need to thank all my friends that I was lucky to meet before coming to Trieste and who continuously kept supporting me through these years. I cannot even count how many of you guys I should thank, starting from the old friends from Rovereto, to the ones with whom I spent some great times in Padova and all the people I met when I was in the Middle East. Let me just say that even if we weren't able to see often, every time we meet for me is as no time has passed.

Finally, thanks a lot to my family for being always there whenever needed, for their unconditional support and for their willingness to help in any possible way.

Bibliography

[1] A. Einstein, B. Podolsky, and N. Rosen, Physical Review **47**, 777 (1935).

[2] E. Schrödinger, Math. Proc. Cambridge Philos. Soc. **31**, 555 (1935).

[3] E. H. Lieb and D. W. Robinson, Commun. Math. Phys. **28**, 251 (1972).

[4] J. S. Bell, Physics **1**, 195 (1964).

[5] C. H. Bennett, G. Brassard, C. Crépeau, R. Jozsa, A. Peres, and W. K. Wootters, Phys. Rev. Lett. **70**, 1895 (1993).

[6] C. H. Bennett, D. P. DiVincenzo, J. A. Smolin, and W. K. Wootters, Phys. Rev. A **54**, 3824 (1996).

[7] C. H. Bennett, H. J. Bernstein, S. Popescu, and B. Schumacher, Phys. Rev. A **53**, 2046 (1996).

[8] L. Amico, R. Fazio, A. Osterloh, and V. Vedral, Rev. Mod. Phys. **80**, 517 (2008).

[9] J. Eisert, M. Cramer, and M. B. Plenio, Rev. Mod. Phys. **82**, 277 (2010).

[10] P. Calabrese, J. Cardy, and B. Doyon, J. Phys. A **42**, 500301 (2009).

[11] M. B. Plenio, J. Eisert, J. Dreißig, and M Cramer, Phys. Rev. Lett. **94**, 060503 (2005).

[12] M. Cramer, J. Eisert, M. B. Plenio, and J. Dreißig, Phys. Rev. A **73**, 012309 (2006).

[13] A. Riera and J. I. Latorre, Phys. Rev. A **74**, 052326 (2006).

[14] M. B. Hastings, J. Stat. Mech. P08024 (2007).

[15] M. M. Wolf, F. Verstraete, M. B. Hastings, and J. I. Cirac, Phys. Rev. Lett. **100**, 070502 (2008).

[16] L. Bombelli, R. K. Koul, J. Lee, and R. D. Sorkin, Phys. Rev. D **34**, 373 (1986).

[17] M. Srednicki, Phys. Rev. Lett. **71**, 666 (1993).

[18] J. D. Bekenstein, Phys. Rev. D **7**, 2333 (1973).

[19] S. W. Hawking, Nature **248**, 30 (1974).

[20] C. Holzhey, F. Larsen, and F. Wilczek, Nucl. Phys. B **424**, 443 (1994).

[21] M. M. Wolf, Phys. Rev. Lett. **96**, 010404 (2006).

[22] G. Vitagliano, A. Riera, and J. I. Latorre, New J. Phys. **12**, 113049 (2010).

[23] A. Kitaev and J. Preskill, Phys. Rev. Lett. **96**, 110404 (2006).

[24] M. Levin and X.-G. Wen, Phys. Rev. Lett. **96**, 110405 (2006).

[25] A. Kitaev, Ann. Phys. **303**, 2 (2003).

[26] R. B. Laughlin, Phys. Rev. Lett. **50**, 1395 (1983).

[27] P. Calabrese and J. Cardy, J. Stat. Mech. P06002 (2004).

[28] I. Affleck and A. W. W. Ludwig, Phys. Rev. Lett. **67**, 161 (1991).

[29] H.-Q. Zhou, T. Barthel, J. O. Fjærestad, and U. Schollwöck, Phys. Rev. A **74**, 050305 (2006).

[30] E. S. Sørensen, M.-S. Chang, N. Laflorencie, and I. Affleck, J. Stat. Mech. L01001 (2007).

[31] E. S. Sørensen, M.-S. Chang, N. Laflorencie, and I. Affleck, J. Stat. Mech. P08003 (2007).

[32] P. Fendley, M. P. A. Fisher, and C. Nayak, J. Stat. Phys. **126**, 1111 (2007).

[33] I. Affleck, N. Laflorencie, and E. S. Sørensen, J. Phys. A **42**, 504009 (2009).

[34] S. Östlund and S. Rommer, Phys. Rev. Lett. **75**, 3537 (1995).

[35] S. Rommer and S. Östlund, Phys. Rev. B **55**, 2164 (1997).

[36] L. Tagliacozzo, T. R. de Oliveira, S. Iblisdir, and J. I. Latorre, Phys. Rev. B **78**, 024410 (2008).

[37] B. Pirvu, G. Vidal, F. Verstraete, and L. Tagliacozzo, Phys. Rev. B **86**, 075117 (2012).

[38] S. R. White, Phys. Rev. Lett. **69**, 2863 (1992).

[39] S. R. White, Phys. Rev. B **48**, 10345 (1993).

[40] M. Fannes, B. Nachtergaele, and R. F. Werner, J. Stat. Phys. **66**, 939 (1992).

[41] G. Vidal, Phys. Rev. Lett. **99**, 220405 (2007).

[42] G. Vidal, Phys. Rev. Lett. **101**, 110501 (2008).

[43] F. Verstraete and J. I. Cirac, arXiv:cond-mat/0407066 (2004).

[44] C. Callan and F. Wilczek, Phys. Lett. B **333**, 55 (1994).

[45] J. L. Cardy, O. A. Castro-Alvaredo, and B. Doyon, J. Stat. Phys. **130**, 129 (2007).

[46] H. Casini, C. D. Fosco, and M. Huerta, J. Stat. Mech. P07007 (2005).

[47] H. Casini and M. Huerta, Class. Quant. Grav. **26**, 185005 (2009).

[48] H. Casini and M. Huerta, J. Stat. Mech. P12012 (2005).

[49] H. Casini and M. Huerta, JHEP **03** (2009) 048.

[50] H. Casini and M. Huerta, Nucl. Phys. B **764**, 183 (2007).

[51] J. Cardy, J. Phys. A **46**, 285402 (2013).

[52] N. Shiba, JHEP **12** (2014) 152.

[53] H. J. Schnitzer, arXiv:1406.1161 (2014).

[54] C. A. Agón, I. Cohen-Abbo, and H. J. Schnitzer, arXiv:1505.03757 (2015).

[55] N. Shiba, JHEP **07** (2012) 100.

[56] H. Casini and M. Huerta, Phys. Lett. B **600**, 142 (2004).

[57] H. Casini and M. Huerta, J. Phys. A **40**, 7031 (2007).

[58] A. B. Zamolodchikov, JETP Lett. **43**, 730 (1986).

[59] Z. Komargodski and A. Schwimmer, JHEP **012** (2011) 99.

[60] Z. Komargodski, JHEP **07** (2012) 069.

[61] J. L. Cardy, Phys. Lett. B **215**, 749 (1988).

[62] R. C. Myers and A. Sinha, Phys. Rev. D **82**, 046006 (2010).

[63] R. C. Myers and A. Sinha, JHEP **01** (2011) 125.

[64] I. R. Klebanov, S. S. Pufu, and B. R. Safdi, JHEP **10** (2011) 038.

[65] D. L. Jafferis, I. R. Klebanov, S. S. Pufu, and B. R. Safdi, JHEP **06** (2011) 102.

[66] H. Casini, M. Huerta, and R. C. Myers, JHEP **05** (2011) 036.

[67] H. Casini and M. Huerta, Phys. Rev. D **85**, 125016 (2012).

[68] H. Liu and M. Mezei, JHEP **4** (2013) 162.

[69] H. Liu and M. Mezei, JHEP **01** (2014) 098.

[70] H. Casini, M. Huerta, R. C. Myers, and A. Yale, arXiv:1506.06195 (2015).

[71] G. T. Hooft, arXiv:gr-qc/9310026 (1993).

[72] L. Susskind, J. Math. Phys. **36**, 33 (1994).

[73] J. Maldacena, Adv. Theor. Math. Phys. **2**, 231 (1998).

[74] S. Ryu and T. Takayanagi, JHEP **08** (2006) 045.

[75] S. Ryu and T. Takayanagi, Phys. Rev. Lett. **96**, 181602 (2006).

[76] V. E. Hubeny, M. Rangamani, and T. Takayanagi, JHEP **07** (2007) 062.

[77] V. E. Hubeny and M. Rangamani, JHEP **03** (2008) 006.

[78] E. Tonni, JHEP **05** (2011) 004.

[79] M. Headrick, Phys. Rev. D **82**, 126010 (2010).

[80] P. Hayden, M. Headrick, and A. Maloney, Phys. Rev. D **87**, 046003 (2013).

[81] J. Abajo-Arrastia, J. Aparício, and E. López, JHEP **11** (2010) 149.

[82] T. Albash and C. V. Johnson, New J. Phys. **13**, 045017 (2011).

[83] J. Aparício and E. López, JHEP **12** (2011) 082.

[84] V. Balasubramanian, A. Bernamonti, J. de Boer, N. Copland, B. Craps, E. Keski-Vakkuri, B. Müller, A. Schäfer, M. Shigemori, and W. Staessens, Phys. Rev. Lett. **106**, 191601 (2011).

[85] V. Balasubramanian, A. Bernamonti, N. Copland, B. Craps, and F. Galli, Phys. Rev. D **84**, 105017 (2011).

[86] V. Balasubramanian, A. Bernamonti, J. de Boer, N. Copland, B. Craps, E. Keski-Vakkuri, B. Müller, A. Schäfer, M. Shigemori, and W. Staessens, Phys. Rev. D **84**, 026010 (2011).

[87] A. Allais and E. Tonni, JHEP **01** (2012) 102.

[88] R. Callan, J. He, and M. Headrick, JHEP **06** (2012) 081.

[89] E. Caceres and A. Kundu, JHEP **09** (2012) 055.

[90] V. E. Hubeny, M. Rangamani, and E. Tonni, JHEP **05** (2013) 136.

[91] T. Hartman and J. Maldacena, JHEP **05** (2013) 014.

[92] A. Buchel, L. Lehner, R. C. Myers, and A. Van Niekerk, JHEP **05** (2013) 067.

[93] H. Liu and S. J. Suh, Phys. Rev. D **89**, 066012 (2014).

[94] H. Liu and S. J. Suh, Phys. Rev. Lett. **112**, 011601 (2014).

[95] P. Fonda, L. Franti, V. Keränen, E. Keski-Vakkuri, L. Thorlacius, and E. Tonni, JHEP **08** (2014) 051.

[96] C. T. Asplund and A. Bernamonti, Phys. Rev. D **89**, 066015 (2014).

[97] T. Faulkner, arXiv:1303.7221 (2013).

[98] T. Hartman, arXiv :1303.6955 (2013).

[99] A. Lewkowycz and J. Maldacena, JHEP **08** (2013) 090.

[100] T. Faulkner, A. Lewkowycz, and J. Maldacena, JHEP **11** (2013) 074.

[101] T. Barrella, X. Dong, S. A. Hartnoll, and V. L. Martin, JHEP **09** (2013) 109.

[102] L. Y. Hung, R. C. Myers, M. Smolkin, and A. Yale, JHEP **12** (2011) 047.

[103] H. Li and F. D. M. Haldane, Phys. Rev. Lett. **101**, 010504 (2008).

[104] P. Calabrese and J. Cardy, J. Stat. Mech. P04010 (2005).

[105] P. Calabrese and J. Cardy, J. Stat. Mech. P10004 (2007).

[106] P. Calabrese and J. Cardy, J. Stat. Mech. P06008 (2007).

[107] F. Pastawski, B. Yoshida, D. Harlow, and J. Preskill, JHEP **06** (2015) 149.

[108] L. Susskind, arXiv:1402.5674 (2014).

[109] B. Swingle, Phys. Rev. D **86**, 065007 (2012).

[110] B. Swingle, arXiv:1209.3304 (2012).

[111] M. Nozaki, S. Ryu, and T. Takayanagi, JHEP **10** (2012) 193.

[112] X.-L. Qi, arXiv:1309.6282 (2013).

[113] M. Miyaji, S. Ryu, T. Takayanagi, and X. Wen, arXiv:1412.6226 (2014).

[114] M. Miyaji and T. Takayanagi, Prog. Theor. Exp. Phys. **2015**, 073B03 (2015).

[115] J. Molina-Vilaplana, arXiv:1503.07699 (2015).

[116] B. Czech, L. Lamprou, S. McCandlish, and J. Sully, arXiv:1505.05515 (2015).

[117] J. Eisert and M. B. Plenio, J. Mod. Opt. **46**, 145 (1999).

[118] K. Życzkowski, P. Horodecki, A. Sanpera, and M. Lewenstein, Phys. Rev. A **58**, 883 (1998).

[119] G. Vidal and R. F. Werner, Phys. Rev. A **65**, 032314 (2002).

[120] A. Peres, Phys. Rev. Lett. **77**, 1413 (1996).

[121] J. Anders and A. Winter, Quant. Inf. Comp. **8**, 10 (2007).

[122] J. Anders, Phys. Rev. A **77**, 062102 (2008).

[123] A. Ferraro, D. Cavalcanti, A. García-Saez, and A. Acín, Phys. Rev. Lett. **100**, 080502 (2008).

[124] D. Cavalcanti, A. Ferraro, A. García-Saez, and A. Acín, Phys. Rev. A **78**, 012335 (2008).

[125] H. Wichterich, J. Molina-Vilaplana, and S. Bose, Phys. Rev. A **80**, 010304 (2009).

[126] S. Marcovitch, A. Retzker, M. B. Plenio, and B. Reznik, Phys. Rev. A **80**, 012325 (2009).

[127] H. Wichterich, J. Vidal, and S. Bose, Phys. Rev. A **81**, 032311 (2010).

[128] A. Bayat, S. Bose, and P. Sodano, Phys. Rev. Lett. **105**, 187204 (2010).

[129] A. Bayat, P. Sodano, and S. Bose, Phys. Rev. B **81**, 064429 (2010).

[130] P. Sodano, A. Bayat, and S. Bose, Phys. Rev. B **81**, 100412 (2010).

[131] R. A. Santos, V. Korepin, and S. Bose, Phys. Rev. A **84**, 062307 (2011).

[132] A. Bayat, S. Bose, P. Sodano, and H. Johannesson, Phys. Rev. Lett. **109**, 066403 (2012).

[133] R. A. Santos and V. E. Korepin, J. Phys. A **45**, 125307 (2012).

[134] P. Calabrese, J. Cardy, and E. Tonni, Phys. Rev. Lett. **109**, 130502 (2012).

[135] P. Calabrese, J. Cardy, and E. Tonni, J. Stat. Mech. P02008 (2013).

[136] P. Calabrese, L. Tagliacozzo, and E. Tonni, J. Stat. Mech. P05002 (2013).

[137] P. Calabrese, J. Cardy, and E. Tonni, J. Phys. A **48**, 015006 (2015).

[138] V. Eisler and Z. Zimborás, New J. Phys. **16**, 123020 (2014).

[139] M. Hoogeveen and B. Doyon, arXiv:1412.7568 (2014).

[140] X. Wen, P.-Y. Chang, and S. Ryu, arXiv:1501.00568 (2015).

[141] C. Castelnovo, Phys. Rev. A **88**, 042319 (2013).

[142] C. Castelnovo, Phys. Rev. A **89**, 042333 (2014).

[143] Y. A. Lee and G. Vidal, Phys. Rev. A **88**, 042318 (2013).

[144] O. Blondeau-Fournier, O. A. Castro-Alvaredo, and B. Doyon, arXiv:1508.04026 (2015).

[145] V. Alba, J. Stat. Mech. P05013 (2013).

[146] C.-M. Chung, V. Alba, L. Bonnes, P. Chen, and A. M. Läuchli, Phys. Rev. B **90**, 064401 (2014).

[147] K. Audenaert, J. Eisert, M. B. Plenio, and R. F. Werner, Phys. Rev. A **66**, 042327 (2002).

[148] I. Peschel and M.-C. Chung, J. Phys. A **32**, 8419 (1999).

[149] I. Peschel, J. Phys. A **36**, L205 (2003).

[150] A. Botero and B. Reznik, Phys. Rev. A **70**, 052329 (2004).

[151] I. Peschel and V. Eisler, J. Phys. A **42**, 504003 (2009).

[152] C. A. Agón, M. Headrick, D. L. Jafferis, and S. Kasko, Phys. Rev. D **89**, 025018 (2014).

[153] M. B. Plenio and S. Virmani, Quant. Inf. Comp. **7**, 25 (2005).

[154] R. Horodecki, P. Horodecki, M. Horodecki, and K. Horodecki, Rev. Mod. Phys. **81**, 865 (2009).

[155] K. Kraus, A. Böhm, J. D. Dollard, and W. H. Wootters, *States, Effects, and Operations Fundamental Notions of Quantum Theory*, Vol. 190, Lecture Notes in Physics (Springer Berlin Heidelberg, 1983).

[156] C. H. Bennett, D. P. DiVincenzo, C. A. Fuchs, T. Mor, E. Rains, P. W. Shor, J. A. Smolin, and W. K. Wootters, Phys. Rev. A **59**, 1070 (1999).

[157] E. Rains, IEEE Trans. Inf. Theory **47**, 2921 (2001).

[158] E. M. Rains, Phys. Rev. A **60**, 173 (1999).

[159] P. Horodecki, Phys. Lett. A **232**, 333 (1997).

[160] M. Horodecki, P. Horodecki, and R. Horodecki, Phys. Rev. Lett. **80**, 5239 (1998).

[161] R. F. Werner, Phys. Rev. A **40**, 4277 (1989).

[162] G. Vidal, J. Mod. Opt. **47**, 355 (2000).

[163] V. Vedral, M. B. Plenio, M. A. Rippin, and P. L. Knight, Phys. Rev. Lett. **78**, 2275 (1997).

[164] V. Vedral and M. B. Plenio, Phys. Rev. A **57**, 1619 (1998).

[165] M. A. Nielsen, Phys. Rev. Lett. **83**, 436 (1999).

[166] M. Horodecki, Quant. Inf. Comp. **1**, 3 (2011).

[167] M. B. Plenio, Phys. Rev. Lett. **95**, 090503 (2005).

[168] E. H. Lieb and M. B. Ruskai, Phys. Rev. Lett. **30**, 434 (1973).

[169] E. H. Lieb, J. Math. Phys. **14**, 1938 (1973).

[170] M. Horodecki, P. Horodecki, and R. Horodecki, Phys. Rev. Lett. **84**, 2014 (2000).

[171] S. Popescu and D. Rohrlich, Phys. Rev. A **56**, R3319 (1997).

[172] M. J. Donald, M. Horodecki, and O. Rudolph, J. Math. Phys. **43**, 4252 (2002).

[173] A. Rényi, *Probability theory* (North-Holland, 1970).

[174] D. Yang, M. Horodecki, R. Horodecki, and B. Synak-Radtke, Phys. Rev. Lett. **95**, 190501 (2005).

[175] P. M. Hayden, M. Horodecki, and B. M. Terhal, J. Phys. A **34**, 6891 (2001).

[176] M. Horodecki, P. Horodecki, and R. Horodecki, Phys. Lett. A **223**, 1 (1996).

[177] R. Simon, Phys. Rev. Lett. **84**, 2726 (2000).

[178] J. Lee, M. S. Kim, Y. J. Park, S. Lee, J. Mod. Opt. **47**, 2151 (2000).

[179] J. Eisert, "Entanglement in quantum information theory", PhD thesis (2001), arXiv:quant-ph/0610253.

[180] K. Audenaert, M. B. Plenio, and J. Eisert, Phys. Rev. Lett. **90**, 027901 (2003).

[181] H. He and G. Vidal, Phys. Rev. A **91**, 012339 (2015).

[182] W. S. Bakr, A. Peng, M. E. Tai, R. Ma, J. Simon, J. I. Gillen, S. Folling, L. Pollet, and M. Greiner, Science **329**, 547 (2010).

[183] J. F. Sherson, C. Weitenberg, M. Endres, M. Cheneau, I. Bloch, and S. Kuhr, Nature **467**, 68 (2010).

[184] K. R. Islam, *Entanglement Detection by Interfering Quantum Many-body Twins*, talk during KITP Program "Entanglement in Strongly-Correlated Quantum Matter", http://online.kitp.ucsb.edu/online/entangled15/islam/, Santa Barbara, Apr. 2015.

[185] M. Greiner, *Measuring Entanglement Entropy in Synthetic Matter*, talk at KITP Conference "Closing the Entanglement Gap", http://online.kitp.ucsb.edu/online/entangled-c15/greiner/, Santa Barbara, June 2015.

[186] R. Islam, R. Ma, P. M. Preiss, M. E. Tai, A. Lukin, M. Rispoli, and M. Greiner, arXiv:1509.01160 (2015).

[187] A. K. Ekert, C. M. Alves, D. K. L. Oi, M. Horodecki, P. Horodecki, and L. C. Kwek, Phys. Rev. Lett. **88**, 217901 (2002).

[188] J. Cardy, Phys. Rev. Lett. **106**, 150404 (2011).

[189] D. A. Abanin and E. Demler, Phys. Rev. Lett. **109**, 020504 (2012).

[190] C. Moura Alves and D. Jaksch, Phys. Rev. Lett. **93**, 110501 (2004).

[191] A. J. Daley, H. Pichler, J. Schachenmayer, and P. Zoller, Phys. Rev. Lett. **109**, 020505 (2012).

[192] W. S. Bakr, J. I. Gillen, A. Peng, S. Fölling, and M. Greiner, Nature **462**, 74 (2009).

[193] C. Weitenberg, M. Endres, J. F. Sherson, M. Cheneau, P. Schauß, T. Fukuhara, I. Bloch, and S. Kuhr, Nature **471**, 319 (2011).

[194] J. Simon, W. S. Bakr, R. Ma, M. E. Tai, P. M. Preiss, and M. Greiner, Nature **472**, 307 (2011).

[195] P. Rabl, A. J. Daley, P. O. Fedichev, J. I. Cirac, and P. Zoller, Phys. Rev. Lett. **91**, 110403 (2003).

[196] P. Calabrese, J. Cardy, and E. Tonni, J. Stat. Mech. P01021 (2011).

[197] W. W. Ho and D. A. Abanin, arXiv:1508.03784 (2015).

[198] C. K. Hong, Z. Y. Ou, and L. Mandel, Phys. Rev. Lett. **59**, 2044 (1987).

[199] A. A. Belavin, A. M. Polyakov, and A. B. Zamolodchikov, Nucl. Phys. B **241**, 333 (1984).

[200] P. Ginsparg, *Applied Conformal Field Theory*, lecture notes, arXiv:hep-th/9108028, Les Houches, July 1988.

[201] P. Di Francesco, D. Sénéchal, and P. Mathieu, *Conformal field theory* (Springer, 1997).

[202] I. T. Todorov, M. C. Mintchev, and V. B. Petkova, *Conformal invariance in quantum field theory* (Scuola normale superiore Pisa, 1978).

[203] J. Polchinski, Nucl. Phys. B **303**, 226 (1988).

[204] V. Riva and J. Cardy, Phys. Lett. B **622**, 339 (2005).

[205] P. Calabrese and A. Lefevre, Phys. Rev. A **78**, 032329 (2008).

[206] P. Calabrese and J. Cardy, J. Phys. A **42**, 504005 (2009).

[207] A. Zamolodchikov, Nucl. Phys. B **285**, 481 (1987).

[208] L. Dixon, D. Friedan, E. Martinec, and S. Shenker, Nucl. Phys. B **282**, 13 (1987).

[209] L. Alvarez-Gaumé, G. Moore, and C. Vafa, Commun. Math. Phys. **106**, 1 (1986).

[210] E. Verlinde and H. Verlinde, Nucl. Phys. B **288**, 357 (1987).

[211] L. Alvarez-Gaumé, J.-B. Bost, G. Moore, P. Nelson, and C. Vafa, Commun. Math. Phys. **112**, 503 (1987).

[212] V. G. Knizhnik, Commun. Math. Phys. **112**, 567 (1987).

[213] M. Bershadsky and A. Radul, Int. J. Mod. Phys. A **02**, 165 (1987).

[214] R. Dijkgraaf, E. Verlinde, and H. Verlinde, Commun. Math. Phys. **115**, 649 (1988).

[215] J. D. Fay, *Theta Functions on Riemann Surfaces*, Vol. 352, Lecture Notes in Mathematics (Springer Berlin Heidelberg, 1973).

[216] D. Mumford, *Tata lectures on theta II*, Vol. 43 (Springer, 2007).

[217] J.-I. Igusa, *Theta Functions* (Springer Berlin Heidelberg, Berlin, Heidelberg, 1972).

[218] M. Caraglio and F. Gliozzi, JHEP **11** (2008) 076.

[219] S. Furukawa, V. Pasquier, and J. Shiraishi, Phys. Rev. Lett. **102**, 170602 (2009).

[220] V. Alba, L. Tagliacozzo, and P. Calabrese, Phys. Rev. B **81**, 060411 (2010).

[221] F. Gliozzi and L. Tagliacozzo, J. Stat. Mech. P01002 (2010).

[222] M. Fagotti and P. Calabrese, J. Stat. Mech. P04016 (2010).

[223] V. Alba, L. Tagliacozzo, and P. Calabrese, J. Stat. Mech. P06012 (2011).

[224] M. Fagotti, EPL **97**, 17007 (2012).

[225] M. A. Rajabpour and F. Gliozzi, J. Stat. Mech. P02016 (2012).

[226] P. Calabrese, J. Cardy, and E. Tonni, J. Stat. Mech. P11001 (2009).

[227] P. Calabrese, J. Stat. Mech. P09013 (2010).

[228] M. Headrick, A. Lawrence, and M. Roberts, J. Stat. Mech. P02022 (2013).

[229] B. Chen and J.-J. Zhang, JHEP **11** (2013) 164.

[230] T. Nishioka, S. Ryu, and T. Takayanagi, J. Phys. A **42**, 504008 (2009).

[231] P. Fonda, L. Giomi, A. Salvio, and E. Tonni, JHEP **02** (2014) 005.

[232] M. Rangamani and M. Rota, JHEP **10** (2014) 060.

[233] M. Kulaxizi, A. Parnachev, and G. Policastro, JHEP **09** (2014) 010.

[234] V. Enolski and T. Grava, Int. Math. Res. Not. **2004**, 1619 (2004).

[235] A. Coser, L. Tagliacozzo, and E. Tonni, J. Stat. Mech. P01008 (2014).

[236] C. De Nobili, A. Coser, and E. Tonni, J. Stat. Mech. P06021 (2015).

[237] A. Coser, E. Tonni, and P. Calabrese, J. Stat. Mech. P12017 (2014).

[238] A. Coser, E. Tonni, and P. Calabrese, J. Stat. Mech. P08005 (2015).

[239] A. Coser, E. Tonni, and P. Calabrese, arXiv:1508.00811 (2015).

[240] G. Ciarrapico, M. Torre, and L. Vendruscolo, BORIS **1**, 03 (2007).

[241] H. Exton, *Multiple hypergeometric functions and applications* (Ellis Horwood, 1976).

[242] V. Z. Enolski and T. Grava, Lett. Math. Phys. **76**, 187 (2006).

[243] F. Iglói and I. Peschel, EPL **89**, 40001 (2010).

[244] T. D. Schultz, D. C. Mattis, and E. H. Lieb, Rev. Mod. Phys. **36**, 856 (1964).

[245] J. I. Latorre, E. Rico, and G. Vidal, Quant. Inf. Comp. **4**, 26 (2003).

[246] L. Tagliacozzo, G. Evenbly, and G. Vidal, Phys. Rev. B **80**, 235127 (2009).

[247] G. Evenbly and G. Vidal, J. Stat. Phys. **145**, 891 (2011).

[248] S. R. White and R. M. Noack, Phys. Rev. Lett. **68**, 3487 (1992).

[249] G. Vidal, Phys. Rev. Lett. **91**, 147902 (2003).

[250] F. Verstraete and J. I. Cirac, Phys. Rev. B **73**, 094423 (2006).

[251] F. Pollmann, S. Mukerjee, A. M. Turner, and J. E. Moore, Phys. Rev. Lett. **102**, 255701 (2009).

[252] F. Verstraete, J. I. Cirac, J. I. Latorre, E. Rico, and M. M. Wolf, Phys. Rev. Lett. **94**, 140601 (2005).

[253] M. B. Hastings, I. González, A. B. Kallin, and R. G. Melko, Phys. Rev. Lett. **104**, 157201 (2010).

[254] L. Wang, Z.-C. Gu, F. Verstraete, and X.-G. Wen, arXiv:1112.3331 (2011).

[255] S. Humeniuk and T. Roscilde, Phys. Rev. B **86**, 235116 (2012).

[256] B. Pirvu, F. Verstraete, and G. Vidal, Phys. Rev. B **83**, 125104 (2011).

[257] F. Verstraete, D. Porras, and J. I. Cirac, Phys. Rev. Lett. **93**, 227205 (2004).

[258] P. Pippan, S. R. White, and H. G. Evertz, Phys. Rev. B **81**, 081103 (2010).

[259] N. Laflorencie, E. S. Sørensen, M.-S. Chang, and I. Affleck, Phys. Rev. Lett. **96**, 100603 (2006).

[260] P. Calabrese, M. Campostrini, F. Essler, and B. Nienhuis, Phys. Rev. Lett. **104**, 095701 (2010).

[261] J. Cardy and P. Calabrese, J. Stat. Mech. P04023 (2010).

[262] P. Calabrese and F. H. L. Essler, J. Stat. Mech. P08029 (2010).

[263] M. Fagotti and P. Calabrese, J. Stat. Mech. P01017 (2011).

[264] J. C. Xavier and F. C. Alcaraz, Phys. Rev. B **85**, 024418 (2012).

[265] M. Fannes, B. Nachtergaele, and R. F. Werner, Commun. Math. Phys. **144**, 443 (1992).

[266] T. Giamarchi, *Quantum physics in one dimension* (Oxford University Press, New York, 2004).

[267] M. P. Zaletel, J. H. Bardarson, and J. E. Moore, Phys. Rev. Lett. **107**, 020402 (2011).

[268] A. Chandran, V. Khemani, and S. L. Sondhi, Phys. Rev. Lett. **113**, 060501 (2014).

[269] A. Polkovnikov, K. Sengupta, A. Silva, and M. Vengalattore, Rev. Mod. Phys. **83**, 863 (2011).

[270] J. Eisert, M. Friesdorf, and C. Gogolin, Nature Phys. **11**, 124 (2015).

[271] P. Calabrese and J. Cardy, Phys. Rev. Lett. **96**, 136801 (2006).

[272] J.-S. Caux and F. H. L. Essler, Phys. Rev. Lett. **110**, 257203 (2013).

[273] D. Iyer and N. Andrei, Phys. Rev. Lett. **109**, 115304 (2012).

[274] A. J. Daley, C. Kollath, U. Schollwöck, and G. Vidal, J. Stat. Mech. P04005 (2004).

[275] S. R. White and A. E. Feiguin, Phys. Rev. Lett. **93**, 076401 (2004).

[276] G. Vidal, Phys. Rev. Lett. **98**, 070201 (2007).

[277] U. Schollwöck, Ann. Phys. **326**, 96 (2011).

[278] J. Cardy, Phys. Rev. Lett. **112**, 220401 (2014).

[279] M. Cheneau, P. Barmettler, D. Poletti, M. Endres, P. Schauß, T. Fukuhara, C. Gross, I. Bloch, C. Kollath, and S. Kuhr, Nature **481**, 484 (2012).

[280] S. Sotiriadis and J. Cardy, J. Stat. Mech. P11003 (2008).

[281] A. Gambassi and A. Silva, Phys. Rev. Lett. **109**, 250602 (2012).

[282] A. Gambassi and A. Silva, arXiv:1106.2671 (2011).

[283] M. Marcuzzi and A. Gambassi, Phys. Rev. B **89**, 134307 (2014).

[284] M. Nozaki, T. Numasawa, and T. Takayanagi, Phys. Rev. Lett. **112**, 111602 (2014).

[285] M. Nozaki, JHEP **10** (2014) 147.

[286] V. Eisler and I. Peschel, J. Stat. Mech. P06005 (2007).

[287] V. Eisler, D. Karevski, T. Platini, and I. Peschel, J. Stat. Mech. P01023 (2008).

[288] J.-M. Stéphan and J. Dubail, J. Stat. Mech. P08019 (2011).

[289] V. Eisler and I. Peschel, EPL **99**, 20001 (2012).

[290] M. Collura and P. Calabrese, J. Phys. A **46**, 175001 (2013).

[291] P. Calabrese, C. Hagendorf, and P. L. Doussal, J. Stat. Mech. P07013 (2008).

[292] J. Cardy, *Quantum Quench in Conformal Field Theory from a General Short-Ranged State*, talk at GGI conference "New quantum states of matter in and out of equilibrium", http://www.ggi.fi.infn.it/talkfiles/slides/talk2326.pdf, Florence, May 2012.

[293] S. Sotiriadis and J. Cardy, Phys. Rev. B **81**, 134305 (2010).

[294] A. Gambassi and P. Calabrese, EPL **95**, 66007 (2011).

[295] S. Sotiriadis, G. Takacs, and G. Mussardo, Phys. Lett. B **734**, 52 (2014).

[296] D. Fioretto and G. Mussardo, New J. Phys. **12**, 055015 (2010).

[297] S. Sotiriadis, D. Fioretto, and G. Mussardo, J. Stat. Mech. P02017 (2012).

[298] H. Casini, J. Stat. Mech. P08019 (2010).

[299] D. D. Blanco and H. Casini, Class. Quant. Grav. **28**, 215015 (2011).

[300] M. Headrick and T. Takayanagi, Phys. Rev. D **76**, 106013 (2007).

[301] J. Molina-Vilaplana and P. Sodano, JHEP **10** (2011) 011.

[302] I. A. Morrison and M. M. Roberts, JHEP **07** (2013) 081.

[303] N. Shiba, Phys. Rev. D **83**, 065002 (2011).

[304] M. Fagotti and P. Calabrese, Phys. Rev. A **78**, 010306 (2008).

[305] P. Calabrese, F. H. L. Essler, and M. Fagotti, Phys. Rev. Lett. **106**, 227203 (2011).

[306] P. Calabrese, F. H. L. Essler, and M. Fagotti, J. Stat. Mech. P07016 (2012).

[307] P. Calabrese, F. H. L. Essler, and M. Fagotti, J. Stat. Mech. P07022 (2012).

[308] M. J. Bhaseen, J. P. Gauntlett, B. D. Simons, J. Sonner, and T. Wiseman, Phys. Rev. Lett. **110**, 015301 (2013).

[309] A. M. Läuchli and C. Kollath, J. Stat. Mech. P05018 (2008).

[310] M. Cramer, C. M. Dawson, J. Eisert, and T. J. Osborne, Phys. Rev. Lett. **100**, 030602 (2008).

[311] M. Cramer and J. Eisert, New J. Phys. **12**, 055020 (2010).

[312] T. Barthel and U. Schollwöck, Phys. Rev. Lett. **100**, 100601 (2008).

[313] S. Sotiriadis, P. Calabrese, and J. Cardy, EPL **87**, 20002 (2009).

[314] I. Peschel and V. Eisler, J. Phys. A **45**, 155301 (2012).

[315] S. Sotiriadis and P. Calabrese, J. Stat. Mech. P07024 (2014).

[316] M. G. Nezhadhaghighi and M. A. Rajabpour, Phys. Rev. B **90**, 205438 (2014).

[317] B. Doyon, A. Lucas, K. Schalm, and M. J. Bhaseen, J. Phys. A **48**, 095002 (2015).

[318] T. Yu and J. H. Eberly, Science **323**, 598 (2009).

[319] C. T. Asplund, A. Bernamonti, F. Galli, and T. Hartman, arXiv:1506.03772 (2015).

[320] S. Leichenauer and M. Moosa, arXiv:1505.04225 (2015).

[321] A. Zamolodchikov and A. Zamolodchikov, Nucl. Phys. B **477**, 577 (1996).

[322] M. Fagotti, Phys. Rev. B **87**, 165106 (2013).

[323] L. Bucciantini, M. Kormos, and P. Calabrese, J. Phys. A **47**, 175002 (2014).

[324] M. Kormos, L. Bucciantini, and P. Calabrese, EPL **107**, 40002 (2014).

[325] B.-Q. B.-Q. Jin and V. E. Korepin, J. Stat. Phys. **116**, 79 (2004).

[326] P. Calabrese, M. Mintchev, and E. Vicari, Phys. Rev. Lett. **107**, 020601 (2011).

[327] P. Calabrese, M. Mintchev, and E. Vicari, J. Stat. Mech. P09028 (2011).

[328] G. Vidal, J. I. Latorre, E. Rico, and A. Kitaev, Phys. Rev. Lett. **90**, 227902 (2003).

[329] F. Iglói and R. Juhász, EPL **81**, 57003 (2008).

[330] J. I. Latorre and A. Riera, J. Phys. A **42**, 504002 (2009).

[331] V. Eisler and Z. Zimborás, New J. Phys. **17**, 53048 (2015).

[332] S. Sachdev, *Quantum phase transitions* (Cambridge University Press, 2001).

[333] P. Facchi, G. Florio, C. Invernizzi, and S. Pascazio, Phys. Rev. A **78**, 052302 (2008).

[334] J. C. Xavier and F. C. Alcaraz, Phys. Rev. B **83**, 214425 (2011).

[335] M. Dalmonte, E. Ercolessi, and L. Taddia, Phys. Rev. B **84**, 085110 (2011).

[336] M. Dalmonte, E. Ercolessi, and L. Taddia, Phys. Rev. B **85**, 165112 (2012).

[337] H. Kleinert, *Path integrals in quantum mechanics, statistics, polymer physics, and financial markets* (World Scientific, 2009).

[338] H. Bateman and A. Erdélyi, *Higher Trascendental Functions, Vol. I* (McGraw-Hill, New York, 1953).

[339] B. Derrida, M. Mendès France, and J. Peyrière, J. Stat. Phys. **45**, 439 (1986).

[340] E. Perlmutter, M. Rangamani, and M. Rota, arXiv:1506.01679 (2015).